Doctoral Dissertation
博士論文

Theoretical study of spin transport in a magnetic junction with two-dimensional electron gas
(二次元電子ガスを用いた磁気接合におけるスピン輸送の理論研究)

A Dissertation Submitted for the Degree of Doctor of Philosophy
December 2024
令和６年１２月博士 (理学) 申請

Department of Physics, Graduate School of Science,
The University of Tokyo
東京大学大学院理学系研究科物理学専攻

Masaki Yama
山 正樹

Abstract

The Rashba spin-orbit coupling (SOC) and Dresselhaus SOC, arising from spatial inversion asymmetry, have drawn significant attention due to their role in spin-momentum locking and their potential applications in advancing gate-tunable spintronic devices. This dissertation develops a comprehensive theoretical framework for spin transport phenomena in systems where two-dimensional electron gases (2DEGs) with these SOCs are interfaced with ferromagnetic insulators (FIs).

First, we develop a theory for spin pumping (SP) from an FI to a 2DEG. Spin pumping, induced by ferromagnetic resonance (FMR) in the FI under microwave irradiation, enhances the linewidths of the FMR absorption spectrum, associated with an increase in the Gilbert damping. We calculate this enhancement with the vertex corrections and reveal that it exhibits prominent peaks at both low and high FMR frequencies. Notably, when the Rashba and Dresselhaus SOCs are of equal strength, the width of the low-frequency peak vanishes, reflecting the spin conservation law in the 2DEG. Furthermore, the theory elucidates the behavior of FMR resonance frequency shifts induced by SP.

Next, we investigate the inverse Rashba-Edelstein effect (IREE), wherein spins injected from the FI into the 2DEG via SP are converted into a charge current. We analyze the spin density and charge current density induced by the IREE with respect to their dependence on the FMR resonance frequency, the orientation of localized FI spins, and the ratio of the Rashba to Dresselhaus SOC strengths. These dependencies are shown to originate from spin splitting and spin textures of the 2DEG Fermi surface caused by the SOCs. This analysis not only reveals the physical mechanisms underlying the IREE but also provides insights for the design of spintronic devices with various tunable functionalities.

Finally, we theoretically explore the Rashba-Edelstein magnetoresistance (REMR), which describes the change in electrical resistance of the 2DEG depending on the orientation of localized spins in the FI under the application of a DC charge current. Our results show that the REMR is highly sensitive to the state of the FI-2DEG interface: Its sign reverses between dirty and clean interface conditions. This reversal is attributed to differing dominant mechanisms—static processes, such as transverse magnetic field effects, dominate in dirty interfaces, while dynamical processes, such as magnon absorption and emission, dominate in clean interfaces.

While traditional theoretical studies in spintronics have predominantly relied on phenomeno-

logical approaches, such as the Landau-Lifshitz-Gilbert (LLG) equation and spin-mixing conductance, this dissertation consistently employs a microscopic Hamiltonian-based framework. This approach provides a robust theoretical foundation for spintronics and offers guidelines for the development of semiconductor spintronic devices with versatile functionalities.

Acknowledgements

During my doctoral studies and in the process of writing this dissertation, I received warm support and invaluable guidance from many individuals. I would like to take this opportunity to express my deepest gratitude.

This research was supported by JST SPRING (Grant No. JPMJSP2108) and JSPS KAKENHI (Grant No. JP24KJ0624). Furthermore, a three-month research stay in Germany was made possible through the International Student Dispatch Program of the Institute for Solid State Physics, The University of Tokyo. I am deeply grateful for these financial supports.

I am sincerely grateful to my supervisor, Takeo Kato, for providing continuous guidance throughout my master and doctoral studies. Through discussions and guidance on research directions, I gained comprehensive understanding of diverse research insights, methodologies, and theories. His meticulous advice on conference presentations, manuscript preparation, and research funding proposals greatly contributed to building my academic foundation. This thoughtful and dedicated supervision enabled me to lead a fulfilling and rewarding research life, for which I am sincerely grateful.

I would also like to express my sincere gratitude to Mamoru Matsuo for sharing profound expertise and creative insights in the field of spintronics. His valuable advice during research discussions and manuscript preparation played a crucial role in advancing my work.

I extend my great appreciation to Taisuke Ozaki, who provided insightful guidance as a secondary advisor under the SPRING GX program. Regular discussions and his expertise in first-principle calculations greatly enhanced my understanding and enriched the scope of my research.

I am deeply indebted to Yusuke Kato and Yuta Suzuki for their insightful discussions, which allowed me to acquire valuable knowledge in theoretical modeling using the Boltzmann equation. In particular, I would like to express my heartfelt appreciation to Yuta Suzuki for offering constructive and detailed feedback on specific calculations.

I would also like to extend my sincere thanks to Makoto Kohda, Hao Ding, and Jun Ishihara of Tohoku University for discussing the Rashba and Dresselhaus SOCs with me. Their experimental perspectives greatly enriched my understanding and broadened the scope of my research.

During my three-month research stay at the Forschungszentrum Jülich in Germany, I received considerable support from many individuals. I am sincerely grateful to Dongwook Go and Yuriy

Mokrousov for generously sharing their valuable expertise in orbitronics. I also deeply appreciate the thoughtful care and attention provided by Stefan Blügel regarding my life and health during my stay. I am especially thankful to Hiroshi Katsumoto for his extensive support in managing my daily life, and to both him and Johannes Wasmer for accompanying me to the hospital when I experienced health issues. Their kindness and assistance were truly invaluable. Additionally, discussions and interactions with Guihyun Han were highly enriching, and I am very appreciative of the insights I gained through our exchanges.

I would like to thank all members of the Kato Research Group for their substantial support. In particular, I am deeply thankful to Tomohiro Tamaya for engaging in extensive discussions on my research and assisting with the preparation of research funding proposals. My peer, Takuto Ishikawa, shared this academic life with me, and our discussions and joint study sessions provided invaluable mutual support. The experiences I gained through collaborative research with Masahiro Tatsuno during my master program also proved highly beneficial for my doctoral research. Engaging with Tsuyoshi Yamamoto, Tetsuya Sato, Kota Fukuzawa, Koji Yamada, Naoki Nishimura, Kaiji Hosokawa, Fumihiro Murabayashi, and Ryuji Okuyama greatly enhanced the quality and enjoyment of my research activities. I am also grateful to Hiroko Eguchi, the secretary of Kato's research group, who provided administrative support in managing research funding procedures.

Finally, I would like to extend my sincere gratitude to everyone who supported and contributed to this research. Without their assistance, the completion of this doctoral dissertation would not have been possible. Thank you very much.

List of Publications

The following is a list of publications related to the work in this dissertation.

Journal Articles

1. M. Yama, M. Matsuo, and T. Kato, "Effect of vertex corrections on the enhancement of Gilbert damping in spin pumping into a two-dimensional electron gas", Phys. Rev. B **107** 174414 (2023).
   DOI: https://doi.org/10.1103/PhysRevB.107.174414

2. M. Yama, M. Matsuo, and T. Kato, "Theory of inverse Rashba-Edelstein effect induced by spin pumping into a two-dimensional electron gas", Phys. Rev. B **108** 144430 (2023).
   DOI: https://doi.org/10.1103/PhysRevB.108.144430

Preprints

1. M. Yama, M. Matsuo, and T. Kato, "Microscopic Theory of Rashba-Edelstein Magnetoresistance", arXiv:2409.00874 (2024).
   DOI: https://doi.org/10.48550/arXiv.2409.00874

Conference Proceedings

1. M. Yama, M. Matsuo, and T. Kato, "Theory of spin pumping and inverse Rashba-Edelstein effect in a two-dimensional electron gas", Proc. SPIE 13119, Spintronics XVII, 131190J (2024).
   DOI: https://doi.org/10.1117/12.3027001

2. M. Yama, M. Matsuo, and T. Kato, "Theory of spin pumping and inverse Rashba-Edelstein effect in a two-dimensional electron gas (Erratum)", Proc. SPIE 13119, Spintronics XVII, 131190O (2024).
   DOI: https://doi.org/10.1117/12.3055848

Contents

Chapter 1

Introduction

This chapter outlines the background of this dissertation. Section 1.1 introduces the background of spintronics, followed by Sec.1.2, which addresses the extension of spintronics to two-dimensional electron gases (2DEGs). Section 1.3 presents the research purposes of this dissertation, and finally, Sec.1.4 describes the structure of this dissertation.

1.1 Spintronics

Electrons possess two degrees of freedom: charge and spin. While in semiconductors such as transistors and diodes, the technology to control the flow of electric charges carried by electrons to extract various functions is called electronics, the field of electronics that also utilizes the properties of spin is called *spintronics*. An early example of the spintronic device that used spin degrees of freedom is the application of anisotropic magnetoresistance (AMR) in the read heads of hard disk drives (HDDs) [1]. Progress in microfabrication methods, such as molecular beam epitaxy (MBE) during the mid-1980s, enabled the fabrication of multilayers with nanometer-scale thickness [2]. This progress led to the discovery of giant magnetoresistance (GMR) in magnetic multilayers, marking the beginning of spintronics, a new field focusing on the microscopic utilization of spin degrees of freedom [3–5]. Subsequently, tunneling magnetoresistance (TMR) was observed at room temperature by replacing the nonmagnetic metal spacer in GMR structures with an insulating barrier, finally achieving a magnetoresistance of 200% [6–9]. TMR has also been applied to magnetoresistive random-access memory (MRAM), offering advantages such as non-volatility, low power consumption, and instantaneous startup, inspiring active research in this field.

In development of MRAM, control of a torque for reversing magnetization in ferromagnets is one of the key ingredients. One way to generate a torque on magnetization is to utilize spin transfer torque (STT), due to a spin current (a flow of spin angular momentum) induced by charge current in a ferromagnetic metal. However, reversal of magnetization by STT requires high energy consumption. To address this issue, research has focused on another method called

spin-orbit torque (SOT), which utilizes spin-orbit interactions in a heavy metal. For example, by applying a charge current to a metal with strong spin-orbit interactions, a spin current is generated in the direction perpendicular to the charge current, resulting in spin accumulation at surfaces or interfaces. This phenomenon, which is called spin Hall effect (SHE), can be used to reverse magnetization of an adjacent ferromagnet without passing a charge current directly into the magnetic layer [1, 10–12].

To further advance spintronic devices, it is not enough to rely solely on the equilibrium spin polarization of ferromagnetic materials. It is also necessary to generate, control, and detect non-equilibrium spins [13, 14]. A representative method of spin current generation involves charge-to-spin conversion driven by spin-orbit interaction such as SHE. As for spin-to-charge conversion, the inverse spin Hall effect (ISHE) [15, 16] is utilized to electrically detect spin polarization. Moreover, optical methods such as the magneto-optical Kerr effect and Faraday rotation are commonly applied to detect spin accumulation [14]. Spin pumping (SP) [17–20], a method of injecting spins into adjacent materials by microwave irradiation of a ferromagnet, is also employed widely for spin injection into adjacent materials.

1.2 Two-Dimensional Electron Gas (2DEG)

Spintronics combined with semiconductor technology has been an attracting choice for realizing integrated devices of various functionalities [14, 21]. A notable example is the field-effect spin transistor (Spin-FET), proposed by Datta and Das in 1990 [22]. The Spin-FET allows for efficient spin manipulation by utilizing gate voltages instead of external magnetic fields. It is expected to facilitate integration with existing semiconductor-based electronic devices [21]. Since the interfacial electronic states govern these spin-dependent transport phenomena in these devices, two-dimensional electron gas (2DEG) plays an essential role.

As illustrated in Fig. 1.1, the Spin-FET consists of a 2DEG with the Rashba SOC, sandwiched between two ferromagnetic electrodes [13]. When electrons with spins aligned in the direction indicated by the black arrow are injected into the 2DEG from the source electrode on the left, these spins experience an effective magnetic field $\mathbf{\Omega}$ generated by the Rashba SOC. This interaction causes the spins to precess around $\mathbf{\Omega}$. The precession angle is determined by the strength of the effective magnetic field, which can be tuned by a gate electrode perpendicular to the plane. As a result, the spin precession angle can be precisely controlled via the gate voltage. At the drain electrode, which is the ferromagnetic electrode on the right, only electrons with spins aligned to the drain's spin orientation contribute to the charge current, while electrons with opposite spin orientations are blocked, resulting in no charge current flow. Therefore, the Spin-FET operates as a spintronic switching device, in which the charge current flow is modulated by adjusting the voltage applied to the gate electrode. The Rashba SOC is central to this switching mechanism. The ability of the Rashba SOC to generate an effective magnetic

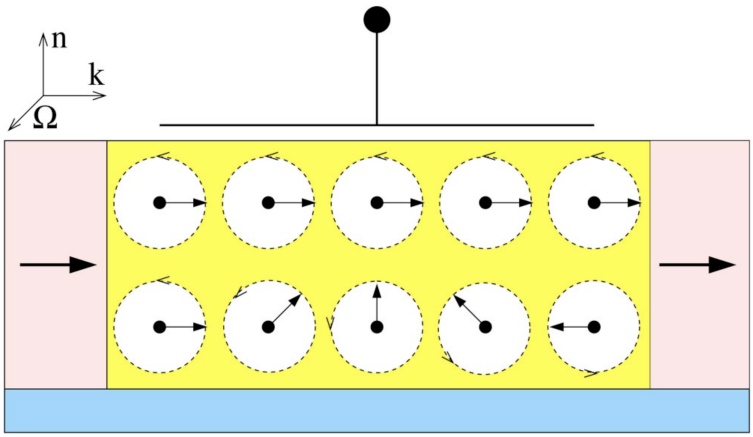

Figure 1.1: Schematic illustration of the field-effect spin transistor (Spin-FET) proposed by Datta and Das. The 2DEG with the Rashba SOC, shown in yellow, is sandwiched between two ferromagnetic electrodes depicted in red. The black arrow indicates the spin direction. The strength of the Rashba SOC can be tuned via the gate electrode. Adapted from Ref. [13].

field, induce spin splitting in the energy bands, and allow tunability via the gate electrode are indispensable properties for the realization of spintronic devices.

For 2DEGs, various spin-related phenomena can be induced by the Rashba spin-orbit coupling (Rashba SOC), observed in systems with broken structural inversion symmetry [23, 24]. Since the Rashba SOC is an interface effect, its impact is more significant in 2DEGs formed in systems such as semiconductor heterostructures or LAO/STO interfaces, compared to three-dimensional systems [25]. Furthermore, the Rashba SOC in 2DEGs exhibits high tunability via gate voltage [26], enabling precise control over the effective magnetic field it generates and facilitating localized manipulation of electron spins. The spin-FET features a structure with a 2DEG possessing Rashba SOC, controlling the precession rate of spins by tuning the Rashba SOC strength through gate voltage [22]. The Rashba SOC in 2DEG also leads to spin-momentum locking, enabling the generation of non-equilibrium spin accumulation via the Rashba-Edelstein effect (REE) [27–32]. This efficient charge-to-spin conversion is expected to be used in next-generation spintronics devices, such as SOT-MRAM [25]. Its inverse phenomenon, called the inverse Rashba-Edelstein effect (IREE) [33–38], is utilized for detection of a spin current. The Rashba SOC-based electron spin resonance (ESR), which does not require an external magnetic field, also shows potential for quantum information technologies [14, 39, 40]. Additionally, devices such as Aharonov-Casher (AC) spin interferometers and Stern-Gerlach spin filters have been designed based on the Rashba SOC [14, 39, 40].

In zinc-blende III-V and II-IV semiconductors, in addition to the Rashba SOC, Dresselhaus spin-orbit coupling (Dresselhaus SOC) [41] arises from broken bulk inversion symmetry. While both SOCs induce spin-momentum locking, they generate distinct spin textures [42]. In systems where the Rashba and Dresselhaus SOCs coexist, diverse spin textures can be achieved by tuning

the SOC ratio through gate voltage [14, 26]. Notably, when the strengths of the Rashba and Dresselhaus SOCs are equal, a persistent spin helix (PSH) state emerges [43–47], leading to prolonged electron spin lifetimes. Research on the PSH state is actively progressing, with a focus on its potential for device applications in long-distance spin transport [14, 40].

1.3 Purpose of the Dissertation

As described in previous sections, 2DEGs with the Rashba and Dresselhaus SOCs are attracting significant attention in spintronics due to features such as gate-tunable charge-spin interconversion and localized spin manipulation [14, 25, 39, 40]. In this dissertation, spin transport in junction systems comprising a ferromagnetic insulator (FI) and 2DEG with the Rashba and Dresselhaus SOCs is discussed theoretically. Specifically, the focus is placed on three research subjects, which are briefly summarized as follows [48–50] (for a detail, see Sec. 2.6).

First, a theoretical framework is developed for spin pumping (SP) induced by ferromagnetic resonance (FMR) when the FI is exposed to microwave irradiation [48]. SP transfers spins from the FI into the 2DEG, resulting in an enhancement of the Gilbert damping in the localized spins of the FI. This enhancement reflects the properties of the 2DEG as the adjacent material, making spin pumping a probe for exploring the 2DEG's characteristics. By analyzing the behavior of the enhanced Gilbert damping, we elucidate the properties of the 2DEG with coexisting the Rashba and Dresselhaus SOCs. When these SOCs have equal magnitudes, the spin of 2DEG electrons is conserved. In this case, it is demonstrated that the enhancement of the Gilbert damping exhibits qualitatively different behaviors depending on whether the vertex corrections for impurity scattering are included.

Next, a theoretical framework is established for the spin-charge conversion phenomenon, in which spins injected from the FI into the 2DEG via SP are converted into a charge current in the 2DEG through the inverse Rashba-Edelstein effect (IREE) [49]. Using the Boltzmann equation, we derive analytical expressions for the spin density and charge current density induced by the IREE in the 2DEG. Their dependence on the orientation of the localized spins in the FI, the resonance frequency of the FMR, and the ratio of the two SOCs is clarified. We elucidate the physical mechanism underlying the IREE and discuss its relationship with experimental observations. Additionally, results obtained by computing the collision term for impurity scattering of 2DEG electrons using Fermi's golden rule are compared with those obtained using the relaxation-time approximation [51, 52]. It is revealed that these two approaches yield qualitatively different behaviors when the magnitudes of the Rashba and Dresselhaus SOCs are equal.

Finally, a theoretical framework is developed for the Rashba-Edelstein magnetoresistance (REMR), in which the electrical resistance of the 2DEG depends on the orientation of the localized spins in the FI under the application of a DC charge current [50]. Using the Boltzmann

equation, we analyze the modulation of spin density and charge current density in the 2DEG induced by the REMR, focusing on their dependence on the orientation of the FI's localized spins and the ratio of the two SOCs. Two types of interfaces are considered for the FI-2DEG interface: the dirty interface, in which the in-plane momentum of 2DEG electrons is not conserved, and the clean interface, in which it is conserved. The behavior of the REMR in each case is clarified, revealing that the sign of the REMR reverses between these scenarios. The underlying physical mechanisms responsible for this sign reversal are identified, and comparisons are made with prior experimental studies on the REMR.

In spintronics, the generation, control, and detection of spins are fundamental processes [13, 14]. In this dissertation, we develop theoretical frameworks for spin generation in the contexts of SP and the IREE, as well as spin detection in the REMR. A central focus of this dissertation is establishing a comprehensive theory for the generation and detection of spins in a 2DEG with the Rashba and Dresselhaus SOCs.

1.4 Structure of the Dissertation

This dissertation is structured as follows. Chapter 2 reviews prior studies and, building on this foundation, outlines the motivation and objectives of this dissertation. Chapter 3 introduces a microscopic Hamiltonian to describe the FI-2DEG junction system, which forms the basis for the analyses in Chap. 4, 5, and 6. In Chap. 4, the theory of spin pumping (SP) is developed, clarifying the enhancement of the Gilbert damping of localized spins in the FI induced by SP [48]. Chapter 5 constructs the theoretical framework of the inverse Rashba-Edelstein effect (IREE) arising from spin injection from the FI into the 2DEG via SP [49]. Chapter 6 develops the theory of the Rashba-Edelstein magnetoresistance (REMR) and examines the spin density and charge current density induced in the 2DEG by the REMR under both dirty and clean FI-2DEG interface conditions [50]. Finally, Chap. 7 provides a summary of this dissertation and future challenges.

Chapter 2

Review

The precise control of electron spin is essential for the development of spintronics devices. While electron spin can be manipulated by external magnetic fields due to its magnetic moment in principle, its implementation is considered challenging in practice. An alternative approach to controlling spin involves the use of spin-orbit interaction. The spin-orbit interaction, a relativistic effect, enables the conversion of electric fields into effective magnetic fields felt by the electron spin. In solid-state systems, the spin-orbit interaction is significantly stronger than in vacuum, allowing for precise electrical control of spin by using the spin-orbit interaction without applying an external magnetic field. From this perspective, the field-effect spin transistor (Spin-FET) has been proposed as a spintronics device [22]. In Spin-FETs, spin is controlled by a gate electrode rather than an external magnetic field, using the Rashba spin-orbit coupling (SOC) [23, 24, 42], a type of spin-orbit interaction. The Rashba SOC arises from the breaking of structure inversion symmetry in surface systems and junction interfaces, while the Dresselhaus SOC [41, 42], found in III-V or II-IV semiconductors with zinc-blende crystal structures, results from the breaking of crystal inversion symmetry.

This chapter will review the origins of these SOCs and examine previous studies on phenomena such as charge-spin conversion and magnetoresistance effects resulting from these SOCs. Additionally, the chapter will provide an overview of spin pumping, a method of injecting spin into various materials, including those containing 2DEGs. Finally, the purpose of this dissertation will be stated in a detail.

2.1 Spin-Orbit Coupling (SOC)

2.1.1 Rashba spin-orbit coupling

Rashba SOC appears in systems with inversion asymmetry and leads to spin splitting. This type of SOC is reviewed following Ref. [53]. The appearance of such spin splitting is intuitively explained as follows. If a crystal has spatial inversion symmetry, the energy eigenvalues of

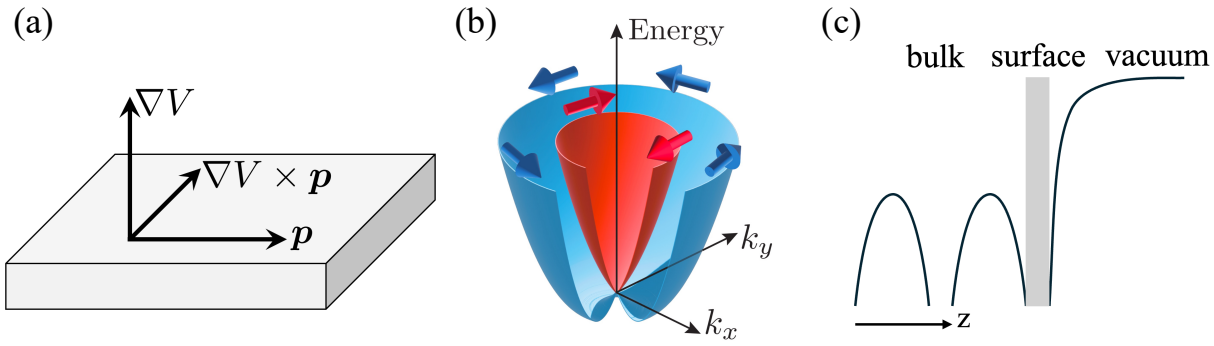

Figure 2.1: (a) Schematic diagram of a surface system. Electrons in the surface system, moving with momentum $\boldsymbol{p}$, experience an effective Zeeman field $\nabla V \times \boldsymbol{p}$ due to the atomic spin-orbit interaction. As a result, the electron energy bands undergo spin splitting. (b) Spin splitting of the conduction electron energy bands due to the Rashba SOC. Adapted from Ref. [48]. (c) Electric field perpendicular to the surface. Near the surface atoms, a strong nuclear potential results in a large out-of-plane electric field E_z.

electrons satisfy $E(\boldsymbol{k},\uparrow) = E(-\boldsymbol{k},\uparrow)$, where $\boldsymbol{k}$ and $\uparrow$ ($\downarrow$) are the wavevector and up-spin (down-spin) state of electrons, respectively. Combining this relation with time-reversal symmetry represented by $E(\boldsymbol{k},\uparrow) = E(-\boldsymbol{k},\downarrow)$, different spin states becomes degenerate ($E(\boldsymbol{k},\uparrow) = E(\boldsymbol{k},\downarrow)$), leading to no spin splitting. This indicates that spatial inversion asymmetry is required to realize spin splitting in electron bands.

The origin of Rashba SOC lies in the atomic spin-orbit interaction. The Hamiltonian of electrons in a crystal, considering the atomic spin-orbit interaction, can be expressed as follows:

$$H = -\frac{\hbar^2}{2m}\Delta + V_0(\boldsymbol{r}) + \frac{\hbar}{4m^2c^2}\hat{\boldsymbol{\sigma}} \cdot (\nabla V \times \boldsymbol{p}). \tag{2.1}$$

Here, m represents the electron mass, $V_0(\boldsymbol{r})$ denotes the periodic potential of the crystal, c is the speed of light, and $\hat{\boldsymbol{\sigma}}$ stands for the Pauli matrices. Now, consider a situation in which electrons in a 2DEG on the x-y plane surface move with momentum $\boldsymbol{p}$, as shown in Fig. 2.1(a). These electrons experience an electric field in the z-direction perpendicular to the surface, $\nabla V = (0, 0, E_z)$, which results in $\nabla V \times \boldsymbol{p}$ pointing in the in-plane direction. Focusing on the spin-orbit interaction term, the second term in Eq. (2.1), we can interpret that the electrons experience an effective Zeeman field $\nabla V \times \boldsymbol{p}$. Consequently, the Rashba effect arises, leading to spin splitting of the electron energy bands as

$$E(k) = \frac{\hbar^2 k^2}{2m^*} \pm \alpha k, \tag{2.2}$$

where m^* is the effective mass of the electron, α denotes the magnitude of the Rashba SOC, and $k \equiv |\boldsymbol{k}|$. The resultant spin-splitting energy band is shown in Fig. 2.1(b).

From a microscopic viewpoint, the Rashba SOC originates from an out-of-plane electric

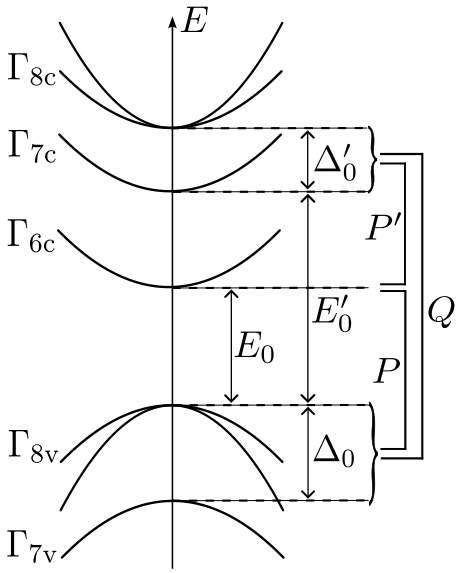

Figure 2.2: Energy bands of materials belonging to point groups T_d or O_h, considering the atomic spin-orbit interaction.

field at an interface. As shown in Fig. 2.1(c), this interfacial electric field reaches large values near the nuclei of the surface atoms. The magnitude of α can be evaluated using this out-of-plane electric field E_z as follows [54, 55]:

$$\alpha \propto \int dz\, E_z |\psi|^2. \tag{2.3}$$

Here, ψ represents the wave function of the surface band. This wave function oscillates intensely near the surface due to the influence of the strong nuclear potential from the atoms, resulting in a larger amplitude. Thus, heavier elements with stronger atomic spin-orbit interactions tend to have larger Rashba SOC magnitudes, leading to greater spin-splitting in the energy bands. For instance, bismuth (Bi), which is the heaviest atom among non-radioactive elements, is known to exhibit significant Rashba SOC [56]. Particularly, on the Bi/Ag(111) adsorption surface, a remarkably large Rashba SOC with $\alpha = 3.05$ eVÅ—even greater than that of Bi surfaces—has been observed via angle-resolved photoemission spectroscopy (ARPES) [57].

2.1.2 SOC in semiconductors

The Rashba and Dresselhaus SOCs in semiconductors are next reviewed following Ref. [42]. The Hamiltonian for the Rashba SOC is derived as follows. The energy bands for materials belonging to the point groups O_h (diamond structure) or T_d (zinc blende structure) are shown in Figure 2.2. Due to the atomic spin-orbit interaction, the p-orbital bands in the valence band split into the heavy hole and light hole bands (Γ_{8v}) and the spin-split off band (Γ_{7v}). By using the

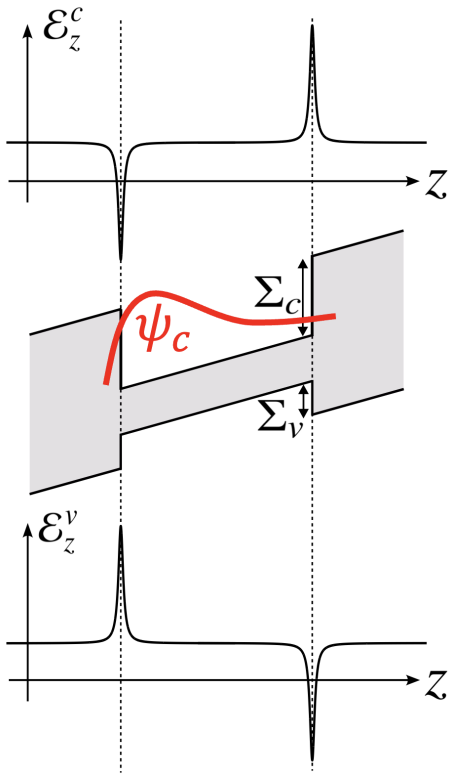

Figure 2.3: Central panel: Quantum well (QW) with an applied external electric field and wave function of conduction electrons, ψ_c. Top (bottom) panel: Position dependence of the effective electric field along the out-of-plane axis for the conduction band (valence band) in the QW.

wavefunctions of Γ_{8v}, Γ_{7v}, and the s-orbital conduction band (Γ_{6c}) as the basis states, denoted by $\psi_{8v}, \psi_{7v}, \psi_c$, the matrix elements of the Hamiltonian in Eq. (2.1) within the framework of the extended Kane model are calculated. This leads to the following eigenvalue equation for the wavefunction of the conduction electrons:

$$\begin{aligned}
&\Big\{\frac{P^2}{3}\Big[\frac{2}{E_0}+\frac{1}{E_0+\Delta_0}\Big]k^2 + V_c - \frac{P^2}{3}\Big[\frac{1}{E_0}-\frac{1}{E_0+\Delta_0}\Big]\frac{e}{\hbar}\hat{\boldsymbol{\sigma}}\cdot\boldsymbol{B} \\
&+\frac{eP^2}{3}\Big[\frac{1}{E_0^2}-\frac{1}{(E_0+\Delta_0)^2}\Big]\hat{\boldsymbol{\sigma}}\cdot\boldsymbol{k}\times\boldsymbol{\mathcal{E}}_v - \frac{eP^2}{6}\Big[\frac{2}{E_0^2}+\frac{1}{(E_0+\Delta_0)^2}\Big]\nabla\cdot\boldsymbol{\mathcal{E}}_v \\
&-\frac{P^2}{3}\Big[\frac{2}{E_0^2}+\frac{1}{(E_0+\Delta_0)^2}\Big]\{V_c-V_v,k^2\}+\frac{P^2}{3}\Big[\frac{1}{E_0^2}-\frac{1}{(E_0+\Delta_0)^2}\Big]\frac{e}{\hbar}(V_c-V_v)\hat{\boldsymbol{\sigma}}\cdot\boldsymbol{B}\Big\}\tilde{\psi}_c = \tilde{E}\tilde{\psi}_c.
\end{aligned} \tag{2.4}$$

Here, $\tilde{\psi}_c$ represents the conduction electron wavefunction incorporating the effects of the valence band and is defined as follows:

$$\tilde{\psi}_c = \Big[1+\frac{P^2}{12}\Big(\frac{2k^2-(e/\hbar)\hat{\boldsymbol{\sigma}}\cdot\boldsymbol{B}}{E_0}+\frac{k^2+(e/\hbar)\hat{\boldsymbol{\sigma}}\cdot\boldsymbol{B}}{E_0+\Delta_0}\Big)\Big]\psi_c. \tag{2.5}$$

Here, $\boldsymbol{k} = (k_x, k_y, k_z)$ is an electron wavenumber, $\hat{\boldsymbol{\sigma}}$ is the Pauli matrix, E_0 and Δ_0 represent the energy splitting widths shown in Fig. 2.2, and P is defined as $P = \frac{\hbar}{m}\langle S|p_x|X\rangle$, where $|S\rangle$ and $|X\rangle$ are the eigenstates of the s-orbital of Γ_{6c} and the p_x-orbital of Γ_{8v}, Γ_{7v}, respectively. Additionally, $\boldsymbol{B}$ denotes the Zeeman magnetic field, V_c (V_v) is the effective potential for the conduction (valence) band, and $\boldsymbol{\mathcal{E}}_c = \nabla V_c/e$ ($\boldsymbol{\mathcal{E}}_v = \nabla V_v/e$) represents the effective electric field in the conduction (valence) band. The potentials V_c and V_v are defined as follows:

$$V_c(\boldsymbol{r}) = V(\boldsymbol{r}) + E_c(\boldsymbol{r}) - \langle E_c\rangle, \;\; V_v(\boldsymbol{r}) = V(\boldsymbol{r}) + E_v(\boldsymbol{r}) - \langle E_v\rangle. \tag{2.6}$$

Here, $V(\boldsymbol{r})$ represents the external potential or the built-in potential at junction interfaces. Additionally, $E_c(\boldsymbol{r})$ ($E_v(\boldsymbol{r})$) denotes the band-edge energy of the conduction (valence) band, with $\langle E_c\rangle$ ($\langle E_v\rangle$) being its spatial average. The first term in the second line of Eq. (2.4),

$$\frac{eP^2}{3}\Big[\frac{1}{E_0^2} - \frac{1}{(E_0+\Delta_0)^2}\Big]\hat{\boldsymbol{\sigma}}\cdot\boldsymbol{k}\times\boldsymbol{\mathcal{E}}_v, \tag{2.7}$$

represents the Rashba SOC term. Using the spatial average of $\boldsymbol{\mathcal{E}}_v$, we obtain the Hamiltonian for the Rashba SOC in the following form:

$$H_R = \alpha(k_y\hat{\sigma}_x - k_x\hat{\sigma}_y). \tag{2.8}$$

This Rashba SOC leads to spin splitting of the Fermi surface of conduction electrons, as already shown in Fig. 2.1(b).

The difference between the effective electric fields of the conduction and valence bands, $\boldsymbol{\mathcal{E}}_c$ and $\boldsymbol{\mathcal{E}}_v$, is examined in the quantum well (QW) along the z-direction in the central panel of Fig. 2.3. An external electric field $\mathcal{E}_z^{\text{ext}} = \partial_z V/e$ is applied to this QW, and the effective electric field for the conduction band can be expressed as follows:

$$\mathcal{E}_z^c = \partial_z(V + E_c(z))/e = \mathcal{E}_z^{\text{ext}} + \partial_z E_c(z)/e. \tag{2.9}$$

The spatial dependence of this $\mathcal{E}_z^c$ is shown in the top panel of Fig. 2.3. In a 2DEG on the x-y plane, the average value of the conduction electron's momentum in the z-direction is zero. Therefore, by Ehrenfest's theorem, the expectation value of $\mathcal{E}_z^c$ also becomes zero:

$$\langle\mathcal{E}_z^c\rangle_c = 0. \tag{2.10}$$

Here, $\langle\cdots\rangle_c$ denotes the quantum mechanical expectation value taken using the conduction electron wavefunction shown in the central panel of Fig 2.3. Next, the effective electric field for the valence band is given by

$$\mathcal{E}_z^v = \partial_z(V + E_v(z))/e = \mathcal{E}_z^{\text{ext}} + \partial_z E_v(z)/e. \tag{2.11}$$

The spatial dependence of this effective potential is shown in the bottom panel of Fig. 2.3. It is evident that this effective potential has the opposite sign to $\mathcal{E}_z^c$ in the top panel of Fig. 2.3, and from Eq. (2.10), it can be concluded that the expectation value of $\mathcal{E}_z^v$ with respect to the conduction electron wavefunction is not zero.

$$\langle \mathcal{E}_z^v \rangle_c \neq 0. \tag{2.12}$$

The specific expression for $\langle \mathcal{E}_z^v \rangle_c$ can be determined as follows. First, from Eqs. (2.9) and (2.10), the following equation is obtained:

$$-\langle \partial_z E_c(z)/e \rangle = \langle \mathcal{E}_z^{\rm ext} \rangle. \tag{2.13}$$

Then, by denoting the band offsets of the conduction and valence bands as Σ_c and Σ_v, respectively, and using Eq. (2.13), we obtain the following equation:

$$\langle \partial_z E_v(z)/e \rangle = -\frac{\Sigma_v}{\Sigma_c} \langle \partial_z E_c(z)/e \rangle = \frac{\Sigma_v}{\Sigma_c} \langle \mathcal{E}_z^{\rm ext} \rangle. \tag{2.14}$$

Using this, we can calculate the expectation value of Eq. (2.9) as follows:

$$\langle \mathcal{E}_z^c \rangle = \langle \mathcal{E}_z^{\rm ext} \rangle + \langle \partial_z E_c(z)/e \rangle = \frac{\Sigma_c + \Sigma_v}{\Sigma_c} \langle \mathcal{E}_z^{\rm ext} \rangle. \tag{2.15}$$

From this equation and Eq. (2.7), it can be seen that the magnitude of the Rashba SOC is proportional to the external electric field.

As described above, the Rashba SOC appears in materials with structure inversion asymmetry, such as Si and Ge with point group $\mathrm{O_h}$, and GaAs and InAs with point group $\mathrm{T_d}$. On the other hand, since $\mathrm{T_d}$ also has bulk inversion asymmetry, the Dresselhaus SOC, originating from this asymmetry, also emerges. In deriving the Dresselhaus SOC, not only the wavefunctions $\psi_{8\mathrm{v}}, \psi_{7\mathrm{v}}, \psi_{\mathrm{c}}$ for $\Gamma_{8\mathrm{v}}$, $\Gamma_{7\mathrm{v}}$, and $\Gamma_{6\mathrm{c}}$ shown in Fig. 2.2 are used, but also the wavefunctions $\psi_{8\mathrm{c}}$ and $\psi_{7\mathrm{c}}$ for $\Gamma_{8\mathrm{c}}$ and $\Gamma_{7\mathrm{c}}$ are included in the basis states. By using these wavefunctions, the matrix elements of Eq. (2.1) are calculated up to the third order in $\boldsymbol{k}$, and the matrix elements of the s-orbital conduction electron band $\Gamma_{6\mathrm{c}}$ can be expressed as follows:

$$H_{\rm D} = b_{6\mathrm{c}}(\{k_x, k_y^2 - k_z^2\}\hat{\sigma}_x + \{k_y, k_z^2 - k_x^2\}\hat{\sigma}_y + \{k_z, k_x^2 - k_y^2\}\hat{\sigma}_z), \tag{2.16}$$

$$b_{6\mathrm{c}} = -\frac{4i}{3} PP'Q \Big[\frac{1}{(E_0 + \Delta_0)(E_0 - E_0' - \Delta_0')} - \frac{1}{E_0(E_0 - E_0')} \Big]. \tag{2.17}$$

Here, E_0' and Δ_0' represent the energy splitting widths shown in Fig. 2.2, and $\{A, B\} \equiv (AB + BA)/2$. Let $|X'\rangle$ ($|Z'\rangle$) denote the eigenstate of the p_x (p_z) orbital of $\Gamma_{8\mathrm{c}}$ and $\Gamma_{7\mathrm{c}}$ with $P' = \frac{\hbar}{m}\langle S|p_x|X'\rangle$ and $Q = \frac{\hbar}{m}\langle X|p_y|Z'\rangle$. For materials with point group $O_{\rm h}$, parity conservation results in $P' = 0$, hence the Dresselhaus SOC does not appear. Equation (2.16) is referred to as

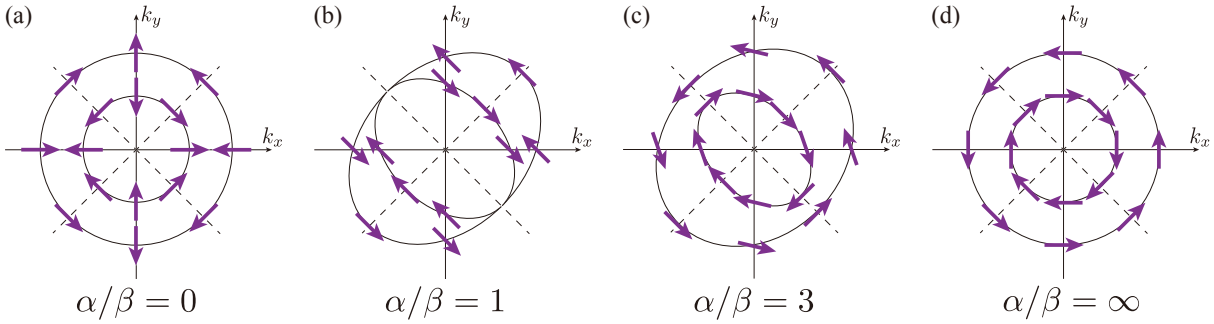

Figure 2.4: Spin texture on the spin-split Fermi surface: (a) $\alpha/\beta = 0$, (b) $\alpha/\beta = 1$, (c) $\alpha/\beta = 3$, and (d) $\alpha/\beta = \infty$. Here, α and β represent the magnitudes of the Rashba and Dresselhaus SOCs, respectively. Purple arrows represent the spins of 2DEG. Adapted from Ref. [49].

the Dresselhaus term or the k^3 term. After the spatial average with respect to the wavefunction in the z direction, the Hamiltonian for the Dresselhaus SOC is obtained as follows:

$$H_{\mathrm{D}} = \beta(k_x\hat{\sigma}_x - k_y\hat{\sigma}_y), \tag{2.18}$$

where β represents the magnitude of the Dresselhaus SOC. The effective magnetic field of the Dresselhaus SOC and the resulting spin texture of the Fermi surface depend on the crystal growth direction. Figure 2.4(a) illustrates the case when the crystal growth axis is [001], in which the z-component of the electron spin is zero. In contrast, when the crystal growth axis is [110], the x and y components of the electron spin are zero, and only the z component has a finite value.

2.1.3 Coexistence of Rashba and Dresselhaus SOCs

In heterostructures such as AlGaAs/GaAs, which exhibit both structure inversion asymmetry and bulk inversion asymmetry, the Rashba SOC and the Dresselhaus SOC coexist. If the Dresselhaus SOC dominates the Rashba SOC, there occurs spin splitting of the Fermi surface of conduction electrons, as shown in Fig. 2.4(a). On the other hand, by adjusting the gate voltage applied perpendicular to the 2DEG, the magnitude of the Rashba SOC can be varied [26], allowing for control over the ratio of these SOCs. This results in various spin textures, as Figs. 2.4(b) and 2.4(c) illustrate. Finally, if the Rashba SOC is much larger than the Dresselhaus SOC, there occurs spin splitting shown in Fig. 2.4(d). Notably, when the ratio of the two SOCs is unity, a persistent spin helix (PSH) state [43–47] emerges, and the spin quantization axis aligns in a single direction as shown in Fig. 2.4(b), leading to an infinite spin lifetime. In addition to this effect, the Aharonov-Casher (AC) effect in systems where the Rashba and Dresselhaus SOCs coexist has also been investigated [58]. In this manner, research on the coexistence of these two types of SOC has attracted significant attention in the field of semiconductor spintronics [14].

Research on systems in which the Rashba and Dresselhaus SOCs coexist has been actively pursued, particularly focusing on the phenomenon of the PSH, which arises when the mag-

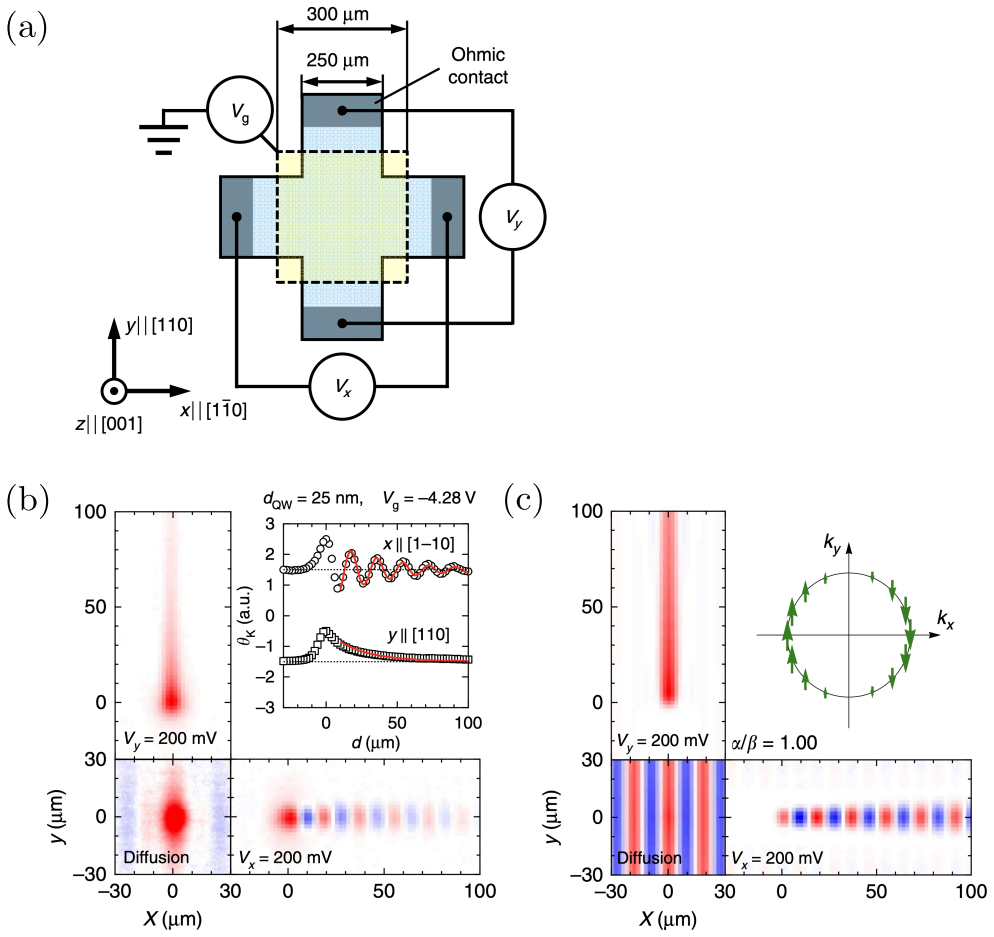

Figure 2.5: (a) Experimental setup for observing the persistent spin helix (PSH). (b) Experimental results of the PSH. Here, d represents the distance from the origin, and θ_K denotes the Kerr rotation angle. (c) Theoretical results based on the spin drift-diffusion model corresponding to the situation in (b). The inset illustrates the effective magnetic field when the Rashba and Dresselhaus SOCs have equal magnitudes. Adapted from Ref. [59].

nitudes of these SOCs are equal. The experimental setup for observing PSH is illustrated in Fig. 2.5(a) [59]. The sample consists of a two-dimensional electron system in a GaAs/AlGaAs quantum well, grown along the (001) direction using molecular beam epitaxy, and is fabricated with four ohmic contacts. Electron transport within the quantum well is controlled by applying voltages V_x and V_y to the ohmic contacts, while the strength of the Rashba SOC is tunable via a gate voltage V_g applied perpendicular to the plane. To generate electron spins aligned along the z-direction at $(x, y) = (0, 0)$, circularly polarized pump light is employed. The spin density is subsequently measured by detecting the magneto-optic Kerr rotation θ_K using linearly polarized probe light, as the Kerr rotation angle is proportional to the spin density. When the Rashba and Dresselhaus SOCs have equal magnitudes, the observed Kerr rotation data, shown in Fig. 2.5(b), reveal alternating $+z$ and $-z$ spin orientations (depicted in red and blue, respectively) along the x-

direction, while $+z$-oriented spins dominate along the y-direction. Electrons propagating along the x-direction undergo precession around the effective magnetic fields generated by the Rashba and Dresselhaus SOCs. This precession gives rise to the observed stripe pattern of alternating $+z$ and $-z$ spins, a hallmark of the PSH state. Notably, this spin precession is maintained over long distances, reflecting the spin's prolonged lifetime. The theoretical results derived from the spin drift-diffusion model, under the condition of equal Rashba and Dresselhaus SOC strengths ($\alpha/\beta = 1$), are shown in Fig. 2.5(c), and they reproduce the experimental behavior in Fig. 2.5(b) with high fidelity.

The enhanced spin lifetimes observed under these conditions have significant implications for the development of spintronics devices enabling long-distance spin transport. Thus, constructing a theoretical framework for spin transport phenomena in systems in which the Rashba and Dresselhaus SOCs coexist is considered a critical step toward advancing spintronics technologies.

2.2 Ferromagnetic Resonance (FMR)

In a ferromagnet under an external magnetic field, the magnetization within the ferromagnet undergoes precession around the external magnetic field (the Larmor precession). When microwaves are applied to this ferromagnet, the microwave absorption intensity increases significantly if the microwave frequency matches the Larmor precession frequency. This phenomenon is known as ferromagnetic resonance (FMR) [60]. Section 2.2.1 reviews the theory of the FMR using the Landau-Lifshitz-Gilbert (LLG) equation. In Sec. 2.2.2, the theory of the FMR in ferromagnetic insulators (FIs) is introduced using the magnon Green's function.

2.2.1 Landau-Lifshitz-Gilbert (LLG) equation

In this section, the FMR absorption spectrum is derived using the Landau-Lifshitz-Gilbert (LLG) equation, which describes the magnetization dynamics in ferromagnets. When a static magnetic field is applied to a ferromagnet, the motion of the localized spin $\boldsymbol{S}$ follows the Heisenberg equation given below:

$$\frac{d\boldsymbol{S}}{dt} = -\frac{i}{\hbar}[\boldsymbol{S}, H_{\text{Zeeman}}]. \tag{2.19}$$

We denote the effective magnetic field as $\boldsymbol{H}_{\text{eff}}$, which is usually the sum of an external magnetic field and an effective field induced from magnetic anisotropy. Then, the Hamiltonian H_{Zeeman} for describing dynamics of the magnetic moment $\boldsymbol{M} = \hbar\gamma_{\text{g}}\boldsymbol{S}$ can be expressed as follows:

$$H_{\text{Zeeman}} = -\boldsymbol{M} \cdot \boldsymbol{H}_{\text{eff}}. \tag{2.20}$$

By substituting Eq. (2.20) into Eq. (2.19), using the gyromagnetic ratio γ_{g}, and applying the commutation relation, $\boldsymbol{S} \times \boldsymbol{S} = i\hbar \boldsymbol{S}$, we obtain the following equation:

$$\frac{d\boldsymbol{M}}{dt} = -\gamma_{\mathrm{g}} \boldsymbol{M} \times \boldsymbol{H}_{\mathrm{eff}}. \tag{2.21}$$

This equation represents the precessional motion of the magnetic moment $\boldsymbol{M}$ around the effective magnetic field $\boldsymbol{H}_{\mathrm{eff}}$. In real materials, there are numerous magnetic moments and they tend to relax into the direction of the magnetic field. This effect is known as the Gilbert damping [61]. When taking this damping into account, we describe the dynamics of the magnetization $\boldsymbol{M}$ by the following equation:

$$\frac{d\boldsymbol{M}}{dt} = -\gamma_{\mathrm{g}} \boldsymbol{M} \times \boldsymbol{H}_{\mathrm{eff}} + \frac{\alpha_{\mathrm{G}}}{|\boldsymbol{M}|} \boldsymbol{M} \times \frac{d\boldsymbol{M}}{dt}. \tag{2.22}$$

This is called the Landau-Lifshitz-Gilbert (LLG) equation. The phenomenologically introduced parameter α_{G} is called the Gilbert damping constant.

Below, the effective magnetic field is set to $\boldsymbol{H}_{\mathrm{eff}} = (H_x, H_y, H_z) = (H_0 e^{-i\omega t}, H_0 i e^{-i\omega t}, H)$, where H_x and H_y are the magnetic fields of circularly polarized microwave and $H(\gg H_x, H_y)$ is the static effective magnetic field. The magnetization $\boldsymbol{M}$ undergoes precessional motion around the z-axis, and the x and y components of Eq. (2.22) are expressed as follows [62]:

$$\begin{pmatrix} \frac{d}{dt} & \gamma_{\mathrm{g}} H + \alpha_{\mathrm{G}} \frac{d}{dt} \\ -\gamma_{\mathrm{g}} H - \alpha_{\mathrm{G}} \frac{d}{dt} & \frac{d}{dt} \end{pmatrix} \begin{pmatrix} M_x \\ M_y \end{pmatrix} = \gamma_{\mathrm{g}} |\boldsymbol{M}| \begin{pmatrix} H_y \\ -H_x \end{pmatrix}. \tag{2.23}$$

Here, assuming that the z-component of the magnetization is significantly larger than the x and y components, we set it to $M_z = |\boldsymbol{M}|$. The solution after a sufficient amount of time can be written as $(M_0 e^{-i\omega t}, M_0 i e^{-i\omega t})$. Substituting this into equation (2.23) yields the following solution:

$$M_0 = \chi H_0, \quad \chi = \frac{-\gamma_{\mathrm{g}} |\boldsymbol{M}|}{\omega - \gamma_{\mathrm{g}} H + i\alpha_{\mathrm{G}} \omega}. \tag{2.24}$$

The microwave absorption is proportional to the imaginary part of the above response function, which represents energy dissipation:

$$\mathrm{Im}\, \chi = \frac{\gamma_{\mathrm{g}} |\boldsymbol{M}| \alpha_{\mathrm{G}} \omega}{(\omega - \gamma_{\mathrm{g}} H)^2 + (\alpha_{\mathrm{G}} \omega)^2}. \tag{2.25}$$

The frequency at which this absorption is maximized, $\omega = \omega_{\boldsymbol{0}} = \gamma_{\mathrm{g}} H$, corresponds to the resonance frequency of the FMR, and the resonance linewidth is given by $\alpha_{\mathrm{G}} \omega_{\boldsymbol{0}}$. Thus, by observing the FMR absorption spectrum, the magnitude of the Gilbert damping constant α_{G} can be experimentally determined by the linewidth of the spectrum.

2.2.2 Green's function

The LLG equation only treats dynamics of the average of the magnetization in a classical way. To consider quantum effects such as magnon excitation, it is necessary to employ another theoretical framework. In this section, the Green's function is used to derive expressions for the absorption rate in the FMR. Since electrons are localized in FIs, the FI is described by the Heisenberg model using only spin operators as follows:

$$H_{\mathrm{FI}} = \sum_{\langle i,j\rangle} J_{ij} \boldsymbol{S}_i \cdot \boldsymbol{S}_j - \hbar\gamma_{\mathrm{g}} h_{\mathrm{dc}} \sum_i S_i^z \tag{2.26}$$

$$= \sum_{\langle i,j\rangle} J_{ij} \left[S_i^x S_j^x + \frac{1}{2}(S_i^+ S_j^- + S_i^- S_j^+) \right] - \hbar\gamma_{\mathrm{g}} h_{\mathrm{dc}} \sum_i S_i^z. \tag{2.27}$$

Here, $\boldsymbol{S}_i = (S_i^x, S_i^y, S_i^z)$ denotes the localized spin operator, $S_i^{\pm} = S_i^x \pm i S_i^y$ represent the creation and annihilation operators of the localized spin, and $\langle i, j\rangle$ indicates the nearest-neighbor pair. The coefficient $J_{ij}(< 0)$ is the ferromagnetic exchange interaction, $\gamma_{\mathrm{g}}(< 0)$ is the gyromagnetic ratio, and h_{dc} represents the static magnetic field. Assuming that the system is at a sufficiently low temperature compared to the ferromagnetic transition temperature, we can express the localized spin operators using the magnon creation and annihilation operators, $b_i^\dagger$ and b_i, as follows (the Holstein-Primakoff transformation):

$$S_i^- = b_i^\dagger (2S_0 - b_i^\dagger b_i)^{1/2}, \quad S_i^+ = (2S_0 - b_i^\dagger b_i)^{1/2} b_i, \quad S_i^z = S_0 - b_i^\dagger b_i. \tag{2.28}$$

Furthermore, when the magnitude of the localized spin S_0 is sufficiently large compared to unity, the following approximated expression can be obtained:

$$S_i^- \simeq \sqrt{2S_0} b_i^\dagger, \quad S_i^+ \simeq \sqrt{2S_0} b_i, \quad S_i^z = S_0 - b_i^\dagger b_i. \tag{2.29}$$

We introduce the Fourier transformation

$$b_i = \frac{1}{\sqrt{N_{\mathrm{FI}}}} \sum_{\boldsymbol{k}} e^{i\boldsymbol{k}\cdot\boldsymbol{r}_i} b_{\boldsymbol{k}}, \tag{2.30}$$

where N_{FI} is the number of unit cells in the FI and $\boldsymbol{r}_i$ is the position of the localized spin. Then, the Hamiltonian can be rewritten as

$$H_{\mathrm{FI}} = \sum_{\boldsymbol{k}} \hbar\omega_{\boldsymbol{k}} b_{\boldsymbol{k}}^\dagger b_{\boldsymbol{k}}, \tag{2.31}$$

where $\hbar\omega_{\boldsymbol{k}} = \hbar\omega_{\boldsymbol{k}}^0 + \hbar\gamma_{\mathrm{g}} h_{\mathrm{dc}}$ is the magnon dispersion. When considering the three-dimensional simple cubic lattice with the nearest-neighbor exchange coupling J, $\hbar\omega_{\boldsymbol{k}}^0$ takes the following

form:

$$\hbar\omega_{\boldsymbol{k}}^{0} = 2JS_0[3 - \cos(k_x a) - \cos\big(k_y a\big) - \cos(k_z a)] \simeq JS_0 a^2 \boldsymbol{k}^2 \equiv \mathcal{D}\boldsymbol{k}^2, \tag{2.32}$$

where a represents the lattice constant of the FI and $\mathcal{D}$ denotes the spin stiffness. In the above equation, the long-wavelength approximation was employed.

Next, the temperature Green's function for magnons is introduced. Using the spin operators $S_{\boldsymbol{k}}^{\pm}(\tau)$, we define the Green's function for the FI as follows:

$$G_0(\boldsymbol{k}, \tau) \equiv -\frac{1}{\hbar}\langle T_\tau S_{\boldsymbol{k}}^{+}(\tau) S_{\boldsymbol{k}}^{-}(0)\rangle, \quad (-\hbar\beta < \tau < \hbar\beta), \tag{2.33}$$

where $S_{\boldsymbol{k}}^{\pm}(\tau) = e^{H_{\mathrm{FI}}\tau/\hbar} S_{\boldsymbol{k}}^{\pm} e^{-H_{\mathrm{FI}}\tau/\hbar}$, T_τ denotes the time-ordering operator with respect to the imaginary time τ, and β denotes the inverse temperature. Using Eq. (2.29), we can rewrite Eq. (2.33) in terms of the magnon creation and annihilation operators as follows:

$$G_0(\boldsymbol{k}, \tau) = -\frac{2S_0}{\hbar}\langle T_\tau b_{\boldsymbol{k}}(\tau) b_{\boldsymbol{k}}^{\dagger}\rangle. \tag{2.34}$$

Using $b_{\boldsymbol{k}}(\tau) = e^{-\omega_{\boldsymbol{k}}\tau} b_{\boldsymbol{k}}$, we obtain the Fourier transformation of the Green's function as

$$G_0(\boldsymbol{k}, i\omega_n) = \int_0^{\hbar\beta} d\tau G_0(\boldsymbol{k}, \tau) e^{i\omega_n \tau} = \frac{2S_0/\hbar}{i\omega_n - \omega_{\boldsymbol{k}}}, \tag{2.35}$$

where $n_{\mathrm{B}}(\omega) = 1/(e^{\beta\hbar\omega} - 1)$ is the Bose distribution function and $\omega_n = 2n\pi/(\hbar\beta)$ is the bosonic Matsubara frequency. The retarded Green's function is obtained by analytic continuation:

$$G_0^R(\boldsymbol{k}, \omega) = G_0(\boldsymbol{k}, i\omega_n \to \omega + i\delta) = \frac{2S_0/\hbar}{\omega - \omega_{\boldsymbol{k}} + i\delta}, \tag{2.36}$$

where δ is a positive infinitesimal. In real bulk ferromagnets, magnon-phonon scattering and other interactions induce the Gilbert damping. Since deriving this effect microscopically is challenging, the Gilbert damping constant α_{G} is introduced phenomenologically. After replacing δ with α_{G} in Eq. (2.36), the following expression is obtained:

$$G_0^R(\boldsymbol{k}, \omega) = \frac{2S_0/\hbar}{\omega - \omega_{\boldsymbol{k}} + i\alpha_{\mathrm{G}}\omega}. \tag{2.37}$$

Finally, let us derive the expression for the absorption spectrum of the FMR in the FI [63]. The Hamiltonian for the circularly polarized microwave applied externally can be written as follows:

$$H_{\mathrm{rf}} = -\frac{\hbar\gamma_{\mathrm{g}} h_{\mathrm{rf}}}{2} \sum_i (S_i^{-} e^{-i\omega t} + S_i^{+} e^{i\omega t}). \tag{2.38}$$

Here, h_{rf} represents the strength of the magnetic field of the microwave. By using the following Fourier transform of the spin operator

$$S_{\boldsymbol{k}}^{\pm} = \frac{1}{\sqrt{N_{\mathrm{FI}}}} \sum_i S_i^{\pm} e^{-i\boldsymbol{k}\cdot\boldsymbol{r}_i}, \tag{2.39}$$

Eq. (2.38) can be rewritten as follows:

$$H_{\mathrm{rf}} = -\frac{\hbar\gamma_{\mathrm{g}} h_{\mathrm{rf}}\sqrt{N_{\mathrm{FI}}}}{2} \sum_i (S_{\boldsymbol{0}}^{-} e^{-i\omega t} + S_{\boldsymbol{0}}^{+} e^{i\omega t}). \tag{2.40}$$

According to linear response theory, the change in the expectation value of $S_{\boldsymbol{0}}^{+}$ in response to the first term of Eq. (2.40), which generates magnons in the FI, can be written as follows:

$$\delta\langle S_{\boldsymbol{0}}^{+}\rangle_{\omega} = G_0^R(\boldsymbol{k}=\boldsymbol{0},\omega) \times \frac{\hbar\gamma_{\mathrm{g}} h_{\mathrm{rf}}\sqrt{N_{\mathrm{FI}}}}{2}. \tag{2.41}$$

When circularly polarized microwaves are applied to the FI, the localized spins in the FI absorb energy, and magnons with wavevector $\boldsymbol{k} = 0$ are excited. A steady state is reached when the energy absorbed by the localized spins from the microwave is balanced by the energy lost through spin relaxation. Therefore, the microwave absorption rate is proportional to the imaginary part of the retarded Green's function, which represents energy dissipation:

$$-\operatorname{Im} G_0^R(\boldsymbol{k}=\boldsymbol{0},\omega) = \frac{2S_0}{\hbar} \frac{\alpha_{\mathrm{G}}\omega}{(\omega-\omega_{\boldsymbol{0}})^2 + (\alpha_{\mathrm{G}}\omega)^2}. \tag{2.42}$$

The frequency dependence of Eq. (2.42) matches that of Eq. (2.25), which was derived from the Landau-Lifshitz-Gilbert (LLG) equation.

2.3 Spin Pumping (SP)

This section discusses spin pumping (SP), a method of injecting spins from ferromagnetic materials into various substances. Section 2.3.1 provides an overview of SP, followed by a review of theoretical studies on SP using spin mixing conductance in Sec. 2.3.2. In Sec. 2.3.3, an analytical approach to SP using Green's functions is presented.

2.3.1 Overview of SP

The injection of spin currents into materials is often achieved through the spin Hall effect (SHE) [66, 67] and spin pumping (SP) [17–20]. The SHE refers to the phenomenon of a charge current being converted into a spin current in the bulk of systems with strong spin-orbit interactions, such as heavy metals. By applying a charge current to a heavy metal and inducing

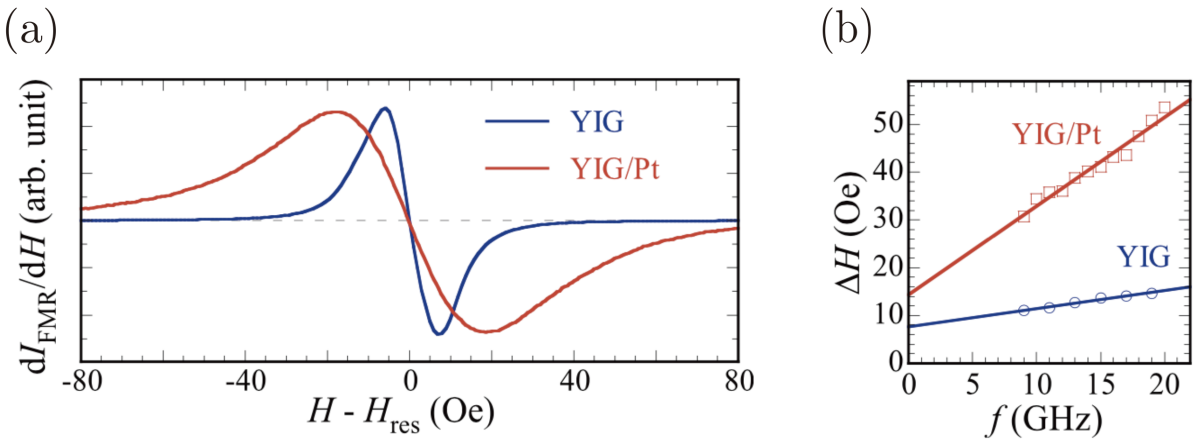

Figure 2.6: Absorption spectra for YIG(20nm) alone and YIG(20nm)/Pt(5nm). (a) Magnetic field dependence of the FMR absorption spectra. Here, H_{res} is a resonance magnetic field of the FMR. (b) Linewidth of (a) as a function of frequency. Adapted from Ref. [64, 65].

the SHE, spin currents can be injected into an adjacent material. On the other hand, in SP, spin currents are generated by the FMR [60] in a ferromagnetic material through microwave irradiation and are then injected into the adjacent material.

SP generates a spin current via the FMR rather than a charge current, enabling it to occur in both ferromagnetic metals and insulators. In ferromagnetic insulators (FIs), the spin current is carried by magnons, referred to as spin-wave spin current. Furthermore, because SP induced by the FMR injects relaxed spins from the ferromagnet into an adjacent material, the Gilbert damping in SP is enhanced compared to the FMR in the ferromagnet alone. This enhancement in the Gilbert damping can be experimentally observed as a broadening of the FMR absorption spectrum [18–20]. An example of the FMR spectrum in Yttrium-Iron-Garnet (YIG) alone and YIG/Pt is shown in Fig. 2.6 [64, 65]. As illustrated in Fig. 2.6(a), the linewidth of the absorption spectrum in YIG/Pt increases compared to that of YIG alone, due to the occurrence of SP. From the slope of the plot in Fig. 2.6(b), the magnitude of the Gilbert damping can be evaluated, obtaining a value of $(9.1 \pm 0.6) \times 10^{-4}$ for YIG (20 nm) alone, and $(4.5 \pm 0.3) \times 10^{-3}$ for YIG (20 nm)/Pt (5 nm) [64, 65].

2.3.2 Spin mixing conductance

SP is usually analyzed by the concept of spin mixing conductance [18, 68]. Let us consider a system where a ferromagnet is sandwiched between two normal-metals, as shown in Fig. 2.7. In this system, the 2×2 current operator, which accounts for the spin degrees of freedom, is defined as follows:

$$\hat{I} = \frac{1}{2}\hat{1} I_c - \frac{e}{\hbar}\hat{\boldsymbol{\sigma}} \cdot \boldsymbol{I}_s. \tag{2.43}$$

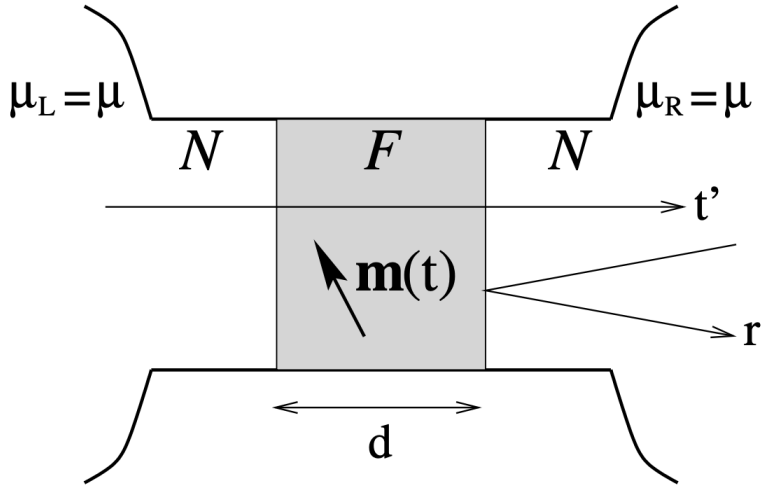

Figure 2.7: A ferromagnetic film (F) sandwiched between two normal-metals (N). The two normal-metals serve as reservoirs in the same thermal equilibrium state. The magnetization orientation vector $\boldsymbol{m}(t)$ in the ferromagnetic material undergoes precession around the static magnetic field, and the spin current flowing into the right lead is described by the reflection amplitude r and the transmission amplitude t'. Adapted from Ref. [18].

Here, $\hat{1}$ represents the identity matrix, $\hat{\boldsymbol{\sigma}} = (\hat{\sigma}_x, \hat{\sigma}_y, \hat{\sigma}_z)$ are the Pauli matrices, I_c is the charge current, and $\boldsymbol{I}_s$ is the spin current. The spin current $\boldsymbol{I}_s$ can be expressed as $\boldsymbol{I}_s = \boldsymbol{I}_s^{(0)} + \boldsymbol{I}_s^{\text{pump}}$, where $\boldsymbol{I}_s^{\text{pump}}$ is the spin current flowing from the ferromagnet into the normal-metal due to SP and $\boldsymbol{I}_s^{(0)}$ is the backflow spin current entering the ferromagnet due to spin accumulation in the normal-metal. In the following, the normal-metal is assumed to be an ideal sink with no spin accumulation, such that $\boldsymbol{I}_s^{(0)} = 0$. Labeling the left and right leads connected to the ferromagnet as $l = L, R$, we can express the expectation value of the current operator in each lead l as follows:

$$I_l^{\sigma\sigma'} = \frac{e}{\hbar} \sum_m \int d\epsilon d\epsilon' [\langle a_{m,l}^{\sigma'}(\epsilon)^\dagger a_{m,l}^{\sigma}(\epsilon') \rangle - \langle b_{m,l}^{\sigma'}(\epsilon)^\dagger b_{m,l}^{\sigma}(\epsilon') \rangle]. \tag{2.44}$$

Here, $a_{n,l}^{\sigma}(\epsilon)$ is the annihilation operator for an electron with spin σ and energy ϵ flowing into the ferromagnet through the nth channel from lead l and $b_{n,l}^{\sigma}(\epsilon)$ is the annihilation operator for an electron flowing out of the ferromagnet into leads. The two normal-metals in Fig. 2.7 are thermal reservoirs, and the number of electrons flowing out from these reservoirs can be expressed using the Fermi distribution function $f_l^{\sigma'\sigma}(\epsilon)$ as follows (the first term in Eq. (2.44)):

$$\langle a_{n,l}^{\sigma}(\epsilon)^\dagger a_{n',l'}^{\sigma'}(\epsilon') \rangle = f_l^{\sigma'\sigma}(\epsilon) \delta_{ll'} \delta_{nn'} \delta(\epsilon - \epsilon'). \tag{2.45}$$

The annihilation operator $b_{n,l}^{\sigma}(\epsilon)$ for electrons scattered by the ferromagnet, which acts as a scatterer, and flowing into the lead can be written using the scattering matrix elements $s_{nn',ll'}^{\sigma\sigma'}$ as

follows:

$$b^{\sigma}_{n,l}(\epsilon) = \sum_{\sigma',n',l'} s^{\sigma\sigma'}_{nn',ll'}(\epsilon) a^{\sigma'}_{n',l'}(\epsilon). \tag{2.46}$$

The projection matrices onto the magnetization direction $\boldsymbol{m}$ ($|\boldsymbol{m}| = 1$) are defined as

$$\hat{u}^{\uparrow} = \frac{1}{2}(\hat{1} + \hat{\boldsymbol{\sigma}} \cdot \boldsymbol{m}), \quad \hat{u}^{\downarrow} = \frac{1}{2}(\hat{1} - \hat{\boldsymbol{\sigma}} \cdot \boldsymbol{m}). \tag{2.47}$$

Using these, we can write the scattering matrix as follows:

$$\hat{s}_{nn',ll'} = s^{\uparrow}_{nn',ll'}\hat{u}^{\uparrow} + s^{\downarrow}_{nn',ll'}\hat{u}^{\downarrow}. \tag{2.48}$$

Here, when $l = l'$ ($l \neq l'$), $s^{\sigma}_{nn',ll'}$ represents the reflection (transmission) coefficient $r^{\sigma}_{nn'}$ ($t^{\sigma}_{nn'}$). When the scattering matrix depends on a time-dependent parameter $X(t)$, the current operator introduced in Eq. (2.43) can be written as follows:

$$\hat{I}(t)^{\text{pump}} = e\frac{d\hat{n}_l}{dX}\frac{dX(t)}{dt}, \tag{2.49}$$

$$\frac{d\hat{n}_l}{dX} = \frac{1}{4\pi i}\sum_{nn'l'}\frac{\partial \hat{s}_{nn',ll'}}{\partial X}\hat{s}^{\dagger}_{nn',ll'} + \text{h.c.} \tag{2.50}$$

Here, h.c. represents the Hermitian conjugate. Assuming the magnetization in the ferromagnet precesses around the z-axis, $\boldsymbol{m} = (\cos\varphi(t), \sin\varphi(t), 0)$, and setting $X(t) = \varphi(t)$, we transform Eq. (2.50) as

$$\frac{d\hat{n}_R}{d\varphi} = \frac{1}{4\pi}\left[A_i(\hat{\sigma}_x \sin\varphi - \hat{\sigma}_y \cos\varphi) - A_r\hat{\sigma}_z\right], \tag{2.51}$$

where

$$A_r = \frac{1}{2}\sum_{mn}[|r^{\uparrow}_{mn} - r^{\downarrow}_{mn}|^2 + |t'^{\uparrow}_{mn} - t'^{\downarrow}_{mn}|^2], \tag{2.52}$$

$$A_i = \text{Im}\sum_{mn}[r^{\uparrow}_{mn}(r^{\downarrow}_{mn})^* + t'^{\uparrow}_{mn}(t'^{\downarrow}_{mn})^*]. \tag{2.53}$$

Introducing $g^{\sigma\sigma'}$ and $t^{\uparrow\downarrow}$, defined by the following equations

$$g^{\sigma\sigma'} = \sum_{mn}\left[\delta_{mn} - r^{\sigma}_{mn}(r^{\sigma'}_{mn})^*\right], \tag{2.54}$$

$$t^{\uparrow\downarrow} = \sum_{nm} t'^{\uparrow}_{mn}(t'^{\downarrow}_{mn})^*, \tag{2.55}$$

we can summarize Eqs. (2.52) and (2.53) as follows:

$$A_r + iA_i = g^{\uparrow\downarrow} - t^{\uparrow\downarrow}. \tag{2.56}$$

Here, $g^{\uparrow\downarrow}$ is called the spin-mixing conductance. By substituting Eq. (2.51) into Eq. (2.49) and comparing it with Eq. (2.43), the following expressions for the charge and spin currents generated by SP are obtained:

$$I_{c,R}^{\mathrm{pump}} = 0, \tag{2.57}$$

$$\boldsymbol{I}_{s,R}^{\mathrm{pump}} = \frac{\hbar}{4\pi}\left(A_r \boldsymbol{m} \times \frac{d\boldsymbol{m}}{dt} - A_i \frac{d\boldsymbol{m}}{dt}\right). \tag{2.58}$$

Furthermore, the bilayer system where a normal-metal is attached to a ferromagnet corresponds to the case in which the film thickness d of the ferromagnet in Fig. 2.7 is sufficiently large, resulting in a transmission coefficient of zero ($t^{\uparrow\downarrow} = 0$). Thus, the spin current in Eq. (2.58) is determined by the spin-mixing conductance $g^{\uparrow\downarrow} = g_r^{\uparrow\downarrow} + ig_i^{\uparrow\downarrow}$. Additionally, in the second term of Eq. (2.58), which is proportional to $d\boldsymbol{m}/dt$ and represents the effect of the effective magnetic field, the coefficient $A_i = g_i^{\uparrow\downarrow}$ is typically of the order $g_i^{\uparrow\downarrow} \lesssim 0.1 g_r^{\uparrow\downarrow}$ in transition-metal ferromagnets. Thus, by neglecting $g_i^{\uparrow\downarrow}$, Eq. (2.58) can be written as follows:

$$\boldsymbol{I}_{s,R}^{\mathrm{pump}} = \frac{\hbar}{4\pi} g_r^{\uparrow\downarrow} \boldsymbol{m} \times \frac{d\boldsymbol{m}}{dt}. \tag{2.59}$$

Next, the expression for the modulation of the Gilbert damping due to SP is derived. In the setup shown in Fig. 2.7, the total spin current generated by SP can be expressed using Eq. (2.58) as follows:

$$\boldsymbol{I}_s = \sum_l \boldsymbol{I}_{s,l}^{\mathrm{pump}} = \frac{\hbar}{4\pi}\left[(A_r^{(L)} + A_r^{(R)})\boldsymbol{m} \times \frac{d\boldsymbol{m}}{dt} - (A_i^{(L)} + A_i^{(R)})\frac{d\boldsymbol{m}}{dt}\right]. \tag{2.60}$$

The Landau-Lifshitz-Gilbert (LLG) equation for a ferromagnet alone is expressed as

$$\partial_t \boldsymbol{m} = -\gamma_{\mathrm{g}} \boldsymbol{m} \times \boldsymbol{H}_{\mathrm{eff}} + \alpha_{\mathrm{G}} \boldsymbol{m} \times \partial_t \boldsymbol{m}. \tag{2.61}$$

However, when the spin current described by Eq. (2.60) is generated through SP in the junction system shown in Fig. 2.7, the magnetization in the ferromagnet experiences a spin-transfer torque, $\boldsymbol{\tau} = -\boldsymbol{m} \times \boldsymbol{I}_s \times \boldsymbol{m}$, which alters its dynamics. As a result, the following term is added to the right-hand side of the LLG equation:

$$\left.\frac{\partial \boldsymbol{m}}{\partial t}\right|_{\mathrm{torque}} = \frac{\gamma_{\mathrm{g}}'}{MV} \boldsymbol{m} \times \boldsymbol{I}_s \times \boldsymbol{m}. \tag{2.62}$$

Here, V and M represent the volume and the total magnetic moment of the ferromagnet,

respectively. This means that, due to SP, the gyromagnetic ratio and the Gilbert damping are modulated as follows:

$$\frac{1}{\gamma'_{\rm g}} = \frac{1}{\gamma_{\rm g}}[1 + g_L(A_i^{(L)} + A_i^{(R)})/4\pi M], \tag{2.63}$$

$$\alpha'_{\rm G} = \frac{\gamma'_{\rm g}}{\gamma_{\rm g}}[\alpha_{\rm G} + g_L(A_r^{(L)} + A_r^{(R)})/4\pi M]. \tag{2.64}$$

Here, g_L represents the Landé factor (g-factor). It should be noted that the modulation of the gyromagnetic ratio and the Gilbert damping corresponds to the shift in the FMR resonance field and the increase in the resonance linewidth, respectively. Furthermore, as done previously in Eq. (2.59), by neglecting $A_i = g_i^{\uparrow\downarrow}$, Eqs. (2.63) and (2.64) are simplified to the following form:

$$\gamma'_{\rm g} = \gamma_{\rm g}, \tag{2.65}$$

$$\alpha'_{\rm G} = \alpha_{\rm G} + g_L[A_r^{(L)} + A_r^{(R)}]/4\pi M. \tag{2.66}$$

2.3.3 Green's function

While the concept of the spin-mixing conductance is useful for analysis of spin transport at an interface, it has several drawbacks. In particular, the spin-mixing conductance is obtained from experimental observations while its temperature dependence cannot be predicted theoretically. This drawback originates from a classical treatment of the magnetization in ferromagnets. One way to overcome this problem is to express the modulation of the Gilbert damping in terms of Green's functions. In this section, the modulation of the Gilbert damping is discussed when spins are injected from the ferromagnetic insulator (FI) into an adjacent material via SP using Green's functions.

In a junction system, the temperature Green's function for magnons in the FI can be written with the Dyson equation as follows:

$$G(\boldsymbol{k}, i\omega_n) = \frac{1}{G_0(\boldsymbol{k}, i\omega_n)^{-1} - \Sigma(\boldsymbol{k}, i\omega_n)}. \tag{2.67}$$

Here, $G_0(\boldsymbol{k}, i\omega_n)$ represents the Green's function of magnons in the isolated FI, as introduced in Eq. (2.35), while $\Sigma(\boldsymbol{k}, i\omega_n)$ denotes the magnon self-energy resulting from the interaction between the FI and the adjacent material. By performing analytic continuation in Eq. (2.67), replacing the Matsubara frequency as $i\omega_n \to \omega + i\delta$, and substituting Eq. (2.37), the retarded component of Green's function is obtained as

$$G^R(\boldsymbol{k}, \omega) = \frac{2S_0/\hbar}{\omega - \omega_{\boldsymbol{k}} + i\alpha_{\rm G}\omega - \frac{2S_0}{\hbar}\Sigma^R(\boldsymbol{k}, \omega)}, \tag{2.68}$$

where $\Sigma^R(\boldsymbol{k}, \omega) = \Sigma^R(\boldsymbol{k}, i\omega_n \to \omega + i\delta)$ is the retarded component of the self-energy. The

real and imaginary parts of the self-energy $\Sigma^R(\boldsymbol{k},\omega)$ respectively give the shift of the resonant frequency $\delta\omega_{\boldsymbol{k}}$ and the increase in the Gilbert damping $\delta\alpha_{\rm G}$ as follows:

$$G^R(\boldsymbol{k},\omega) = \frac{2S_0/\hbar}{\omega - (\omega_{\boldsymbol{k}} + \delta\omega_{\boldsymbol{k}}) + i(\alpha_{\rm G} + \delta\alpha_{\rm G})\omega}, \tag{2.69}$$

$$\delta\omega_{\boldsymbol{k}} = \frac{2S_0}{\hbar}\,{\rm Re}\,\Sigma^R(\boldsymbol{k},\omega), \tag{2.70}$$

$$\delta\alpha_{\rm G} = -\frac{2S_0}{\hbar\omega}\,{\rm Im}\,\Sigma^R(\boldsymbol{k},\omega). \tag{2.71}$$

The self-energy $\Sigma(\boldsymbol{k}, i\omega_n)$ can be calculated by second-order perturbation with respect to the interface interaction Hamiltonian between the FI and the adjacent material.

As a simple example, let us consider the increase in the Gilbert damping, $\delta\alpha_{\rm G}$, for a FI and normal-metal (NM) junction [69]. The Hamiltonian of this junction system can be expressed as follows:

$$H = H_{\rm NM} + H_{\rm FI} + H_{\rm int}. \tag{2.72}$$

Here, $H_{\rm NM}$ represents the Hamiltonian of the NM, expressed as the following free electron Hamiltonian:

$$H_{\rm NM} = \sum_{\boldsymbol{k}\sigma} \xi_{\boldsymbol{k}} c^\dagger_{\boldsymbol{k}\sigma} c_{\boldsymbol{k}\sigma}. \tag{2.73}$$

Here, $c^\dagger_{\boldsymbol{k},\sigma}$ and $c_{\boldsymbol{k},\sigma}$ denote the electron creation and annihilation operators, respectively. The electronic energy dispersion is given by $\epsilon_{\boldsymbol{k}}$, and $\xi_{\boldsymbol{k}} = \epsilon_{\boldsymbol{k}} - \mu$ represents the energy relative to the chemical potential μ. The second term $H_{\rm FI}$ is the Hamiltonian of the FI, as introduced in Eq. (2.31). The third term $H_{\rm int}$ denotes the interfacial interaction between the FI and the NM, which can be expressed as follows [48, 49, 63, 70–79]:

$$H_{\rm int} = \sum_{\boldsymbol{k}}\sum_{\boldsymbol{q}} (T_{\boldsymbol{k},\boldsymbol{q}} S^+_{\boldsymbol{k}} s^-_{\boldsymbol{q}} + T^*_{\boldsymbol{k},\boldsymbol{q}} S^-_{\boldsymbol{k}} s^+_{\boldsymbol{q}}) + \sum_{\boldsymbol{q}} \mathcal{T}_{\boldsymbol{0},\boldsymbol{q}} S_0 s^z_{\boldsymbol{q}}, \tag{2.74}$$

where $T_{\boldsymbol{k},\boldsymbol{q}}$ and $\mathcal{T}_{\boldsymbol{0},\boldsymbol{q}}$ represent the strengths of the interfacial interaction. Additionally, $S^\pm_{\boldsymbol{k}}$ denotes the creation and annihilation operators for the localized spins in the FI, as introduced in Eq. (2.39), and $s^\pm_{\boldsymbol{k}}$ are the creation and annihilation operators for the electron spin in the NM, defined as follows:

$$s^\pm_{\boldsymbol{k}} = \frac{1}{2}\sum_{\sigma,\sigma'}\sum_{\boldsymbol{k}'} c^\dagger_{\boldsymbol{k}'\sigma} (\hat{\sigma}^\pm)_{\sigma\sigma'} c_{\boldsymbol{k}'+\boldsymbol{k}\sigma'}. \tag{2.75}$$

Here, $\hat{\sigma}^\pm = \hat{\sigma}_x \pm i\hat{\sigma}_y$ represents the Pauli matrices associated with the creation and annihilation of spin in the z-direction. The first term on the right-hand side of Eq. (2.74) describes the

absorption and emission of magnons at the FI-NM interface. Meanwhile, the final term on the right-hand side can be interpreted as a Zeeman field $\mathcal{T}_{\mathbf{0},\bar{\boldsymbol{q}}}S_0$ acting on the electrons of the NM, representing the effect of exchange bias at the interface. Since this does not affect the increase of the Gilbert damping due to spin injection into the NM, the final term on the right-hand side of Eq. (2.74) will be neglected hereafter. Note that this static Zeeman term becomes important in considering the Rashba-Edelstein magnetoresistance discussed in Chap. 6. Accordingly, the following Hamiltonian is used:

$$H_{\rm int} \simeq \sum_{\boldsymbol{k}} \sum_{\boldsymbol{q}} (T_{\boldsymbol{k},\boldsymbol{q}} S_{\boldsymbol{k}}^{+} s_{\boldsymbol{q}}^{-} + T_{\boldsymbol{k},\boldsymbol{q}}^{*} S_{\boldsymbol{k}}^{-} s_{\boldsymbol{q}}^{+}). \tag{2.76}$$

Then, calculating the magnon self-energy appearing in Eq. (2.68) within the framework of second-order perturbation theory for this interfacial interaction Hamiltonian yields the following result:

$$\Sigma^{R}(\boldsymbol{k},\omega) = -\sum_{\boldsymbol{q}} |T_{\boldsymbol{k},\boldsymbol{q}}|^2 \hbar V \chi^{R}(\boldsymbol{q},\omega), \tag{2.77}$$

$$\chi^{R}(\boldsymbol{q},\omega) = -\frac{1}{V}\sum_{\boldsymbol{k}} \frac{f_0(\xi_{\boldsymbol{k}+\boldsymbol{q}}) - f_0(\xi_{\boldsymbol{k}})}{\hbar\omega + \xi_{\boldsymbol{k}+\boldsymbol{q}} - \xi_{\boldsymbol{k}} + i\delta}, \tag{2.78}$$

where V represents the volume of the NM, $\chi^{R}(\boldsymbol{q},\omega)$ denotes the Lindhard function, which represents the spin susceptibility of conduction electrons in the NM, $f_0(\xi_{\boldsymbol{k}}) = (e^{\beta\xi_{\boldsymbol{k}}}+1)^{-1}$ represents the Fermi distribution function, and δ is a positive infinitesimal quantity. Thus, within the framework of second-order perturbation theory for $H_{\rm int}$, the magnon self-energy is proportional to the spin susceptibility of electrons in the NM. In the case of a dirty FI-NM interface, the electron wavevector in the NM is not conserved, whereas it is conserved in a clean interface. Accordingly, the coefficient $T_{\boldsymbol{k},\boldsymbol{q}}$ at each type of interface in Eq. (2.76) can be expressed as follows:

$$\text{dirty interface} : T_{\boldsymbol{k},\boldsymbol{q}} = \bar{T}, \tag{2.79}$$

$$\text{clean interface} : T_{\boldsymbol{k},\boldsymbol{q}} = \bar{T}\delta_{\boldsymbol{k},\boldsymbol{q}}, \tag{2.80}$$

where $\delta_{\boldsymbol{k},\boldsymbol{q}}$ denotes the Kronecker delta. The increase in the Gilbert damping due to SP induced by the FMR at a dirty interface can be calculated by substituting Eq. (2.79) into Eq. (2.77) and applying Eq. (2.71), resulting in the following expression:

$$\delta\alpha_{\rm G}(\omega_{\mathbf{0}}) = -\frac{2S_0}{\hbar\omega_{\mathbf{0}}} \,{\rm Im}\,\Sigma^{R}(\boldsymbol{k}=\mathbf{0},\omega_{\mathbf{0}}) = 2\pi\hbar S_0 |\bar{T}|^2 V^2 D^2(\epsilon_{\rm F}). \tag{2.81}$$

Here, $\omega_{\mathbf{0}}$ denotes the resonance frequency of the FMR, and $D(\epsilon_{\rm F})$ represents the density of states of the NM at the Fermi level. Thus, in an FI-NM junction with a dirty interface, the

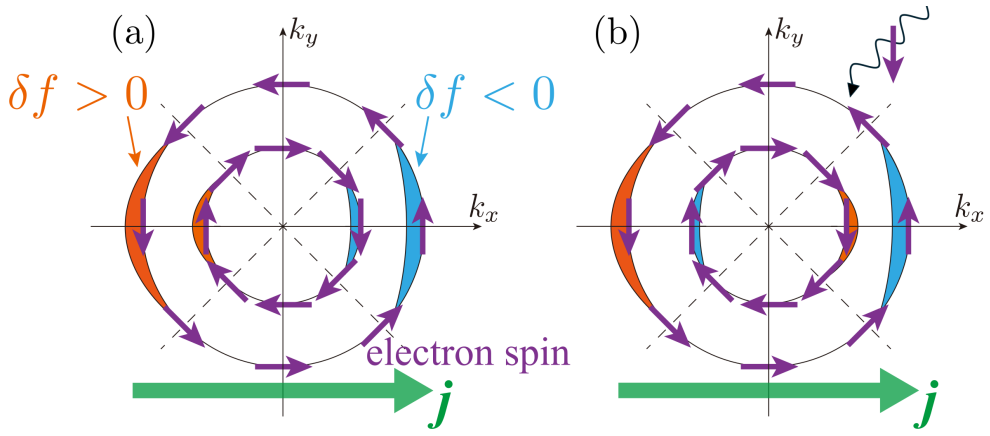

Figure 2.8: (a) A schematic picture for explaining the REE induced by the Rashba SOC. When an external charge current $\Delta \boldsymbol{j}$ is applied in the $+x$ direction in a Rashba system, the Fermi surface of the electrons shifts towards the $-x$ direction, resulting in spin accumulation polarized in the $-y$ direction. The orange (blue) regions represent an increase (decrease) in the electron distribution function from the equilibrium state. (b) A schematic picture for explaining the IREE induced by the Rashba SOC. When spin polarized in the $-y$ direction is injected into a Rashba system, the distribution function of electrons with this spin orientation increases, generating a charge current in the $+x$ direction.

modulation of the Gilbert damping is proportional to the square of the density of states. For a clean interface, it can be shown that the Gilbert damping due to spin pumping becomes zero in the regime of second-order perturbation by applying Eqs. (2.71), (2.77), and (2.80):

$$\delta\alpha_{\mathrm{G}}(\omega_{\boldsymbol{0}}) = -\frac{2S_0}{\hbar\omega_{\boldsymbol{0}}} \operatorname{Im}\Sigma^R(\boldsymbol{k}=\boldsymbol{0},\omega_{\boldsymbol{0}}) = 0. \tag{2.82}$$

In Chap. 4, a 2DEG with the Rashba and Dresselhaus SOCs is considered instead of the normal-metal, and it is demonstrated that modulation of the Gilbert damping is non-zero even for a clean interface.

2.4 Rashba-Edelstein effect (REE) and Inverse Rashba-Edelstein effect (IREE)

2.4.1 Overview

As discussed in Sec. 2.1.3, the Rashba and Dresselhaus SOCs in 2DEG cause spin-momentum locking, and the orientation of the electron spin is determined by its momentum. In the presence of the spin-momentum locking, there occur two types of spin-charge conversion phenomena in 2DEG; the conversion from charge to spin known as the Rashba-Edelstein effect (REE) [27–32, 80–83] and the conversion from spin to charge known as the inverse Rashba-Edelstein effect

(IREE) [33–38, 49, 79, 81, 84, 85]. The mechanisms of the REE and the IREE are summarized as follows:

REE: When a charge current is applied in the $+x$ direction to a 2DEG with spin-momentum locking, such as in a Rashba system, the Fermi surface shifts in the direction opposite to the charge current. As a result, as illustrated in Fig. 2.8(a), spins aligned along the $-y$ ($+y$) direction accumulate on the outer (inner) Fermi surface. Although these spin accumulations cancel each other partially, the contribution from the outer band is dominant, leading to a net spin accumulation polarized in the $-y$ direction.

IREE: As shown in Fig. 2.8(b), when spins polarized along the $-y$ direction are injected into a Rashba system, the outer (inner) Fermi surface shifts in the $-x$ ($+x$) direction. As a result, the outer Fermi surface generates a charge current in the $+x$ direction, while the inner Fermi surface generates a charge current in the $-x$ direction. Due to the dominant contribution from the outer band, the net charge current flows in the $+x$ direction.

It should be noted that the REE or the IREE plays an important role also for three-dimensional systems with an interface. Usually, spin-charge conversion in three-dimensional bulk systems occurs through the spin Hall effect (SHE) and the inverse spin Hall effect (ISHE); a charge current can be converted into a spin current by the SHE, while a spin current is converted into a charge current by the ISHE. These conversion phenomena arise in the bulk of heavy metals due to strong spin-orbit interactions. While the SHE and the ISHE are always caused in bulk systems, the REE and the IREE induced by interfacial (surface) electronic states may overwhelm them in some junction systems because of a strong Rashba SOC induced by electric field near the interface and existence of heavy elements (see also the discussion in Sec. 2.1.1).

In early studies of the IREE, non-equilibrium spin accumulation was achieved via optical spin orientation [36]. In recent years, experimental studies on the IREE using SP have become prevalent across various systems, such as Ag/Bi [37, 86–89], topological insulators [90–99], STO [100–107], atomic layers [108–111], and semiconductors [112, 113]. Figure 2.9 provides a representative example of such an experiment [37]; a spin current is injected from a ferromagnetic NiFe layer into an Ag(111)/Bi interface with the Rashba SOC via SP, leading to a charge current generated by the IREE (Fig. 2.9(i)). The results presented in Fig. 2.9(ii) demonstrate that a substantial charge current is observed only at the Ag/Bi interface, where the carrier density and the Rashba SOC are large. This strongly suggests that the charge current observed at the Ag/Bi interface is generated by the IREE.

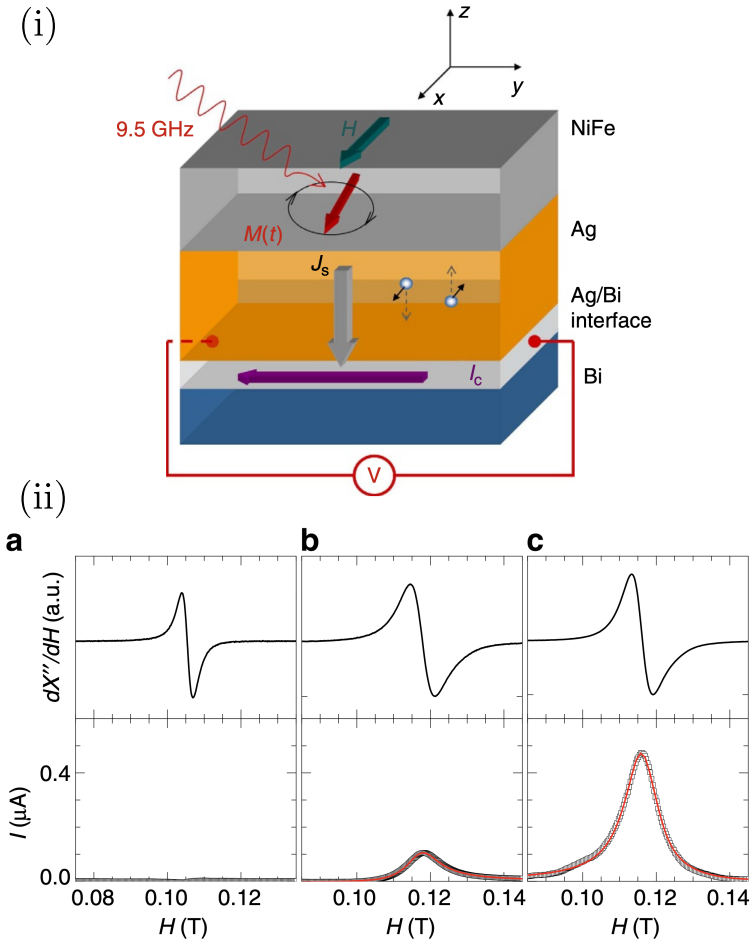

Figure 2.9: Experimental setup for the IREE using SP [37]. (i) Schematic of the experimental setup. A spin current is injected from the ferromagnetic NiFe layer into the Ag(111)/Bi with the Rashba SOC via SP. (ii) FMR absorption spectra (upper panels) and charge currents (lower panels) for junction systems composed of NiFe and (a) Ag, (b) Bi, and (c) Ag/Bi. The horizontal axis represents the external DC magnetic field. Adapted from Ref. [37].

2.4.2 Theory of REE

This section reviews the theory of the REE in a 2DEG with the Rashba SOC, as presented in Ref. [80]. The Hamiltonian for this 2DEG is given by

$$H_{\mathrm{2DEG}} = \frac{\hbar^2 k^2}{2m^*}\hat{1} + \alpha(k_y\hat{\sigma}_x - k_x\hat{\sigma}_y). \tag{2.83}$$

Here, m^* is the effective mass of the conduction electrons, $\hat{1}$ is the 2×2 identity matrix, and α denotes the magnitude of the Rashba SOC. The first term in Eq. (2.83) represents the kinetic energy of the conduction electrons in the 2DEG, while the second term is the Rashba

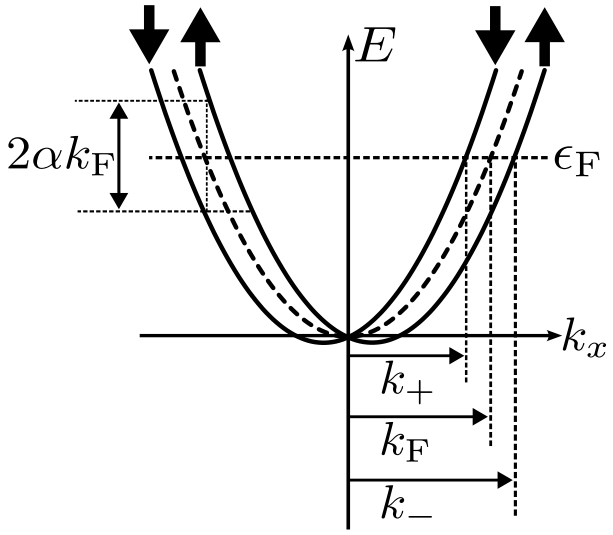

Figure 2.10: The spin-split energy bands of conduction electrons in a Rashba system.

Hamiltonian. The energy eigenvalues of Eq. (2.83) are given by:

$$E_{\boldsymbol{k}}^{\gamma} = \frac{\hbar^2 k^2}{2m^*} + \gamma \alpha k. \tag{2.84}$$

Here, $\gamma = \pm$ is a label that specifies the spin-split subbands. When the Fermi energy without the Rashba SOC is denoted as $\epsilon_{\mathrm{F}} = \hbar^2 k_{\mathrm{F}}^2 / 2m^*$, the corresponding Fermi wavevector is $k_{\mathrm{F}} = \sqrt{2\pi n}$, where n is the electron density. The wavevector $k_{\gamma=\pm}$ for each subband at this Fermi energy, as illustrated in Fig. 2.10, can be expressed as follows:

$$k_{\gamma} = (1 - \gamma \bar{\zeta}) k_{\mathrm{F}}. \tag{2.85}$$

Here, $\bar{\zeta}$ is a parameter that represents the difference between the two Fermi surfaces and can be expressed using the magnitude of the Rashba SOC, α, as follows:

$$\bar{\zeta} = \frac{\alpha k_{\mathrm{F}}}{2\epsilon_{\mathrm{F}}}. \tag{2.86}$$

In the following, only terms up to the first order of the Rashba SOC are considered. In this case, the energy splitting at the Fermi surface is $2\alpha k_{\mathrm{F}}$, and the density of states for each subband can be expressed as follows:

$$D_{\gamma}(E) = \frac{k_{\gamma}}{2\pi\hbar v_{\mathrm{F}}} = \frac{k_{\gamma}}{k_{\mathrm{F}}} \frac{n}{2\epsilon_{\mathrm{F}}}. \tag{2.87}$$

Note that the Fermi velocities of the two subbands are given by $v_{\mathrm{F}}^{\gamma} = \hbar k_{\mathrm{F}} / m^* = v_{\mathrm{F}}$ with the same magnitude regardless of the subband.

In the following, the charge current density and spin density generated by the REE are calculated for a 2DEG in the x-y plane with the Rashba SOC, under an external electric field $E_x(>0)$ applied in the x-direction, as shown in Fig. 2.8(a). Here, the weak-scattering limit, where the impurity scattering rate in the 2DEG is low, is considered. In this case, the spin relaxation time τ_s and the momentum relaxation time τ_ρ can be effectively considered the same [1]: $\tau_s \simeq \tau_\rho$. First, the displacement of the Fermi surface under an applied external electric field E_x can be expressed as follows:

$$\delta k_\gamma = \frac{eE_x\tau_\gamma}{\hbar}. \tag{2.88}$$

Here, $e\ (<0)$ represents the electron charge. Additionally, τ_γ denotes the momentum relaxation time for each spin-split subband and can be expressed as follows, using $\bar{\zeta}$ from Eq. (2.86) and the averaged momentum relaxation time $\tau\ (=(\tau_+ + \tau_-)/2 = \tau_\rho \simeq \tau_s)$:

$$\tau_\gamma = \tau(1 - \gamma\bar{\zeta}). \tag{2.89}$$

Then, expressing the electron wavevector in polar coordinates as $\boldsymbol{k} = (k\cos\varphi, k\sin\varphi)$, the contributions to the x-component of the charge current density, j_γ, and to the y-component of the spin density, S_γ, from each subband can be calculated as follows [114]:

$$j_\gamma = \frac{e}{4\pi^2}\int_0^{2\pi} k_\gamma d\varphi\ \delta k_\gamma \cos\varphi \cdot v_\mathrm{F}\cos\varphi = \frac{e^2E_x\tau_\gamma v_\mathrm{F}k_\gamma}{4\pi\hbar}, \tag{2.90}$$

$$S_\gamma = -\frac{1}{4\pi^2}\frac{\hbar}{2}\int_0^{2\pi} k_\gamma d\varphi\ \delta k_\gamma \cos\varphi \cdot \gamma\cos\varphi = -\frac{\gamma}{2}\frac{eE_x\tau_\gamma k_\gamma}{4\pi}. \tag{2.91}$$

From Eq. (2.90), the x-component of the total charge current density, j, is given by

$$j \equiv j_+ + j_- = \frac{e^2\tau k_\mathrm{F}}{2\pi\hbar}E_x. \tag{2.92}$$

Note that, since only terms up to the first order of the Rashba SOC are considered, terms involving $\bar{\zeta}^2$ are omitted. Additionally, from Eq. (2.91), the y-component of the total spin polarization is given by

$$S \equiv \frac{2(S_+ + S_-)}{\hbar n} = \frac{2e\tau\bar{\zeta}}{\hbar k_\mathrm{F}}E_x = \frac{\alpha k_\mathrm{F}}{\epsilon_\mathrm{F}}\frac{j}{ne}. \tag{2.93}$$

Here, $k_\mathrm{F} = \sqrt{2\pi n}$ and Eq. (2.86) have been used. Equation (2.93) represents the spin polarization

[1] As a spin relaxation mechanism, the D'yakonov-Perel (DP) mechanism is considered dominant, and electron spins relax due to precession around the effective magnetic field generated by the Rashba SOC. In the weak-scattering limit, where the momentum relaxation time τ_ρ is long, the electron spin undergoes sufficient relaxation through the DP mechanism before being scattered by impurities. Thus, τ_s can be effectively regarded as equal to τ_ρ.

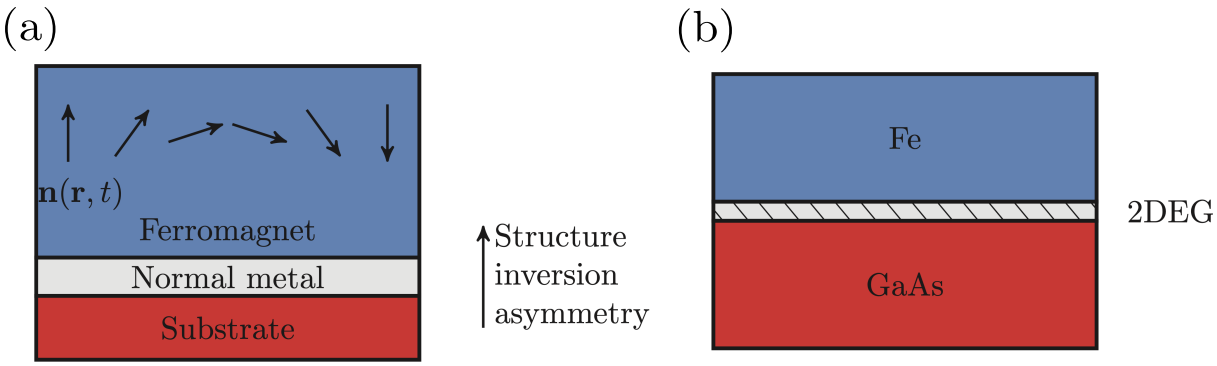

Figure 2.11: Setup for the IREE induced by SP. $\boldsymbol{n}(\boldsymbol{r},t)$ represents the magnetization direction of the ferromagnet, which can be either a ferromagnetic metal or a ferromagnetic insulator. The normal-metal can be a two-dimensional system consisting of a few monolayers or a three-dimensional system with a thickness of several tens of nanometers. (b) An experimental realization of SP. A spin current is injected from Fe into the 2DEG at the Fe-GaAs interface via SP, inducing a charge current in the 2DEG through the IREE. Adapted from Ref. [115].

converted from the charge current via the REE.

In this section, a phenomenological description of the REE was reviewed, following Ref. [80]. The same result can be obtained by using the Boltzmann equation [32]. For detailed calculation by the Boltzmann equation, refer to Appendix A.

2.4.3 Theory of IREE

This section briefly reviews recent theories on the IREE driven by SP using the Boltzmann equation [115, 116].

Reference [115] developed a theoretical framework for the IREE induced by SP in a junction system composed of a ferromagnet and a normal-metal, as shown in Fig. 2.11(a). As an experimentally feasible setup, the study proposed an Fe/GaAs junction system illustrated in Fig. 2.11(b). The analysis focused on the condition where the spin splitting width of the energy band for 2DEG electrons due to the Rashba SOC, Δ_{so}, is significantly smaller than the impurity scattering strength, satisfying $\Delta_{\mathrm{so}}\tau/\hbar \ll 1$, where τ denotes the momentum relaxation time. It was assumed that proximity-induced magnetization arises in the normal-metal, and the itinerant s-electrons and localized d-electrons are coupled via the following s-d interaction:

$$H_{\mathrm{sd}} = \Delta_{\mathrm{xc}}\boldsymbol{n}(\boldsymbol{r},t)\cdot\frac{\hat{\boldsymbol{\sigma}}}{2}. \tag{2.94}$$

Here, $\hat{\boldsymbol{\sigma}}$ represents the Pauli matrices, Δ_{xc} denotes the ferromagnetic exchange band splitting, and $\boldsymbol{n}$ indicates the magnetization direction of the ferromagnet. The study considers the following

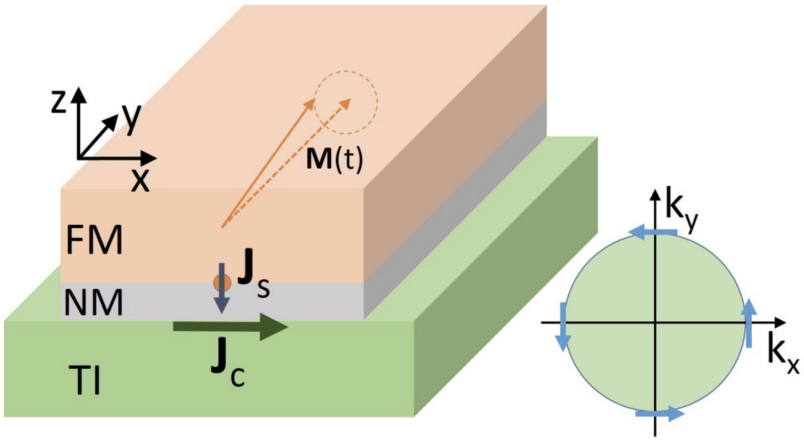

Figure 2.12: Setup for the IREE in TI surface states induced by SP. In the FM, a magnetization $\boldsymbol{M}(t)$ rotating around the y-axis generates a spin current density $\boldsymbol{J}_s$ in the z-direction, injecting spins polarized along the y-axis into the NM. These spins are converted into a charge current density $\boldsymbol{J}_c$ flowing in the x-direction on the TI surface via spin-momentum locking, as illustrated by the Fermi surface on the right. Adapted from Ref. [116].

Rashba SOC and extrinsic SOC due to impurities:

$$H_{\mathrm{R}} = -\frac{\alpha}{\hbar}\hat{\boldsymbol{\sigma}} \times \hat{\boldsymbol{z}} \cdot \boldsymbol{p}, \tag{2.95}$$

$$H_{\mathrm{ext}} = -\frac{\lambda^2}{4\hbar}\hat{\boldsymbol{\sigma}} \times \nabla V(\boldsymbol{r}) \cdot \boldsymbol{p}, \tag{2.96}$$

where α represents the magnitude of the Rashba SOC, $\hat{\boldsymbol{z}}$ is the unit vector perpendicular to the plane, $\boldsymbol{p}$ denotes the momentum of conduction electrons, λ is the effective Compton wavelength, and $V(\boldsymbol{r})$ represents the impurity potential. In Ref. [115], the Boltzmann equation for the distribution function was derived for this model and was utilized to analyze the charge current converted from the spin current generated by SP via the IREE under the condition $\Delta_{\mathrm{so}}\tau/\hbar \ll 1$.

Reference [116] developed a theoretical framework for the IREE in a junction system consisting of a ferromagnetic metal (FM), a normal-metal (NM), and a topological insulator (TI), as illustrated in Fig. 2.12. In this system, the spin current generated in the FM by SP is converted into a charge current in the surface states of the TI through the IREE induced by spin-momentum locking, as shown in the right panel of Fig. 2.12. In the surface states of the TI, the spin orientation is entirely locked to the momentum direction. In other words, this situation corresponds to the regime where the spin splitting is exceedingly large, such that $\Delta_{\mathrm{so}} \gg \hbar/\tau, \epsilon_{\mathrm{F}}$, where ϵ_{F} denotes the Fermi energy. The study specifically elucidated the impact of the interface between the NM and TI on the IREE. The Boltzmann equation for the surface states of the TI is given as

follows:

$$\partial_T \hat{g}_{\boldsymbol{p}} + \boldsymbol{v} \cdot \nabla_{\boldsymbol{R}} \hat{g}_{\boldsymbol{p}} = \sum_{\boldsymbol{k}} \Gamma_{\boldsymbol{k}\boldsymbol{p}} (\hat{f}_{\boldsymbol{k}} - \hat{g}_{\boldsymbol{p}}) + \sum_{\boldsymbol{p}'} \Delta_{\boldsymbol{p}\boldsymbol{p}'} (\hat{g}_{\boldsymbol{p}'} - \hat{g}_{\boldsymbol{p}}). \tag{2.97}$$

Here, $\hat{f}_{\boldsymbol{k}}$ and $\hat{g}_{\boldsymbol{p}}$ denote the nonequilibrium distribution functions for the NM and the surface states of the TI, respectively. The vector $\boldsymbol{k}$ represents the three-dimensional momentum in the NM, while $\boldsymbol{p}$ corresponds to the two-dimensional momentum in the TI surface states. Additionally, $\boldsymbol{v}$ is the velocity of electrons in the TI surface states, ∂_T denotes the time derivative, and $\nabla_{\boldsymbol{R}}$ represents the spatial derivative with respect to the position $\boldsymbol{R}$ on the TI surface. The parameter $\Gamma_{\boldsymbol{k}\boldsymbol{p}}$ is the tunneling probability at the interface between the NM and the TI surface states and $\Delta_{\boldsymbol{p}\boldsymbol{p}'}$ represents the scattering probability caused by defects or impurities in the TI surface states. The tunneling probability $\Gamma_{\boldsymbol{k}\boldsymbol{p}}$ is modeled for both dirty and clean interface conditions as follows:

$$\text{dirty interface} : \Gamma_{\boldsymbol{k}\boldsymbol{q}} = \frac{\pi v_0^2 n_s C_t}{\hbar A} [\hat{1} + \hat{\boldsymbol{\sigma}} \cdot (\hat{\boldsymbol{z}} \times \hat{\boldsymbol{p}})] \delta(\epsilon_{\boldsymbol{k}} - \epsilon_{\boldsymbol{p}}), \tag{2.98}$$

$$\text{clean interface} : \Gamma_{\boldsymbol{k}\boldsymbol{q}} = \frac{\pi v_c^2 C_t}{\hbar A} [\hat{1} + \hat{\boldsymbol{\sigma}} \cdot (\hat{\boldsymbol{z}} \times \hat{\boldsymbol{p}})] (2\pi)^2 \delta(\boldsymbol{k}_{\parallel} - \boldsymbol{p}) \delta(\epsilon_{\boldsymbol{k}} - \epsilon_{\boldsymbol{p}}). \tag{2.99}$$

Here, v_0 and v_c represent the magnitudes of the tunneling potential at the interface between the NM and the TI surface states, n_s is the roughness defect density at the interface, A denotes the surface area, $\hat{1}$ is the identity matrix, $\hat{\boldsymbol{\sigma}}$ represents the Pauli matrices, $\hat{\boldsymbol{z}}$ is the unit vector normal to the surface, and $\hat{\boldsymbol{p}}$ is the unit vector indicating the direction of $\boldsymbol{p}$. The parameter C_t characterizes the overlap of the wave functions of the NM and the TI surface states in the tunneling region, which is assumed to be independent of the electron momentum involved in the tunneling process [117]. It should be noted that, for a clean interface, the in-plane momentum $\boldsymbol{k}_{\parallel}$ is conserved during the tunneling process. Reference [116] calculates the two-dimensional charge current density generated on the TI surface via the IREE induced by SP for both dirty and clean interfaces. The study reveals that the spin-to-charge conversion efficiency of the IREE differs between these two types of interfaces.

2.5 Rashba-Edelstein Magnetoresistance (REMR)

In junction systems composed of ferromagnetic materials and heavy metals, it is well-established that applying an electric current to the heavy metal induces the spin Hall magnetoresistance (SMR) [73, 119–121]. This effect is driven by the combination of the SHE and the ISHE within the bulk of the heavy metal, causing its electrical resistance to vary depending on the spin orientation of the adjacent ferromagnetic material. For a long time, the SMR has been described by using a phenomenological theory combining spin diffusion theory with spin-

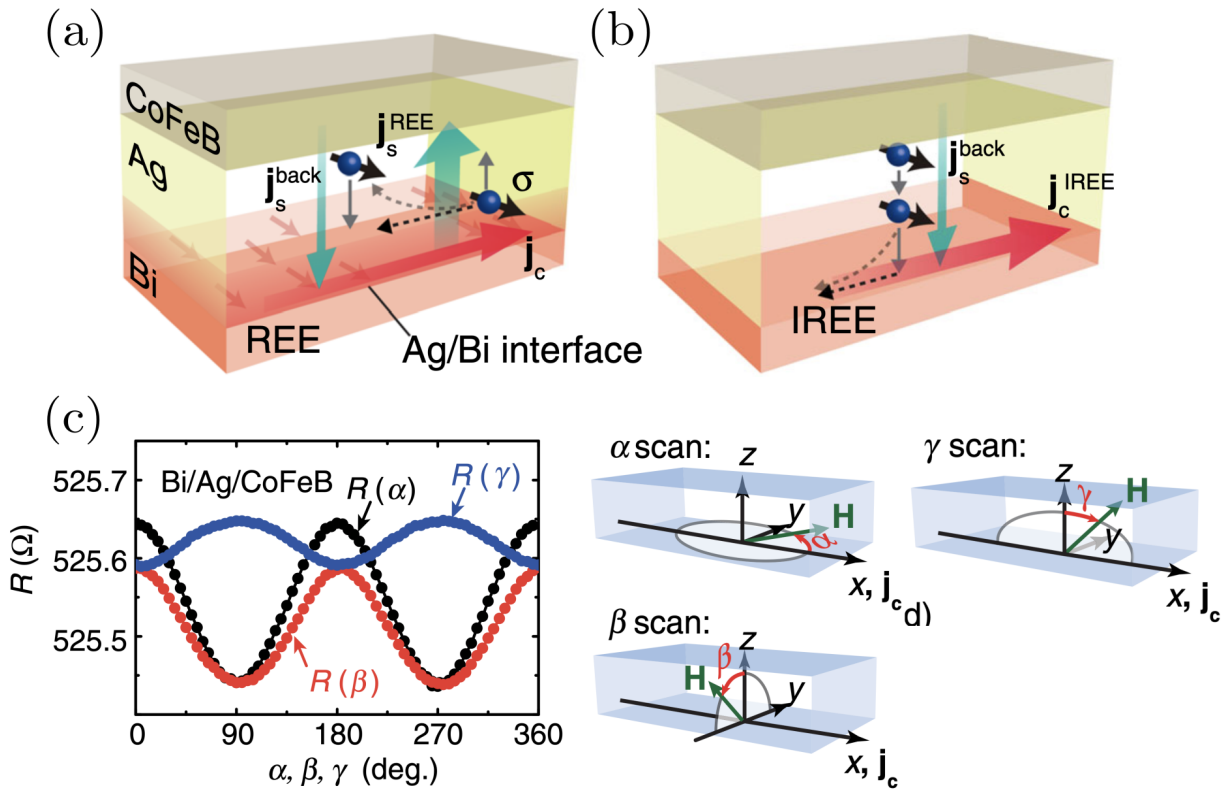

Figure 2.13: Experimental results of the REMR in CoFeB/Ag/Bi [118]. (a) When a charge current $\boldsymbol{j}_c$ is applied at the Ag/Bi interface, spin accumulation occurs due to the REE, generating a spin current $\boldsymbol{j}_s^{\mathrm{REE}}$ directed towards CoFeB. (b) A backflow spin current $\boldsymbol{j}_s^{\mathrm{back}}$ from CoFeB is converted into a charge current $\boldsymbol{j}_c^{\mathrm{IREE}}$ at the Ag/Bi interface via the IREE. (c) Experimental results of longitudinal resistance in the REMR. α, β, and γ represent the angle of the external magnetic field applied to CoFeB. Adapted from Ref. [118].

mixing conductance at an interface [120]. Recently, a microscopic theory for the SMR has been proposed [73, 122] and has been applied to several junction systems [121, 123, 124].

Recently, a magnetoresistance effect arising from combination of the REE and the IREE at the interface has been observed. This phenomenon, called the Rashba-Edelstein magnetoresistance (REMR), has been reported in various junction systems, such as Bi/Ag/CoFeB [118, 125, 126], CoFe/Cu/Bi_2O_3 [127], Pt/Co [128, 129], Cu[Pt]/YIG [130], LAO/STO [131], YIG/atomic layer materials [132], and Cr/YIG [25]. Figure 2.13 illustrates an experimental example of the REMR [118]. In the study, the REMR was observed in a system consisting of a ferromagnetic CoFeB layer interfaced with Ag/Bi, which exhibits the Rashba SOC. When a charge current is applied to the Ag/Bi interface, it is converted into a spin current flowing into the CoFeB layer via the REE, as shown in Fig. 2.13(a). A portion of this spin current is absorbed by CoFeB, while the rest returns to the Ag/Bi interface as a backflow spin current. As depicted in Fig. 2.13(b), this backflow spin current is converted into an electric current at the Ag/Bi interface via the IREE, modulating the charge current and electrical resistance at the interface. Since the magnitudes

of the backflow spin current and the current converted from it depend on the orientation of the localized spins in CoFeB, the electrical resistance of Ag/Bi becomes dependent on the spin orientation of CoFeB. Figure 2.13(c) presents experimental results showing the longitudinal resistance of the REMR as a function of the DC magnetic field applied to the ferromagnetic material, demonstrating that the electrical resistance at the Ag/Bi interface varies with the spin orientation in the ferromagnetic material.

Although theoretical studies on the REMR are actively being conducted [133–140], many rely on phenomenological descriptions, which limits their predictive capability regarding the spin-orientation dependence of electrical resistance. Moreover, the physical mechanism behind the REMR remains not fully understood.

2.6 Detailed Purpose of this dissertation

Building on the review of prior studies provided earlier, the motivation and the research purposes of this dissertation are presented in detail as follows. After describing the motivation behind in Sec. 2.6.1, the three subjects studied in this dissertation are elaborated in the subsequent subsections.

2.6.1 Motivation

In theoretical studies addressing spin injection at interfaces in magnetic junctions between ferromagnets and other substances, the LLG equation and spin mixing conductance, as introduced in Sec. 2.3.2, have been widely adopted. However, spin mixing conductance, being a phenomenological description based on scattering matrices, is insufficient for capturing dynamic processes involving magnon exchange at the interface. To address this, this dissertation employs a microscopic Hamiltonian that describes interfacial interactions in FI-2DEG systems to incorporate contributions from magnon-driven dynamic processes. By constructing a theory based on microscopic Hamiltonian rather than phenomenological parameters, this dissertation provides a foundation that is useful for comparison with experimental findings.

Additionally, as noted in Sec. 2.3.2, the concept of spin current has been predominantly used in prior studies to describe spin transport. However, in systems with the Rashba SOC or the Dresselhaus SOC, spin conservation does not hold, and hence the use of spin current has several problems for describing spin transport phenomena [141, 142]. This dissertation adopts an alternative framework [81] that characterizes spin transport without relying on the concept of spin current, instead utilizing the Boltzmann equation.

Furthermore, in systems where the Rashba SOC and the Dresselhaus SOC are of equal magnitude, several characteristic phenomena such as enhancement of spin relaxation time and the persistent spin helix (PSH) state emerge (see Sec. 2.1.3). These phenomena are closely related to the spin conservation law in 2DEG when the Rashba SOC and the Dresselhaus

SOC have completely the same amplitude. However, theoretical approaches employing the relaxation-time approximation, such as those discussed in Sec. 2.4.2, fail to incorporate the spin conservation law properly. This dissertation develops a theoretical framework that accounts for spin conservation and demonstrates that this consideration leads to qualitatively distinct results compared to those obtained without it, when the Rashba SOC and the Dresselhaus SOC are of equal magnitude.

2.6.2 Spin pumping into 2DEG

As outlined in Sec. 2.3.2, previous studies on SP have relied on a phenomenological framework based on the LLG equation and spin-mixing conductance. In my master thesis [69], a microscopic theory of SP was developed for a junction system comprising an FI and a 2DEG with the Rashba and Dresselhaus SOCs, which shares the same setup as this doctoral dissertation. However, the calculations in the master thesis, which focused on the enhancement of the Gilbert damping, did not account for impurity scattering-induced vertex corrections, thereby failing to adequately incorporate the effects of spin conservation that arise when the two SOCs are of equal strength. In Chap. 4, the enhancement of the Gilbert damping is re-evaluated with the vertex corrections included, highlighting the critical role of these corrections when the two SOCs are of nearly equal magnitude [48]. Furthermore, the chapter extends the discussion to the resonance frequency shift in the FMR induced by SP [48].

2.6.3 IREE by SP

As described in Sec. 2.4.3, the IREE induced by SP has been studied previously in some references. Ref. [115] focuses on the regime where the spin splitting of the conduction electron energy band due to the Rashba SOC, $\Delta_{\rm so}$, is much smaller than the impurity scattering strength, Γ, and the Fermi energy. On the other hand, Ref. [116] treated surface states of topological insulators, which has only one spin-polarized band, indicating the limit of the large spin-orbit interaction compared to Γ and the Fermi energy. In clean 2DEGs typically formed on semiconductor surfaces, however, the regime where $\Delta_{\rm so}$ is much larger than the impurity scattering and is much smaller than the Fermi energy is often realized [49, 143]. Accordingly, Chap. 5 develops a theoretical framework for the IREE induced by SP for such a regime based on the Boltzmann equation derived from a microscopic model [81]. Furthermore, we solve the Boltzmann equation without relaxation-time approximation for incorporating the spin conservation law, which becomes important when the Rashba and Dressenhaus SOCs are of nearly equal magnitude [49]. We note that this treatment corresponds to the consideration of the vertex correction in spin pumping discussed in Chap. 4.

2.6.4 Rashba-Edelstein magnetoresistance (REMR)

As introduced in Sec. 2.5, the REMR has been studied both experimentally and theoretically. However, most theoretical approaches rely on phenomenological models, such as those involving spin-mixing conductance. The anisotropic magnetoresistance (AMR) effect in diluted magnetic semiconductors with the Rashba or Dresselhaus SOCs has been analyzed using the Boltzmann equation [144, 145]. Their calculations can also be applied to the REMR in 2DEG since its effective model is similar as their model. However, these analyses neglect dynamic contributions from magnons in a ferromagnet. In Chap. 6, a theoretical framework for the REMR is constructed using the Boltzmann equation derived from a microscopic model, incorporating dynamic processes mediated by magnons [50]. It is also demonstrated that the results for the REMR are strongly dependent on the interfacial states [50].

Chapter 3

Model

In this chapter, we introduce a microscopic Hamiltonian for a junction system composed of 2DEG and FI, as shown in Fig. 3.1(a). This model is commonly used in the theoretical studies given in Chaps. 4, 5, and 6.

3.1 Two-Dimensional Electron Gas (2DEG)

The Hamiltonian of the 2DEG with the Rashba and Dresselhaus SOCs is given by

$$H_{\rm kin} = \sum_{\boldsymbol{k}} \begin{pmatrix} c^\dagger_{\boldsymbol{k}\uparrow} & c^\dagger_{\boldsymbol{k}\downarrow} \end{pmatrix} \hat{h}_{\boldsymbol{k}} \begin{pmatrix} c_{\boldsymbol{k}\uparrow} \\ c_{\boldsymbol{k}\downarrow} \end{pmatrix}, \tag{3.1}$$

$$\hat{h}_{\boldsymbol{k}} = (\epsilon_{\boldsymbol{k}} - \mu)\hat{1} + \alpha(k_y\hat{\sigma}_x - k_x\hat{\sigma}_y) + \beta(k_x\hat{\sigma}_x - k_y\hat{\sigma}_y), \tag{3.2}$$

Here, $c^\dagger_{\boldsymbol{k}\sigma}$ and $c_{\boldsymbol{k}\sigma}$ are the creation and annihilation operators for conduction electrons with wavevector $\boldsymbol{k} = (k_x, k_y)^T$ and spin $\sigma = \uparrow, \downarrow$, $\epsilon_{\boldsymbol{k}} = \hbar^2(k_x^2 + k_y^2)/2m^*$ is the kinetic energy, m^* is the effective mass, μ is the chemical potential, $\hat{1}$ is the identity matrix, α and β are the strengths of the Rashba SOC and Dresselhaus SOC, and $\hat{\boldsymbol{\sigma}} = (\hat{\sigma}_x, \hat{\sigma}_y)^T$ are the Pauli matrices. When the wavevector is expressed in polar coordinates as $\boldsymbol{k} = (|\boldsymbol{k}|\cos\varphi, |\boldsymbol{k}|\sin\varphi)^T$, we can rewrite Eq. (3.2) as follows:

$$\hat{h}_{\boldsymbol{k}} = (\epsilon_{\boldsymbol{k}} - \mu)\hat{1} - \boldsymbol{h}_{\rm eff}(\boldsymbol{k}) \cdot \hat{\boldsymbol{\sigma}}, \tag{3.3}$$

$$\boldsymbol{h}_{\rm eff}(\boldsymbol{k}) = |\boldsymbol{k}| \begin{pmatrix} -\alpha\sin\varphi - \beta\cos\varphi \\ \alpha\cos\varphi + \beta\sin\varphi \end{pmatrix}. \tag{3.4}$$

Here, $\boldsymbol{h}_{\rm eff} = (h_x, h_y)^T$ represents the effective Zeeman field felt by the conduction electrons. In the following, assuming that the spin-splitting width due to SOC, $k_{\rm F}\alpha$ and $k_{\rm F}\beta$, is sufficiently

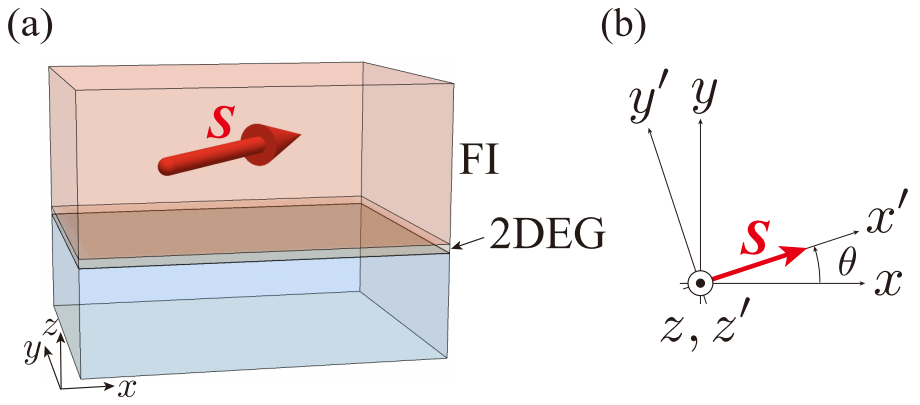

Figure 3.1: (a) The junction system studied in this dissertation. The red arrow $\boldsymbol{S}$ represents the localized spin in the FI. (b) The relationship between the laboratory frame (x, y, z) and the coordinate system (x', y', z') fixed to the localized spin in the FI.

small compared to the Fermi energy $\epsilon_{\rm F} = \hbar^2 k_{\rm F}^2 / 2m^*$ [1], we can approximate Eq. (3.4) using the Fermi wavevector $k_{\rm F}$ as follows:

$$\boldsymbol{h}_{\rm eff}(\boldsymbol{k}) \simeq \boldsymbol{h}_{\rm eff}(\varphi) \equiv k_{\rm F} \begin{pmatrix} -\alpha \sin\varphi - \beta \cos\varphi \\ \alpha \cos\varphi + \beta \sin\varphi \end{pmatrix}. \tag{3.5}$$

The magnitude of this effective Zeeman field is given by

$$h_{\rm eff}(\varphi) \equiv |\boldsymbol{h}_{\rm eff}(\varphi)| = k_{\rm F} \sqrt{\alpha^2 + \beta^2 + 2\alpha\beta \sin 2\varphi}, \tag{3.6}$$

and using this, the eigenvalues of Eq. (3.3) can be written as follows:

$$E_{\boldsymbol{k}}^{\gamma} = \epsilon_{\boldsymbol{k}} + \gamma h_{\rm eff}(\varphi). \tag{3.7}$$

This represents the energy dispersion of the 2DEG conduction electrons, which are split into two spin-polarized branches due to the Rashba and Dresselhaus SOCs. The label γ $(= \pm)$ is used to denote these two spin-polarized subbands. The eigenstates corresponding to these energy

[1] In semiconductor heterostructures, the spin splitting widths $k_{\rm F}\alpha$ and $k_{\rm F}\beta$ induced by SOC are typically less than 1 meV. For instance, in GaAs/AlGaAs heterostructures [146], using values for the electron density $n = 5.0 \times 10^{15}\ \mathrm{m}^{-2}$ and the effective mass $m^* = 0.067m$ [147], where m is an electron mass, $k_{\rm F}\alpha$ can be estimated to be 0.07 meV. At this electron density, the Fermi wavenumber is $k_{\rm F} = \sqrt{2\pi n} \simeq 1.8 \times 10^8\ \mathrm{m}^{-1}$, and the Fermi energy is $\epsilon_{\rm F} \simeq 20$ meV. Therefore, the condition $\epsilon_{\rm F} \gg k_{\rm F}\alpha$ is well satisfied.

eigenvalues are given by:

$$|\boldsymbol{k}\gamma\rangle = \frac{1}{\sqrt{2}}\begin{pmatrix} C(\varphi) \\ \gamma \end{pmatrix}, \tag{3.8}$$

$$C(\varphi) \equiv \frac{-h_x(\varphi) + ih_y(\varphi)}{h_{\mathrm{eff}}(\varphi)}. \tag{3.9}$$

From these eigenstates, we can derive the transformation relation between the annihilation operators for the 2DEG electrons in the σ (=$\uparrow, \downarrow$) basis and the γ (= $\pm$) basis

$$c_{\boldsymbol{k}\sigma} = \sum_{\gamma} C_{\sigma\gamma}(\varphi) c_{\boldsymbol{k}\gamma}, \tag{3.10}$$

$$C_{\uparrow\gamma} = C(\varphi)/\sqrt{2}, \;\; C_{\downarrow\gamma} = \gamma/\sqrt{2}. \tag{3.11}$$

For impurity scattering in the 2DEG, we use the following Hamiltonian for non-magnetic impurity scattering

$$H_{\mathrm{imp}} = \sum_i \sum_{\sigma} \int d\boldsymbol{r}\, v(\boldsymbol{r} - \boldsymbol{R}_i) \psi^{\dagger}_{\sigma}(\boldsymbol{r}) \psi_{\sigma}(\boldsymbol{r}). \tag{3.12}$$

Here, $\psi_{\sigma}(\boldsymbol{r}) = \mathcal{A}^{-1/2} \sum_{\boldsymbol{k}} e^{i\boldsymbol{k}\cdot\boldsymbol{r}} c_{\boldsymbol{k}\sigma}$ represents the field operator for conduction electrons in the 2DEG with spin σ. The term $v(\boldsymbol{r})$ is the impurity potential, $\boldsymbol{R}_i$ denotes the position of the impurities, and $\mathcal{A}$ is the area of the junction interface between the 2DEG and FI. For simplicity, the impurity potential is assumed to be point-like and is described as $v(\boldsymbol{r}) = u\delta(\boldsymbol{r})$, where u is a constant representing the strength of the impurity scattering. In this case, the momentum relaxation time τ due to non-magnetic impurity scattering can be expressed as $\tau = \hbar/\Gamma$, where $\Gamma = 2\pi n_{\mathrm{imp}} u^2 D(\epsilon_{\mathrm{F}})$ is the energy broadening, n_{imp} is the impurity concentration, and $D(\epsilon_{\mathrm{F}})$ is the density of states per unit area and per spin at the Fermi energy. In the following, the focus will be on the weak-impurity condition, $\Gamma \ll \max(k_{\mathrm{F}}\alpha, k_{\mathrm{F}}\beta)$, where the effect of spin-momentum locking in the 2DEG becomes prominent.

3.2 Ferromagnetic Insulator (FI)

We use the Heisenberg model as the Hamiltonian for the FI, given by

$$H_{\mathrm{FI}} = \sum_{\langle i,j \rangle} J_{ij} \boldsymbol{S}_i \cdot \boldsymbol{S}_j - \hbar\gamma_{\mathrm{g}} \sum_i \boldsymbol{h}_{\mathrm{dc}} \cdot \boldsymbol{S}_i, \tag{3.13}$$

$$\boldsymbol{h}_{\mathrm{dc}} = (-h_{\mathrm{dc}} \cos\theta, -h_{\mathrm{dc}} \sin\theta, 0), . \tag{3.14}$$

Here, J_{ij} (< 0) represents the ferromagnetic exchange interaction, $\langle i, j \rangle$ denotes pairs of nearest-neighbor localized spins, $\gamma_{\mathrm{g}}(< 0)$ is the gyromagnetic ratio, and $\boldsymbol{h}_{\mathrm{dc}}$ is the static magnetic

field applied externally in the x-y plane. The magnitude of this static magnetic field is denoted by h_{dc}, and θ represents the angle between the static magnetic field and the x-axis. In the laboratory coordinate system (x, y, z), the expectation value of the localized spin in the FI is $\langle \boldsymbol{S}_i \rangle = (\langle S_i^x \rangle, \langle S_i^y \rangle, \langle S_i^z \rangle) = (S_0 \cos\theta, S_0 \sin\theta, 0)$. However, in the coordinate system (x', y', z') where the x'-axis is fixed to the direction of the localized spin, as shown in Fig. 3.1(b), the expectation value is $\langle \boldsymbol{S}_i \rangle = (\langle S_i^{x'} \rangle, \langle S_i^{y'} \rangle, \langle S_i^{z'} \rangle) = (S_0, 0, 0)$. The spin operators in these coordinate systems are related through the following transformation:

$$\begin{pmatrix} S_i^{x'} \\ S_i^{y'} \\ S_i^{z'} \end{pmatrix} = \begin{pmatrix} \cos\theta & \sin\theta & 0 \\ -\sin\theta & \cos\theta & 0 \\ 0 & 0 & 1 \end{pmatrix} \begin{pmatrix} S_i^x \\ S_i^y \\ S_i^z \end{pmatrix}. \tag{3.15}$$

Assuming that the temperature of the FI is much lower than the ferromagnetic transition temperature and applying the Holstein-Primakoff transformation in the coordinate system (x', y', z'), we can approximate the localized spin operators using the magnon creation and annihilation operators under the condition that the magnitude of the localized spin S_0 is much larger than unity, as follows:

$$S_j^{x'+} = S_j^{y'} + iS_j^{z'} \simeq (2S_0)^{1/2} b_j, \tag{3.16}$$

$$S_j^{x'-} = S_j^{y'} - iS_j^{z'} \simeq (2S_0)^{1/2} b_j^\dagger, \tag{3.17}$$

$$S_j^{x'} = S_0 - b_j^\dagger b_j. \tag{3.18}$$

Using the Fourier transform of the magnon annihilation operator, $b_j = N_{\mathrm{FI}}^{-1/2} \sum_{\boldsymbol{q}} e^{i\boldsymbol{q}\cdot\boldsymbol{r}_j} b_{\boldsymbol{q}}$, we can reduce the Hamiltonian of the FI in Eq. (3.13) to a harmonic oscillator-type Hamiltonian in the leading order of $1/S_0$ as follows (see also Sec. 2.2.2):

$$H_{\mathrm{FI}} = \sum_{\boldsymbol{q}} \hbar\omega_{\boldsymbol{q}} b_{\boldsymbol{q}}^\dagger b_{\boldsymbol{q}}, \tag{3.19}$$

$$\hbar\omega_{\boldsymbol{q}} = \mathcal{D}\boldsymbol{q}^2 + \hbar|\gamma_{\mathrm{g}}|h_{\mathrm{dc}}. \tag{3.20}$$

Here, N_{FI} represents the number of unit cells in the FI, $\boldsymbol{q} = (q_x, q_y, q_z)$ is the three-dimensional wavevector of the magnons, $\hbar\omega_{\boldsymbol{q}}$ is the magnon energy, and $\mathcal{D}$ denotes the spin stiffness.

3.3 FI/2DEG Interface

In the laboratory frame, using the Pauli matrices $\hat{\sigma}_a$ $(a = x, y, z)$, we can express the spin operator for the conduction electrons in the 2DEG as follows:

$$s^a_{\bar{\boldsymbol{q}}} = \sum_{\sigma,\sigma'} \sum_{\boldsymbol{k}} c^\dagger_{\boldsymbol{k}\sigma} (\hat{\sigma}_a)_{\sigma\sigma'} c_{\boldsymbol{k}+\bar{\boldsymbol{q}}\sigma}, \quad (a = x, y, z), \tag{3.21}$$

Here, $\bar{\boldsymbol{q}} = (\bar{q}_x, \bar{q}_y)$ represents the wavevector of the conduction electrons in the 2DEG. The spin operators in the laboratory frame (x, y, z) and the spin operators in the coordinate system (x', y', z'), introduced in Sec. 3.2, are related through the following transformation:

$$\begin{pmatrix} s_i^{x'} \\ s_i^{y'} \\ s_i^{z'} \end{pmatrix} = \begin{pmatrix} \cos\theta & \sin\theta & 0 \\ -\sin\theta & \cos\theta & 0 \\ 0 & 0 & 1 \end{pmatrix} \begin{pmatrix} s_i^{x} \\ s_i^{y} \\ s_i^{z} \end{pmatrix}. \tag{3.22}$$

From this relation, the spin operators in the wavevector representation in the (x', y', z') coordinate system can be expressed as follows:

$$s^{x'}_{\bar{\boldsymbol{q}}} = \frac{1}{2} \sum_{\sigma,\sigma'} \sum_{\boldsymbol{k}} c^\dagger_{\boldsymbol{k}\sigma} (\hat{\sigma}^{x'})_{\sigma\sigma'} c_{\boldsymbol{k}+\bar{\boldsymbol{q}}\sigma'}, \tag{3.23}$$

$$s^{x'\pm}_{\bar{\boldsymbol{q}}} = \frac{1}{2} \sum_{\sigma,\sigma'} \sum_{\boldsymbol{k}} c^\dagger_{\boldsymbol{k}\sigma} (\hat{\sigma}^{x'\pm})_{\sigma\sigma'} c_{\boldsymbol{k}\pm\bar{\boldsymbol{q}}\sigma'}. \tag{3.24}$$

Here, $\hat{\sigma}^{x'}$ and $\hat{\sigma}^{x'\pm}$ are given by the following expressions:

$$\hat{\sigma}^{x'} = \cos\theta\ \hat{\sigma}_x + \sin\theta\ \hat{\sigma}_y, \tag{3.25}$$

$$\hat{\sigma}^{x'\pm} = -\sin\theta\ \hat{\sigma}_x + \cos\theta\ \hat{\sigma}_y \pm i\hat{\sigma}_z. \tag{3.26}$$

We describe the interfacial exchange coupling between the localized spins in the FI and the spins of the 2DEG electrons at the FI/2DEG interface by the following Hamiltonian, using the spin operators in the (x', y', z') coordinate system [48, 49, 63, 70–79]:

$$H_{\rm int} = \sum_{\boldsymbol{q}} \sum_{\bar{\boldsymbol{q}}} (T_{\boldsymbol{q},\bar{\boldsymbol{q}}} S^{x'+}_{\boldsymbol{q}} s^{x'-}_{\bar{\boldsymbol{q}}} + T^*_{\boldsymbol{q},\bar{\boldsymbol{q}}} S^{x'-}_{\boldsymbol{q}} s^{x'+}_{\bar{\boldsymbol{q}}}) + \sum_{\bar{\boldsymbol{q}}} \mathcal{T}_{\boldsymbol{0},\bar{\boldsymbol{q}}} S_0 s^{x'}_{\bar{\boldsymbol{q}}}, \tag{3.27}$$

The first term in this Hamiltonian represents the effect of magnon absorption and emission at the FI/2DEG interface, while the second term reflects the effect of the interfacial exchange bias, which can be interpreted as the effective Zeeman field felt by the conduction electrons in the 2DEG. Here, $T_{\boldsymbol{q},\bar{\boldsymbol{q}}}$ and $\mathcal{T}_{\boldsymbol{0},\bar{\boldsymbol{q}}}$ represent the strength of the interfacial exchange coupling; these terms take different forms depending on whether the FI/2DEG interface is dirty or clean, as

follows:

$$\text{dirty interface} : T_{\boldsymbol{q},\bar{\boldsymbol{q}}} = \bar{T},\ \mathcal{T}_{\boldsymbol{0},\bar{\boldsymbol{q}}} = \bar{\mathcal{T}}, \tag{3.28}$$

$$\text{clean interface} : T_{\boldsymbol{q},\bar{\boldsymbol{q}}} = \bar{T}\delta_{\boldsymbol{q}_\parallel,\bar{\boldsymbol{q}}},\ \mathcal{T}_{\boldsymbol{0},\bar{\boldsymbol{q}}} = \bar{\mathcal{T}}\delta_{\bar{\boldsymbol{q}},\boldsymbol{0}}, \tag{3.29}$$

Here, $\boldsymbol{q}_\parallel = (q_x, q_y)$ represents the in-plane component of the magnon wavevector $\boldsymbol{q} = (q_x, q_y, q_z)$, $\delta_{\boldsymbol{q}_\parallel,\bar{\boldsymbol{q}}}$ and $\delta_{\bar{\boldsymbol{q}},\boldsymbol{0}}$ are Kronecker deltas, and $\bar{T}$ and $\bar{\mathcal{T}}$ are constants independent of the wavevector [117,148]. The key point is that at a clean interface, the in-plane momentum of the conduction electrons in the 2DEG is conserved, while at a dirty interface, it is not conserved.

Chapter 4

Spin pumping

This chapter presents our study [48], which investigates a system composed of a ferromagnetic insulator (FI) and a two-dimensional electron gas (2DEG) with the Rashba and Dresselhaus spin-orbit couplings (SOCs), as shown in Fig. 4.1. In this setup, microwaves are applied to the FI, leading to the ferromagnetic resonance (FMR) and consequent spin pumping (SP), which injects a spin current from the FI into the 2DEG. This process results in enhanced Gilbert damping in the FI/2DEG junction compared to the standalone FI, thereby broadening the FMR absorption spectrum linewidth. Additionally, a shift in the FMR frequency occurs.

The broadening of the FMR absorption spectrum due to SP in junction systems, corresponding to an enhancement of the Gilbert damping, is a well-established phenomenon. Its analysis has conventionally employed a phenomenological approach based on the Landau-Lifshitz-Gilbert (LLG) equation and spin mixing conductance. In this chapter, we analyze the enhancement of the Gilbert damping using the microscopic Hamiltonian introduced in Chap. 3. This analysis clarifies the contribution of magnon absorption and emission, represented by the first term in Eq. (3.27), to the enhancement of the Gilbert damping. Moreover, the microscopic SP theory, utilizing the interfacial interaction Hamiltonian in Eq. (3.27), has been applied to a variety of systems in which ferromagnetic insulators are coupled with materials such as nickel-palladium alloys [70], superconductors [72, 76], graphene [74], and bismuth [63]. In this study, we develop a theoretical framework for SP in a two-dimensional electron gas (2DEG) system featuring spin-split energy bands induced by the Rashba and Dresselhaus spin-orbit couplings (SOCs).

This chapter addresses the calculation of both the enhanced Gilbert damping and the FMR frequency shift, taking into account the vertex corrections due to impurity scattering in the 2DEG. In the previous work [78], we calculated the enhancement of the Gilbert damping without the vertex corrections for the same setup [69]. The vertex corrections enable the inclusion of various conservation laws [149, 150], suggesting that the spin conservation law, which holds when the Rashba SOC and the Dresselhaus SOC are of equal magnitude, can be effectively taken into account. This chapter reveals significant differences between the results with and without the vertex corrections when these two SOC strengths are identical.

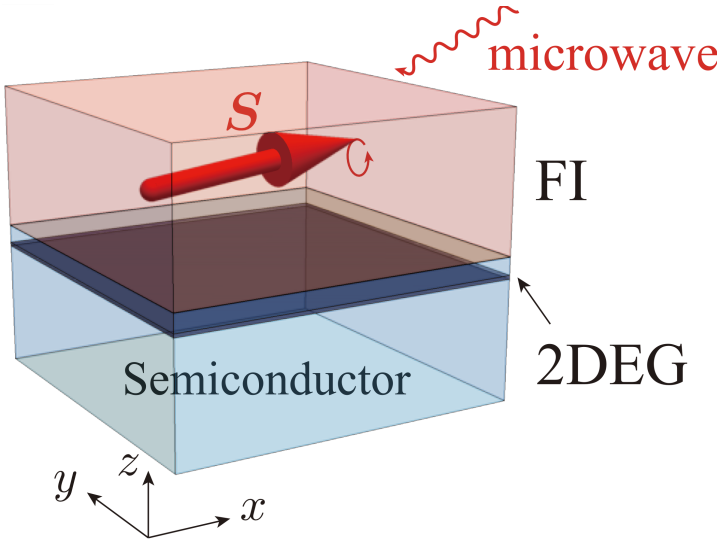

Figure 4.1: The junction system examined in this chapter. Microwave irradiation induces the ferromagnetic resonance (FMR), resulting in spin injection from the ferromagnetic insulator (FI) into the two-dimensional electron gas (2DEG) via spin pumping.

The chapter is structured as follows: in Sec. 4.1 we derive the temperature Green's function for the 2DEG, incorporating impurity scattering. In Sec. 4.2, we derive the magnon Green's function for the FI-2DEG junction and demonstrate that the enhanced Gilbert damping and FMR frequency shift can be expressed through the spin susceptibility of the 2DEG. In Sec. 4.3 we then calculate the spin susceptibility of the 2DEG, both with and without the vertex corrections and obtain the expressions for the enhanced Gilbert damping and FMR frequency shift for each case. Finally, in Secs. 4.4 and 4.5 we plot these results and discuss the effects of the vertex corrections.

4.1 Green's Function for a 2DEG

The temperature Green's function for conduction electrons in a 2DEG is defined in the absence of impurities as follows:

$$g_{\sigma\sigma'}(\boldsymbol{k},\tau) = -\frac{1}{\hbar}\langle T_\tau c_{\boldsymbol{k}\sigma}(\tau) c^\dagger_{\boldsymbol{k}\sigma'}\rangle, \qquad (-\hbar\beta < \tau < \hbar\beta) \tag{4.1}$$

$$c_{\boldsymbol{k}\sigma}(\tau) = e^{H_{\rm kin}\tau/\hbar} c_{\boldsymbol{k}\sigma} e^{-H_{\rm kin}\tau/\hbar}. \tag{4.2}$$

Here, τ represents imaginary time, T_τ denotes the imaginary-time-ordered product, β is the inverse temperature, $c^\dagger_{\boldsymbol{k},\sigma}$, $c_{\boldsymbol{k},\sigma}$ are the creation and annihilation operators for conduction electrons in the 2DEG, and $H_{\rm kin}$ is the Hamiltonian of the 2DEG introduced in Eq. (3.1). The equation of motion for the temperature Green's function of electrons in the absence of impurities, $\hat{g}_0(\boldsymbol{k},\tau)$,

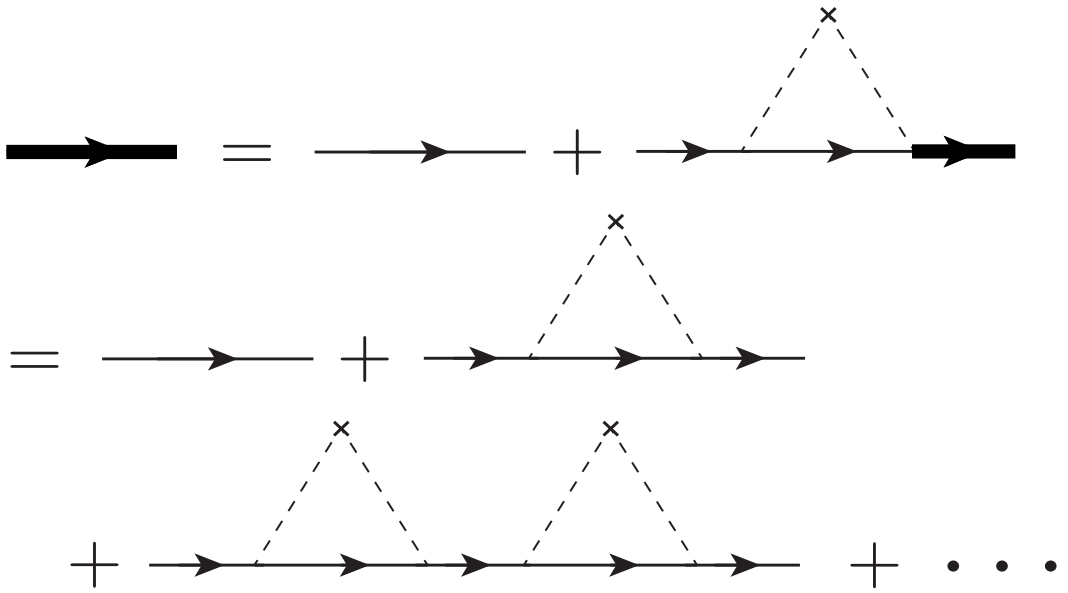

Figure 4.2: The Dyson equation under the Born approximation for the Green's function of conduction electrons in a 2DEG. The bold (thin) line represents the Green's function with (without) impurity scattering, and the dashed line represents impurity scattering. Adapted from Ref. [48].

is given by

$$\left(-\hbar\hat{1}\frac{\partial}{\partial\tau}-\hat{h}_{\boldsymbol{k}}\right)\hat{g}_0(\boldsymbol{k},\tau)=\delta(\tau)\hat{1},\qquad(-\hbar\beta<\tau<\hbar\beta). \tag{4.3}$$

Here, $\hat{1}$ denotes the 2×2 identity matrix. Using the fermionic Matsubara frequency $\omega_m = (2m+1)\pi/(\hbar\beta)$, where m is an integer, we can write the Fourier expansions of the temperature Green's function and the delta function as follows:

$$\hat{g}_0(\boldsymbol{k},\tau)=\frac{1}{\hbar\beta}\sum_{\omega_m}e^{-i\omega_m\tau}\hat{g}_0(\boldsymbol{k},i\omega_m),\qquad\delta(\tau)=\frac{1}{\hbar\beta}\sum_{\omega_m}e^{-i\omega_m\tau}. \tag{4.4}$$

By substituting these into Eq. (4.3), we obtain the temperature Green's function,

$$\hat{g}_0(\boldsymbol{k},i\omega_m)=(i\hbar\omega_m\hat{1}-\hat{h}_{\boldsymbol{k}})^{-1}=\frac{(i\hbar\omega_m-\xi_{\boldsymbol{k}})\hat{1}-\boldsymbol{h}_{\rm eff}\cdot\hat{\boldsymbol{\sigma}}}{(i\hbar\omega_m-E^+_{\boldsymbol{k}})(i\hbar\omega_m-E^-_{\boldsymbol{k}})}. \tag{4.5}$$

Here, $\hat{A}^{-1}$ represents the inverse of matrix $\hat{A}$, and $\xi_{\boldsymbol{k}}=\epsilon_{\boldsymbol{k}}-\mu$, where μ is the chemical potential.

Next, we calculate the temperature Green's function for conduction electrons in a 2DEG considering the effect of impurities, $\hat{g}(\boldsymbol{k},i\omega_n)$, using the Dyson equation corresponding to the

Feynman diagram in Fig. 4.2:

$$(\hat{g}(\boldsymbol{k}, i\omega_m))^{-1} = (\hat{g}_0(\boldsymbol{k}, i\omega_m))^{-1} - \hat{\Gamma}(i\omega_m). \tag{4.6}$$

Here, $\hat{\Gamma}(i\omega_m)$ represents the self-energy due to the effect of impurity scattering. Within the second-order perturbation theory of the impurity Hamiltonian H_{imp}, as given in Eq. (3.12), we can calculate the Feynman diagram for this self-energy shown in Fig. 4.3(a) as follows:

$$\hat{\Gamma}(i\omega_m) = \frac{n_{\text{imp}} u^2}{\mathcal{A}} \sum_{\boldsymbol{k}} \hat{g}_0(\boldsymbol{k}, i\omega_m) = -\frac{i\Gamma}{2} \text{sgn}(\omega_m) \hat{1}. \tag{4.7}$$

This calculation corresponds to the Born approximation. Here, $\text{sgn}(x)$ denotes the sign function, and $\Gamma \equiv 2\pi n_{\text{imp}} u^2 D(\epsilon_{\text{F}})$ is the parameter representing the strength of nonmagnetic impurity scattering. Substituting Eqs. (4.5) and (4.7) into the Dyson equation, Eq. (4.6), yields the following expression:

$$(\hat{g}(\boldsymbol{k}, i\omega_m))^{-1} = \begin{pmatrix} i\hbar\omega_m - \xi_{\boldsymbol{k}} + \frac{i\Gamma}{2}\text{sgn}(\omega_m) & h_x - ih_y \\ h_x + ih_y & i\hbar\omega_m - \xi_{\boldsymbol{k}} + \frac{i\Gamma}{2}\text{sgn}(\omega_m) \end{pmatrix}. \tag{4.8}$$

By calculating the inverse of this matrix, we obtain the expression for the temperature Green's function, considering the effect of impurities,

$$\hat{g}(\boldsymbol{k}, i\omega_m) = \frac{[i\hbar\omega_m - \xi_{\boldsymbol{k}} + i\Gamma\text{sgn}(\omega_m)/2]\hat{1} - \boldsymbol{h}_{\text{eff}} \cdot \hat{\boldsymbol{\sigma}}}{\prod_{\gamma=\pm}[i\hbar\omega_m - E^{\gamma}_{\boldsymbol{k}} + i\Gamma\text{sgn}(\omega_m)/2]}. \tag{4.9}$$

It should be noted that Eq. (4.7) represents the self-energy within the Born approximation. However, when $\hat{g}_0(\boldsymbol{k}, i\omega_m)$ in Eq. (4.7) is replaced with $\hat{g}(\boldsymbol{k}, i\omega_m)$ from Eq. (4.9), which corresponds to the self-consistent Born approximation in Fig. 4.3(b), the self-energy yields the same result:

$$\hat{\Gamma}(i\omega_m) = \frac{n_i u^2}{\mathcal{A}} \sum_{\boldsymbol{k}} \hat{g}(\boldsymbol{k}, i\omega_m) = -\frac{i\Gamma}{2} \text{sgn}(\omega_m) \hat{1}. \tag{4.10}$$

Therefore, the temperature Green's function for conduction electrons in Eq. (4.9) is also a solution under the self-consistent Born approximation.

4.2 Magnon Green's Function in the FI/2DEG Junction System

In this section, we derive the magnon Green's function in the FI/2DEG junction system. Let the sum of the Hamiltonians for the 2DEG and FI, as given in Eq. (3.1) and Eq. (3.19), respectively,

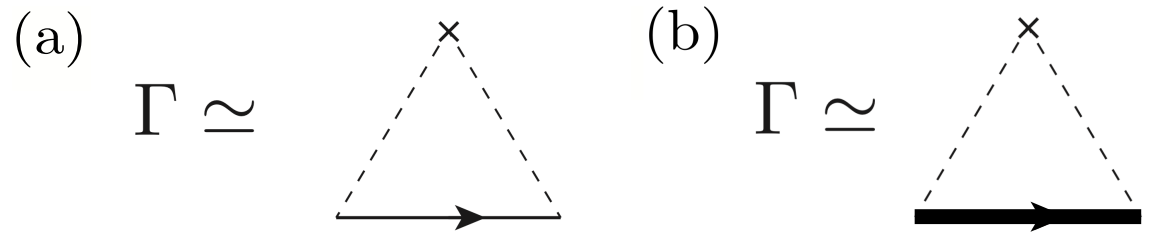

Figure 4.3: (a) Self-energy in the Born approximation. The thin line represents $\hat{g}_0(\boldsymbol{k}, i\omega_m)$. (b) Self-energy in the self-consistent Born approximation. The bold line denotes $\hat{g}(\boldsymbol{k}, i\omega_m)$.

be the unperturbed Hamiltonian $H_0 = H_{\text{kin}} + H_{\text{FI}}$, and the interfacial exchange interaction Hamiltonian in Eq. (3.27), H_{int}, be the perturbative Hamiltonian. The perturbative expansion of the magnon Green's function with respect to H_{int} can formally be written as

$$G(\boldsymbol{k}, \tau) = -\frac{1}{\hbar}\left\langle T_\tau S^{x'+}_{I,\boldsymbol{k}}(\tau) S^{x'-}_{I,\boldsymbol{k}}(0) \exp\left(-\frac{1}{\hbar}\int_0^{\hbar\beta} d\tau'' H_{I,\text{int}}(\tau'')\right)\right\rangle_c . \tag{4.11}$$

Here, T_τ denotes the imaginary-time ordering operator, and $\langle \cdots \rangle_c$ indicates the thermal average with respect to the unperturbed Hamiltonian, taken only for connected diagrams. Additionally,

$$S^{x'\pm}_{I,\boldsymbol{k}}(\tau) = e^{H_0\tau/\hbar} S^{x'\pm}_{\boldsymbol{k}} e^{-H_0\tau/\hbar}, \tag{4.12}$$

$$H_{I,\text{int}}(\tau) = e^{H_0\tau/\hbar} H_{\text{int}} e^{-H_0\tau/\hbar} \tag{4.13}$$

are operators in the interaction picture. However, from this point onward, the subscript I indicating the interaction picture will be omitted. Considering up to second-order perturbation terms in the expansion of Eq. (4.11), we obtain the following expression:

$$G(\boldsymbol{k}, \tau) = G_0(\boldsymbol{k}, \tau) + \delta G(\boldsymbol{k}, \tau), \tag{4.14}$$

$$\delta G(\boldsymbol{k}, \tau) = \frac{1}{2!}\left(-\frac{1}{\hbar}\right)^3 \int_0^{\hbar\beta} d\tau_1 \int_0^{\hbar\beta} d\tau_2 \langle T_\tau S^{x'+}_{\boldsymbol{k}}(\tau) S^{x'-}_{\boldsymbol{k}}(0) H_{\text{int}}(\tau_1) H_{\text{int}}(\tau_2)\rangle_c . \tag{4.15}$$

Here, $G_0(\boldsymbol{k}, \tau)$ is the magnon Green's function with respect to the unperturbed Hamiltonian H_0, given by the following equation:

$$G_0(\boldsymbol{k}, \tau) = -\frac{1}{\hbar}\langle T_\tau S^{x'+}_{\boldsymbol{k}}(\tau) S^{x'-}_{\boldsymbol{k}}(0)\rangle_0 . \tag{4.16}$$

By substituting the interfacial exchange Hamiltonian for a clean interface system given in Eqs. (3.27) and (3.29),

$$H_{\text{int}}(\tau) = \sum_{\boldsymbol{k}} [\bar{T} S^{x'+}_{\boldsymbol{k}}(\tau) s^{x'-}_{\boldsymbol{k}}(\tau) + \bar{T}^* S^{x'-}_{\boldsymbol{k}}(\tau) s^{x'+}_{\boldsymbol{k}}(\tau)], \tag{4.17}$$

into Eq. (4.15) and applying the Bloch-De Dominicis theorem, we obtain the following equation,

$$\begin{aligned}\delta G(\boldsymbol{k},\tau) &= \left(-\frac{1}{\hbar}\right)^3 |\bar{T}|^2 \int_0^{\hbar\beta} d\tau_1 d\tau_2 \\ &\quad \times \left[\langle T_\tau S_{\boldsymbol{k}}^{x'+}(\tau) S_{\boldsymbol{k}}^{x'-}(\tau_2)\rangle_0 \langle T_\tau S_{\boldsymbol{k}}^{x'+}(\tau_1) S_{\boldsymbol{k}}^{x'-}(0)\rangle_0 \langle T_\tau s_{\boldsymbol{k}}^{x'+}(\tau_2) s_{\boldsymbol{k}}^{x'-}(\tau_1)\rangle_0\right] \\ &= \int_0^{\hbar\beta} d\tau_1 d\tau_2 G_0(\boldsymbol{k},\tau-\tau_2)\Sigma(\boldsymbol{k},\tau_2-\tau_1)G_0(\boldsymbol{k},\tau_1). \end{aligned} \tag{4.18}$$

Here, $\Sigma(\boldsymbol{k},\tau)$ represents the magnon self-energy with respect to the unperturbed Hamiltonian H_0 and is expressed by the following equation:

$$\Sigma(\boldsymbol{k},\tau) = -\frac{|\bar{T}|^2}{\hbar}\langle T_\tau s_{\boldsymbol{k}}^{x'+}(\tau) s_{\boldsymbol{k}}^{x'-}(0)\rangle_0. \tag{4.19}$$

Using the Fourier transforms with respect to the bosonic Matsubara frequency $\omega_n = 2\pi n/(\hbar\beta)$, where n is an integer

$$\delta G(\boldsymbol{k}, i\omega_n) = \int_0^{\hbar\beta} d\tau\, e^{i\omega_n\tau}\delta G(\boldsymbol{k},\tau), \quad \delta G(\boldsymbol{k},\tau) = \frac{1}{\hbar\beta}\sum_{i\omega_n} e^{-i\omega_n\tau}\delta G(\boldsymbol{k}, i\omega_n), \tag{4.20}$$

$$\Sigma(\boldsymbol{k}, i\omega_n) = \int_0^{\hbar\beta} d\tau\, e^{i\omega_n\tau}\Sigma(\boldsymbol{k},\tau), \quad \Sigma(\boldsymbol{k},\tau) = \frac{1}{\hbar\beta}\sum_{i\omega_n} e^{-i\omega_n\tau}\Sigma(\boldsymbol{k}, i\omega_n), \tag{4.21}$$

we can rewrite Eq. (4.18) as follows:

$$\delta G(\boldsymbol{k}, i\omega_n) = G_0(\boldsymbol{k}, i\omega_n)\Sigma(\boldsymbol{k}, i\omega_n)G_0(\boldsymbol{k}, i\omega_n). \tag{4.22}$$

The Feynman diagram for this equation corresponds to the second term on the right-hand side of Fig. 4.4. As shown in Fig. 4.4, $G(\boldsymbol{k}, i\omega_n)$ can be expanded perturbatively through the repeated structure of the same type of diagram. This expansion can be written as follows:

$$\begin{aligned} G(\boldsymbol{k}, i\omega_n) &= G_0(\boldsymbol{k}, i\omega_n) + G_0(\boldsymbol{k}, i\omega_n)\Sigma(\boldsymbol{k}, i\omega_n)G_0(\boldsymbol{k}, i\omega_n) \\ &\quad + G_0(\boldsymbol{k}, i\omega_n)\Sigma(\boldsymbol{k}, i\omega_n)G_0(\boldsymbol{k}, i\omega_n)\Sigma(\boldsymbol{k}, i\omega_n)G_0(\boldsymbol{k}, i\omega_n) + \cdots \\ &= \frac{G_0(\boldsymbol{k}, i\omega_n)}{1 - G_0(\boldsymbol{k}, i\omega_n)\Sigma(\boldsymbol{k}, i\omega_n)} = \frac{1}{G_0(\boldsymbol{k}, i\omega_n)^{-1} - \Sigma(\boldsymbol{k}, i\omega_n)}. \end{aligned} \tag{4.23}$$

This is the Dyson equation for the magnon Green's function. Here, $G_0(\boldsymbol{k}, i\omega_n)$ represents the magnon Green's function in the FI system alone. Using Eq. (4.16) and the Fourier transform for the Green's function given by Eq. (4.20), we can express $G_0(\boldsymbol{k}, i\omega_n)$ as follows:

$$G_0(\boldsymbol{k}, i\omega_n) = \frac{2S_0/\hbar}{i\omega_n - \omega_{\boldsymbol{k}} - \alpha_{\mathrm{G}}|\omega_n|}. \tag{4.24}$$

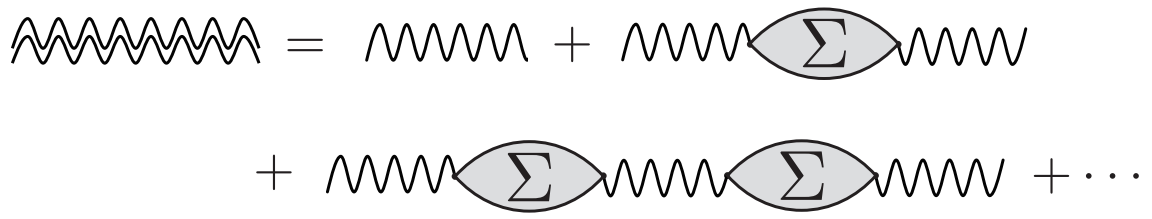

Figure 4.4: The Dyson equation for the magnon Green's function. The wavy line represents G_0, while the double wavy line denotes G.

Here, $\alpha_{\rm G}$ is the phenomenologically introduced the Gilbert damping constant. The expression for $\Sigma(\boldsymbol{k}, i\omega_n)$ in Eq. (4.23) is given by Eqs. (4.19) and (4.21) within the framework of second-order perturbation theory with respect to the interfacial interaction. Using the expression for the spin susceptibility per unit area of the 2DEG,

$$\chi(\boldsymbol{k},\tau) = -\frac{1}{\hbar\mathcal{A}}\langle T_\tau s_{\boldsymbol{k}}^{x'+}(\tau) s_{\boldsymbol{k}}^{x'-}(0)\rangle_0, \quad \chi(\boldsymbol{k}, i\omega_n) = \int_0^{\hbar\beta} d\tau\, \chi(\boldsymbol{k},\tau) e^{i\omega_n\tau}. \tag{4.25}$$

we can rewrite Eqs. (4.19) and (4.21) as follows:

$$\Sigma(\boldsymbol{k}, i\omega_n) = |\bar{T}|^2 \mathcal{A}\chi(\boldsymbol{k}, i\omega_n). \tag{4.26}$$

In other words, within the second-order perturbation theory of the interfacial interaction, the effect of the interfacial interaction appears only in the coefficient of Eq. (4.26). Therefore, to obtain the magnon self-energy, it is sufficient to calculate the spin susceptibility of the conduction electrons in the 2DEG alone.

The retarded component of Green's function can be obtained by performing the analytic continuation, replacing the Matsubara frequency with $i\omega_n \to \omega + i\delta$. Applying this analytic continuation to Eq. (4.23) and setting $\boldsymbol{k} = 0$ gives the retarded magnon Green's function, which corresponds to the uniform precession of localized spins in the FI during the FMR:

$$G^R(\boldsymbol{0},\omega) = \frac{2S_0/\hbar}{\omega - (\omega_{\boldsymbol{0}} + \delta\omega_{\boldsymbol{0}}) + i(\alpha_{\rm G} + \delta\alpha_{\rm G})\omega}, \tag{4.27}$$

$$\frac{\delta\omega_{\boldsymbol{0}}}{\omega_{\boldsymbol{0}}} \simeq \frac{2S_0|\bar{T}|^2\mathcal{A}}{\hbar\omega_{\boldsymbol{0}}} \,\mathrm{Re}\,\chi^R(\boldsymbol{0},\omega_{\boldsymbol{0}}), \tag{4.28}$$

$$\delta\alpha_{\rm G} \simeq -\frac{2S_0|\bar{T}|^2\mathcal{A}}{\hbar\omega_{\boldsymbol{0}}} \,\mathrm{Im}\,\chi^R(\boldsymbol{0},\omega_{\boldsymbol{0}}). \tag{4.29}$$

Here, $\omega_{\boldsymbol{k}=\boldsymbol{0}} = \gamma_{\rm g} h_{\rm dc}$ represents the FMR frequency, and $\delta\omega_{\boldsymbol{0}}$ and $\delta\alpha_{\rm G}$ represent the shift in the FMR resonance frequency and the modulation of the Gilbert damping, respectively, due to the junction between the FI and the 2DEG. In Eqs. (4.28) and (4.29), we assume that the linewidth of the FMR absorption spectrum is sufficiently narrow ($\alpha_{\rm G} + \delta\alpha_{\rm G} \ll 1$), and replace the microwave

$$\chi_0(\boldsymbol{k}, i\omega_n) =$$

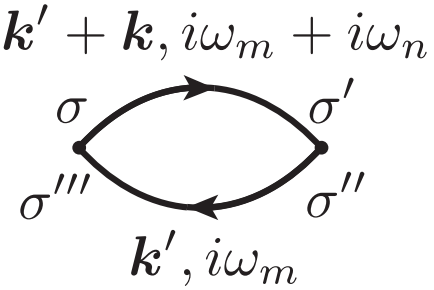

Figure 4.5: Spin susceptibility without considering the vertex corrections. The bold line represents the Green's function of the 2DEG, $\hat{g}(\boldsymbol{k}, i\omega_m)$, which accounts for impurity scattering and is given by Eq. (4.9).

frequency ω by the FMR frequency $\omega_{\mathbf{0}}$. From Eqs. (4.28) and (4.29), it is clear that $\delta\omega_{\mathbf{0}}$ and $\delta\alpha_{\mathrm{G}}$ are determined by the uniform spin susceptibility of the conduction electrons in the 2DEG, $\chi^R(\mathbf{0}, \omega_{\mathbf{0}})$.

4.3 Spin Susceptibility of the 2DEG

4.3.1 Calculation without vertex corrections

In this section, we calculate the spin susceptibility χ_0 of the 2DEG without considering the vertex corrections after Ref. [78]. First, by substituting Eq. (3.24) into Eq. (4.25), the spin susceptibility for $0 < \tau < \hbar\beta$ can be expressed as follows:

$$\begin{aligned}\chi(\boldsymbol{k}, \tau) &= -\frac{1}{\hbar\mathcal{A}}\langle T_\tau s_{\boldsymbol{k}}^{x'+}(\tau) s_{\boldsymbol{k}}^{x'-}(0)\rangle_0 \\ &= -\frac{1}{4\hbar\mathcal{A}} \sum_{\sigma,\sigma',\sigma'',\sigma'''} \sum_{\boldsymbol{k}_1,\boldsymbol{k}_2} (\sigma^{x'+})_{\sigma\sigma'} (\sigma^{x'-})_{\sigma''\sigma'''} \langle T_\tau c^\dagger_{\boldsymbol{k}_1\sigma}(\tau) c_{\boldsymbol{k}_1+\boldsymbol{k}\sigma'}(\tau) c^\dagger_{\boldsymbol{k}_2\sigma''}(0) c_{\boldsymbol{k}_2-\boldsymbol{k}\sigma'''}(0)\rangle_c .\end{aligned} \tag{4.30}$$

By incorporating the impurity potential given by Eq. (3.12) perturbatively and considering only the contributions from the Feynman diagrams in Fig. 4.5, the spin susceptibility in Eq. (4.30) can be expressed as follows:

$$\chi_0(\boldsymbol{k}, \tau) = \frac{\hbar}{4\mathcal{A}} \sum_{\sigma,\sigma',\sigma'',\sigma'''} \sum_{\boldsymbol{k}'} (\sigma^{x'+})_{\sigma\sigma'} (\sigma^{x'-})_{\sigma''\sigma'''} g_{\sigma'''\sigma}(\boldsymbol{k}', -\tau) g_{\sigma'\sigma''}(\boldsymbol{k}' + \boldsymbol{k}, \tau). \tag{4.31}$$

Then, by applying the Fourier transform with respect to imaginary time τ to the above equation, where ω_m is the Matsubara frequency for electrons, we obtain the following expression

$$\chi_0(\boldsymbol{k}, i\omega_n) = \frac{1}{4\beta\mathcal{A}} \sum_{\boldsymbol{k}', i\omega_m} \mathrm{Tr}\left[\hat{g}(\boldsymbol{k}', i\omega_m)\hat{\sigma}^{x'+}\hat{g}(\boldsymbol{k}'+\boldsymbol{k}, i\omega_m + i\omega_n)\hat{\sigma}^{x'-}\right]. \tag{4.32}$$

Here, $\hat{g}(\boldsymbol{k}, i\omega_m)$ is the temperature Green's function of the 2DEG, which accounts for impurity scattering and is given by Eq. (4.9). By substituting this Green's function into Eq. (4.32) and conducting analytic continuation $i\omega_n \rightarrow \omega + i\delta$, we obtain the following expression for the retarded component of the uniform spin susceptibility

$$\chi_0^R(\boldsymbol{0}, \omega) = \mathrm{Re}\,\chi_0^R(\boldsymbol{0}, \omega) + i\,\mathrm{Im}\,\chi_0^R(\boldsymbol{0}, \omega), \tag{4.33}$$

$$\begin{aligned}\mathrm{Re}\,\chi_0^R(\boldsymbol{0}, \omega) = &-\frac{1}{4}\sum_{\gamma,\gamma'} D(\epsilon_\mathrm{F}) \int_0^{2\pi} \frac{d\varphi}{2\pi}[1 - \gamma\hat{\boldsymbol{h}}_\mathrm{eff}(\varphi)\cdot\hat{\boldsymbol{m}}][1 + \gamma'\hat{\boldsymbol{h}}_\mathrm{eff}(\varphi)\cdot\hat{\boldsymbol{m}}] \\ &\times \frac{(E_{\boldsymbol{k}}^{\gamma} - E_{\boldsymbol{k}}^{\gamma'})(\hbar\omega + E_{\boldsymbol{k}}^{\gamma} - E_{\boldsymbol{k}}^{\gamma'}) + \Gamma^2}{(\hbar\omega + E_{\boldsymbol{k}}^{\gamma} - E_{\boldsymbol{k}}^{\gamma'})^2 + \Gamma^2},\end{aligned} \tag{4.34}$$

$$\begin{aligned}\mathrm{Im}\,\chi_0^R(\boldsymbol{0}, \omega) = &-\frac{1}{4}\sum_{\gamma,\gamma'} D(\epsilon_\mathrm{F}) \int_0^{2\pi} \frac{d\varphi}{2\pi}[1 - \gamma\hat{\boldsymbol{h}}_\mathrm{eff}(\varphi)\cdot\hat{\boldsymbol{m}}][1 + \gamma'\hat{\boldsymbol{h}}_\mathrm{eff}(\varphi)\cdot\hat{\boldsymbol{m}}] \\ &\times \frac{\Gamma\hbar\omega}{(\hbar\omega + E_{\boldsymbol{k}}^{\gamma} - E_{\boldsymbol{k}}^{\gamma'})^2 + \Gamma^2}.\end{aligned} \tag{4.35}$$

Here, $D(\epsilon_\mathrm{F})$ is the density of states per unit area and per spin at the Fermi energy of the 2DEG electrons, $\hat{\boldsymbol{h}}_\mathrm{eff}(\varphi) = \boldsymbol{h}_\mathrm{eff}(\varphi)/h_\mathrm{eff}(\varphi)$ is the unit vector representing the direction of the effective Zeeman magnetic field generated by the Rashba and Dresselhaus SOCs, and $\hat{\boldsymbol{m}} = (\cos\theta, \sin\theta)$ is the vector representing the direction of the localized spins in the FI. Using Eqs. (4.28), (4.29), (4.34) and (4.35), we can write the shift in the FMR frequency and the modulation of the Gilbert damping without considering the vertex corrections as follows:

$$\frac{\delta\omega_{\boldsymbol{0}}^{\mathrm{nv}}}{\omega_{\boldsymbol{0}}} \simeq \frac{2S_0|\bar{T}|^2\mathcal{A}}{\hbar\omega_{\boldsymbol{0}}}\,\mathrm{Re}\,\chi_0^R(\boldsymbol{0}, \omega_{\boldsymbol{0}}), \tag{4.36}$$

$$\delta\alpha_\mathrm{G}^{\mathrm{nv}} \simeq -\frac{2S_0|\bar{T}|^2\mathcal{A}}{\hbar\omega_{\boldsymbol{0}}}\,\mathrm{Im}\,\chi_0^R(\boldsymbol{0}, \omega_{\boldsymbol{0}}). \tag{4.37}$$

Equation (4.37) can be written as the sum of three contributions as follows [78]:

$$\delta\alpha_{\mathrm{G}} = \delta\alpha_{\mathrm{G},1} + \delta\alpha_{\mathrm{G},2} + \delta\alpha_{\mathrm{G},3} \tag{4.38}$$

$$\delta\alpha_{\mathrm{G},1} = \alpha_{\mathrm{G},0}\int_0^{2\pi}\frac{d\varphi}{2\pi}\,F(\hbar\omega_{\mathbf{0}})\frac{1-(\hat{\boldsymbol{h}}_{\mathrm{eff}}\cdot\hat{\boldsymbol{m}})^2}{2}, \tag{4.39}$$

$$\delta\alpha_{\mathrm{G},2} = \alpha_{\mathrm{G},0}\int_0^{2\pi}\frac{d\varphi}{2\pi}\,F(\hbar\omega_{\mathbf{0}}-2h_{\mathrm{eff}})\frac{(1+\hat{\boldsymbol{h}}_{\mathrm{eff}}\cdot\hat{\boldsymbol{m}})^2}{4}, \tag{4.40}$$

$$\delta\alpha_{\mathrm{G},3} = \alpha_{\mathrm{G},0}\int_0^{2\pi}\frac{d\varphi}{2\pi}\,F(\hbar\omega_{\mathbf{0}}+2h_{\mathrm{eff}})\frac{(1-\hat{\boldsymbol{h}}_{\mathrm{eff}}\cdot\hat{\boldsymbol{m}})^2}{4}, \tag{4.41}$$

$$F(x) = \frac{\Gamma/\pi\Delta_0}{(x/\Delta_0)^2+(\Gamma/\Delta_0)^2}. \tag{4.42}$$

Here, $\Delta_0 = k_{\mathrm{F}}\alpha$ is a constant with the dimension of energy, $\alpha_{\mathrm{G},0} = 2\pi S_0|\bar{T}|^2\mathcal{A}D(\epsilon_{\mathrm{F}})/\Delta_0$ is a dimensionless constant, and $F(x)$ is a Lorentzian function. The term $\delta\alpha_{\mathrm{G},1}$ peaks when $\hbar\omega_{\mathbf{0}} = 0$ and $\hat{\boldsymbol{h}}_{\mathrm{eff}} \perp \hat{\boldsymbol{m}}$, representing an elastic process of the magnon sensing the effective Zeeman field of the 2DEG conduction electrons as a transverse field. Additionally, $\delta\alpha_{\mathrm{G},2}$ ($\delta\alpha_{\mathrm{G},3}$) peaks when $\hbar\omega_{\mathbf{0}} = 2h_{\mathrm{eff}}$ ($\hbar\omega_{\mathbf{0}} = -2h_{\mathrm{eff}}$) and $\hat{\boldsymbol{h}}_{\mathrm{eff}} \parallel \hat{\boldsymbol{m}}$ ($\hat{\boldsymbol{h}}_{\mathrm{eff}} \parallel -\hat{\boldsymbol{m}}$), representing an inelastic process of magnons being absorbed (emitted) by conduction electrons in the 2DEG, causing the electrons to undergo spin-flip transitions between spin-split subbands.

4.3.2 Vertex corrections

In this section, we calculate the spin susceptibility of conduction electrons in a 2DEG following Ref. [48], considering the vertex corrections within the framework of the Born approximation [151] and the ladder approximation [148, 152]. This spin susceptibility is described by the Feynman diagram shown in Fig. 4.6(a), which corresponds to

$$\chi(\mathbf{0}, i\omega_n) = \frac{1}{4\beta\mathcal{A}}\sum_{\boldsymbol{k},i\omega_m}\mathrm{Tr}\Big[\hat{g}(\boldsymbol{k},i\omega_m)\hat{\Gamma}(\boldsymbol{k},i\omega_m,i\omega_n)\hat{g}(\boldsymbol{k},i\omega_m+i\omega_n)\hat{\sigma}^{x'-}\Big]. \tag{4.43}$$

Here, $\hat{\Gamma}(\boldsymbol{k},i\omega_m,i\omega_n)$ is the 2×2 matrix vertex function, which follows the Bethe-Salpeter equation corresponding to Fig. 4.6 (b) as given below:

$$\begin{aligned}&\Gamma_{\sigma'\sigma}(\boldsymbol{k},i\omega_m,i\omega_n)\\ &= (\hat{\sigma}^{x'+})_{\sigma'\sigma} + \frac{u^2 n_{\mathrm{imp}}}{\mathcal{A}}\sum_{\boldsymbol{q}}\sum_{\sigma_1\sigma_2} g_{\sigma'\sigma_2}(\boldsymbol{q},i\omega_m)\Gamma_{\sigma_2\sigma_1}(\boldsymbol{q},i\omega_m,i\omega_n)g_{\sigma_1\sigma}(\boldsymbol{q},i\omega_m+i\omega_n).\end{aligned} \tag{4.44}$$

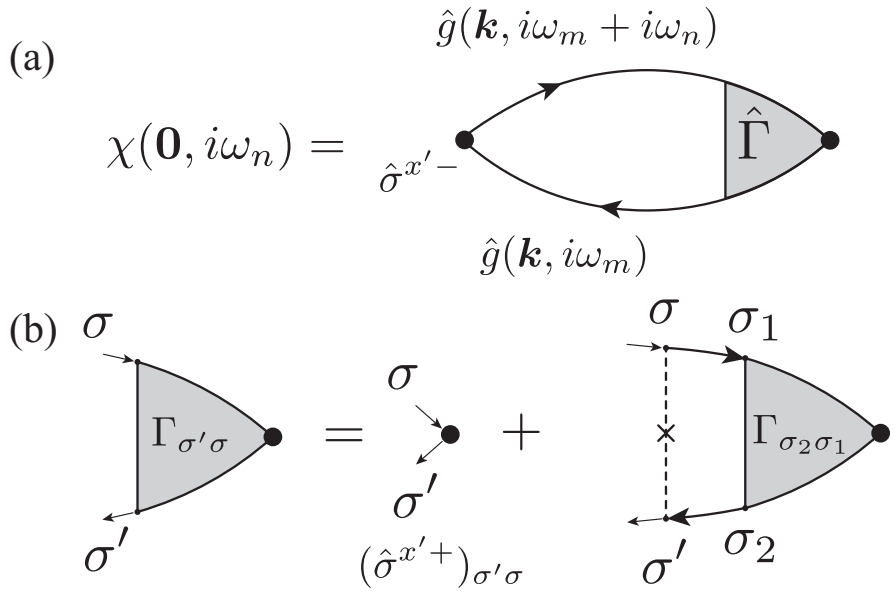

Figure 4.6: (a) Uniform spin susceptibility, considering the vertex corrections. (b) The Bethe-Salpeter equation for the ladder-type vertex function within the framework of the Born approximation. The dashed line represents impurity scattering. Adapted from Ref. [48].

Since the right-hand side is independent of the wavevector $\boldsymbol{k}$, the vertex function is henceforth written as $\hat{\Gamma}(i\omega_m, i\omega_n)$. We expand this vertex function using Pauli matrices as follows:

$$\hat{\Gamma}(i\omega_m, i\omega_n) \equiv E\hat{1} + X\hat{\sigma}^{x'} + Y\hat{\sigma}^{y'} + Z\hat{\sigma}^{z'}. \tag{4.45}$$

Equation (4.44) is solved below to determine E, X, Y, and Z self-consistently. The Green's function of the 2DEG conduction electrons in Eq. (4.44) is given by Eq. (4.9) as follows:

$$\hat{g}(\boldsymbol{q}, i\omega_m) = \frac{A\hat{1} + B\hat{\sigma}^{x'} + C\hat{\sigma}^{y'}}{D}, \tag{4.46}$$

$$A(i\omega_m) = i\hbar\omega_m - \xi_{\boldsymbol{q}} + \frac{i\Gamma}{2}\mathrm{sgn}(\omega_m), \tag{4.47}$$

$$B = -h_{\mathrm{eff}}\cos(\phi - \theta), \tag{4.48}$$

$$C = -h_{\mathrm{eff}}\sin(\phi - \theta), \tag{4.49}$$

$$D(i\omega_m) = \prod_{\gamma=\pm}[i\hbar\omega_m - E^{\gamma}_{\boldsymbol{q}} + \frac{i\Gamma}{2}\mathrm{sgn}(\omega_m)]. \tag{4.50}$$

Here, ϕ is the azimuthal angle of the effective Zeeman field, defined as

$$\boldsymbol{h}_{\mathrm{eff}}(\varphi) = (h_{\mathrm{eff}}\cos\phi, h_{\mathrm{eff}}\sin\phi, 0), \tag{4.51}$$

$$h_{\mathrm{eff}}(\varphi) \equiv |\boldsymbol{h}_{\mathrm{eff}}(\varphi)| \simeq k_{\mathrm{F}}\sqrt{\alpha^2 + \beta^2 + 2\alpha\beta\sin 2\varphi}. \tag{4.52}$$

Using Eqs. (4.45) and (4.46), we can write the second term of Eq. (4.44) as follows:

$$\frac{u^2 n_{\mathrm{imp}}}{\mathcal{A}} \sum_{\boldsymbol{q}} \hat{g}(\boldsymbol{q}, i\omega_m)\hat{\Gamma}(i\omega_m, i\omega_n)\hat{g}(\boldsymbol{q}, i\omega_m + i\omega_n) = E'\hat{1} + X'\hat{\sigma}^{x'} + Y'\hat{\sigma}^{y'} + Z'\hat{\sigma}^{z'}. \tag{4.53}$$

Here, the coefficients of the identity matrix and Pauli matrices in Eqs. (4.53) and (4.45) are related by the following expressions:

$$\begin{pmatrix} E' \\ X' \\ Y' \\ Z' \end{pmatrix} = \begin{pmatrix} \Lambda_0 + \Lambda_1 & 0 & 0 & 0 \\ 0 & \Lambda_0 + \Lambda_2 & \Lambda_3 & 0 \\ 0 & \Lambda_3 & \Lambda_0 - \Lambda_2 & 0 \\ 0 & 0 & 0 & \Lambda_0 - \Lambda_1 \end{pmatrix} \begin{pmatrix} E \\ X \\ Y \\ Z \end{pmatrix}, \tag{4.54}$$

where $\Lambda_j(i\omega_m, i\omega_n)$ $(j = 0, 1, 2, 3)$ can be expressed as follows:

$$\Lambda_0(i\omega_m, i\omega_n) = \frac{u^2 n_{\mathrm{imp}}}{\mathcal{A}} \sum_{\boldsymbol{q}} \frac{A(i\omega_m)A(i\omega_m + i\omega_n)}{D(i\omega_m)D(i\omega_m + i\omega_n)}, \tag{4.55}$$

$$\Lambda_1(i\omega_m, i\omega_n) = \frac{u^2 n_{\mathrm{imp}}}{\mathcal{A}} \sum_{\boldsymbol{q}} \frac{h_{\mathrm{eff}}^2}{D(i\omega_m)D(i\omega_m + i\omega_n)}, \tag{4.56}$$

$$\Lambda_2(i\omega_m, i\omega_n) = \frac{u^2 n_{\mathrm{imp}}}{\mathcal{A}} \sum_{\boldsymbol{q}} \frac{h_{\mathrm{eff}}^2 \cos 2(\phi - \theta)}{D(i\omega_m)D(i\omega_m + i\omega_n)}, \tag{4.57}$$

$$\Lambda_3(i\omega_m, i\omega_n) = \frac{u^2 n_{\mathrm{imp}}}{\mathcal{A}} \sum_{\boldsymbol{q}} \frac{h_{\mathrm{eff}}^2 \sin 2(\phi - \theta)}{D(i\omega_m)D(i\omega_m + i\omega_n)}. \tag{4.58}$$

Here, we used the following fact: by replacing the summation over the wavevectors with the following formula

$$\frac{1}{\mathcal{A}} \sum_{\boldsymbol{q}} (\cdots) \simeq D(\epsilon_{\mathrm{F}}) \int_{-\infty}^{\infty} d\xi \int_0^{2\pi} \frac{d\varphi}{2\pi} (\cdots), \tag{4.59}$$

where integrals are taken over the energy $\xi \equiv \xi_{\boldsymbol{q}}$ and the wavevector angle φ, the first-order terms of B and C vanish due to the integration over the wavevector angle. Using Eq. (4.59), we

can rewrite Eqs. (4.55)-(4.58) as follows:

$$\Lambda_0(i\omega_m, i\omega_n) = \frac{i\Gamma}{4}\int_0^{2\pi}\frac{d\varphi}{2\pi}\sum_{\gamma,\gamma'} I_{\gamma\gamma'}, \tag{4.60}$$

$$\Lambda_1(i\omega_m, i\omega_n) = \frac{i\Gamma}{4}\int_0^{2\pi}\frac{d\varphi}{2\pi}\sum_{\gamma,\gamma'} \gamma\gamma' I_{\gamma\gamma'}, \tag{4.61}$$

$$\Lambda_2(i\omega_m, i\omega_n) = \frac{i\Gamma}{4}\int_0^{2\pi}\frac{d\varphi}{2\pi}\cos 2(\varphi-\theta)\sum_{\gamma,\gamma'} \gamma\gamma' I_{\gamma\gamma'}, \tag{4.62}$$

$$\Lambda_3(i\omega_m, i\omega_n) = \frac{i\Gamma}{4}\int_0^{2\pi}\frac{d\varphi}{2\pi}\sin 2(\varphi-\theta)\sum_{\gamma,\gamma'} \gamma\gamma' I_{\gamma\gamma'}. \tag{4.63}$$

Here, $I_{\gamma\gamma'}$ is defined as follows:

$$I_{\gamma\gamma'} = \int_{-\infty}^{\infty}\frac{d\xi}{2\pi i}\frac{1}{i\hbar\omega_m - \xi - \gamma h_{\text{eff}} + i(\Gamma/2)\text{sgn}(\omega_m)} \times \frac{1}{i\hbar(\omega_m+\omega_n) - \xi - \gamma' h_{\text{eff}} + i(\Gamma/2)\text{sgn}(\omega_m+\omega_n)}. \tag{4.64}$$

In Eq. (4.64), $I_{\gamma\gamma'} = 0$ for $\omega_m > 0$ and $\omega_m + \omega_n > 0$, as indicated by the residue theorem, since both poles of the integral are located in the upper half-plane of the complex ξ-plane. Similarly, for $\omega_m < 0$ and $\omega_m + \omega_n < 0$, we find $I_{\gamma\gamma'} = 0$ because both poles are located in the lower half-plane of the complex ξ-plane. Assuming $\omega_n > 0$, we evaluate $I_{\gamma\gamma'}$ for $\omega_m < 0$ and $\omega_m + \omega_n > 0$ using the residue theorem as follows:

$$I_{\gamma\gamma'} = \frac{1}{i\hbar\omega_n + (\gamma-\gamma')h_{\text{eff}} + i\Gamma}. \tag{4.65}$$

Using these results, we obtain the following expression:

$$\Lambda_j(i\omega_m, i\omega_n) = \theta(-\omega_m)\theta(\omega_m+\omega_n)\tilde{\Lambda}_j(i\omega_n), \tag{4.66}$$

$$\tilde{\Lambda}_j(i\omega_n) = \frac{i\Gamma}{4}\int_0^{2\pi}\frac{d\varphi}{2\pi}\sum_{\gamma,\gamma'=\pm}\frac{f_j(\gamma,\gamma',\varphi)}{i\hbar\omega_n + (\gamma-\gamma')h_{\text{eff}}(\varphi) + i\Gamma}. \tag{4.67}$$

Here, $\theta(x)$ is the step function and $f_j(\gamma,\gamma',\varphi)$ $(j = 0, 1, 2, 3)$ is written as follows:

$$f_0(\gamma,\gamma',\varphi) = 1, \tag{4.68}$$

$$f_1(\gamma,\gamma',\varphi) = \gamma\gamma', \tag{4.69}$$

$$f_2(\gamma,\gamma',\varphi) = \gamma\gamma'\cos 2[\phi(\varphi)-\theta], \tag{4.70}$$

$$f_3(\gamma,\gamma',\varphi) = \gamma\gamma'\sin 2[\phi(\varphi)-\theta]. \tag{4.71}$$

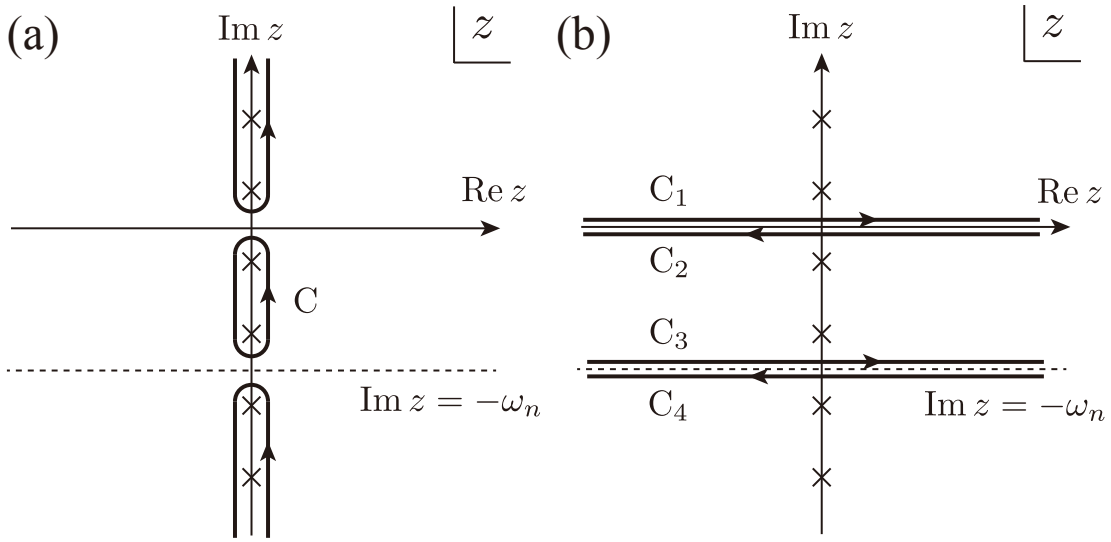

Figure 4.7: Schematic of the complex integration contour: (a) the original contour, and (b) the modified contour. Adapted from Ref. [48].

Upon substituting Eqs. (4.45) and (4.53) into Eq. (4.44), the resulting expression is as follows:

$$E\hat{1} + X\hat{\sigma}^{x'} + Y\hat{\sigma}^{y'} + Z\hat{\sigma}^{z'} = \hat{\sigma}^{x'+} + E'\hat{1} + X'\hat{\sigma}^{x'} + Y'\hat{\sigma}^{y'} + Z'\hat{\sigma}^{z'}. \tag{4.72}$$

Substituting Eq. (4.54) into E', X', Y', Z' in the equation above, we obtain the following solutions for E, X, Y, Z

$$E = 0, \tag{4.73}$$

$$X = \frac{\Lambda_3}{(1-\Lambda_0)^2 - \Lambda_2^2 - \Lambda_3^2}, \tag{4.74}$$

$$Y = \frac{1-\Lambda_0-\Lambda_2}{(1-\Lambda_0)^2 - \Lambda_2^2 - \Lambda_3^2}, \tag{4.75}$$

$$Z = \frac{i}{1-\Lambda_0+\Lambda_1}. \tag{4.76}$$

In this manner, the vertex function $\hat{\Gamma}(i\omega_m, i\omega_n)$ in Eq. (4.45) is determined self-consistently.

Substituting the vertex function in Eq. (4.45) along with the Green's function from Eq. (4.46) into Eq. (4.43) yields the following expression:

$$\chi(\mathbf{0}, i\omega_n) = \frac{1}{4\beta\mathcal{A}} \sum_{\boldsymbol{k}, i\omega_m} \frac{2}{DD'} \Big[2BCX + (AA' - B^2 + C^2)Y - i(AA' - B^2 - C^2)Z \Big]. \tag{4.77}$$

Then, by introducing $(X_1, X_2, X_3) = (X, Y, Z)$ and

$$\mathcal{I}_{\gamma\gamma',j} \equiv \frac{1}{\beta}\sum_{i\omega_m} \frac{X_j}{i\hbar\omega_m - E_{\boldsymbol{k}}^{\gamma} + i\Gamma/2\,\mathrm{sgn}(\omega_m)} \cdot \frac{1}{i\hbar\omega_m + i\hbar\omega_n - E_{\boldsymbol{k}}^{\gamma'} + i\Gamma/2\,\mathrm{sgn}(\omega_m+\omega_n)}, \quad (4.78)$$

we can rewrite Eq. (4.77) as follows:

$$\chi(\mathbf{0}, i\omega_n) = \frac{1}{8\mathcal{A}}\sum_{\boldsymbol{k}}\sum_{\gamma,\gamma'}\left[\gamma\gamma'\sin 2(\phi-\theta)\,\mathcal{I}_{\gamma\gamma',1} + \left\{1-\gamma\gamma'\cos 2(\phi-\theta)\right\}\mathcal{I}_{\gamma\gamma',2} - i(1-\gamma\gamma')\mathcal{I}_{\gamma\gamma',3}\right]. \quad (4.79)$$

According to the method of residue integration, $\mathcal{I}_{\gamma\gamma',j}$ for $\omega_n > 0$ can be evaluated by performing a complex integration along the contour C shown in Fig. 4.7 (a). This contour can be decomposed into the four contours C_l ($l = 1, 2, 3, 4$) depicted in Fig. 4.7 (b), allowing $\mathcal{I}_{\gamma\gamma',j}$ to be expressed as follows:

$$\mathcal{I}_{\gamma\gamma',j} = \sum_{l=1}^{4}\mathcal{I}_{\gamma\gamma',j}^{\mathrm{C}_l}, \quad (4.80)$$

$$\mathcal{I}_{\gamma\gamma',j}^{\mathrm{C}_l} = -\int_{\mathrm{C}_l}\frac{dz}{2\pi i}\frac{f(z)X_j(z,i\omega_n)}{z - E_{\boldsymbol{k}}^{\gamma} + i\Gamma/2\,\mathrm{sgn}(\mathrm{Im}\,z)} \cdot \frac{1}{z + i\hbar\omega_n - E_{\boldsymbol{k}}^{\gamma'} + i\Gamma/2\,\mathrm{sgn}(\mathrm{Im}\,z+\omega_n)}, \quad (4.81)$$

Here, $f(z) = 1/(e^{\beta z}+1)$ is the Fermi distribution function. First, for contributions from the contours C_2 and C_3, in the region $0 < \mathrm{Im}\,z < \omega_n$, $X_j(z, i\omega_n)$ is independent of z. Defining this as $\tilde{X}_j(i\omega_n)$, we can calculate the contributions as follows:

$$\mathcal{I}_{\gamma\gamma',j}^{\mathrm{C}_2} + \mathcal{I}_{\gamma\gamma',j}^{C_3} = -\tilde{X}_j(i\omega_n)\int\frac{dE}{2\pi i}f(E)\left[-\frac{1}{E - E_{\boldsymbol{k}}^{\gamma} - i\Gamma/2}\frac{1}{E + i\hbar\omega_n - E_{\boldsymbol{k}}^{\gamma'} + i\Gamma/2}\right.$$
$$\left. + \frac{1}{E - i\hbar\omega_n - E_{\boldsymbol{k}}^{\gamma} - i\Gamma/2}\frac{1}{E - E_{\boldsymbol{k}}^{\gamma'} + i\Gamma/2}\right]. \quad (4.82)$$

Here, from Eqs. (4.74)-(4.76), we can express $\tilde{X}_j(i\omega_n)$ as follows:

$$\tilde{X}_1(i\omega_n) = \frac{\tilde{\Lambda}_3(i\omega_n)}{(1-\tilde{\Lambda}_0(i\omega_n))^2 - \tilde{\Lambda}_2(i\omega_n)^2 - \tilde{\Lambda}_3(i\omega_n)^2}, \quad (4.83)$$

$$\tilde{X}_2(i\omega_n) = \frac{1-\tilde{\Lambda}_0(i\omega_n) - \tilde{\Lambda}_2(i\omega_n)}{(1-\tilde{\Lambda}_0(i\omega_n))^2 - \tilde{\Lambda}_2(i\omega_n)^2 - \tilde{\Lambda}_3(i\omega_n)^2}, \quad (4.84)$$

$$\tilde{X}_3(i\omega_n) = \frac{i}{1-\tilde{\Lambda}_0(i\omega_n) + \tilde{\Lambda}_1(i\omega_n)}. \quad (4.85)$$

Then, by changing the integration variable in the first term (second term) of Eq. (4.82) to

$E' = E - E_{\boldsymbol{k}}^{\gamma}$ ($E' = E_{\boldsymbol{k}}^{\gamma'} - E$), we obtain the following expression:

$$\mathcal{I}_{\gamma\gamma',j}^{\mathrm{C}_2} + \mathcal{I}_{\gamma\gamma',j}^{\mathrm{C}_3} = -\tilde{X}_j(i\omega_n) \int \frac{dE'}{2\pi i} \frac{1}{E' - i\Gamma/2} \left[\frac{f(-E' + E_{\boldsymbol{k}}^{\gamma'}) - f(E' + E_{\boldsymbol{k}}^{\gamma})}{E' + i\hbar\omega_n + E_{\boldsymbol{k}}^{\gamma} - E_{\boldsymbol{k}}^{\gamma'} + i\Gamma/2} \right]. \tag{4.86}$$

By converting the summation over $\boldsymbol{k}$ in Eq. (4.79) to integrals over ξ and φ using Eq. (4.59), we can evaluate the ξ integral as follows:

$$-\int_{-\infty}^{\infty} d\xi \, [f(E' + E_{\boldsymbol{k}}^{\gamma}) - f(-E' + E_{\boldsymbol{k}}^{\gamma'})] = 2E' + E_{\boldsymbol{k}}^{\gamma} - E_{\boldsymbol{k}}^{\gamma'}. \tag{4.87}$$

Then, by performing the E' integral, we obtain the following expression:

$$\int_{-\infty}^{\infty} d\xi \, (\mathcal{I}_{\gamma\gamma',j}^{\mathrm{C}_2} + \mathcal{I}_{\gamma\gamma',j}^{\mathrm{C}_3}) = \frac{i\hbar\omega_n \tilde{X}_j(i\omega_n)}{E_{\boldsymbol{k}}^{\gamma} - E_{\boldsymbol{k}}^{\gamma'} + i\hbar\omega_n + i\Gamma}. \tag{4.88}$$

Next, we calculate the contributions from C_1 and C_4. In these contours, $X_j(z, i\omega_n)$ is independent of z, which is denoted as $\tilde{X}'_j(i\omega_n)$ ($j = 1, 2, 3$). From Eq. (4.66), since $\Lambda_j(z, i\omega_n)$ ($j = 0, 1, 2, 3$) is zero for $\mathrm{Im}\, z < 0$ or $\omega_n < \mathrm{Im}\, z$, $\tilde{X}'_j(i\omega_n)$ is given by the following expression:

$$\tilde{X}'_1(i\omega_n) = 0, \quad \tilde{X}'_2(i\omega_n) = 1, \quad \tilde{X}'_3(i\omega_n) = i. \tag{4.89}$$

Then, by performing similar calculations as for C_2 and C_3, we find that the contributions from C_1 and C_4 are given by the following expression:

$$\int_{-\infty}^{\infty} d\xi \, (\mathcal{I}_{\gamma\gamma',j}^{\mathrm{C}_1} + \mathcal{I}_{\gamma\gamma',j}^{\mathrm{C}_4}) = -\tilde{X}'_j(i\omega_n). \tag{4.90}$$

Substituting Eqs. (4.88) and (4.90) into Eq. (4.79) yields the following expression:

$$\begin{aligned} \chi(\boldsymbol{0}, i\omega_n) = \frac{D(\epsilon_{\mathrm{F}})}{8} \sum_{\gamma,\gamma'} \int_0^{2\pi} \frac{d\varphi}{2\pi} \Big[& \gamma\gamma' \sin 2(\phi - \theta)\, \tilde{x}_1(i\omega_n) \\ & + [1 - \gamma\gamma' \cos 2(\phi - \theta)][-1 + \tilde{x}_2(i\omega_n)] - i(1 - \gamma\gamma')[-i + \tilde{x}_3(i\omega_n)] \Big]. \end{aligned} \tag{4.91}$$

Here, $\tilde{x}_j(i\omega_n)$ is defined as follows:

$$\tilde{x}_j(i\omega_n) = \frac{i\hbar\omega_n \tilde{X}_j(i\omega_n)}{E_{\boldsymbol{k}}^{\gamma} - E_{\boldsymbol{k}}^{\gamma'} + i\hbar\omega_n + i\Gamma}. \tag{4.92}$$

By substituting the expression for $\tilde{X}_j(i\omega_n)$ into Eq. (4.91) and performing the analytic continuation $i\omega_n \to \omega + i\delta$, we obtain the retarded component of the uniform spin susceptibility for the

conduction electrons in the 2DEG[1]:

$$\chi^R(\mathbf{0},\omega) = \frac{D(\epsilon_\mathrm{F})\hbar\omega}{2i\Gamma}\left[\frac{\tilde{\Lambda}_0^R(1-\tilde{\Lambda}_0^R)-\tilde{\Lambda}_2^R(1-\tilde{\Lambda}_2^R)+(\tilde{\Lambda}_3^R)^2}{(1-\tilde{\Lambda}_0^R)^2-(\tilde{\Lambda}_2^R)^2-(\tilde{\Lambda}_3^R)^2}+\frac{\tilde{\Lambda}_0^R-\tilde{\Lambda}_1^R}{1-\tilde{\Lambda}_0^R+\tilde{\Lambda}_1^R}\right]-D(\epsilon_\mathrm{F}), \quad (4.93)$$

where, $\tilde{\Lambda}_j^R$ $(j=0,1,2,3)$ is the analytic continuation of $\tilde{\Lambda}_j(i\omega_n)$ in Eq. (4.67):

$$\tilde{\Lambda}_j^R = \tilde{\Lambda}_j^R(\omega) = \tilde{\Lambda}_j(i\omega_n \to \omega + i\delta) = \frac{i\Gamma}{4\Delta_0}\int_0^{2\pi}\frac{d\varphi}{2\pi}\sum_{\gamma\gamma'}\frac{f_j(\gamma,\gamma',\varphi)}{\hbar\omega/\Delta_0+(\gamma-\gamma')h_\mathrm{eff}/\Delta_0+i\Gamma/\Delta_0}. \quad (4.94)$$

Here, $\Delta_0 = k_\mathrm{F}\alpha$ is a normalization constant with the dimension of energy. By substituting Eq. (4.93) into Eqs. (4.28) and (4.29), we obtain the following expressions for the shift in the FMR frequency and the modulation of the Gilbert damping, taking into account the vertex correction:

$$\frac{\delta\omega_\mathbf{0}}{\omega_\mathbf{0}} = \alpha_{\mathrm{G},0}\,\mathrm{Re}\,F(\omega_\mathbf{0}), \quad (4.95)$$

$$\delta\alpha_\mathrm{G} = -\alpha_{\mathrm{G},0}\,\mathrm{Im}\,F(\omega_\mathbf{0}), \quad (4.96)$$

$$F(\omega) = \frac{\Delta_0}{2\pi i\Gamma}\left[\frac{\tilde{\Lambda}_0^R(1-\tilde{\Lambda}_0^R)-\tilde{\Lambda}_2^R(1-\tilde{\Lambda}_2^R)+(\tilde{\Lambda}_3^R)^2}{(1-\tilde{\Lambda}_0^R)^2-(\tilde{\Lambda}_2^R)^2-(\tilde{\Lambda}_3^R)^2}+\frac{\tilde{\Lambda}_0^R-\tilde{\Lambda}_1^R}{1-\tilde{\Lambda}_0^R+\tilde{\Lambda}_1^R}\right]-\frac{\Delta_0}{\pi\hbar\omega}. \quad (4.97)$$

Here, $\alpha_{\mathrm{G},0} = 2\pi S_0|\bar{T}|^2\mathcal{A}D(\epsilon_\mathrm{F})/\Delta_0$ is a dimensionless constant representing the strength of the interfacial interaction. Equations (4.95), (4.96), and (4.97) are the main results of this chapter.

Retaining only the first-order term of $\tilde{\Lambda}_j^R$ in Eq. (4.93), we obtain the following expression:

$$\begin{aligned}\chi_0^R(\mathbf{0},\omega) &\simeq \frac{\hbar\omega D(\epsilon_\mathrm{F})}{2i\Gamma}\left[2\tilde{\Lambda}_0^R-\tilde{\Lambda}_1^R-\tilde{\Lambda}_2^R\right]-D(\epsilon_\mathrm{F})\\ &= \hbar\omega D(\epsilon_\mathrm{F})\int\frac{d\varphi}{2\pi}\left[\frac{1}{\hbar\omega+i\Gamma}\frac{1-\cos^2(\phi(\varphi)-\theta)}{2}+\frac{1}{\hbar\omega-2h_\mathrm{eff}(\varphi)+i\Gamma}\frac{1+\cos^2(\phi(\varphi)-\theta)}{4}\right.\\ &\quad\left.+\frac{1}{\hbar\omega+2h_\mathrm{eff}(\varphi)+i\Gamma}\frac{1+\cos^2(\phi(\varphi)-\theta)}{4}\right]-D(\epsilon_\mathrm{F}). \quad (4.98)\end{aligned}$$

This represents the spin susceptibility without considering the vertex correction. By substituting this into Eqs. (4.28) and (4.29), we obtain the expressions for the shift in the FMR frequency

[1]Using the Sommerfeld expansion, it is found that when $k_\mathrm{B}T$ is sufficiently small compared to the Fermi energy ϵ_F, the contribution of the temperature-dependent term to the uniform spin susceptibility becomes negligible. Consequently, the uniform spin susceptibility can be expressed as temperature-independent, as shown in Eq. (4.93).

and the modulation of the Gilbert damping without the vertex correction:

$$\frac{\delta\omega_{\mathbf{0}}^{\mathrm{nv}}}{\omega_{\mathbf{0}}} = \alpha_{\mathrm{G},0}\,\mathrm{Re}\,F_{\mathrm{nv}}(\omega_{\mathbf{0}}), \tag{4.99}$$

$$\delta\alpha_{\mathrm{G}}^{\mathrm{nv}} = -\alpha_{\mathrm{G},0}\,\mathrm{Im}\,F_{\mathrm{nv}}(\omega_{\mathbf{0}}), \tag{4.100}$$

$$F_{\mathrm{nv}}(\omega) = \frac{\Delta_0}{2\pi i\Gamma}\left[2\tilde{\Lambda}_0^R - \tilde{\Lambda}_1^R - \tilde{\Lambda}_2^R\right] - \frac{\Delta_0}{\pi\hbar\omega}. \tag{4.101}$$

These reproduce the results of Eqs. (4.36) and (4.37).

4.4 Modulation of Gilbert damping

In this section, we present the results of the modulation of the Gilbert damping from Eq. (4.96). Section 4.4.1 shows the outcomes of $\delta\alpha_{\mathrm{G}}$ from Eq. (4.96) for the cases of $\beta/\alpha = 0, 1, 3$, and compares them with the results for the modulation of the Gilbert damping without the vertex correction, $\delta\alpha_{\mathrm{G}}^{\mathrm{nv}}$, from Eq. (4.100). In Sec. 4.4.2, it is demonstrated that $\delta\alpha_{\mathrm{G}}$ exhibits a sharp increase in the low-frequency region near $\beta/\alpha = 1$.

4.4.1 Effect of vertex corrections

First, we present the situation where only the Rashba SOC is considered, i.e., $\beta/\alpha = 0$. Note that the modulation of the Gilbert damping yields the same result in the case in which only the Dresselhaus SOC is present, i.e., $\alpha/\beta = 0$. The effective Zeeman field $\boldsymbol{h}_{\mathrm{eff}}$ generated by the Rashba SOC at the Fermi surface is shown in Fig. 4.8(a). Figures 4.8(b) and 4.8(c) illustrate the modulation of the Gilbert damping as a function of the FMR frequency $\omega_{\mathbf{0}} = \gamma_{\mathrm{g}} h_{\mathrm{dc}}$ in the cases without and with the vertex correction, respectively. The spin-splitting width of the energy bands near the Fermi surface is constant at $2h_{\mathrm{eff}} = 2k_{\mathrm{F}}\alpha$, regardless of the wavevector direction. As a result, we find that the modulation of the Gilbert damping does not depend on the orientation θ of the localized spin $\boldsymbol{S}$ in the FI. The four curves in Figs. 4.8(b) and 4.8(c) correspond to impurity scattering strengths of $\Gamma/\Delta_0 = 0.1, 0.2, 0.5$, and 1. The electron mobility in GaAs/AlGaAs at low temperatures ranges from the order of 10^5 cm^2/Vs to 10^7 cm^2/Vs [143, 153]. By using these values, the effective mass $m^* = 0.067m$ [147], and $\Delta_0 \equiv k_{\mathrm{F}}\alpha \simeq 0.07$ meV, Γ/Δ_0 is estimated to be on the order of 10^{-2} to 1. Both Figs. 4.8(b) and 4.8(c) show peaks at $\omega_{\mathbf{0}} = 0$ and $\omega_{\mathbf{0}} = 2\Delta_0$ $(= 2k_{\mathrm{F}}\alpha)$, with the peak widths decreasing as Γ decreases. As described in Sec. 4.3.1, the low-frequency peak corresponds to an elastic process in which magnons relax by perceiving the effective Zeeman field of the 2DEG as a transverse field. In contrast, the high-frequency peak corresponds to an inelastic process in which 2DEG electrons are excited to different subbands through the absorption or emission of magnons [78]. In the case of $\beta/\alpha = 0$, the qualitative behavior of the modulation of the Gilbert damping remains unchanged whether or not the vertex correction is considered. However, quantitatively, the peak widths at $\omega_{\mathbf{0}} = 0$ and $\omega_{\mathbf{0}} = 2\Delta_0$

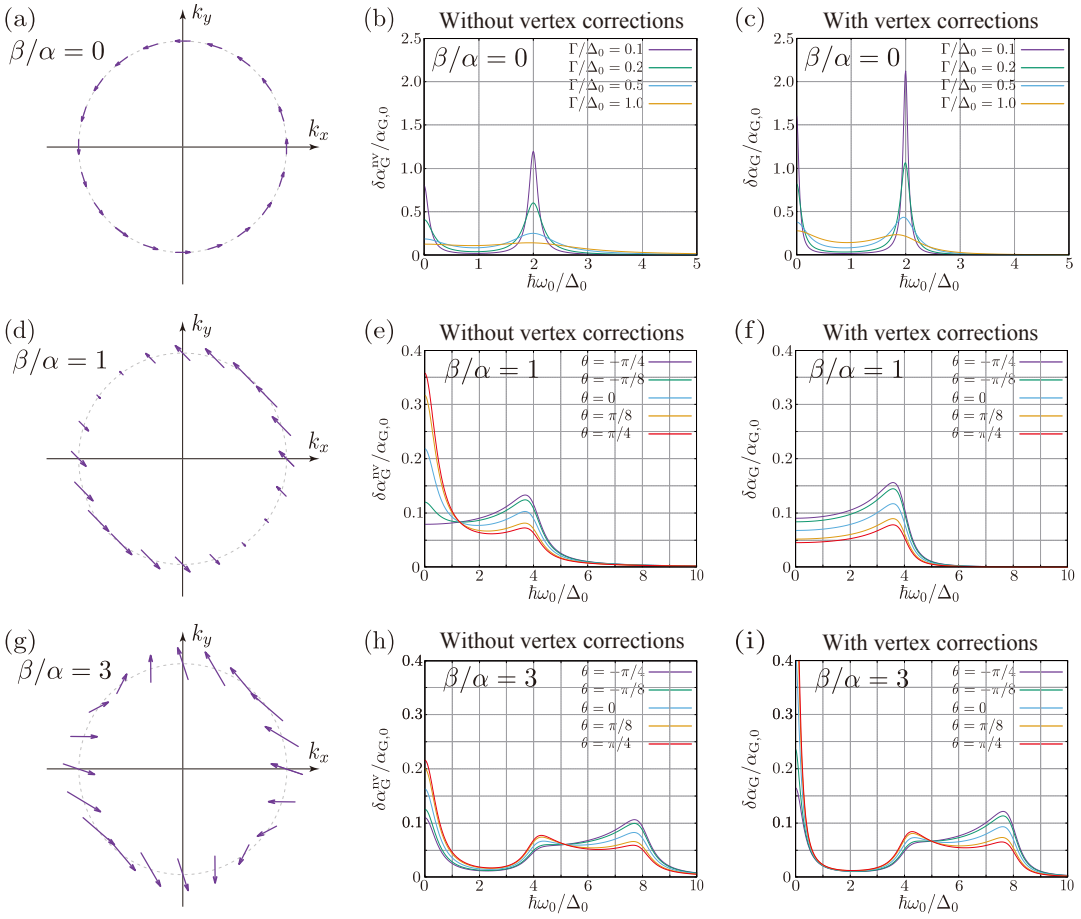

Figure 4.8: (Left panels) Effective Zeeman field $\boldsymbol{h}_{\rm eff}$ at the Fermi surface. (Middle panels) Modulation of the Gilbert damping $\delta\alpha_{\rm G}^{\rm nv}$ without the vertex correction. (Right panels) Modulation of the Gilbert damping $\delta\alpha_{\rm G}$ with the vertex correction. In the middle and right panels, the modulation of the Gilbert damping is plotted as a function of the FMR frequency $\omega_{\boldsymbol{0}} = \gamma_{\rm g} h_{\rm dc}$ for various orientations θ of the localized spin $\boldsymbol{S}$ in the FI. Here, $\Gamma/\Delta_0 = 0.5$ is used. The ratio of the Rashba SOC (α) to the Dresselhaus SOC (β) is set as follows: (a), (b), (c): $\beta/\alpha = 0$; (d), (e), (f): $\beta/\alpha = 1$; (g), (h), (i): $\beta/\alpha = 3$. Note that (b), (e), and (h) yield essentially the same results as in Ref. [78]. Adapted from Ref. [48].

become narrower when the vertex correction is taken into account. For an analytical expression of this peak width, refer to Appendix B.

Next, we examine the case of $\beta/\alpha = 1$. In this situation, the effective Zeeman field generated by the Rashba and Dresselhaus SOCs points in the $(-1, 1)$ or $(1, -1)$ directions, as illustrated in Fig. 4.8(d). The magnitude of this effective Zeeman field, $h_{\rm eff}(\varphi) \equiv |\boldsymbol{h}_{\rm eff}(\varphi)|$, changes with the wavevector direction φ, as described by the following equation:

$$h_{\rm eff}(\varphi) = 2\Delta_0 |\sin(\varphi + \pi/4)|. \tag{4.102}$$

Thus, the spin-splitting width of the 2DEG conduction electron energy band, written as $2h_{\rm eff}(\varphi)$, also depends on the wavevector direction, varying within the range $0 \le 2h_{\rm eff} \le 4\Delta_0$. Fig-

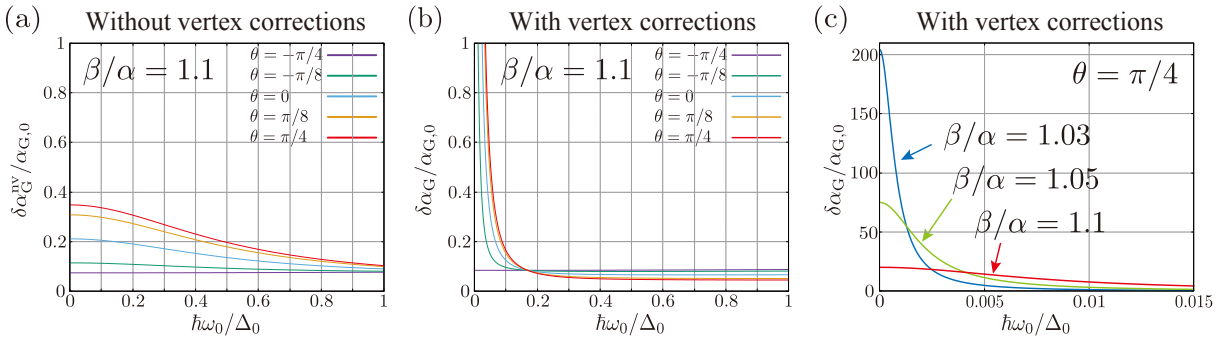

Figure 4.9: The modulation of the Gilbert damping for $\beta/\alpha = 1.1$ is shown as a function of the FMR frequency $\omega_{\mathbf{0}}$ for (a) without the vertex correction and (b) with the vertex correction. The five curves correspond to different orientations of the localized spin $\boldsymbol{S}$ in the FI: $\theta = -\pi/4, -\pi/8, 0, \pi/8$, and $\pi/4$. In (c), the modulation of the Gilbert damping with the vertex correction is plotted as a function of $\omega_{\mathbf{0}}$ for $\beta/\alpha = 1.03$, 1.05, and 1.1, with θ fixed at $\pi/4$. In all plots, $\Gamma/\Delta_0 = 0.5$ is used. Adapted from Ref. [48].

ures 4.8(e) and 4.8(f) plot the modulation of the Gilbert damping for $\Gamma/\Delta_0 = 0.5$, with and without the vertex correction, respectively. First, in the case of $\beta/\alpha = 1$, since the spin-splitting width is $0 \leq 2h_{\text{eff}} \leq 4\Delta_0$, the modulation of the Gilbert damping in both Figs. 4.8 (e) and 4.8(f) takes large values when the FMR energy $\hbar\omega_{\mathbf{0}}$ on the horizontal axis lies within the range $0 \leq \hbar\omega_{\mathbf{0}} \leq 4\Delta_0$, where it matches the spin-splitting width. The five curves in these figures represent plots for the orientation of the localized spin in the FI for $\theta = -\pi/4, -\pi/8, 0, \pi/8$, and $\pi/4$. The most remarkable difference between Figs. 4.8(e) and 4.8(f) is that while $\delta\alpha_{\text{G}}^{\text{nv}}(\omega_{\mathbf{0}})$, in which we do not take the vertex corrections into account, exhibits a peak around $\omega_{\mathbf{0}} = 0$, $\delta\alpha_{\text{G}}(\omega_{\mathbf{0}})$, which includes the vertex corrections, shows no such peak. In the next section, it will be shown that $\delta\alpha_{\text{G}}(\omega_{\mathbf{0}})$ has a delta function-like singularity at $\omega_{\mathbf{0}} = 0$, reflecting that for $\beta/\alpha = 1$, the effective Zeeman field $\boldsymbol{h}_{\text{eff}}$ aligns in a single direction, preserving the total spin of the conduction electrons in the 2DEG along that direction. For an analytical expression of the modulation of the Gilbert damping at $\beta/\alpha = 1$, refer to Appendix B.

Finally, we consider the case of $\beta/\alpha = 3$. The effective Zeeman field $\boldsymbol{h}_{\text{eff}}$ is depicted in Fig. 4.8(g), where the magnitude of the field, h_{eff}, varies depending on the direction of the wavevector. Figures 4.8(h) and 4.8(i) present the modulation of the Gilbert damping for $\Gamma/\Delta_0 = 0.5$, without and with the vertex corrections, respectively. In both cases, large values appear in the low-frequency region around $\omega_{\mathbf{0}} = 0$, as well as in the high-frequency range $4\Delta_0 \leq \hbar\omega_{\mathbf{0}} \leq 8\Delta_0$, which corresponds to the spin-splitting width of the 2DEG energy band, $2h_{\text{eff}}$. In the low-frequency region, elastic processes dominate, and hence magnons relax by sensing the effective Zeeman field as a transverse magnetic field. In contrast, in the high-frequency region, inelastic processes dominate, and hence 2DEG conduction electrons absorb magnons and transition from the lower to the upper spin-split subband via spin-flip transitions. A comparison of Figs. 4.8(h) and 4.8(i) reveals that, similar to the case of $\beta/\alpha = 0$, the vertex

corrections induce only a moderate change in the modulation of the Gilbert damping. While the inclusion of the vertex corrections sharpens the peak around $\omega_{\mathbf{0}} = 0$, the peak does not disappear, unlike the behavior observed for $\beta/\alpha = 1$.

4.4.2 Sharp Increase in Gilbert Damping

This section examines the sharp increase in the Gilbert damping that occurs near $\beta/\alpha = 1$. For $\beta/\alpha = 1$, as shown in Fig. 4.8(d), the effective Zeeman field in the 2DEG is aligned in a single direction. Defining the spin operator along this direction

$$s_{\rm tot}^{3\pi/4} \equiv \frac{1}{2}\sum_{\boldsymbol{k}} \left(c_{\boldsymbol{k}+}^{\dagger} c_{\boldsymbol{k}+} - c_{\boldsymbol{k}-}^{\dagger} c_{\boldsymbol{k}-} \right), \tag{4.103}$$

$$\begin{pmatrix} c_{\boldsymbol{k}+} \\ c_{\boldsymbol{k}-} \end{pmatrix} = \begin{pmatrix} \frac{1}{\sqrt{2}} & \frac{e^{-i3\pi/4}}{\sqrt{2}} \\ \frac{-e^{i3\pi/4}}{\sqrt{2}} & \frac{1}{\sqrt{2}} \end{pmatrix} \begin{pmatrix} c_{\boldsymbol{k}\uparrow} \\ c_{\boldsymbol{k}\downarrow} \end{pmatrix}, \tag{4.104}$$

we find that the relation $[H_{\rm kin} + H_{\rm imp}, s_{\rm tot}^{3\pi/4}] = 0$ holds. Therefore, when $\beta/\alpha = 1$, the total spin of the 2DEG conduction electrons in the $3\pi/4$ direction is conserved, indicating that no spin relaxation occurs. In the case $\beta/\alpha \simeq 1$, this spin conservation law is slightly broken, leading to slow spin relaxation. To confirm this, Figs. 4.9(a) and 4.9(b) plot the modulation of the Gilbert damping for $\beta/\alpha = 1.1$, both with and without considering the vertex corrections. The five curves represent the results for various azimuthal angles θ of the localized spin $\boldsymbol{S}$ in the FI, with the energy broadening set to $\Gamma/\Delta_0 = 0.5$. The comparison between Figs. 4.9(a) and 4.9(b) demonstrates that the modulation of the Gilbert damping exhibits a sharp increase in the low-frequency region only when the vertex corrections are considered. Figure 4.9 (c) shows the modulation of the Gilbert damping $\delta\alpha_{\rm G}$ with the vertex corrections in three cases: $\beta/\alpha = 1.03$, 1.05, and 1.1, with $\Gamma/\Delta_0 = 0.5$ and $\theta = \pi/4$. From this figure, it is evident that as β/α approaches unity, the value of $\delta\alpha_{\rm G}$ at $\omega_{\mathbf{0}} = 0$ increases significantly. For $\beta/\alpha \simeq 1$, $\delta\alpha_{\rm G}$ in the low-frequency region can be approximated by the following expression (for a detailed derivation, refer to Appendix B):

$$\frac{\delta\alpha_{\rm G}}{\alpha_{\rm G,0}} \simeq \frac{\Delta_0}{2\pi} \frac{\Gamma_s}{(\hbar\omega_{\mathbf{0}})^2 + \Gamma_s^2} \sin^2\left(\theta + \frac{\pi}{4}\right), \tag{4.105}$$

$$\Gamma_s \equiv \frac{2}{\Gamma}\int_0^{2\pi} \frac{d\varphi}{2\pi} \frac{(h_x + h_y)^2}{1 + (2h_{\rm eff}/\Gamma)^2}. \tag{4.106}$$

Here, Γ_s represents the linewidth of the peak at $\omega_{\mathbf{0}} = 0$ in Figs. 4.9(b) and 4.9(c), and it is proportional to δ^2 for $\beta/\alpha = 1 + \delta$ ($\delta \ll 1$). This implies that Γ_s corresponds to the spin relaxation rate. Since spin conservation holds for $\beta/\alpha = 1$, no spin relaxation occurs, leading to divergent behavior of $\delta\alpha_{\rm G}(\omega_{\mathbf{0}})$ at $\omega_{\mathbf{0}} = 0$ as a δ-function-like singularity with zero linewidth. For $\beta/\alpha \simeq 1$, this conservation law is slightly broken, resulting in very slow spin relaxation.

Consequently, sharp peaks with narrow line widths appear, as observed in Figs. 4.9(b) and 4.9(c). It should be noted that the divergence with zero linewidth at $\omega_{\mathbf{0}} = 0$ for $\beta/\alpha = 1$ is not visible in Fig. 4.8(f). In contrast to Figs. 4.9(b) and 4.9(c), the absence of a sharp peak in the low-frequency region in Fig. 4.9(a) can be attributed to the lack of the vertex corrections, which prevents the incorporation of spin conservation.

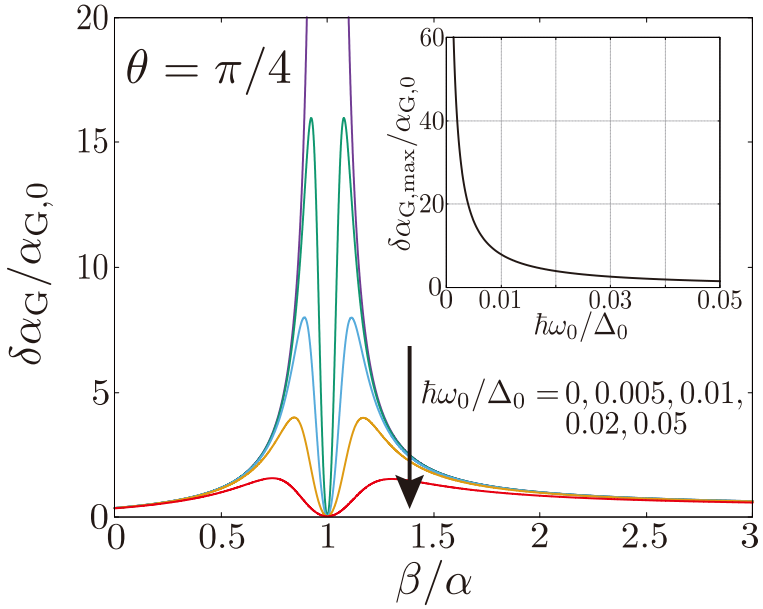

Figure 4.10: The modulation of the Gilbert damping $\delta\alpha_G$ with the vertex corrections is plotted as a function of β/α for $\theta = \pi/4$. The five curves correspond to $\hbar\omega_{\mathbf{0}}/\Delta_0 = 0,\ 0.005,\ 0.01,\ 0.02,$ and 0.05. The inset shows the maximum value of $\delta\alpha_G$, denoted as $\delta\alpha_{G,max}$, as a function of $\omega_{\mathbf{0}}$ when varying β/α. All plots assume $\Gamma/\Delta_0 = 0.5$. Adapted from Ref. [48].

In Fig. 4.10, $\delta\alpha_G$ is shown as a function of β/α with $\Gamma/\Delta_0 = 0.5$ and $\theta = \pi/4$. The five curves in this figure correspond to $\hbar\omega_{\mathbf{0}}/\Delta_0 = 0, 0.005, 0.01, 0.02,$ and 0.05. From this figure, it is clear that at low frequencies of $\omega_{\mathbf{0}}$, $\delta\alpha_G$ increases sharply around $\beta/\alpha \simeq 1$. The inset of Fig. 4.10 plots the maximum value of $\delta\alpha_G/\alpha_{G,0}$ as a function of $\hbar\omega_{\mathbf{0}}/\Delta_0$ when varying β/α. In other words, the vertical axis of the inset represents the peak maximum for each $\hbar\omega_{\mathbf{0}}/\Delta_0$ in the main panel. From this inset, it can be observed that the maximum value of $\delta\alpha_G$ increases as $\omega_{\mathbf{0}}$ approaches zero.

4.5 Shift of the FMR Frequency

In this section, the results of the FMR frequency shift with the vertex corrections are presented. Figures 4.11(a), 4.11(b), and 4.11(c) represent the modulation of the Gilbert damping, $\delta\alpha_G$, with the vertex corrections, corresponding to Figs. 4.8(c), 4.8(f), and 4.8(i), respectively. Figures 4.11(d), 4.11(e), and 4.11(f) show the shift in the FMR frequency, $\delta\omega_{\mathbf{0}}$, also with the vertex corrections. The common features of $\delta\alpha_G$ and $\delta\omega_{\mathbf{0}}$ are as follows: (i) they depend on

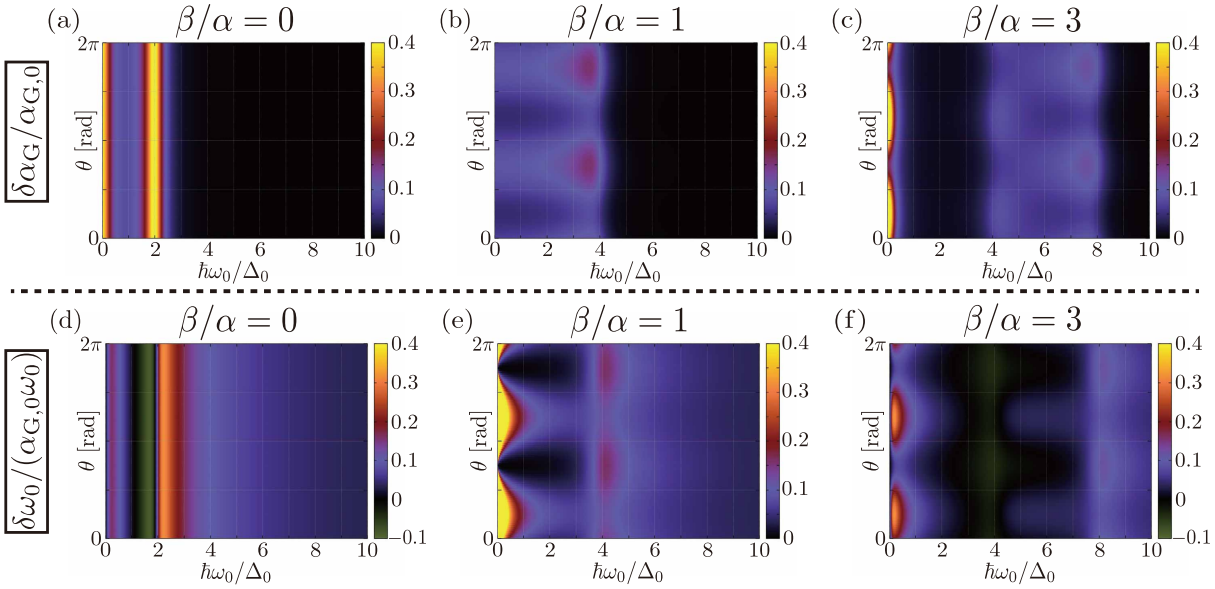

Figure 4.11: (Upper panels) Modulation of the Gilbert damping with the vertex corrections for (a) $\beta/\alpha = 0$, (b) $\beta/\alpha = 1$, and (c) $\beta/\alpha = 3$. (Lower panels) FMR frequency shift with the vertex corrections for (d) $\beta/\alpha = 0$, (e) $\beta/\alpha = 1$, and (f) $\beta/\alpha = 3$. In all panels, the horizontal axis represents the FMR frequency $\omega_{\mathbf{0}} = \gamma_{\rm g} h_{\rm dc}$, the vertical axis represents the orientation θ of the localized spin $\boldsymbol{S}$ in the FI, and the impurity strength is set to $\Gamma/\Delta_0 = 0.5$. Note that in (a), (c), and (e), values exceeding the upper limit of the color bar are represented in the same color. Additionally, (b) exhibits a δ-function-like singularity at $\omega_{\mathbf{0}} = 0$, which is not visible in the plot (see Sec. 4.4.2). Adapted from Ref. [48].

the orientation of the localized spins θ in the FI when $\beta/\alpha > 0$, but do not depend on θ when $\beta/\alpha = 0$; (ii) on the low-frequency side around $\omega_{\mathbf{0}} = 0$, a peak arises due to an elastic process in which magnons experience the effective Zeeman field of the 2DEG as a transverse magnetic field; and (iii) on the high-frequency side, a peak appears due to an inelastic process in which 2DEG electrons absorb magnons. The differences between $\delta\alpha_{\rm G}$ and $\delta\omega_{\mathbf{0}}$ are as follows: (iv) when $\beta/\alpha = 0$, $\delta\omega_{\mathbf{0}}$ exhibits a dip-and-peak structure at $\hbar\omega_{\mathbf{0}}/\Delta_0 = 2$, whereas $\delta\alpha_{\rm G}$ shows only a single peak; (v) $\delta\omega_{\mathbf{0}}$ has a tail on the high-frequency side, with slower decay compared to $\delta\alpha_{\rm G}$; (vi) for $\beta/\alpha = 1$, $\delta\alpha_{\rm G}$ takes small values around $\omega_{\mathbf{0}} = 0$, while $\delta\omega_{\mathbf{0}}$ has large values near $\omega_{\mathbf{0}} = 0$. These features are consistent with the fact that $\delta\omega_{\mathbf{0}}$ and $\delta\alpha_{\rm G}$ are expressed as the real and imaginary parts of the retarded spin susceptibility of the 2DEG, respectively, and are therefore related by the Kramers-Kronig relation. For example, the small value of $\delta\omega_{\mathbf{0}}$ at $\hbar\omega_{\mathbf{0}}/\Delta_0 = 2$ is due to the Kramers-Kronig relation, which subtracts the contribution of the peak in $\delta\alpha_{\rm G}$ at $\hbar\omega_{\mathbf{0}}/\Delta_0 = 2$. Furthermore, the large value of $\delta\omega_{\mathbf{0}}$ at $\omega_{\mathbf{0}} \simeq 0$ when $\beta/\alpha = 1$, except for $\theta = 3\pi/4$ and $7\pi/4$, can be explained by the influence of the δ-function-like divergence of $\delta\alpha_{\rm G}$ at $\omega_{\mathbf{0}} = 0$, as dictated by the Kramers-Kronig relation.

The main panel of Fig. 4.12 shows $\delta\omega_{\mathbf{0}}$ as a function of $\omega_{\mathbf{0}}$ for $\beta/\alpha = 1.1$. The five curves in this figure represent different spin orientations θ within the FI. The inset of Fig. 4.12 presents

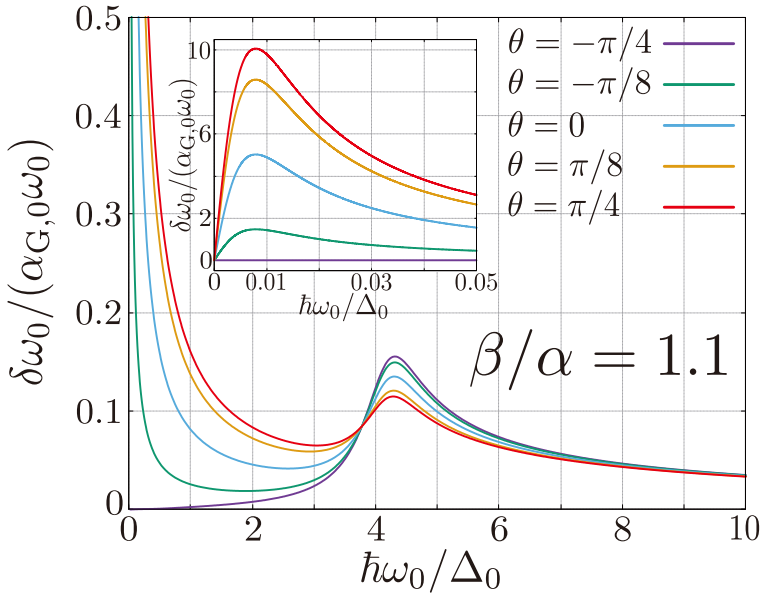

Figure 4.12: A plot of the FMR frequency shift $\delta\omega_{\mathbf{0}}$ with the vertex corrections considered for $\beta/\alpha = 1.1$, shown as a function of $\omega_{\mathbf{0}}$. The inset presents the same data as the main panel with modified ranges for both the vertical and horizontal axes. The impurity strength is set to $\Gamma/\Delta_0 = 0.5$. Adapted from Ref. [48].

the same data as the main panel but over a narrower range of the horizontal axis. This inset demonstrates that as $\omega_{\mathbf{0}}$ approaches zero, $\delta\omega_{\mathbf{0}}$ tends to zero. As derived in Appendix B, for $\beta/\alpha = 1 + \delta$ ($\delta \ll 1$), $\delta\omega_{\mathbf{0}}$ can be approximated in the low-frequency region as follows:

$$\frac{\delta\omega_{\mathbf{0}}}{\alpha_{G,0}\omega_{\mathbf{0}}} \simeq \frac{\Delta_0}{2\pi}\frac{\hbar\omega_{\mathbf{0}}}{(\hbar\omega_{\mathbf{0}})^2 + \Gamma_s^2}\sin^2\left(\theta + \frac{\pi}{4}\right). \tag{4.107}$$

Here, Γ_s is the spin relaxation rate introduced in Eq. (4.106).

Chapter 5

Inverse Rashba-Edelstein Effect by Spin Pumping

This chapter discusses the inverse Rashba-Edelstein effect (IREE) induced by spin pumping (SP) in a junction system comprising a ferromagnetic insulator (FI) and a two-dimensional electron gas (2DEG) with the Rashba and Dresselhaus spin-orbit couplings (SOCs) [49]. The setup of this study is illustrated in Fig. 5.1, where an external microwave is applied to induce the ferromagnetic resonance (FMR), thereby injecting a spin current into the 2DEG by SP. In the 2DEG, the non-equilibrium spin accumulation caused by this spin current is converted into a charge current via the IREE. In this chapter, we calculate the spin density and charge current in the 2DEG induced by the IREE using the microscopic Hamiltonian introduced in Chap. 3 and the Boltzmann equation. In particular, we elucidate the dependence of these physical quantities on the FMR frequency, the orientation of localized spins in the FI, and the ratio of the Rashba to Dresselhaus SOCs, and present the physical mechanisms explaining this behavior.

Theoretical studies on the IREE driven by SP have been conducted for systems such as the 2DEG in Fe-GaAs junctions [115] and ferromagnetic metal-nonmagnetic metal-topological insulator junctions [116]. However, these studies do not account for the effects of magnon absorption and emission on the IREE. In this work, we focus on elucidating the role of magnons in the IREE induced by SP in FI-2DEG junction systems. By employing the microscopic interfacial interaction Hamiltonian described in Eq. (3.27), we provide a theoretical framework to capture these effects.

This chapter is organized as follows: In Sec. 5.1, we formulate the IREE using the Boltzmann equation and derive expressions for the spin density and charge current induced in the 2DEG by the IREE. In Sec. 5.2, the results for the spin density and charge current are plotted, clarifying their dependence on the FMR frequency and the orientation of localized spins in the FI. Furthermore, we reveal the dependence of their maximum values on the ratio of the Rashba to Dresselhaus SOCs. In Sec. 5.3, we discuss the relevance of these results to experiments.

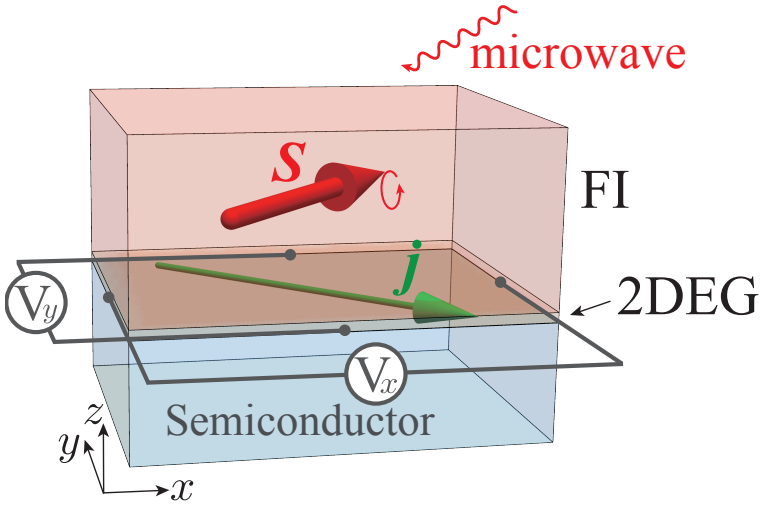

Figure 5.1: Setup of the study on the IREE induced by SP. The red arrow $\boldsymbol{S}$ represents the localized spins in the FI, and the green arrow $\boldsymbol{j}$ denotes the charge current density generated by the IREE. Adapted from Ref. [49].

5.1 Formulation

In this section, we formulate the conversion from spin to charge via the inverse Rashba-Edelstein effect (IREE). First, in Sec. 5.1.1, we introduce the Boltzmann equation describing the IREE. Next, we calculate the collision terms due to impurity scattering and SP in Secs. 5.1.3 and 5.1.2, respectively. Finally, in Sec. 5.1.4, we solve the Boltzmann equation and calculate the spin density and current density induced in the 2DEG by the IREE.

5.1.1 Boltzmann equation

Due to the spin splitting of the energy bands of conduction electrons in the 2DEG caused by the Rashba and Dresselhaus SOCs, the Boltzmann equation for this system generally takes the form of a matrix equation for a 2×2 density matrix that accounts for spin degrees of freedom. In this study, we consider the weak-impurity limit, in which the impurity scattering rate Γ is much smaller than the spin-splitting energy caused by the SOCs. Under this condition, as explained in Appendix C, it is sufficient to consider only the distribution function $f(\boldsymbol{k}, \gamma)$, which corresponds to the diagonal components of the density matrix in the basis of $|\boldsymbol{k}\gamma\rangle$ in Eq. (3.8). The Boltzmann equation for this distribution function is expressed as follows [32, 81]:

$$\frac{\partial f(\boldsymbol{k},\gamma)}{\partial t} + \boldsymbol{v}(\boldsymbol{k},\gamma) \cdot \frac{\partial f(\boldsymbol{k},\gamma)}{\partial \boldsymbol{r}} + e\boldsymbol{E} \cdot \frac{\partial f(\boldsymbol{k},\gamma)}{\hbar \partial \boldsymbol{k}} = \left.\frac{\partial f(\boldsymbol{k},\gamma)}{\partial t}\right|_{\text{coll}}, \tag{5.1}$$

where, $\boldsymbol{v}(\boldsymbol{k},\gamma) \equiv \partial E_{\boldsymbol{k}}^{\gamma}/\hbar\partial\boldsymbol{k}$ represents the electron velocity, e (< 0) is the electron charge, and $\boldsymbol{E}$ is the external electric field. The right-hand side corresponds to the collision term. In this

study, we consider the steady-state solution for a spatially uniform system. Furthermore, since no external electric field is applied in the IREE, the left-hand side of Eq. (5.1) is set to zero. The resulting Boltzmann equation to be solved in this chapter is given by:

$$0 = \left.\frac{\partial f(\boldsymbol{k},\gamma)}{\partial t}\right|_{\text{coll}} = \left.\frac{\partial f(\boldsymbol{k},\gamma)}{\partial t}\right|_{\text{imp}} + \left.\frac{\partial f(\boldsymbol{k},\gamma)}{\partial t}\right|_{\text{pump}}. \tag{5.2}$$

Here, $\partial f/\partial t|_{\text{imp}}$ represents the collision term due to impurity scattering and $\partial f/\partial t|_{\text{pump}}$ corresponds to the one due to SP. It is important to note that in this formulation we do not use spin current, which is ambiguously defined in 2DEGs with the Rashba or Dresselhaus SOCs [141, 142]. Spin pumping drives the 2DEG out of equilibrium, and the analysis focuses on the system's linear response to this driving. In this case, we can write the non-equilibrium distribution function $f(\boldsymbol{k},\gamma)$ as

$$f(\boldsymbol{k},\gamma) = f_0(E^\gamma_{\boldsymbol{k}} - \delta\mu(\boldsymbol{k},\gamma)) \simeq f_0(E^\gamma_{\boldsymbol{k}}) - \frac{\partial f_0(E^\gamma_{\boldsymbol{k}})}{\partial E^\gamma_{\boldsymbol{k}}}\delta\mu(\boldsymbol{k},\gamma). \tag{5.3}$$

Here, $f_0(\epsilon) = (\exp[\beta(\epsilon-\mu)]+1)^{-1}$ represents the Fermi distribution function, where β is the inverse temperature and μ is the chemical potential in equilibrium. The term $\delta\mu(\boldsymbol{k},\gamma)$ denotes the non-equilibrium shift in the chemical potential induced by SP.

5.1.2 Collision term due to impurity scattering

In this section, we calculate the collision term $\partial f(\boldsymbol{k},\gamma)/\partial t|_{\text{imp}}$ due to impurity scattering, which appears as the first term on the right-hand side of Eq. (5.2). This collision term can be expressed using the non-equilibrium distribution function $f(\boldsymbol{k},\gamma)$ as follows:

$$\left.\frac{\partial f(\boldsymbol{k},\gamma)}{\partial t}\right|_{\text{imp}} = \sum_{\boldsymbol{k}'}\sum_{\gamma'=\pm}\Big[P_{\boldsymbol{k}'\gamma'\to\boldsymbol{k}\gamma} f(\boldsymbol{k}',\gamma')(1-f(\boldsymbol{k},\gamma)) - P_{\boldsymbol{k}\gamma\to\boldsymbol{k}'\gamma'} f(\boldsymbol{k},\gamma)(1-f(\boldsymbol{k}',\gamma'))\Big]. \tag{5.4}$$

Here, $P_{\boldsymbol{k}\gamma\to\boldsymbol{k}'\gamma'}$ represents the transition rate from the initial state $|\boldsymbol{k},\gamma\rangle$ to the final state $|\boldsymbol{k}',\gamma'\rangle$ due to the point-like non-magnetic impurity Hamiltonian in Eq. (3.12). Within the framework of the Born approximation, we can write this transition rate using Fermi's golden rule as follows:

$$P_{\boldsymbol{k}\gamma\to\boldsymbol{k}'\gamma'} = \frac{2\pi}{\hbar}\left|\langle\boldsymbol{k}',\gamma'|H_{\text{imp}}(\boldsymbol{R})|\boldsymbol{k},\gamma\rangle\right|^2 \delta\Big(E^{\gamma'}_{\boldsymbol{k}'} - E^\gamma_{\boldsymbol{k}}\Big). \tag{5.5}$$

It should be noted that this formulation using Fermi's golden rule is valid only in the weak-impurity limit, in which the impurity scattering rate Γ is sufficiently smaller than the spin-splitting energy caused by the Rashba and Dresselhaus SOCs. For further details, refer to Appendix C.

We calculate the collision term in Eq. (5.4) below. A key aspect of the following calculation is that the transition rate, $P_{\boldsymbol{k}\gamma\to\boldsymbol{k}'\gamma'}$, depends on the overlap between the spinor wavefunctions of the initial state $|\boldsymbol{k},\gamma\rangle$ and the final state $|\boldsymbol{k}',\gamma'\rangle$. This effect is described by the coefficient $C_{\sigma\gamma}$, introduced in Eq. (3.11). Substituting Eq. (5.5) into Eq. (5.4) and taking the random average over impurity sites yields the following equation:

$$\left.\frac{\partial f(\boldsymbol{k},\gamma)}{\partial t}\right|_{\mathrm{imp}} = \frac{2\pi u^2 n_{\mathrm{imp}}}{\hbar\mathcal{A}} \sum_{\boldsymbol{k}',\gamma'} \sum_{\sigma,\sigma'} C^*_{\sigma\gamma'}(\varphi') C_{\sigma\gamma}(\varphi) C_{\sigma'\gamma'}(\varphi') C^*_{\sigma'\gamma}(\varphi) \times [f(\boldsymbol{k}',\gamma') - f(\boldsymbol{k},\gamma)]\delta(E^{\gamma'}_{\boldsymbol{k}'} - E^{\gamma}_{\boldsymbol{k}}). \tag{5.6}$$

By summing over the spin variables $\sigma, \sigma' = \uparrow, \downarrow$, we obtain the following equation:

$$\left.\frac{\partial f(\boldsymbol{k},\gamma)}{\partial t}\right|_{\mathrm{imp}} = \frac{\pi u^2 n_{\mathrm{imp}}}{\hbar\mathcal{A}} \sum_{\boldsymbol{k}',\gamma'} [1 + \gamma\gamma' \hat{\boldsymbol{h}}_{\mathrm{eff}}(\varphi) \cdot \hat{\boldsymbol{h}}_{\mathrm{eff}}(\varphi')] \cdot [f(\boldsymbol{k}',\gamma') - f(\boldsymbol{k},\gamma)]\delta(E^{\gamma'}_{\boldsymbol{k}'} - E^{\gamma}_{\boldsymbol{k}}). \tag{5.7}$$

Next, the expression for $f(\boldsymbol{k},\gamma)$ from Eq. (5.3) is substituted into Eq. (5.7) and the summation over the wavevector is replaced with an integral using the following formula:

$$\frac{1}{\mathcal{A}} \sum_{\boldsymbol{k}} (\cdots) = \frac{1}{2\pi} \int_0^\infty dk\ |\boldsymbol{k}| \int_0^{2\pi} \frac{d\varphi}{2\pi} (\cdots). \tag{5.8}$$

Additionally, assuming that the chemical potential μ is equal to the Fermi energy $\epsilon_{\mathrm{F}} = \hbar^2 k_{\mathrm{F}}^2/2m^*$ for a 2DEG without spin splitting from SOC and applying the approximation

$$-\frac{\partial f_0(E^{\gamma}_{\boldsymbol{k}})}{\partial E^{\gamma}_{\boldsymbol{k}}} \simeq \delta(E^{\gamma}_{\boldsymbol{k}} - \mu) \simeq \frac{1}{\hbar v_{\mathrm{F}}} \delta(|\boldsymbol{k}| - k(\varphi,\gamma)), \tag{5.9}$$

$$k(\varphi,\gamma) = k_{\mathrm{F}} - 2\pi\gamma D(\epsilon_{\mathrm{F}}) \sqrt{\alpha^2 + \beta^2 + 2\alpha\beta \sin 2\varphi}, \tag{5.10}$$

we perform the radial integral over the wavevector and obtain the following form for Eq. (5.6):

$$\left.\frac{\partial f(\boldsymbol{k},\gamma)}{\partial t}\right|_{\mathrm{imp}} \simeq \frac{\Gamma}{2\hbar k_{\mathrm{F}}} \sum_{\gamma'=\pm} \int_0^{2\pi} \frac{d\varphi'}{2\pi} k(\varphi',\gamma') [1 + \gamma\gamma' \hat{\boldsymbol{h}}_{\mathrm{eff}}(\varphi) \cdot \hat{\boldsymbol{h}}_{\mathrm{eff}}(\varphi')] \times [\delta\mu(\varphi',\gamma') - \delta\mu(\boldsymbol{k},\gamma)]\delta(E^{\gamma}_{\boldsymbol{k}} - \mu). \tag{5.11}$$

Here, $\Gamma = 2\pi n_{\mathrm{imp}} u^2 D(\epsilon_{\mathrm{F}})$ represents the energy broadening due to impurity scattering, $D(\epsilon_{\mathrm{F}}) = m^*/(2\pi\hbar^2) = k_{\mathrm{F}}/(2\pi\hbar v_{\mathrm{F}})$ is the density of states per unit area, and $v_{\mathrm{F}} = \hbar k_{\mathrm{F}}/m^*$ is the Fermi velocity. Furthermore, $\hat{\boldsymbol{h}}_{\mathrm{eff}}(\varphi) \equiv \boldsymbol{h}_{\mathrm{eff}}(\varphi)/h_{\mathrm{eff}}(\varphi)$ denotes the direction of the effective Zeeman field induced by the Rashba and Dresselhaus SOCs, where $\boldsymbol{h}_{\mathrm{eff}}(\varphi)$ and $h_{\mathrm{eff}}(\varphi)$ were introduced in Eqs. (3.5) and (3.6), respectively. Additionally, $\delta\mu(\varphi,\gamma)$ represents the non-equilibrium shift

of the chemical potential at the wavenumber $k(\varphi, \gamma)$.

$$\delta\mu(\varphi, \gamma) = \delta\mu(|\boldsymbol{k}|, \gamma)|_{|\boldsymbol{k}|=k(\varphi,\gamma)}. \tag{5.12}$$

5.1.3 Collision Term Due to Spin Pumping

In this section, we calculate the collision term $\partial f(\boldsymbol{k}, \gamma)/\partial t|_{\text{pump}}$ due to SP, which appears as the second term on the right-hand side of Eq. (5.2). This collision term can be expressed as follows:

$$\left.\frac{\partial f(\boldsymbol{k}, \gamma)}{\partial t}\right|_{\text{pump}} = \sum_{\boldsymbol{k}'} \sum_{\gamma'=\pm} \Big[Q_{\boldsymbol{k}'\gamma'\to\boldsymbol{k}\gamma} f(\boldsymbol{k}', \gamma')(1 - f(\boldsymbol{k}, \gamma)) - Q_{\boldsymbol{k}\gamma\to\boldsymbol{k}'\gamma'} f(\boldsymbol{k}, \gamma)(1 - f(\boldsymbol{k}', \gamma')) \Big], \tag{5.13}$$

Here, $Q_{\boldsymbol{k}\gamma\to\boldsymbol{k}'\gamma'}$ represents the transition rate from the initial state $|\boldsymbol{k}, \gamma\rangle$ to the final state $|\boldsymbol{k}', \gamma'\rangle$. In this chapter, we consider the case of a clean FI-2DEG interface and use the following Hamiltonians introduced in Eqs. (3.27) and (3.29) as the interface interaction:

$$H_{\text{int}} = \sum_{\boldsymbol{q}} (\bar{T} S_{\boldsymbol{q}}^{x'+} s_{\boldsymbol{q}}^{x'-} + \bar{T}^* s_{\boldsymbol{q}}^{x'+} S_{\boldsymbol{q}}^{x'-}) + \bar{\mathcal{T}} S_0 s_{\boldsymbol{0}}^{x'}. \tag{5.14}$$

Here, the first term in Eq. (5.14) is a dynamical term representing spin injection (magnon transfer) at the FI-2DEG interface. On the other hand, the final term in Eq. (5.14) is a static term representing the exchange bias at the interface, which acts as an effective Zeeman field on the 2DEG conduction electrons. In other words, this static term does not induce spin injection or non-equilibrium spin accumulation in the 2DEG, and thus does not contribute to the IREE. Therefore, in the following, we omit the static term and retain only the dynamical magnon term. Additionally, since the localized spins in the FI undergo uniform precession due to the FMR during SP, the long-wavelength approximation can be applied, and only magnons with $\boldsymbol{q} = 0$ need to be considered. Thus, we rewrite Eq. (5.14) as follows:

$$H_{\text{pump}} = \bar{T} S_{\boldsymbol{0}}^{x'+} s_{\boldsymbol{0}}^{x'-} + \bar{T}^* s_{\boldsymbol{0}}^{x'+} S_{\boldsymbol{0}}^{x'-} = \sqrt{2S_0}(\bar{T} b_{\boldsymbol{0}} s_{\boldsymbol{0}}^{x'-} + \bar{T}^* s_{\boldsymbol{0}}^{x'+} b_{\boldsymbol{0}}^\dagger). \tag{5.15}$$

Using Eq. (5.15), we calculate the transition rate $Q_{\boldsymbol{k}\gamma\to\boldsymbol{k}'\gamma'}$ appearing in Eq. (5.13) based on Fermi's golden rule:

$$Q_{\boldsymbol{k}\gamma\to\boldsymbol{k}'\gamma'} = \sum_{N_{\boldsymbol{0}}} \sum_{\Delta N_{\boldsymbol{0}}=\pm 1} \frac{2\pi}{\hbar} \Big| \langle \boldsymbol{k}', \gamma' | \langle N_{\boldsymbol{0}} + \Delta N_{\boldsymbol{0}} | H_{\text{pump}} | \boldsymbol{k}, \gamma \rangle | N_{\boldsymbol{0}} \rangle \Big|^2 \rho(N_{\boldsymbol{0}}) \delta\Big(E_{\boldsymbol{k}'}^{\gamma'} - E_{\boldsymbol{k}}^{\gamma} + \Delta N_{\boldsymbol{0}} \hbar\omega_{\boldsymbol{0}} \Big). \tag{5.16}$$

Here, $|N_{\boldsymbol{0}}\rangle$ is an eigenstate of the magnon number operator, i.e., $b_{\boldsymbol{0}}^\dagger b_{\boldsymbol{0}} |N_{\boldsymbol{0}}\rangle = N_{\boldsymbol{0}} |N_{\boldsymbol{0}}\rangle$, $\Delta N_{\boldsymbol{0}} = \pm 1$ represents the change in the magnon number, and $\rho(N_{\boldsymbol{0}})$ denotes the non-equilibrium distribution

function of magnons in the FI induced by the FMR. In the following, $\rho(N_{\mathbf{0}})$ is assumed to have a sharp peak at $\langle N_{\mathbf{0}}\rangle \equiv \sum_{N_{\mathbf{0}}} \rho(N_{\mathbf{0}})N_{\mathbf{0}} \gg 1$, and the following approximation is applied for an arbitrary function $F(x)$:

$$\sum_{N_{\mathbf{0}}} \rho(N_{\mathbf{0}})F(N_{\mathbf{0}}) \simeq F(\langle N_{\mathbf{0}}\rangle). \tag{5.17}$$

Within this approximation, the transition rate in Eq. (5.16) is proportional to $\langle N_{\mathbf{0}}\rangle$, which can be regarded as a parameter representing the strength of SP. In the following, $\delta\mu(\boldsymbol{k},\gamma)$ introduced in Eq. (5.3) is evaluated up to the first order in $\langle N_{\mathbf{0}}\rangle$, and the charge current induced by spin pumping is calculated as a linear response to $\langle N_{\mathbf{0}}\rangle$ in Sec. 5.1.4. It should be noted that the above formulation using Fermi's golden rule is valid only when both the impurity scattering rate Γ and the strength of the interface interaction $|\bar{T}|^2$ are sufficiently smaller than the spin splitting of the energy bands due to the Rashba and Dresselhaus SOCs.

In the following, we calculate the collision term in Eq. (5.13). It should be noted that, similar to the impurity scattering transition rate discussed in the previous section, the transition rate $Q_{\boldsymbol{k}\gamma\to\boldsymbol{k}'\gamma'}$ due to SP in Eq. (5.16) also depends on the overlap of the spinor wavefunctions between the initial and final states. By substituting this transition rate $Q_{\boldsymbol{k}\gamma\to\boldsymbol{k}'\gamma'}$ and the expression for the non-equilibrium distribution function $f(\boldsymbol{k},\gamma)$ from Eq. (5.3) into Eq. (5.13), we obtain the following equation:

$$\begin{aligned}\left.\frac{\partial f(\boldsymbol{k},\gamma)}{\partial t}\right|_{\text{pump}} \simeq \frac{\pi S_0|\bar{T}|^2\langle N_{\mathbf{0}}\rangle}{\hbar}\sum_{\gamma'=\pm}\sum_{\substack{\sigma_1,\sigma_2,\sigma_3,\sigma_4\\=\uparrow,\downarrow}} C^*_{\sigma_1\gamma'}(\varphi)C_{\sigma_2\gamma}(\varphi)C_{\sigma_3\gamma'}(\varphi)C^*_{\sigma_4\gamma}(\varphi)\\ \times\Big[(\hat{\sigma}^{x'+})_{\sigma_1\sigma_2}(\hat{\sigma}^{x'+})^*_{\sigma_3\sigma_4}[f_0(E^\gamma_{\boldsymbol{k}}-\hbar\omega_{\mathbf{0}})-f_0(E^\gamma_{\boldsymbol{k}})]\delta((\gamma'-\gamma)h_{\text{eff}}(\varphi)+\hbar\omega_{\mathbf{0}})\\ +(\hat{\sigma}^{x'-})_{\sigma_1\sigma_2}(\hat{\sigma}^{x'-})^*_{\sigma_3\sigma_4}[f_0(E^\gamma_{\boldsymbol{k}}+\hbar\omega_{\mathbf{0}})-f_0(E^\gamma_{\boldsymbol{k}})]\delta((\gamma'-\gamma)h_{\text{eff}}(\varphi)-\hbar\omega_{\mathbf{0}})\Big].\end{aligned} \tag{5.18}$$

Here, since the analysis focuses on the linear response with respect to $\langle N_{\mathbf{0}}\rangle$, the second-order terms in $\langle N_{\mathbf{0}}\rangle$, such as the product of $\langle N_{\mathbf{0}}\rangle$ and $\delta\mu(\varphi,\gamma)$, are omitted. Consequently, Eq. (5.18) does not include $\delta\mu(\varphi,\gamma)$. By performing the summation over the spin variables in Eq. (5.18), we obtain the following expression:

$$\begin{aligned}\left.\frac{\partial f(\boldsymbol{k},\gamma)}{\partial t}\right|_{\text{pump}} = -\frac{\pi S_0|\bar{T}|^2\langle N_{\mathbf{0}}\rangle\gamma}{\hbar}\sum_{\gamma'=\pm}\gamma'\\ \times\Big[(\hat{\boldsymbol{h}}_{\text{eff}}(\varphi)\cdot\hat{\boldsymbol{m}}(\theta)-\gamma')(\hat{\boldsymbol{h}}_{\text{eff}}(\varphi)\cdot\hat{\boldsymbol{m}}(\theta)+\gamma)[f_0(E^\gamma_{\boldsymbol{k}}-\hbar\omega_{\mathbf{0}})-f_0(E^\gamma_{\boldsymbol{k}})]\delta((\gamma'-\gamma)h_{\text{eff}}(\varphi)+\hbar\omega_{\mathbf{0}})\\ +(\hat{\boldsymbol{h}}_{\text{eff}}(\varphi)\cdot\hat{\boldsymbol{m}}(\theta)+\gamma')(\hat{\boldsymbol{h}}_{\text{eff}}(\varphi)\cdot\hat{\boldsymbol{m}}(\theta)-\gamma)[f_0(E^\gamma_{\boldsymbol{k}}+\hbar\omega_{\mathbf{0}})-f_0(E^\gamma_{\boldsymbol{k}})]\delta((\gamma'-\gamma)h_{\text{eff}}(\varphi)-\hbar\omega_{\mathbf{0}})\Big].\end{aligned} \tag{5.19}$$

Here, $\hat{\boldsymbol{m}}(\theta) = (\cos\theta, \sin\theta)^T$ represents the direction of the localized spin in the FI.

5.1.4 Spin Density and Current Density Induced by IREE

In this section, we solve the Boltzmann equation in Eq. (5.2) and obtain the expressions for the spin density and current density induced by the IREE. By substituting the collision terms from Eqs. (5.11) and (5.19) into Eq. (5.2), and integrating Eq. (5.2) over $\epsilon_{\boldsymbol{k}}$, we obtain the following integral equation for $\delta\mu(\varphi, \gamma)$:

$$\begin{aligned}\delta\mu(\varphi,\gamma) = \frac{k_{\mathrm{F}}}{k(\varphi,\gamma)}\gamma G(\varphi,\gamma,\theta,\hbar\omega_{\boldsymbol{0}}) \\ + \frac{1}{2}\sum_{\gamma'=\pm}\int_0^{2\pi}\frac{d\varphi'}{2\pi}\frac{k(\varphi',\gamma')}{k_{\mathrm{F}}}[1+\gamma\gamma'\hat{\boldsymbol{h}}_{\mathrm{eff}}(\varphi)\cdot\hat{\boldsymbol{h}}_{\mathrm{eff}}(\varphi')]\delta\mu(\varphi',\gamma'),\end{aligned} \tag{5.20}$$

where, $G(\varphi, \gamma, \theta, \hbar\omega_{\boldsymbol{0}})$ represents the effect of SP and is defined as follows:

$$\begin{aligned}G(\varphi,\gamma,\theta,\hbar\omega_{\boldsymbol{0}}) \equiv -\frac{\pi S_0|\bar{T}|^2\langle N_{\boldsymbol{0}}\rangle\hbar\omega_{\boldsymbol{0}}}{\Gamma}\sum_{\gamma'=\pm}\gamma'\Big[(\hat{\boldsymbol{h}}_{\mathrm{eff}}(\varphi)\cdot\hat{\boldsymbol{m}}(\theta)-\gamma')(\hat{\boldsymbol{h}}_{\mathrm{eff}}(\varphi)\cdot\hat{\boldsymbol{m}}(\theta)+\gamma)L^+ \\ -(\hat{\boldsymbol{h}}_{\mathrm{eff}}(\varphi)\cdot\hat{\boldsymbol{m}}(\theta)+\gamma')(\hat{\boldsymbol{h}}_{\mathrm{eff}}(\varphi)\cdot\hat{\boldsymbol{m}}(\theta)-\gamma)L^-\Big].\end{aligned} \tag{5.21}$$

Here, considering the finite energy broadening due to impurity scattering, we rewrite the delta function $\delta((\gamma'-\gamma)h_{\mathrm{eff}}(\varphi) \pm \hbar\omega_{\boldsymbol{0}})$ appearing in Eq. (5.19) using the following Lorentzian function [48, 78]:

$$L^{\pm} = \frac{\Gamma/2\pi}{(\hbar\omega_{\boldsymbol{0}} \pm (\gamma'-\gamma)h_{\mathrm{eff}}(\varphi))^2 + (\Gamma/2)^2}. \tag{5.22}$$

By solving the integral equation in Eq. (5.20) using the method of successive substitutions, we obtain the following solution:

$$\begin{aligned}&\delta\mu(\varphi,\gamma) \\ &= \frac{k_{\mathrm{F}}}{k(\varphi,\gamma)}\gamma G(\varphi,\gamma,\theta,\hbar\omega_{\boldsymbol{0}}) \\ &\quad + \frac{\gamma}{2}\hat{\boldsymbol{h}}^T_{\mathrm{eff}}(\varphi)\cdot\left(\hat{1}-\int_0^{2\pi}\frac{d\varphi'}{2\pi}\hat{\boldsymbol{h}}_{\mathrm{eff}}(\varphi')\cdot\hat{\boldsymbol{h}}^T_{\mathrm{eff}}(\varphi')\right)^{-1}\cdot\int_0^{2\pi}\frac{d\varphi''}{2\pi}\sum_{\gamma''=\pm}\hat{\boldsymbol{h}}_{\mathrm{eff}}(\varphi'')G(\varphi'',\gamma'',\theta,\hbar\omega_{\boldsymbol{0}}).\end{aligned} \tag{5.23}$$

Here, $\hat{1}$ is the identity matrix and $\boldsymbol{a}\cdot\boldsymbol{a}^T$ is the matrix expressed by the following:

$$\boldsymbol{a}\cdot\boldsymbol{a}^T = \begin{pmatrix} a_x \\ a_y \end{pmatrix}(a_x\ a_y) = \begin{pmatrix} a_x a_x & a_x a_y \\ a_y a_x & a_y a_y \end{pmatrix}. \tag{5.24}$$

Additionally, $\hat{A}^{-1}$ represents the inverse of matrix $\hat{A}$. Here, by introducing

$$\eta = \begin{cases} \beta/\alpha & (\alpha^2 \geq \beta^2) \\ \alpha/\beta & (\beta^2 \geq \alpha^2) \end{cases}, \tag{5.25}$$

we can express

$$\hat{M} \equiv \left(\hat{1} - \int_0^{2\pi} \frac{d\varphi'}{2\pi} \hat{\boldsymbol{h}}_{\rm eff}(\varphi') \cdot \hat{\boldsymbol{h}}_{\rm eff}^T(\varphi') \right)^{-1} = \frac{2}{1-\eta^2} \begin{pmatrix} 1 & -\eta \\ -\eta & 1 \end{pmatrix}, \tag{5.26}$$

in Eq. (5.23), indicating that $\delta\mu(\varphi, \gamma)$ diverges at $\alpha/\beta = 1$. In reality, this divergence is suppressed by spin-flip scattering due to phonons and magnetic impurities, which falls outside the scope of this theory. Nevertheless, the qualitative behavior of $\delta\mu(\varphi, \gamma)$ increasing significantly at $\alpha/\beta = 1$ is considered reasonable (see Sec. 5.2.6). It should be noted that $\delta\mu(\varphi, \gamma)$ in Eq. (5.23) satisfies the following electron number conservation law in the 2DEG:

$$0 = \sum_{\boldsymbol{k}} \sum_{\gamma=\pm} \delta\mu(\boldsymbol{k}, \gamma) \delta(E_{\boldsymbol{k}}^{\gamma} - \mu). \tag{5.27}$$

Then, within the first-order of $\delta\mu(\varphi, \gamma)$, the spin density and charge current density in the 2DEG induced by the IREE can be expressed as follows:

$$\boldsymbol{s} = \frac{\hbar}{2\mathcal{A}} \sum_{\boldsymbol{k},\gamma} \langle \boldsymbol{k}, \gamma | \boldsymbol{\sigma} | \boldsymbol{k}, \gamma \rangle f(\boldsymbol{k}, \gamma) = -\frac{\hbar D(\epsilon_{\rm F})}{2} \sum_{\gamma=\pm} \int_0^{2\pi} \frac{d\varphi}{2\pi} \frac{k(\varphi, \gamma)}{k_{\rm F}} \delta\mu(\varphi, \gamma) \gamma \hat{\boldsymbol{h}}_{\rm eff}(\varphi), \tag{5.28}$$

$$\boldsymbol{j} = \frac{e}{\mathcal{A}} \sum_{\boldsymbol{k},\gamma} \boldsymbol{v}(\boldsymbol{k}, \gamma) f(\boldsymbol{k}, \gamma) = e D(\epsilon_{\rm F}) \sum_{\gamma=\pm} \int_0^{2\pi} \frac{d\varphi}{2\pi} \frac{k(\varphi, \gamma)}{k_{\rm F}} \delta\mu(\varphi, \gamma) \boldsymbol{v}(\boldsymbol{k}, \gamma)|_{|\boldsymbol{k}|=k(\varphi,\gamma)}. \tag{5.29}$$

Here, e (< 0) is the electron charge, and $\boldsymbol{v}(\boldsymbol{k}, \gamma)$ represents the electron velocity, which is defined by the following equation:

$$\boldsymbol{v}(\boldsymbol{k}, \gamma) \equiv \frac{1}{\hbar} \frac{\partial E_{\boldsymbol{k}}^{\gamma}}{\partial \boldsymbol{k}} = \frac{\hbar \boldsymbol{k}}{m^*} + \frac{\gamma}{\hbar} \frac{\partial h_{\rm eff}(\boldsymbol{k})}{\partial \boldsymbol{k}}. \tag{5.30}$$

It should be noted that we calculated the spin density in Eq. (5.28) and the current density in Eq. (5.29) without using the spin current, which is ambiguously defined in systems with the Rashba or Dresselhaus SOCs.

5.2 Results

In this section, we present the results for the spin density and charge current density in the 2DEG induced by the IREE, derived from Eqs. (5.28) and (5.29) in the previous section. The results

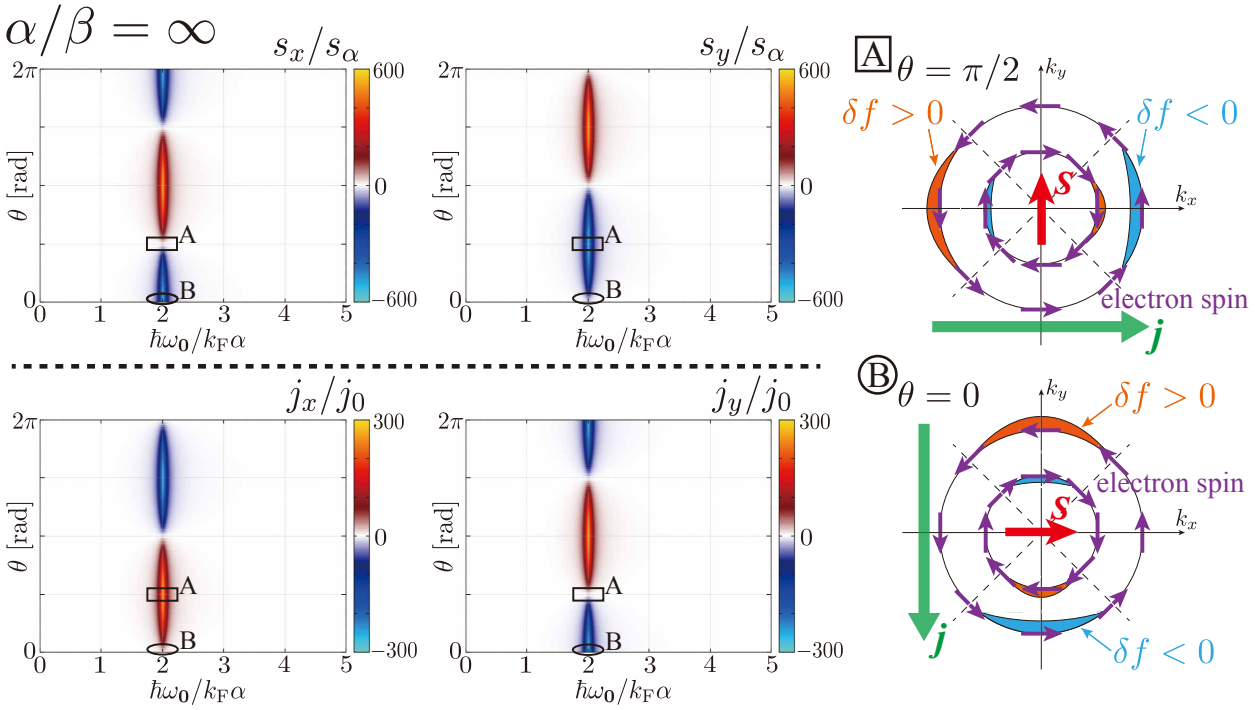

Figure 5.2: Color plot of the spin density $\boldsymbol{s} = (s_x, s_y)$ (two upper panels) and charge current density $\boldsymbol{j} = (j_x, j_y)$ (two lower panels) as functions of the FMR frequency $\omega_{\mathbf{0}}$ and the azimuthal angle θ of the localized spins in the FI for the Rashba SOC ($\alpha/\beta = \infty$). The two insets on the right depict the Fermi surface of the 2DEG electrons and the direction of the current induced by the IREE for $\theta = \pi/2$ and $\theta = 0$. In these insets, the red (blue) regions represent a positive (negative) shift in the electron distribution function of the 2DEG, $\delta f \equiv f(\boldsymbol{k}, \gamma) - f_0(E^\gamma_{\boldsymbol{k}})$. Here, $\Gamma/k_F\alpha = 0.1$ is assumed. Adapted from Ref. [49].

for the cases in which the ratio of the Rashba to Dresselhaus SOCs is $\alpha/\beta = \infty, 0, 1.1, 3$ are shown in Secs. 5.2.1, 5.2.2, 5.2.3, and 5.2.4, respectively, and are compared with relaxation-time approximation in Sec. 5.2.5. In Sec. 5.2.6, we clarify the dependence of the maximum values of the spin density and charge current density on α/β. Below, the spin density is normalized as $s_\alpha \equiv \pi\hbar D(\epsilon_F) S_0 |\bar{T}|^2 \langle N_{\mathbf{0}} \rangle / (2k_F\alpha)$ or $s_\beta \equiv \pi\hbar D(\epsilon_F) S_0 |\bar{T}|^2 \langle N_{\mathbf{0}} \rangle / (2k_F\beta)$, and the charge current density is normalized as $j_0 = \pi |e| D(\epsilon_F) S_0 |\bar{T}|^2 \langle N_{\mathbf{0}} \rangle / (\hbar k_F)$.

5.2.1 Rashba SOC ($\alpha/\beta = \infty$)

This section considers the case in which only the Rashba SOC is present ($\beta = 0$). The effective Zeeman field generated by the Rashba SOC is expressed as $h_{\rm eff}(\varphi) = k_F\alpha$, which is independent of the wavevector angle φ. The four color plots in Fig. 5.2 show the spin density $\boldsymbol{s}/s_\alpha = (s_x/s_\alpha, s_y/s_\alpha)$ and charge current density $\boldsymbol{j}/j_0 = (j_x/j_0, j_y/j_0)$ in the 2DEG as functions of the FMR frequency $\omega_{\mathbf{0}}$ and the azimuthal angle θ of the localized spins in the FI. As indicated in these plots, both the spin density and the charge current density peak when the energy of the

microwave driving the FMR matches the spin-splitting energy, $\hbar\omega_{\mathbf{0}} = 2k_{\mathrm{F}}\alpha$ $(= 2h_{\mathrm{eff}})$.

Next, we discuss the θ dependence. At $\theta = \pi/2$, marked by the square labeled A in the color plot, the spin density $\boldsymbol{s}$ is induced in the $-y$ direction, while the charge current $\boldsymbol{j}$ flows in the $+x$ direction. This behavior can be intuitively understood as follows: through SP, the spin lost by the localized spins $\boldsymbol{S}$ in the FI due to spin relaxation is injected into the 2DEG, resulting in spins opposite to $\boldsymbol{S}$ being injected. Consequently, at $\theta = \pi/2$, spins in the $-y$ direction are injected into the 2DEG, leading to spin accumulation in the $-y$ direction. Accompanying this spin injection, as shown in the upper-right inset of Fig. 5.2, the distribution function of the $-y$ $(+y)$ spin band on the Fermi surface of the 2DEG increases (decreases). In this inset, an increase (decrease) in the distribution function is represented by red (blue). Since the outer Fermi surface has a higher density of states than the inner one, this shift leads to a net flow of electrons in the $-x$ direction, resulting in a charge current flowing in the $+x$ direction. At $\theta = 0$, marked by the ellipse labeled B in the color plot, a spin density in the $-x$ direction and a charge current in the $-y$ direction are generated. This result can be explained in a similar manner to $\theta = \pi/2$, using the lower-right inset of Fig. 5.2.

The picture of the IREE presented here is as follows: spin is injected from the FI into the 2DEG through SP, causing the spins of the electrons at the interface to flip and inducing a spin density in the 2DEG. The resulting changes in the distribution function in the 2DEG give rise to a charge current. While the concept of spin current might aid in an intuitive understanding of this phenomenon, in this study, we calculated the charge current induced by the IREE without relying on the concept of spin current, which is not well-defined in systems with the Rashba and Dresselhaus SOCs.

5.2.2 Dresselhaus SOC ($\alpha/\beta = 0$)

In this section, we consider the case in which only the Dresselhaus SOC is present ($\alpha = 0$). The effective Zeeman field in this case can be written as $h_{\mathrm{eff}}(\varphi) = k_{\mathrm{F}}\beta$, and, similar to the case of the Rashba SOC only, it does not depend on the wavevector angle φ. The four color plots in Fig. 5.3 illustrate the spin density $\boldsymbol{s}/s_\beta = (s_x/s_\beta, s_y/s_\beta)$ and charge current density $\boldsymbol{j}/j_0 = (j_x/j_0, j_y/j_0)$ as functions of the FMR frequency $\omega_{\mathbf{0}}$ and the azimuthal angle θ of the localized spins in the FI. As with the Rashba-only case, these quantities peak when $\hbar\omega_{\mathbf{0}} = 2k_{\mathrm{F}}\beta$ $(= 2h_{\mathrm{eff}})$. However, the dependence on θ behaves differently from the Rashba case.

For $\theta = \pi/2$, indicated by the square labeled A in the color plot, the spin density $\boldsymbol{s}$ is induced in the $-y$ direction, while the charge current density is induced in the $+y$ direction in the Dresselhaus-only case. This result can be intuitively explained in a manner similar to the Rashba case. At $\theta = \pi/2$, spins are injected from the FI into the 2DEG in the $-y$ direction, leading to a spin density in the $-y$ direction in the 2DEG. As a result, as shown in the upper-right inset of Fig. 5.3, a non-equilibrium distribution function shift occurs in the 2DEG, generating a net flow of electrons in the $-y$ direction, and consequently, a charge current flows in the $+y$ direction.

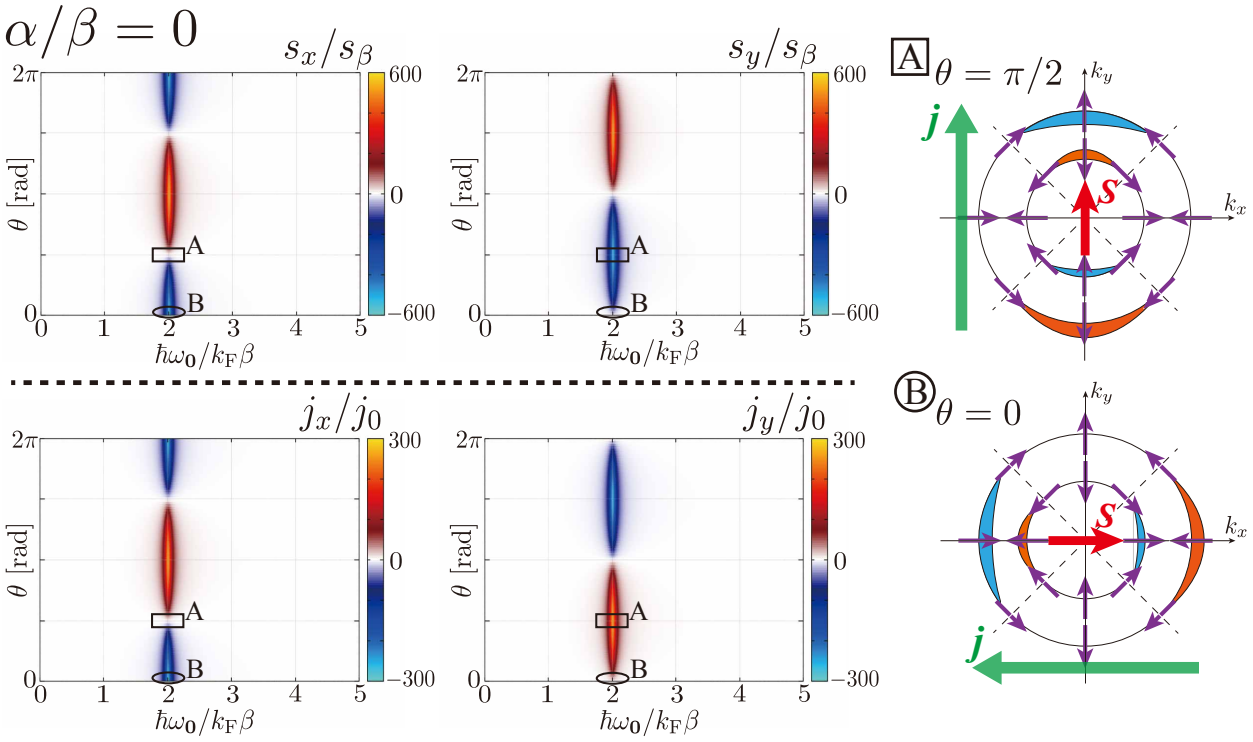

Figure 5.3: Color plot of the spin density $\boldsymbol{s} = (s_x, s_y)$ (two upper panels) and charge current density $\boldsymbol{j} = (j_x, j_y)$ (two lower panels) for the Dresselhaus SOC ($\alpha/\beta = 0$). The two insets on the right show the Fermi surface shift and the direction of the current for $\theta = \pi/2$ and $\theta = 0$. Here, $\Gamma/k_{\mathrm{F}}\beta = 0.1$ is assumed. Adapted from Ref. [49].

Next, at $\theta = 0$, indicated by the ellipse labeled B in the color plot, the spin density $\boldsymbol{s}$ in the $-x$ direction and the charge current in the $-x$ direction are generated in the 2DEG. This result can be understood similarly by referring to the lower-right inset of Fig. 5.3. The difference from the case of the Rashba SOC clearly arises from the distinct spin textures on the Fermi surface, as shown in the right insets of Figs. 5.2 and 5.3.

5.2.3 Case of $\alpha/\beta = 1.1$

When the magnitudes of the Rashba and Dresselhaus SOCs are comparable, the spin density and charge current density exhibit significantly different behavior compared to the case in which only one type of SOC is present. To observe this, this section considers the case of $\alpha/\beta = 1.1$. In this case, the effective Zeeman field depends on the electron wavevector angle φ, and its magnitude ranges from $0 \lesssim h_{\mathrm{eff}}(\varphi) \lesssim 2k_{\mathrm{F}}\beta$. The color plots in Fig. 5.4 show the spin density $\boldsymbol{s}/s_\beta = (s_x/s_\beta, s_y/s_\beta)$ and charge current density $\boldsymbol{j}/j_0 = (j_x/j_0, j_y/j_0)$ as functions of $\omega_{\boldsymbol{0}}$ and θ. Since the transition probability between subbands increases when the energy of the microwave inducing the FMR matches the spin-splitting energy near the Fermi surface, $\hbar\omega_{\boldsymbol{0}} = 2h_{\mathrm{eff}}(\varphi)$, the spin density $\boldsymbol{s}$ and charge current density $\boldsymbol{j}$ take finite values over a wide range of the horizontal

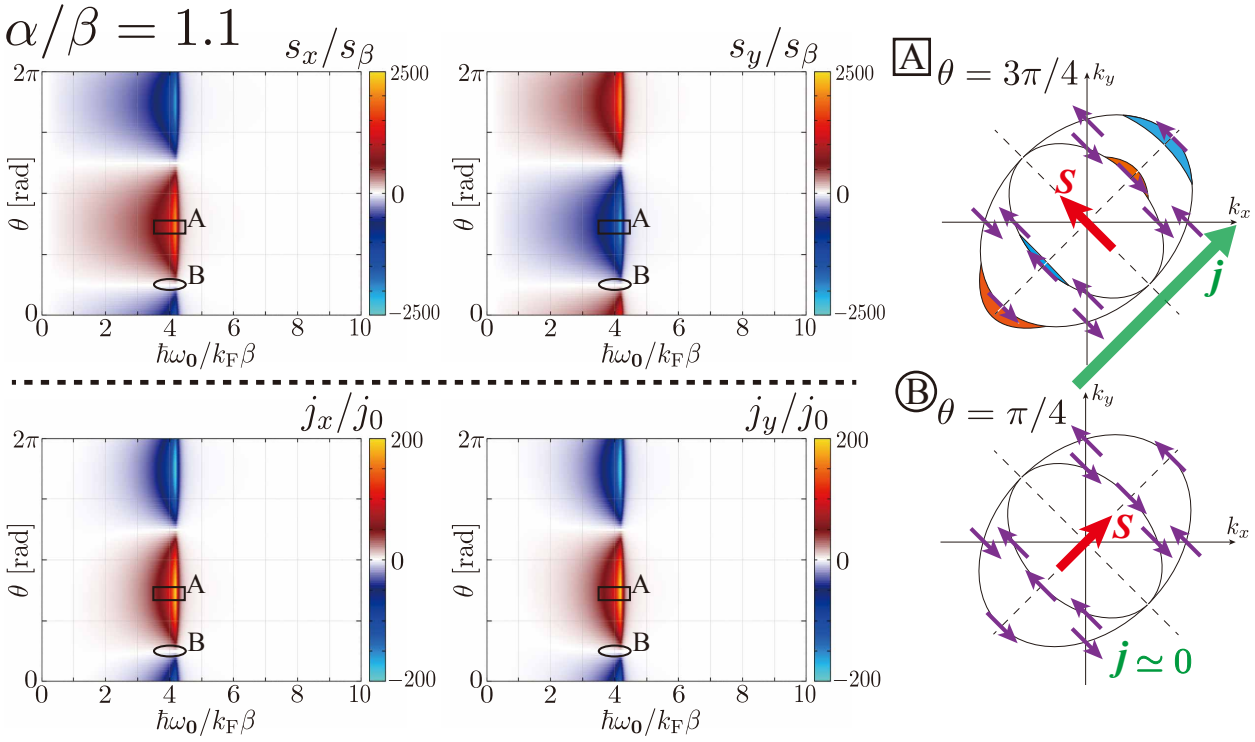

Figure 5.4: Color plot of the spin density $\boldsymbol{s} = (s_x, s_y)$ (two upper panels) and charge current density $\boldsymbol{j} = (j_x, j_y)$ (two lower panels) for $\alpha/\beta = 1.1$. The two insets on the right show the Fermi surface shift and the direction of the current for $\theta = 3\pi/4$ and $\theta = \pi/4$. Here, $\Gamma/k_F\beta = 0.1$ is assumed. Adapted from Ref. [49].

axis in the color plots of Fig. 5.4, $0 \lesssim \hbar\omega_0 \lesssim 4k_F\beta$. In particular, these values become large when the microwave energy is high, around $\hbar\omega_0 \simeq 4k_F\beta$. Moreover, the directions of $\boldsymbol{s}$ and $\boldsymbol{j}$ do not strongly depend on the magnitude of the microwave energy, with $\boldsymbol{s}$ oriented along the $(1, -1)$ direction and $\boldsymbol{j}$ along the $(1, 1)$ direction.

Next, we consider the θ dependence of $\boldsymbol{s}$ and $\boldsymbol{j}$. These quantities reach their maximum values at $\theta = 3\pi/4$ or $7\pi/4$ and become nearly zero at $\theta = \pi/4$ or $5\pi/4$. This behavior can be understood using the upper and lower-right insets of Fig. 5.4 as follows. First, at $\theta = 3\pi/4$, indicated by square A, spins are injected into the 2DEG in the $7\pi/4$ direction, inducing $\boldsymbol{s}$ in that direction. Consequently, as shown in the upper-right inset of Fig. 5.4, the distribution function changes in the $\varphi = \pi/4$ and $5\pi/4$ directions, and this change induces a net electron flow (charge current) in the $\varphi = 5\pi/4$ ($\varphi = \pi/4$) direction. On the other hand, at $\theta = \pi/4$, indicated by ellipse B, the localized spin $\boldsymbol{S}$ is perpendicular to the effective Zeeman field of the 2DEG, i.e., the direction of the spin polarization of the conduction electrons in the 2DEG, as shown in the lower-right inset of Fig. 5.4. Therefore, spin injection into the 2DEG is blocked, and no charge current is induced.

Looking at the scale of the color plot in Fig. 5.4, when the Rashba and Dresselhaus SOCs are comparable, the magnitude of the spin density becomes very large, while the magnitude of

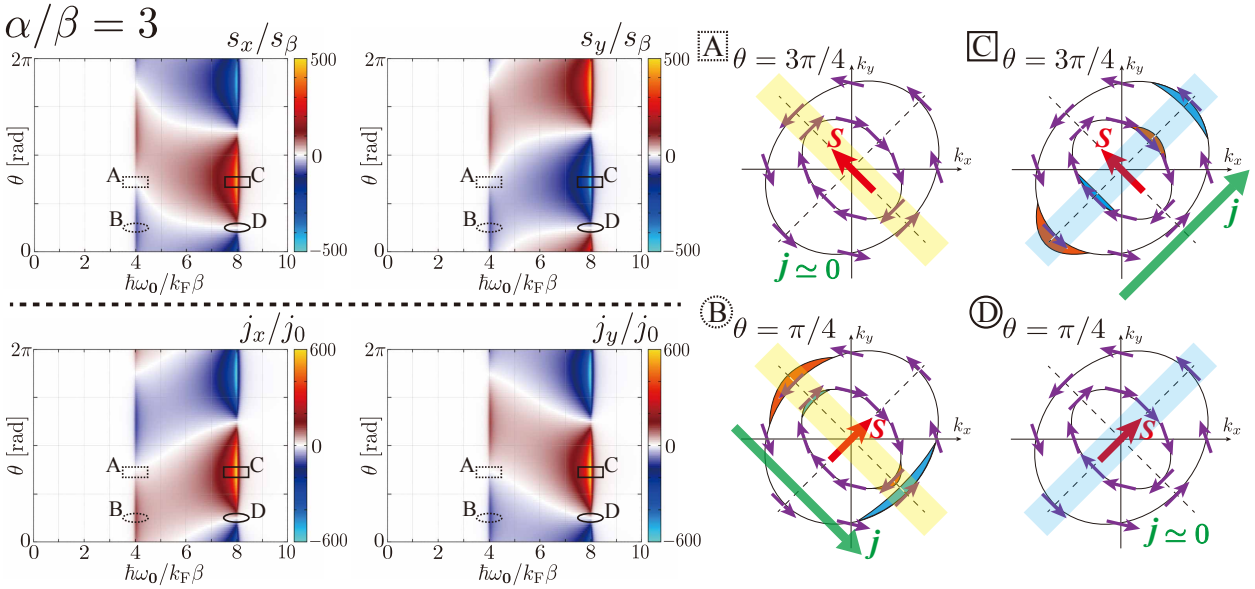

Figure 5.5: Color plot of the spin density $\boldsymbol{s} = (s_x, s_y)$ (two upper panels) and charge current density $\boldsymbol{j} = (j_x, j_y)$ (two lower panels) for $\alpha/\beta = 3$. The four insets on the right show the Fermi surface shift and the direction of the current in the regions labeled A, B, C, and D in the color plot. Here, $\Gamma/k_F\beta = 0.1$ is assumed. Adapted from Ref. [49].

the charge current density is suppressed. The dependence of the spin density and charge current density on α/β is discussed in Sec. 5.2.6.

5.2.4 Case of $\alpha/\beta = 3$

Lastly, we consider the case where the Rashba and Dresselhaus SOCs coexist but have different magnitudes. As an example, this section focuses on the case of $\alpha/\beta = 3$. In this scenario, the effective Zeeman field $h_{\rm eff}(\varphi)$ depends on φ, and its magnitude varies in the range $2k_F\beta \lesssim h_{\rm eff}(\varphi) \lesssim 4k_F\beta$. Figure 5.5 depicts the spin density $\boldsymbol{s}$ and charge current density $\boldsymbol{j}$ as functions of ω_0 and θ in the range $4k_F\beta \lesssim \hbar\omega_0 \lesssim 8k_F\beta$, which corresponds to the spin-splitting energy $2h_{\rm eff}(\varphi)$ near the Fermi surface. It should be noted that the θ dependence of $\boldsymbol{s}$ and $\boldsymbol{j}$ differs in the low-frequency region around $\hbar\omega_0 \simeq 4k_F\beta$ and the high-frequency region around $\hbar\omega_0 \simeq 8k_F\beta$.

Below, we discuss the regions A, B, C, and D in the color plot of Fig. 5.5. The four schematic insets of Fig. 5.5 correspond to these regions. First, the low-frequency regions A and B are considered. In these regions, spin injection across the interface occurs only in the yellow regions, where the spin-splitting energy is small. In the region A, since the localized spins $\boldsymbol{S}$ in the FI are perpendicular to the spins of the 2DEG electrons, no spin is injected from the FI into the 2DEG, and thus, both $\boldsymbol{s}$ and $\boldsymbol{j}$ become zero. In contrast, in the region B, the spins of the 2DEG electrons are parallel to $\boldsymbol{S}$ in the yellow region, resulting in the maximum spin injection, and in the low-frequency region, $\boldsymbol{s}$ and $\boldsymbol{j}$ are maximized in the region B. A

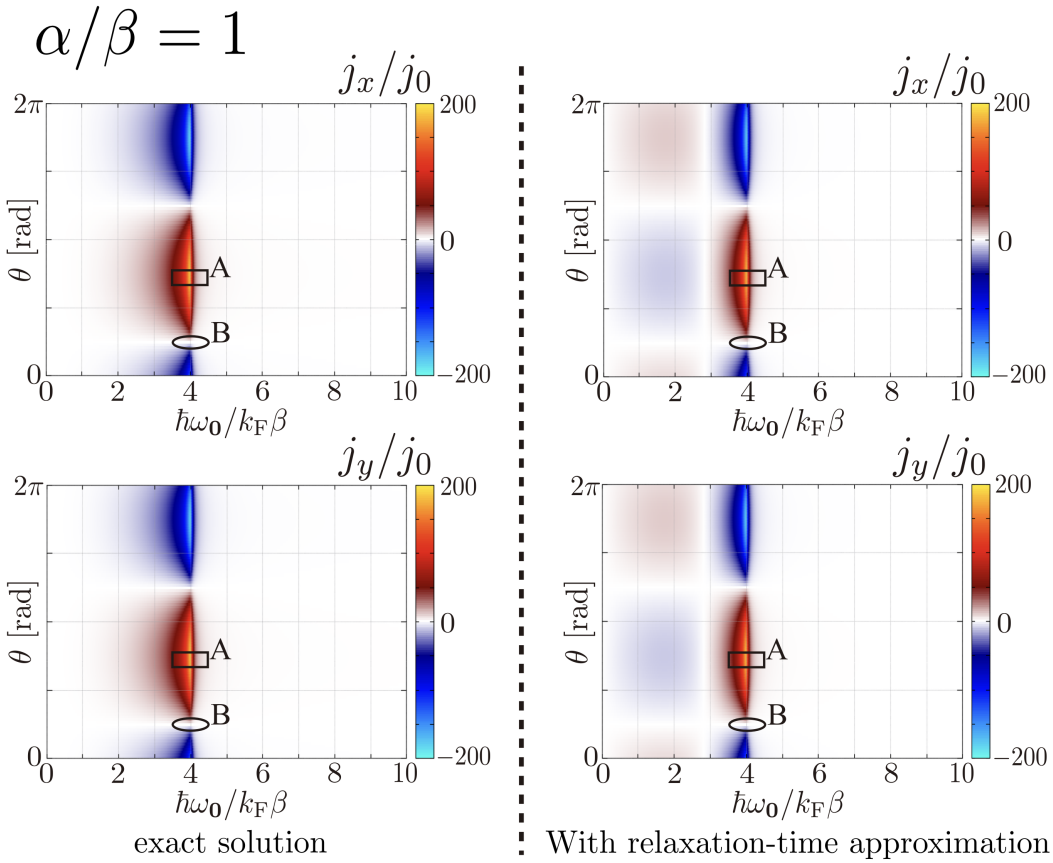

Figure 5.6: Current density $\boldsymbol{j} = (j_x, j_y)$ at $\alpha/\beta = 1$ as a function of the FMR frequency $\omega_{\mathbf{0}}$ and the localized spin orientation θ in the FI. The left two color plots represent the results from the full solution of the Boltzmann equation, while the right two plots show the results obtained with the relaxation-time approximation. Here, $\Gamma = 0.1 k_{\mathrm{F}}\beta$. Adapted from Ref. [51, 52].

similar discussion applies to the regions C and D. However, these regions correspond to the high-frequency range, and spin injection across the interface occurs only in the blue regions, where the spin-splitting energy is the largest, as shown in the insets of Fig. 5.5. In the region C (D), since $\boldsymbol{S}$ is parallel (perpendicular) to the spins in the 2DEG, the spin injection rate is maximized (zero), and consequently, $\boldsymbol{s}$ and $\boldsymbol{j}$ are maximized (minimized).

From Fig. 5.5, it can also be seen that the direction of the current rotates as the FMR frequency changes. For example, at $\hbar\omega_{\mathbf{0}}/k_{\mathrm{F}}\beta = 4$, the direction of the current $\boldsymbol{j}$ is along $\varphi = 7\pi/4$, while at $\hbar\omega_{\mathbf{0}}/k_{\mathrm{F}}\beta = 8$, the current direction is along $\varphi = \pi/4$. This can be explained by the dependence of the spin-splitting width on the electron wavevector angle φ and the spin texture on the Fermi surface.

5.2.5 Comparison with relaxation-time approximation

This section compares the results of the charge current induced by the IREE, as calculated using Fermi's golden rule in the previous sections with those obtained by applying the relaxation-time

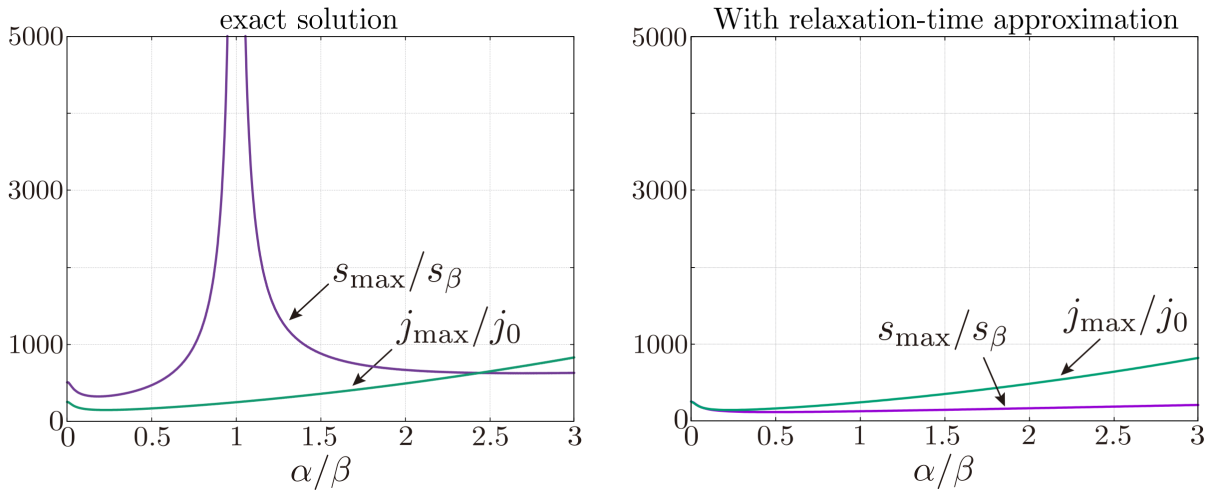

Figure 5.7: Plot of the maximum spin density $s_{\max} \equiv \max(\sqrt{s_x^2 + s_y^2})$ and the maximum current density $j_{\max} \equiv \max(\sqrt{j_x^2 + j_y^2})$ as functions of α/β at $\Gamma/k_F\beta = 0.1$. Left panel: results obtained from the full solution of the Boltzmann equation. Right panel: results obtained from the relaxation-time approximation. Adapted from Ref. [51].

approximation to the impurity scattering term in our work [51,52]. The impurity collision term under the relaxation-time approximation can be expressed as follows [80]:

$$\left.\frac{\partial f(\boldsymbol{k},\gamma)}{\partial t}\right|_{\text{imp}} = -\frac{f(\boldsymbol{k},\gamma) - f_0(\boldsymbol{k},\gamma)}{\tau(\boldsymbol{k},\gamma)}, \tag{5.31}$$

$$\tau(\boldsymbol{k},\gamma) = \tau(1 - \gamma\zeta(\varphi)), \tag{5.32}$$

$$\zeta(\varphi) \equiv \frac{2\pi D(\epsilon_F)}{k_F}\sqrt{\alpha^2 + \beta^2 + 2\alpha\beta\sin 2\varphi}. \tag{5.33}$$

Here, τ denotes the spin-independent relaxation time and $\zeta(\varphi)$ represents its modulation due to the Rashba and Dresselhaus SOCs. Figure 5.6 presents the charge current density induced by the IREE for $\alpha/\beta = 1$; the two color plots on the left show the results from the full solution of the Boltzmann equation and the two color plots on the right display the results obtained using the relaxation-time approximation. From these color plots, it is observed that the charge current calculated with the relaxation-time approximation reverses its sign at $\hbar\omega_{\mathbf{0}} \lesssim 3k_F\beta$, exhibiting qualitatively different behavior from the full solution of the Boltzmann equation. Thus, using the relaxation-time approximation for $\alpha/\beta = 1$ yields inappropriate results. See Appendix D for the comparison between the full solution of the Boltzmann equation and the relaxation-time approximation when α/β is changed from 1.

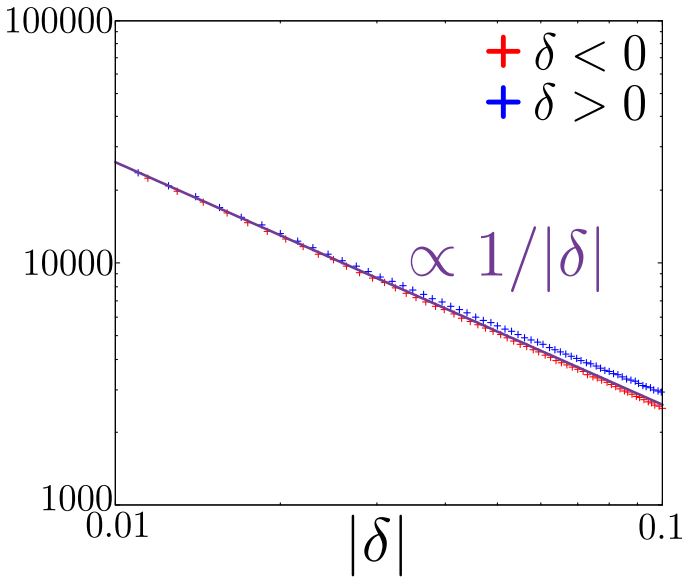

Figure 5.8: Divergence of $s_{\max}/s_\beta$ near $\alpha/\beta \simeq 1$, as observed in the left panel of Fig. 5.7. With $\alpha/\beta = 1 + |\delta|$, the red (blue) points represent the values of $s_{\max}/s_\beta$ as a function of $|\delta|$ for $\delta < 0$ ($\delta > 0$), shown in a log-log plot. The purple line represents a log-log plot of a function proportional to $1/|\delta|$.

5.2.6 Maximum values of spin density and charge current density

In this section, we discuss the dependence of the maximum values of the spin density $\boldsymbol{s}$ and charge current density $\boldsymbol{j}$ generated by the IREE on the ratio α/β. Figure 5.7 presents the maximum spin density, $s_{\max} \equiv \max(\sqrt{s_x^2 + s_y^2})$, and the maximum charge current density, $j_{\max} \equiv \max(\sqrt{j_x^2 + j_y^2})$ as functions of α/β. The plots on the left and right sides of Fig. 5.7 show the results obtained from the full solution of the Boltzmann equation and the relaxation-time approximation, respectively. As α/β approaches 1, the plot for the full solution of the Boltzmann equation (left panel) shows a divergence in $s_{\max}$. This reflects the fact that at $\alpha/\beta = 1$ the spin quantization axis of electrons on the Fermi surface aligns in a single direction, leading to the conservation of the spin component along the $3\pi/4$ direction and resulting in an exceptionally long spin relaxation time [43–48]. Notably, the full solution of the Boltzmann equation corresponds to the inclusion of the vertex corrections in linear response theory, which properly accounts for the spin conservation law [154–156]. In contrast, the plot for the relaxation-time approximation (right panel) fails to reproduce the spin divergence at $\alpha/\beta = 1$, as the relaxation-time approximation does not adequately account for the spin conservation law. Meanwhile, in both the full solution of the Boltzmann equation and the relaxation-time approximation, the magnitude of $j_{\max}$ is suppressed at $\alpha/\beta = 1$. This occurs because in the IREE the charge currents induced from the outer and inner Fermi surfaces are in opposite directions, partially canceling each other. The increase in charge current density with larger α/β in Fig. 5.7 arises from the enhancement of spin splitting caused by the Rashba SOC. As the Rashba SOC becomes stronger,

while keeping the strength of the Dresselhaus SOC fixed, the charge current generated by the IREE correspondingly increases.

To further analyze the divergence behavior of $s_{\max}$, the following discusses its relationship with the spin relaxation time. In Ref. [81], the spin relaxation time was determined by solving the following Boltzmann equation for the Hamiltonian of chiral metals:

$$H_{\text{chiral}} = \alpha_{\parallel} k_z \hat{\sigma}_z + \alpha_{\perp} k_x \hat{\sigma}_x, \tag{5.34}$$

using the collision term for nonmagnetic impurity scattering of Eq. (5.7):

$$\frac{\partial f(t, \boldsymbol{k}, \gamma)}{\partial t} = \frac{\partial f}{\partial t}\Big|_{\text{imp}}. \tag{5.35}$$

The nonequilibrium distribution function is expressed as

$$f(t, \boldsymbol{k}, \gamma) = f_0(E^{\gamma}_{\boldsymbol{k}}) + e^{-t/\tau_s} \varphi_{\tau_s}(\boldsymbol{k}, \gamma)\Big(-\frac{\partial f_0(E^{\gamma}_{\boldsymbol{k}})}{\partial E^{\gamma}_{\boldsymbol{k}}}\Big), \tag{5.36}$$

where τ_s is the spin relaxation time. One of the obtained relaxation modes is given by

$$\frac{\tau}{\tau_s} = \frac{1}{1 + \tan\tilde{\delta}}, \tag{5.37}$$

as reported in Ref. [81]. Here, τ is the momentum relaxation time and $\tilde{\delta}$ is defined by the relation $(\alpha_{\parallel}, \alpha_{\perp}) = (\tilde{\alpha}\cos\tilde{\delta}, \tilde{\alpha}\sin\tilde{\delta})$. As stated in the Supplemental Material of Ref. [81], by applying an appropriate coordinate transformation to Eq. (5.34), it can be rewritten in terms of the Hamiltonian for a system with coexisting the Rashba and Dresselhaus SOCs:

$$H_{\text{SOC}} = \alpha(k_y \hat{\sigma}_x - k_x \hat{\sigma}_y) + \beta(k_x \hat{\sigma}_x - k_y \hat{\sigma}_y). \tag{5.38}$$

The coefficients in Eq. (5.34) and Eq. (5.38) are related as

$$\alpha_{\parallel} = \alpha - \beta, \quad \alpha_{\perp} = \alpha + \beta, \tag{5.39}$$

and Eq. (5.37) can be rewritten as follows:

$$\frac{\tau}{\tau_s} \equiv \frac{1}{1 + \tan\tilde{\delta}} = \frac{1}{2}\Big(1 - \frac{1}{\alpha/\beta}\Big), \tag{5.40}$$

in which τ_s diverges when $\alpha/\beta = 1$. Introducing an infinitesimal deviation δ such that $\alpha/\beta = 1 + \delta$, Eq. (5.40) can be approximated as

$$\frac{\tau}{\tau_s} = \frac{1}{2}\Big(1 - \frac{1}{\alpha/\beta}\Big) \simeq \frac{\delta}{2}. \tag{5.41}$$

In the above expression, the Taylor expansion is performed with respect to the infinitesimal quantity δ. This result indicates that the spin relaxation time diverges as $1/\delta$.

Figure 5.8 presents a log-log plot of $s_{\max}/s_\beta$ as a function of $|\delta|$, corresponding to the left panel of Fig. 5.7. The red (blue) points represent the plot of $s_{\max}/s_\beta$ for $\delta < 0$ ($\delta > 0$), which exhibit the same slope as the purple line proportional to $1/|\delta|$. This indicates that $s_{\max}/s_\beta$ diverges with the order of $1/|\delta|$ around $\alpha/\beta \simeq 1$, similarly to the spin relaxation time given in Eq. (5.41). Therefore, the sharp increase of $s_{\max}/s_\beta$ near $\alpha/\beta = 1$ can be interpreted as a result of strongly suppressed spin relaxation of 2DEG electrons, leading to significant spin accumulation.

In this study, we employ the linearized Boltzmann equation, and thus the divergence of spin density at $\alpha/\beta = 1$ in the left panel of Fig. 5.7 lies beyond the scope of this model. Under the nonmagnetic impurity scattering considered here, no electron relaxation occurs at $\alpha/\beta = 1$, preventing the 2DEG from reaching a steady state and leading to the divergence of spin density. In experiments, we expect this divergence to be suppressed by the effects of magnetic impurities. We consider the qualitative behavior of a large spin density at $\alpha/\beta = 1$ due to spin conservation to be reasonable.

5.3 Experimental Relevance

To observe the IREE discussed in this study, it is necessary to satisfy the weak-impurity limit, $\Gamma \ll 2k_{\rm F}\alpha, 2k_{\rm F}\beta \ll \epsilon_{\rm F}$, where $2k_{\rm F}\alpha$ or $2k_{\rm F}\beta$ represents the energy splitting at the Fermi surface. As an example, consider a 2DEG in an AlGaAs/GaAs system with an electron mobility of $10^6\,{\rm cm}^2/{\rm Vs}$ [143]. For this system, using an electron density of $n = 5 \times 10^{11}$ cm^{-2} and $k_{\rm F}\alpha = 0.1$ meV ($\simeq 25\,{\rm GHz}$) [143, 146], the impurity scattering rate can be estimated as $\Gamma \simeq 10^{-1}(2k_{\rm F}\alpha) \simeq 10^{-3}\epsilon_{\rm F}$ [48, 78], which satisfies the weak-impurity limit. Therefore, it is expected that the results of this study can be observed in a system where an FI, such as YIG, is interfaced with this semiconductor heterostructure.

Another example involves a thin GaAs film, in which only a few transport channels contribute in the thickness direction. Although YIG-GaAs junctions have attracted attention in the field of spintronics [157–159], no experimental studies on IREE have been conducted in this system. On the other hand, IREE has already been observed in Fe-GaAs junctions [112], in which the Rashba SOC was estimated to be 100 meVÅ. Using this Rashba SOC value and the electron mobility $\mu = 10^4$ cm^2/Vs at liquid nitrogen temperature in bulk GaAs with an electron density of $n = 10^{17}$ cm^{-3} [160–163], the impurity scattering rate is estimated as $\Gamma \simeq 0.5(2k_{\rm F}\alpha) \simeq 0.1\epsilon_{\rm F}$. Therefore, high-quality YIG-GaAs junctions nearly satisfy the weak-impurity limit, suggesting that the results of this study may be observable.

Chapter 6

Rashba-Edelstein Magnetoresistance

This chapter establishes a theoretical framework for the Rashba-Edelstein Magnetoresistance (REMR) in a system consisting of a two-dimensional electron gas (2DEG) with the Rashba and Dresselhaus spin-orbit couplings (SOCs) and a ferromagnetic insulator (FI), as depicted in Fig. 6.1 [50]. Using the microscopic Hamiltonian introduced in Chap. 3 and the Boltzmann equation, we calculate spin density and charge current density induced in the 2DEG due to the REMR for both dirty and clean FI-2DEG interfaces. This analysis reveals that the sign of REMR varies with the interface type, elucidating the physical mechanism of REMR.

A theoretical study on the REMR in junction systems consisting of FI and two-dimensional materials has been reported in Ref. [140]. However, this study adopts a phenomenological approach based on spin mixing conductance, which does not account for the effects of magnons or the dependence on interfacial states. The anisotropic magnetoresistance (AMR) in dilute magnetic semiconductors has been theoretically explored in Refs. [144, 145]. While these frameworks could, in principle, be extended to the REMR, they also lack the ability to describe magnon contributions and interfacial state dependence. In this study, we address these limitations by employing the microscopic interfacial interaction Hamiltonian presented in Eq. (3.27). Using this approach, we elucidate the contributions of magnons to the REMR and reveal its dependence on interfacial states, providing a more comprehensive and detailed theoretical framework.

The chapter is organized as follows: Section 6.1 provides the formulation of the REMR using the Boltzmann equation, deriving analytical expressions for the spin density and charge current density induced in the 2DEG for dirty and clean FI-2DEG interfaces. Section 6.2 presents plots of the spin density and charge current density for each type of interface as functions of the orientation of localized spins in the FI, along with an examination of their dependence on the ratio of the Rashba and Dresselhaus SOCs. Section 6.3 discusses the relevance of the theoretical findings of this study to experimental REMR results.

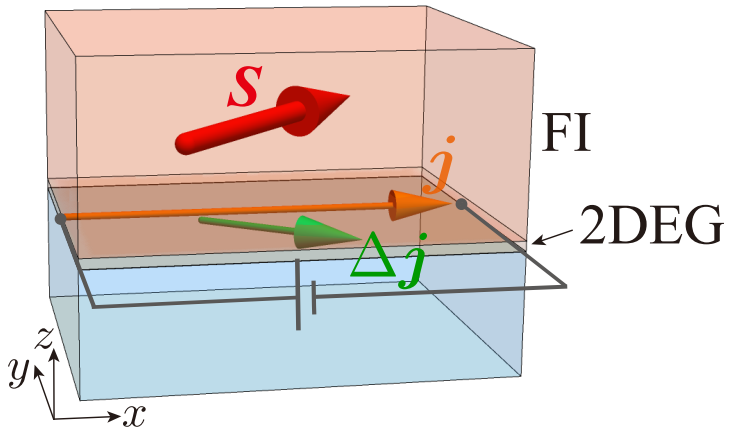

Figure 6.1: The setup of the REMR considered in this study. The red arrow represents the localized spin $\boldsymbol{S}$ in the FI, the orange arrow indicates the current density $\boldsymbol{j}$ generated by an external DC electric field, and the green arrow represents the modulation of current density $\Delta\boldsymbol{j}$ induced by the REMR. Adapted from Ref. [50].

6.1 Formulation

This section presents the formulation of the REMR in the FI-2DEG junction system. Section 6.1.1 introduces the Boltzmann equation for the REMR, followed by the calculation of the REE in the 2DEG in Sec. 6.1.2. The REMR in the FI-2DEG junction system is then analytically evaluated for both dirty and clean interfaces in Secs. 6.1.3 and 6.1.4, respectively.

6.1.1 Boltzmann equation

In this chapter, as in Chap. 5, we consider the weak-impurity limit; the spin splitting in the energy band of conduction electrons in the 2DEG due to the Rashba or Dresselhaus SOCs is assumed to be sufficiently large compared to the strength of impurity scattering. Under this condition, as described in Sec. 5.1.1, the distribution function of 2DEG electrons can be expressed as $f(\boldsymbol{k},\gamma)$, where $\boldsymbol{k}$ is the wavevector and γ is the index for spin-polarized bands. Additionally, as in Chap. 5, we consider the steady-state solution in a system with translational symmetry. In this case, by using perturbation theory for the nonmagnetic impurity scattering Hamiltonian $H_{\rm imp}$ in Eq. (3.12) and the interfacial interaction Hamiltonian $H_{\rm int}$ in Eq. (3.27), the Boltzmann equation for the REMR under an externally applied electric field E_x in the x-direction is given by:

$$\frac{eE_x}{\hbar}\frac{\partial f(\boldsymbol{k},\gamma)}{\partial k_x} = \left.\frac{\partial f(\boldsymbol{k},\gamma)}{\partial t}\right|_{\rm imp} + \left.\frac{\partial f(\boldsymbol{k},\gamma)}{\partial t}\right|_{\rm int}. \tag{6.1}$$

Here, e (< 0) denotes the electron charge. The first and second terms on the right-hand side of the above equation represent the collision terms due to impurity scattering and interfacial

exchange coupling, respectively.

The expression for the collision term due to impurity scattering, given in Eqs. (5.4) and (5.5), is reiterated as follows:

$$\left.\frac{\partial f(\boldsymbol{k},\gamma)}{\partial t}\right|_{\text{imp}} = \sum_{\boldsymbol{k}'}\sum_{\gamma'=\pm}\Big[P_{\boldsymbol{k}'\gamma'\to\boldsymbol{k}\gamma}f(\boldsymbol{k}',\gamma')(1-f(\boldsymbol{k},\gamma)) - P_{\boldsymbol{k}\gamma\to\boldsymbol{k}'\gamma'}f(\boldsymbol{k},\gamma)(1-f(\boldsymbol{k}',\gamma'))\Big], \tag{6.2}$$

$$P_{\boldsymbol{k}\gamma\to\boldsymbol{k}'\gamma'} = \frac{2\pi}{\hbar}|\langle\boldsymbol{k}'\gamma'|H_{\text{imp}}(\{\boldsymbol{R}_i\})|\boldsymbol{k}\gamma\rangle|^2\delta(E^{\gamma'}_{\boldsymbol{k}'}-E^{\gamma}_{\boldsymbol{k}}), \tag{6.3}$$

where $P_{\boldsymbol{k}\gamma\to\boldsymbol{k}'\gamma'}$ represents the transition rate of electrons due to impurity scattering within the Born approximation and $H_{\text{imp}}(\{\boldsymbol{R}_i\})$ is the scattering matrix with matrix elements given by $\langle\boldsymbol{k}'\sigma'|H_{\text{imp}}(\{\boldsymbol{R}_i\})|\boldsymbol{k}\sigma\rangle = (u/\mathcal{A})\delta_{\sigma,\sigma'}\sum_i e^{-i(\boldsymbol{k}'-\boldsymbol{k})\cdot\boldsymbol{R}_i}$ $(\sigma,\sigma' =\uparrow,\downarrow)$. Taking the random average over impurity positions $\{\boldsymbol{R}_i\}$ for Eq. (6.2) yields Eq. (5.7):

$$\left.\frac{\partial f(\boldsymbol{k},\gamma)}{\partial t}\right|_{\text{imp}} = \frac{\pi u^2 n_{\text{imp}}}{\hbar\mathcal{A}}\sum_{\boldsymbol{k}',\gamma'}[1+\gamma\gamma'\hat{\boldsymbol{h}}_{\text{eff}}(\varphi)\cdot\hat{\boldsymbol{h}}_{\text{eff}}(\varphi')][f(\boldsymbol{k}',\gamma')-f(\boldsymbol{k},\gamma)]\delta(E^{\gamma'}_{\boldsymbol{k}'}-E^{\gamma}_{\boldsymbol{k}}). \tag{6.4}$$

Similarly, the collision term due to the interfacial exchange coupling is given by the following equation:

$$\left.\frac{\partial f(\boldsymbol{k},\gamma)}{\partial t}\right|_{\text{int}} = \sum_{\boldsymbol{k}'}\sum_{\gamma'}\Big[Q_{\boldsymbol{k}'\gamma'\to\boldsymbol{k}\gamma}f(\boldsymbol{k}',\gamma')(1-f(\boldsymbol{k},\gamma)) - Q_{\boldsymbol{k}\gamma\to\boldsymbol{k}'\gamma'}f(\boldsymbol{k},\gamma)(1-f(\boldsymbol{k}',\gamma'))\Big], \tag{6.5}$$

where $Q_{\boldsymbol{k}\gamma\to\boldsymbol{k}'\gamma'}$ represents the transition rate of electrons due to the interfacial exchange coupling. We calculate the transition rate using the Hamiltonian of the interfacial exchange coupling, Eq. (3.27), with the conditions given in Eqs. (3.28) and (3.29) for clean and dirty interfaces. These conditions are reiterated as follows:

$$H_{\text{int}} = H_{\text{int,d}} + H_{\text{int,s}}, \tag{6.6}$$

$$H_{\text{int,d}} = \sum_{\boldsymbol{q}}\sum_{\bar{\boldsymbol{q}}}(T_{\boldsymbol{q},\bar{\boldsymbol{q}}}S^{x'+}_{\boldsymbol{q}}s^{x'-}_{\bar{\boldsymbol{q}}} + T^{*}_{\boldsymbol{q},\bar{\boldsymbol{q}}}S^{x'-}_{\boldsymbol{q}}s^{x'+}_{\bar{\boldsymbol{q}}}), \tag{6.7}$$

$$H_{\text{int,s}} = \sum_{\bar{\boldsymbol{q}}}\mathcal{T}_{\boldsymbol{0},\bar{\boldsymbol{q}}}S_0 s^{x'}_{\bar{\boldsymbol{q}}}, \tag{6.8}$$

$$\text{dirty interface}: T_{\boldsymbol{q},\bar{\boldsymbol{q}}} = \bar{T}\sin(q_z a),\ \mathcal{T}_{\boldsymbol{0},\bar{\boldsymbol{q}}} = \bar{\mathcal{T}}, \tag{6.9}$$

$$\text{clean interface}: T_{\boldsymbol{q},\bar{\boldsymbol{q}}} = \bar{T}\sin(q_z a)\delta_{\boldsymbol{q}_\parallel,\bar{\boldsymbol{q}}},\ \mathcal{T}_{\boldsymbol{0},\bar{\boldsymbol{q}}} = \bar{\mathcal{T}}\delta_{\bar{\boldsymbol{q}},\boldsymbol{0}}, \tag{6.10}$$

where $H_{\text{int,d}}$ and $H_{\text{int,s}}$ respectively represents dynamic and static contributions. Here, it should be noted that Eqs. (6.9) and (6.10) contain the factor $\sin(q_z a)$, where q_z is the z-component

of $\boldsymbol{q}$ and a represents the lattice constant of the FI. This factor originates from the fixed-end boundary condition imposed on the magnon wave function at the FI-2DEG interface, as shown in Fig. 6.1. In SP discussed in Chap. 4 and the IREE in Chap. 5, we focused on the FMR, which involves only magnons in the zero-wavenumber mode, allowing this factor to be absorbed into the constant $\bar{T}$. However, in the REMR examined in this chapter, we consider magnons with various wavenumber modes and require the explicit inclusion of the $\sin(q_z a)$ factor. The derivation from Eqs. (6.6)-(6.10) is provided in Appendix E. Within the Born approximation, the transition rate can be expressed as follows:

$$\begin{aligned} Q_{\boldsymbol{k},\gamma\to\boldsymbol{k}',\gamma'} = \sum_{\boldsymbol{q},\boldsymbol{q}'}\sum_{N_{\boldsymbol{q}},N'_{\boldsymbol{q}'}} \frac{2\pi}{\hbar}|\langle \boldsymbol{k}'\gamma'|\langle N'_{\boldsymbol{q}'}|H_{\mathrm{int,d}}|\boldsymbol{k}\gamma\rangle|N_{\boldsymbol{q}}\rangle|^2\delta(E^{\gamma'}_{\boldsymbol{k}'}+N'_{\boldsymbol{q}'}\hbar\omega_{\boldsymbol{q}'}-E^{\gamma}_{\boldsymbol{k}}-N_{\boldsymbol{q}}\hbar\omega_{\boldsymbol{q}})\rho(N_{\boldsymbol{q}}) \\ + \frac{2\pi}{\hbar}|\langle \boldsymbol{k}'\gamma'|H_{\mathrm{int,s}}|\boldsymbol{k}\gamma\rangle|^2\delta(E^{\gamma'}_{\boldsymbol{k}'}-E^{\gamma}_{\boldsymbol{k}}). \end{aligned} \tag{6.11}$$

Here, $|N_{\boldsymbol{q}}\rangle$ represents the eigenstate of the magnon number operator, and $\rho(N_{\boldsymbol{q}})$ is given by $\rho(N_{\boldsymbol{q}}) = e^{-\beta\hbar\omega_{\boldsymbol{q}}N_{\boldsymbol{q}}}/\sum_{N_{\boldsymbol{q}}=0}^{\infty} e^{-\beta\hbar\omega_{\boldsymbol{q}}N_{\boldsymbol{q}}}$.

With the solution $f(\boldsymbol{k},\gamma)$ of the Boltzmann equation in Eq. (6.1), the spin density and charge current density in the 2DEG induced by the REMR can be expressed similarly to Eqs. (5.28) and (5.29) as follows:

$$\boldsymbol{s} = \frac{\hbar}{2\mathcal{A}}\sum_{\boldsymbol{k},\gamma}\langle \boldsymbol{k}\gamma|\hat{\boldsymbol{\sigma}}|\boldsymbol{k}\gamma\rangle f(\boldsymbol{k},\gamma), \tag{6.12}$$

$$\boldsymbol{j} = \frac{e}{\mathcal{A}}\sum_{\boldsymbol{k},\gamma}\boldsymbol{v}(\boldsymbol{k},\gamma)f(\boldsymbol{k},\gamma). \tag{6.13}$$

Here, $\boldsymbol{v}$ represents the electron velocity defined in Eq. (5.30):

$$\boldsymbol{v}(\boldsymbol{k},\gamma) = \frac{1}{\hbar}\frac{\partial E^{\gamma}_{\boldsymbol{k}}}{\partial \boldsymbol{k}} = \frac{\hbar\boldsymbol{k}}{m^*} + \frac{\gamma}{\hbar}\frac{\partial h_{\mathrm{eff}}(\boldsymbol{k})}{\partial \boldsymbol{k}}. \tag{6.14}$$

In the following calculations, the summation over $\boldsymbol{k}$ will be replaced by an integral over $\boldsymbol{k}$ using Eq. (5.8):

$$\frac{1}{\mathcal{A}}\sum_{\boldsymbol{k}}(\cdots) = \frac{1}{2\pi}\int_0^{\infty} dk\,|\boldsymbol{k}|\int_0^{2\pi}\frac{d\varphi}{2\pi}(\cdots). \tag{6.15}$$

6.1.2 Rashba-Edelstein effect (REE)

In this section, we present the formulation of the REE in the 2DEG under a DC electric field $\boldsymbol{E} = (E_x, 0)$. Since the REE arises within the 2DEG alone, the Boltzmann equation for REE excludes the collision term due to the interfacial exchange coupling, which is the second term

on the right-hand side of Eq. (6.1). First, the distribution function is expressed as follows:

$$f(\boldsymbol{k},\gamma) = f_0(E^{\gamma}_{\boldsymbol{k}}) + f_1(\boldsymbol{k},\gamma), \tag{6.16}$$

$$f_1(\boldsymbol{k},\gamma) = -\frac{\partial f_0(E^{\gamma}_{\boldsymbol{k}})}{\partial E^{\gamma}_{\boldsymbol{k}}}\delta\mu_1(\boldsymbol{k},\gamma), \tag{6.17}$$

Here, $f_0(\epsilon) = (\exp[\beta(\epsilon-\mu)]+1)^{-1}$ is the Fermi distribution function, $f_1(\boldsymbol{k},\gamma)$ represents the modulation of the non-equilibrium distribution function due to the DC electric field, and $\delta\mu_1(\boldsymbol{k},\gamma)$ denotes the shift in chemical potential. Note that $\delta\mu_1(\boldsymbol{k},\gamma)$ is proportional to E_x within the linear response to the DC electric field. By substituting Eqs. (6.16) and (6.17) into Eq. (6.1) with the collision term due to the interfacial exchange coupling omitted, and retaining terms up to linear order in E_x, we obtain the following Boltzmann equation for the REE:

$$\frac{eE_x}{\hbar}\frac{\partial f_0(E^{\gamma}_{\boldsymbol{k}})}{\partial k_x} = \frac{\partial f_1(\boldsymbol{k},\gamma)}{\partial t}\Big|_{\mathrm{imp}}. \tag{6.18}$$

By substituting the nonmagnetic impurity collision term from Eq. (6.4) into Eq. (6.18), we obtain the following integral equation for $f_1(\boldsymbol{k},\gamma)$:

$$\begin{aligned} f_1(\boldsymbol{k},\gamma) &= \mathcal{L}(\boldsymbol{k},\gamma) \\ &\quad + \frac{\hbar^2}{2m^*}\int_0^{2\pi}\frac{d\varphi'}{2\pi}\sum_{\gamma'}\int_0^{\infty} dk'\,|\boldsymbol{k}'|[1+\gamma\gamma'\hat{\boldsymbol{h}}_{\mathrm{eff}}(\varphi)\cdot\hat{\boldsymbol{h}}_{\mathrm{eff}}(\varphi')]f_1(\boldsymbol{k}',\gamma')\delta(E^{\gamma'}_{\boldsymbol{k}'}-E^{\gamma}_{\boldsymbol{k}}). \end{aligned} \tag{6.19}$$

Here, $\mathcal{L}(\boldsymbol{k},\gamma)$ is defined as follows:

$$\begin{aligned} \mathcal{L}(\boldsymbol{k},\gamma) &\equiv -\frac{\hbar eE_x}{\Gamma}\cdot\frac{\partial f_0(E^{\gamma}_{\boldsymbol{k}})}{\partial E^{\gamma}_{\boldsymbol{k}}} \\ &\quad\times\left(\frac{\hbar|\boldsymbol{k}|}{m^*}\cos\varphi + \frac{\gamma}{\hbar\sqrt{\alpha^2+\beta^2+2\alpha\beta\sin 2\varphi}}[(\alpha^2+\beta^2)\cos\varphi + 2\alpha\beta\sin\varphi]\right). \end{aligned} \tag{6.20}$$

Then, by iteratively substituting $f_1(\boldsymbol{k},\gamma)$ into the right-hand side of Eq. (6.19), we obtain the following expression as the solution to Eq. (6.19):

$$\begin{aligned} f_1(\boldsymbol{k},\gamma) &= \mathcal{L}(\boldsymbol{k},\gamma) + \frac{\hbar^2}{2m^*}\int_0^{2\pi}\frac{d\varphi''}{2\pi}\sum_{\gamma''}\gamma\gamma''\int_0^{\infty}dk''\,|\boldsymbol{k}''|\,\delta(E^{\gamma''}_{\boldsymbol{k}''}-E^{\gamma}_{\boldsymbol{k}}) \\ &\quad\times\hat{\boldsymbol{h}}^T_{\mathrm{eff}}(\varphi)\left(\hat{1}-\int_0^{2\pi}\frac{d\varphi'}{2\pi}\hat{\boldsymbol{h}}_{\mathrm{eff}}(\varphi')\cdot\hat{\boldsymbol{h}}^T_{\mathrm{eff}}(\varphi')\right)^{-1}\hat{\boldsymbol{h}}_{\mathrm{eff}}(\varphi'')\mathcal{L}(\boldsymbol{k}'',\gamma''). \end{aligned} \tag{6.21}$$

The second term in Eq. (6.21) can be calculated as follows:

$$\begin{aligned}
&\frac{\hbar^2}{2m^*}\int_0^{2\pi}\frac{d\varphi''}{2\pi}\sum_{\gamma''}\gamma\gamma''\int_0^{\infty}dk''\,|\boldsymbol{k}''|\,\delta(E^{\gamma''}_{k''}-E^{\gamma}_{\boldsymbol{k}})\\
&\qquad\times\hat{\boldsymbol{h}}^T_{\rm eff}(\varphi)\left(\hat{1}-\int_0^{2\pi}\frac{d\varphi'}{2\pi}\hat{\boldsymbol{h}}_{\rm eff}(\varphi')\cdot\hat{\boldsymbol{h}}^T_{\rm eff}(\varphi')\right)^{-1}\hat{\boldsymbol{h}}_{\rm eff}(\varphi'')\mathcal{L}(\boldsymbol{k}'',\gamma'')\\
&=\frac{eE_x}{\Gamma}\cdot\frac{\partial f_0(E^{\gamma}_{\boldsymbol{k}})}{\partial E^{\gamma}_{\boldsymbol{k}}}\cdot\frac{\gamma}{\sqrt{\alpha^2+\beta^2+2\alpha\beta\sin 2\varphi}}[(\alpha^2+\beta^2)\cos\varphi+2\alpha\beta\sin\varphi].
\end{aligned}\tag{6.22}$$

Here, we used the following approximation, neglecting second-order terms of the Rashba and Dresselhaus SOCs:

$$\delta(E^{\gamma'}_{k'}-E^{\gamma}_{\boldsymbol{k}})\simeq\frac{m^*}{\hbar^2\sqrt{2m^*E^{\gamma}_{\boldsymbol{k}}/\hbar^2}}\delta(k'-k'(\boldsymbol{k},\gamma,\varphi',\gamma')),\tag{6.23}$$

$$k'(\boldsymbol{k},\gamma,\varphi',\gamma')\simeq\sqrt{2m^*E^{\gamma}_{\boldsymbol{k}}/\hbar^2}-\frac{m^*\gamma'\sqrt{\alpha^2+\beta^2+2\alpha\beta\sin 2\varphi'}}{\hbar^2}.\tag{6.24}$$

By substituting Eq. (6.22) into Eq. (6.21), we obtain the following solution:

$$f_1(\boldsymbol{k},\gamma)=-\frac{\partial f_0(E^{\gamma}_{\boldsymbol{k}})}{\partial E^{\gamma}_{\boldsymbol{k}}}\frac{\hbar^2eE_x|\boldsymbol{k}|}{\Gamma m^*}\cos\varphi.\tag{6.25}$$

Note that this solution satisfies the charge conservation condition $\sum_{\boldsymbol{k},\gamma}f_1(\boldsymbol{k},\gamma)=0$. By comparing Eq. (6.25) with Eq. (6.17), it can be seen that the shift in the chemical potential is given by:

$$\delta\mu_1(\boldsymbol{k},\gamma)=\frac{\hbar^2eE_x|\boldsymbol{k}|}{\Gamma m^*}\cos\varphi.\tag{6.26}$$

It should be noted that this result is consistent with Eq. (A.11) in Appendix A, which was derived in Ref. [32].

6.1.3 Dirty interface

In this section, we consider the REMR at the dirty FI-2DEG interface. In this case, the interfacial interaction Hamiltonian $H_{\rm int}$ is given by Eqs. (6.8) and (6.9). First, the non-equilibrium distribution function of the 2DEG electrons is written in the following form:

$$f(\boldsymbol{k},\gamma)=f_0(E^{\gamma}_{\boldsymbol{k}})+f_1(\boldsymbol{k},\gamma)+f_{\rm D}(\boldsymbol{k},\gamma),\tag{6.27}$$

$$f_{\rm D}(\boldsymbol{k},\gamma)=-\frac{\partial f_0(E^{\gamma}_{\boldsymbol{k}})}{\partial E^{\gamma}_{\boldsymbol{k}}}\delta\mu_{\rm D}(\boldsymbol{k},\gamma),\tag{6.28}$$

Here, $f_1(\boldsymbol{k},\gamma)$ is given by Eq. (6.25), and $f_{\mathrm{D}}(\boldsymbol{k},\gamma)$ represents the modulation of the distribution function due to the interfacial exchange coupling. Considering second-order perturbation theory for the interfacial interaction Hamiltonian H_{int}, the collision term due to interfacial scattering is proportional to $\max(|\bar{T}|^2,|\bar{\mathcal{T}}|^2)$ through the transition rates. Since the distribution function contributing to the REMR is proportional to $\max(|\bar{T}|^2E_x,|\bar{\mathcal{T}}|^2E_x)$, the shift in chemical potential $\delta\mu_{\mathrm{D}}(\boldsymbol{k},\gamma)$ is evaluated at this order. Note that $|\delta\mu_{\mathrm{D}}(\boldsymbol{k},\gamma)| \ll |\delta\mu_1(\boldsymbol{k},\gamma)|$. By substituting Eqs. (6.27) and (6.28) into the Boltzmann equation in Eq. (6.1) and comparing terms of order $\max(|\bar{T}|^2E_x,|\bar{\mathcal{T}}|^2E_x)$ on both sides, we obtain the following equation:

$$0 = \left.\frac{\partial f_{\mathrm{D}}(\boldsymbol{k},\gamma)}{\partial t}\right|_{\mathrm{imp}} + \left.\frac{\partial f_1(\boldsymbol{k},\gamma)}{\partial t}\right|_{\mathrm{int}}. \tag{6.29}$$

Then, by substituting the expressions for the collision terms in Eqs. (6.4) and (6.5) into Eq. (6.29) and carrying out the calculations, we obtain the full solution of the Boltzmann equation as follows:

$$\delta\mu_{\mathrm{D}}(\varphi,\gamma) = \gamma\frac{2\pi D(\epsilon_{\mathrm{F}})S_0eE_x\mathcal{A}}{\Gamma^2}I(T)g(\theta,\varphi), \tag{6.30}$$

$$I(T) = -4|\bar{T}|^2\sum_{\boldsymbol{q}}\langle N_{\boldsymbol{q}}\rangle\sin^2(q_za) + S_0|\bar{\mathcal{T}}|^2, \tag{6.31}$$

$$\begin{aligned} g(\theta,\varphi) = {} & \{[\alpha+\beta\eta]\sin(\varphi-\theta) + [\beta+\alpha\eta]\cos(\varphi+\theta)\} \\ & \times \frac{\alpha\sin\theta-\beta\cos\theta}{(1-\eta^2)\sqrt{\alpha^2+\beta^2+2\alpha\beta\sin 2\varphi}}, \end{aligned} \tag{6.32}$$

where $I(T)$ is a temperature-dependent factor and η is a dimensionless factor defined as follows:

$$\eta = \begin{cases} \beta/\alpha & (\alpha^2 \geq \beta^2) \\ \alpha/\beta & (\beta^2 \geq \alpha^2) \end{cases}. \tag{5.25}$$

Here, terms independent of θ have been omitted as they do not contribute to the REMR. For a detailed derivation, refer to Appendix F.1.

From Eqs. (6.12) and (6.13), the modulation of spin density and charge current density in the 2DEG due to REMR can be expressed using $f_{\mathrm{D}}(\boldsymbol{k},\gamma)$ as follows:

$$\Delta\boldsymbol{s}_{\mathrm{D}}(\theta) = \frac{\hbar}{4\pi}\sum_{\gamma}\int dk\,|\boldsymbol{k}|\int\frac{d\varphi}{2\pi}\langle\boldsymbol{k}\gamma|\hat{\boldsymbol{\sigma}}|\boldsymbol{k}\gamma\rangle f_{\mathrm{D}}(\boldsymbol{k},\gamma), \tag{6.33}$$

$$\Delta\boldsymbol{j}_{\mathrm{D}}(\theta) = \frac{e}{2\pi}\sum_{\gamma}\int_0^{\infty}dk\,|\boldsymbol{k}|\int_0^{2\pi}\frac{d\varphi}{2\pi}\boldsymbol{v}(\boldsymbol{k},\gamma)f_{\mathrm{D}}(\boldsymbol{k},\gamma). \tag{6.34}$$

By substituting the solution of the Boltzmann equation given in Eqs. (6.30)–(6.32) into Eqs. (6.33)

and (6.34), we obtain the following expressions:

$$\Delta \boldsymbol{s}_{\mathrm{D}}(\theta) = \frac{k_{\mathrm{F}} D(\epsilon_{\mathrm{F}}) S_0 e E_x \mathcal{A} I(T)}{2 v_{\mathrm{F}} \Gamma^2} \frac{\alpha \sin\theta - \beta \cos\theta}{1-\eta^2} \begin{pmatrix} \cos\theta & \sin\theta \\ \sin\theta & \cos\theta \end{pmatrix} \begin{pmatrix} 1+\eta^2 \\ -2\eta \end{pmatrix}, \tag{6.35}$$

$$\Delta \boldsymbol{j}_{\mathrm{D}}(\theta) = \frac{e^2 k_{\mathrm{F}} D(\epsilon_{\mathrm{F}}) S_0 E_x \mathcal{A} I(T)}{\hbar^2 v_{\mathrm{F}} \Gamma^2} \begin{pmatrix} (\alpha \sin\theta - \beta \cos\theta)^2 \\ -(\alpha^2+\beta^2) \cos\theta \sin\theta \end{pmatrix}. \tag{6.36}$$

Here, $v_{\mathrm{F}} = \hbar k_{\mathrm{F}}/m^*$ represents the Fermi velocity in the absence of the Rashba and Dresselhaus SOCs. For detailed calculations, refer to Appendix F.1.

6.1.4 Clean interface

In this section, we consider the REMR at a clean interface using H_{int} as given in Eqs. (6.8) and (6.10). The non-equilibrium distribution function of the 2DEG electrons is expressed in the following form:

$$f(\boldsymbol{k},\gamma) \equiv f_0(\boldsymbol{k},\gamma) + f_1(\boldsymbol{k},\gamma) + f_{\mathrm{C}}(\boldsymbol{k},\gamma), \tag{6.37}$$

$$f_{\mathrm{C}}(\boldsymbol{k},\gamma) = -\frac{\partial f_0(E_{\boldsymbol{k}}^{\gamma})}{\partial E_{\boldsymbol{k}}^{\gamma}} \delta\mu_{\mathrm{C}}(\boldsymbol{k},\gamma). \tag{6.38}$$

These expressions are identical to Eqs. (6.27) and (6.28), except that the subscript 'C' is used to denote the clean interface. Note that $\delta\mu_{\mathrm{C}}(\boldsymbol{k},\gamma)$ is of the order $\max(E_x|\bar{T}|^2, E_x|\bar{\mathcal{T}}|^2)$ and that $|\delta\mu_{\mathrm{C}}(\boldsymbol{k},\gamma)| \ll |\delta\mu_1(\boldsymbol{k},\gamma)|$. By substituting Eqs. (6.37) and (6.38) into the Boltzmann equation in Eq. (6.1) and comparing terms of the order $\max(|\bar{T}|^2 E_x, |\bar{\mathcal{T}}|^2 E_x)$ on both sides, we obtain the following equation:

$$0 = \frac{\partial f_{\mathrm{C}}(\boldsymbol{k},\gamma)}{\partial t}\Big|_{\mathrm{imp}} + \frac{\partial f_1(\boldsymbol{k},\gamma)}{\partial t}\Big|_{\mathrm{int}}. \tag{6.39}$$

Then, by using the expressions for the collision terms in Eqs. (6.4) and (6.5) and carrying out the calculations, we obtain the following analytical expressions for the spin density and charge current density:

$$\Delta \boldsymbol{s}_{\mathrm{C}}(\theta) = \frac{2 k_{\mathrm{F}} D(\epsilon_{\mathrm{F}}) S_0 |\bar{T}|^2 \mathcal{A} e E_x}{v_{\mathrm{F}} \Gamma^2} \int_0^{2\pi} \frac{d\varphi}{2\pi} \hat{\boldsymbol{h}}_{\mathrm{eff}}(\varphi) \mathcal{J}(\varphi), \tag{6.40}$$

$$\Delta \boldsymbol{j}_{\mathrm{C}}(\theta) = \frac{4 e^2 m^* D(\epsilon_{\mathrm{F}}) \mathcal{A} S_0 |\bar{T}|^2 E_x}{\hbar^3 \Gamma^2} \int_0^{2\pi} \frac{d\varphi}{2\pi} \frac{1}{\kappa(\varphi)} \begin{pmatrix} (\alpha^2+\beta^2)\cos\varphi + 2\alpha\beta \sin 3\varphi \\ (\alpha^2+\beta^2)\sin\varphi - 2\alpha\beta \cos 3\varphi \end{pmatrix} \mathcal{J}(\varphi). \tag{6.41}$$

Here, $\kappa(\varphi) \equiv \sqrt{\alpha^2+\beta^2+2\alpha\beta\sin 2\varphi}$, and $\mathcal{J}(\varphi)$ is given by the following expression:

$$\mathcal{J}(\varphi) = B(\varphi,\theta) + \int_0^{2\pi} \frac{d\varphi''}{2\pi} B(\varphi'',\theta)\hat{\boldsymbol{h}}_{\rm eff}^T(\varphi)\hat{M}\hat{\boldsymbol{h}}_{\rm eff}(\varphi''), \tag{6.42}$$

$$B(\varphi,\theta) = \mathcal{I}_1(T)\kappa(\varphi)\cos\varphi[\hat{\boldsymbol{h}}_{\rm eff}(\varphi)\cdot\hat{\boldsymbol{m}}(\theta)]^2 - 2\mathcal{I}_2(T)\sin\varphi[\hat{\boldsymbol{h}}_{\rm eff}(\varphi)\cdot\hat{\boldsymbol{m}}(\theta)][\boldsymbol{g}(\varphi)\cdot\hat{\boldsymbol{m}}(\theta)], \tag{6.43}$$

$$\hat{M} = \frac{2}{1-\eta^2}\begin{pmatrix} 1 & -\eta \\ -\eta & 1 \end{pmatrix}, \tag{6.44}$$

$$\boldsymbol{g}(\varphi) = \begin{pmatrix} \alpha\cos\varphi - \beta\sin\varphi \\ \alpha\sin\varphi - \beta\cos\varphi \end{pmatrix}, \tag{6.45}$$

$$\mathcal{I}_1(T) = \sum_{q_z>0}\int_0^{2\pi}\frac{d\varphi}{2\pi}N(\varphi,q_z)\sin^2(q_z a)\cos\varphi[1-2\cos\varphi], \tag{6.46}$$

$$\mathcal{I}_2(T) = \sum_{q_z>0}\int_0^{2\pi}\frac{d\varphi}{2\pi}N(\varphi,q_z)\sin^2(q_z a)\sin^2\varphi, \tag{6.47}$$

$$N(\varphi,q_z) = \frac{1}{e^{\beta\hbar\omega(\varphi,q_z)}-1}, \tag{6.48}$$

$$\hbar\omega(\varphi,q_z) = \hbar|\gamma_{\rm g}|h_{\rm dc} + 4\mathcal{D}k_{\rm F}^2\sin^2\frac{\varphi}{2} + \mathcal{D}q_z^2. \tag{6.49}$$

Note that terms independent of θ have been omitted, as they do not contribute to the REMR. For detailed calculations, see Appendix F.2.

6.2 Results

In this section, we present the results of the spin density and charge current density induced in the 2DEG by the REMR. First, the effect of interface randomness is discussed in Sec. 6.2.1. Next, the results for the dirty interface and clean interface are shown in Secs. 6.2.2 and 6.2.3, respectively. Finally, Sec. 6.2.4 elucidates the α/β dependence of the maximum values of the spin density and charge current density.

6.2.1 The effect of interface randomness

In this section, we discuss the effect of interface randomness through comparison of the results for dirty and clean interfaces. The discussion begins with examination of the coefficient appearing in the dirty interface results as defined in Eq. (6.31):

$$I(T) = -4|\bar{T}|^2\sum_{\boldsymbol{q}}\langle N_{\boldsymbol{q}}\rangle + S_0|\bar{\mathcal{T}}|^2, \tag{6.31}$$

The first term of $I(T)$, which is proportional to $|\bar{T}|^2$, originates from the first term of the interface interaction Hamiltonian in Eq. (3.27), representing the effect of magnon absorption and emission. In contrast, the second term, proportional to $|\bar{\mathcal{T}}|^2$, stems from the second term of the interface interaction Hamiltonian, describing the effect of the exchange bias at the interface. The magnitude of $|\bar{\mathcal{T}}|^2$ is larger than that of $|\bar{T}|^2$ by an order of the number of unit cells in the FI, $N_{\rm FI}$, making the second term in Eq. (6.31) dominant (see Appendix E for a detail). This indicates that for a dirty interface the REMR is primarily induced by the exchange bias at the interface. Therefore, in the following, we approximate $I(T)$ as:

$$I(T) \simeq S_0|\bar{\mathcal{T}}|^2. \tag{6.50}$$

Under this approximation, note that the REMR in the dirty interface is independent of temperature.

Next, we examine the results for the clean interface. In the analytical results for the clean interface, given by Eqs. (6.41)-(6.45), the coupling constant $\bar{\mathcal{T}}$, which represents the effect of exchange bias, does not appear. At clean interfaces, the wavevector conservation of 2DEG electrons holds, meaning that the wavevectors of 2DEG electrons remain unchanged before and after scattering caused by interface disorder. For a 2DEG electron to transition to another state, the electron must exchange magnons with the FI, which causes it to scatter into a state shifted by the magnon wavevector. Therefore, the transitions of 2DEG electrons induced by the exchange bias effect, represented by the last term of Eq. (3.27) in which magnons are absent, do not occur at clean interfaces. Instead, only the magnon absorption and emission effects, described by the first term of Eq. (3.27), contribute to the REMR at clean interfaces. Consequently, the REMR in the clean interface is temperature-dependent. These differences between the dirty and clean interfaces constitute one of the main findings of this chapter.

6.2.2 Dirty interface

In this section, we present the results for the REMR in the dirty interface. We adopt the following normalization constants for the spin density and charge current density:

$$s_{x,\rm D} = -\frac{k_{\rm F}D(\epsilon_{\rm F})S_0^2 eE_x\mathcal{A}|\bar{\mathcal{T}}|^2 x}{2v_{\rm F}\Gamma^2} \quad (x=\alpha,\beta), \tag{6.51}$$

$$j_{x,\rm D},= \frac{e^2k_{\rm F}D(\epsilon_{\rm F})S_0^2E_x\mathcal{A}|\bar{\mathcal{T}}|^2x^2}{\hbar^2v_{\rm F}\Gamma^2} \quad (x=\alpha,\beta). \tag{6.52}$$

Note that these constants are positive when $E_x > 0$. The normalization constant for the charge current density, $j_{x,\rm D}$, is proportional to the square of the Rashba or Dresselhaus SOCs, α^2 or β^2, respectively. This is consistent with the REMR arising from the combination of the REE and IREE, both of which are induced by SOC. In the following section, we provide plots for the spin

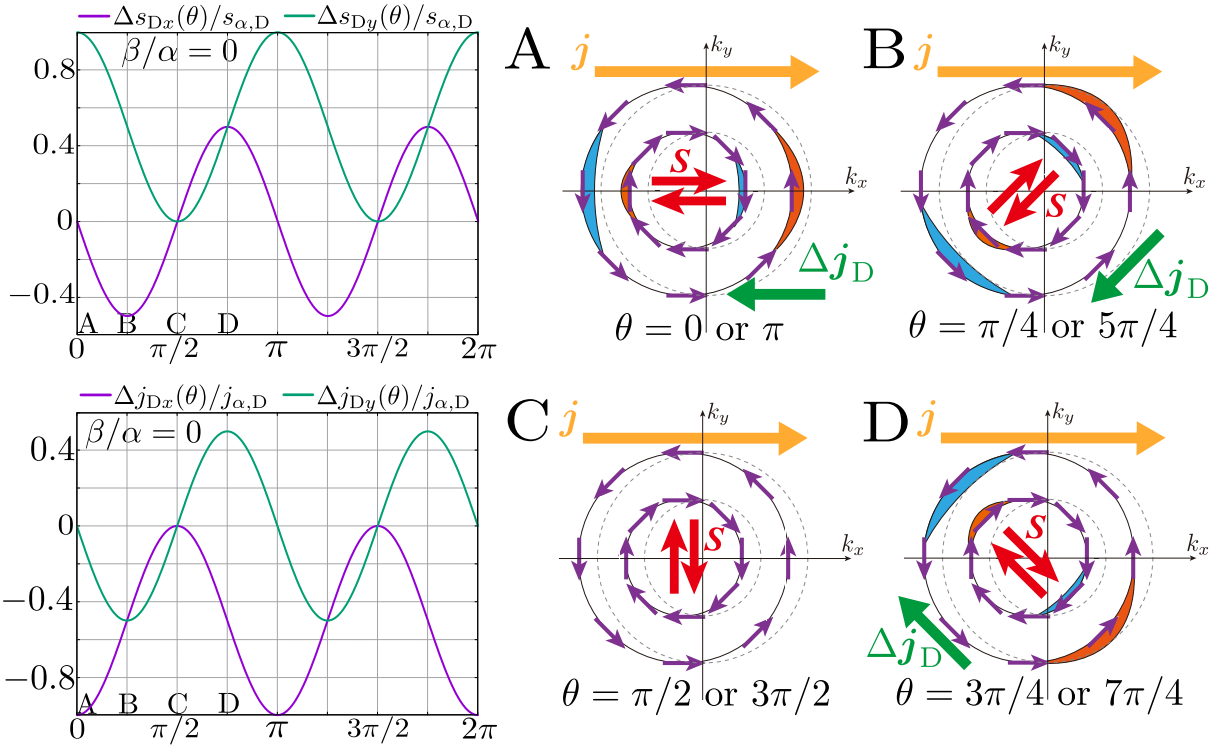

Figure 6.2: Left two panels: For a dirty interface with only the Rashba SOC present ($\beta/\alpha = 0$), these plots display the modulation of spin density and charge current density induced in the 2DEG by the REMR as functions of the localized spin orientation θ in the FI. To simplify interpretation, the modulation is shown relative to reference points at $\theta = \pi/2$ and $3\pi/2$. Right four panels: Schematic representations of the modulation of the 2DEG conduction electron distribution function near the Fermi surface for (A) $\theta = 0, \pi$, (B) $\theta = \pi/4, 5\pi/4$, (C) $\theta = \pi/2, 3\pi/2$, and (D) $\theta = 3\pi/4, 7\pi/4$. Orange (blue) regions indicate areas where the distribution function of 2DEG conduction electrons has increased (decreased) relative to the reference points at $\theta = \pi/2$ and $3\pi/2$. The red and green arrows represent the orientation of the localized spins in the FI and the direction of the charge current density modulation induced in the 2DEG by the REMR, respectively. Adapted from Ref. [50].

density, $\Delta \boldsymbol{s}_D/s_{\alpha,D}$ (or $\Delta \boldsymbol{s}_D/s_{\beta,D}$), and the charge current density, $\Delta \boldsymbol{j}_D/j_{\alpha,D}$ (or $\Delta \boldsymbol{j}_D/j_{\beta,D}$), each normalized by the constants defined in Eqs. (6.51) and (6.52).

Rashba SOC ($\beta/\alpha = 0$)

First, we examine the case of the 2DEG with only the Rashba SOC ($\beta/\alpha = 0$). In the left two panels of Fig. 6.2, we plot the modulation of spin density and charge current density induced in the 2DEG by the REMR as a function of the localized spin orientation θ in the FI. The REMR measurements observe the relative change in these quantities as θ is varied. Thus, the spin density $\Delta \boldsymbol{s}_D(\pi/2)$ and charge current density $\Delta \boldsymbol{j}_D(\pi/2)$ at $\theta = \pi/2$ are set to zero, and the deviations from these reference values are plotted. Both the spin density and charge current density rotate with changing θ, forming periodic functions in θ with a period of π.

These results can be intuitively understood as follows. The right four panels of Fig. 6.2 depict the spin-split Fermi surfaces and modulation of the distribution function for (A) $\theta = 0, \pi$, (B) $\theta = \pi/4, 5\pi/4$, (C) $\theta = \pi/2, 3\pi/2$, and (D) $\theta = 3\pi/4, 7\pi/4$. Since we focus on the relative modulation from the reference points, regions where the distribution function increases (decreases) relative to the baseline case of (C) $\theta = \pi/2, 3\pi/2$ are shown in orange (blue). In these panels, the dashed lines represent the Fermi surface in equilibrium without an applied DC electric field; when a DC electric field is applied in the $+x$ direction, the Fermi surface shifts toward the $-x$ direction, resulting in spin accumulation polarized in the $-y$ direction due to the REE. As discussed in Sec. 6.2.1, the effect of exchange bias at the interface is the dominant contribution to the REMR in the dirty interface. This exchange bias acts as an effective static Zeeman field on conduction electrons near the Fermi surface. Thus, due to the transverse magnetic field effect of this effective Zeeman field, spins of 2DEG conduction electrons polarized perpendicular to the localized spin $\boldsymbol{S}$ in the FI undergo significant relaxation.

As an example, we examine the case of $\theta = 0, \pi$, depicted in diagram A of Fig. 6.2. In this case, the spins of 2DEG conduction electrons polarized in the $\pm y$ direction, which is perpendicular to $\boldsymbol{S}$, undergo spin-flip relaxation due to the exchange bias. Consequently, the distribution function of electrons with spins polarized in the $-y$ ($+y$) direction decreases (increases). Note here that this change in the distribution function acts to reduce the spin accumulation induced by the REE, which is generated by the external DC electric field. In diagram A, the relative change in the distribution function at (A) $\theta = 0, \pi$ compared to (C) $\theta = \pi/2, 3\pi/2$ is shown in the orange and blue regions. This change in the distribution function induces the IREE, resulting in a modulation $\Delta \boldsymbol{j}_{\mathrm{D}}$ of the charge current in the $-x$ direction.

A similar explanation applies to cases (B) $\theta = \pi/4, 5\pi/4$ and (D) $\theta = 3\pi/4, 7\pi/4$. For example, in case (B) with $\theta = \pi/4, 5\pi/4$, the spins of 2DEG conduction electrons polarized in the $3\pi/4$ and $7\pi/4$ directions, which are perpendicular to $\boldsymbol{S}$, undergo spin-flip relaxation due to the exchange bias. Consequently, the distribution function of electrons with spin polarization in the $7\pi/4$ ($3\pi/4$) direction decreases (increases), resulting in a modulation $\Delta \boldsymbol{j}_{\mathrm{D}}$ of the charge current flowing in the $5\pi/4$ direction due to the IREE.

Case of $\alpha/\beta = 1.1$

Next, we consider the case of the Rashba and Dresselhaus SOCs coexisting with comparable magnitudes, $\alpha/\beta = 1.1$. The left two panels of Fig. 6.3 plot the relative modulation of spin density and charge current density measured from the reference point $\theta = 3\pi/4$ for $\alpha/\beta = 1.1$. Compared to the case of $\theta = 3\pi/4$, it is observed that for any other θ, there is a modulation $\Delta \boldsymbol{s}_{\mathrm{D}}$ of the spin density in the $3\pi/4$ direction and a modulation of the charge current in the $5\pi/4$ direction. Furthermore, at $\theta = \pi/4$ and $5\pi/4$, these relative modulations reach their maximum values.

These results can be intuitively understood as follows. The right two panels of Fig. 6.3

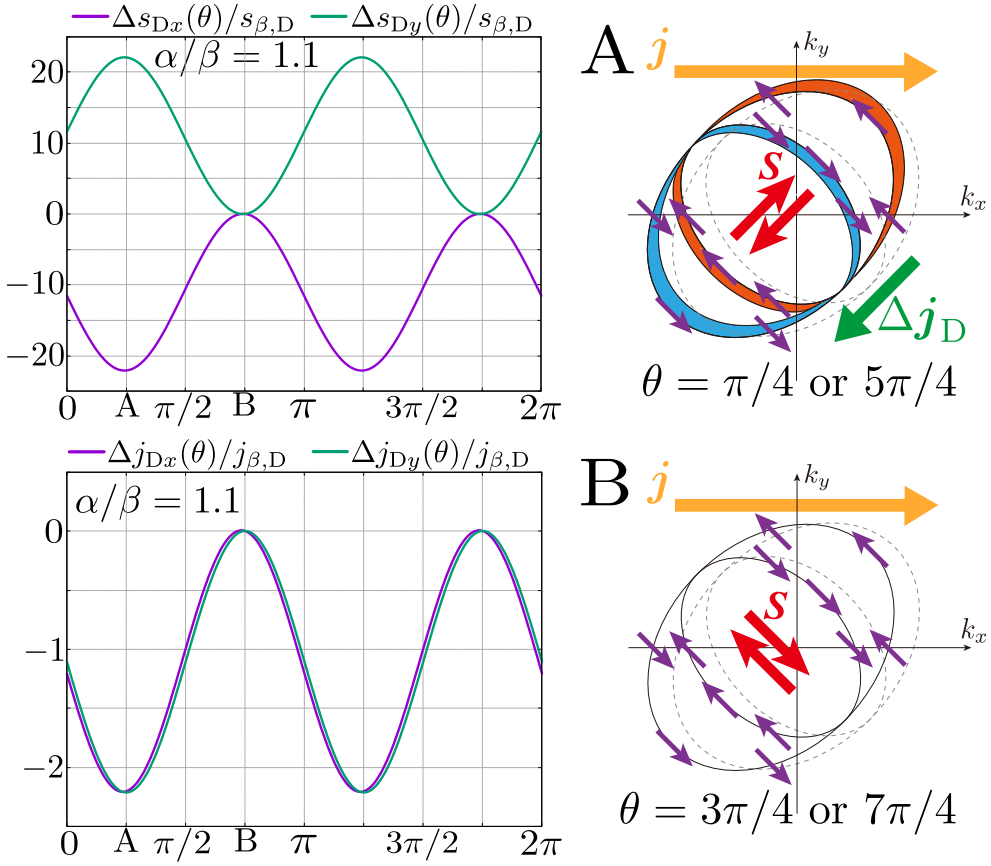

Figure 6.3: Left two panels: For a dirty interface with $\alpha/\beta = 1.1$, these plots show the modulation of spin density and charge current density induced by the REMR as functions of the localized spin orientation θ in the FI, using reference points at $\theta = 3\pi/4$ and $7\pi/4$. Right two panels: Schematic representations of the modulation of the 2DEG conduction electron distribution function for (A) $\theta = \pi/4, 5\pi/4$ and (B) $\theta = 3\pi/4, 7\pi/4$. Orange (blue) regions indicate areas where the distribution function has increased (decreased) relative to the reference points at $\theta = 3\pi/4$ and $7\pi/4$. Adapted from Ref. [50].

schematically show the modulation of the distribution function for (A) $\theta = \pi/4, 5\pi/4$ and (B) $\theta = 3\pi/4, 7\pi/4$. Note that (B) $\theta = 3\pi/4, 7\pi/4$ serves as the reference points, with the modulation set to zero there. First, in both (A) and (B), the Fermi surface shifts in the $-x$ direction due to an external DC electric field applied in the $+x$ direction, resulting in spin accumulation polarized in the $7\pi/4$ direction via the REE. Next, in case (A) with $\theta = \pi/4, 5\pi/4$, the spins of 2DEG electrons polarized in the $3\pi/4$ and $7\pi/4$ directions, which are perpendicular to the localized spin $\boldsymbol{S}$ in the FI, undergo relaxation due to the effective Zeeman field. The relative change in the distribution function for (A) $\theta = \pi/4, 5\pi/4$ compared to (B) $\theta = 3\pi/4, 7\pi/4$ is shown in diagram A of Fig. 6.3 by the orange and blue regions. This change in the distribution function reduces the spin accumulation generated by the REE due to the external DC electric field. As a result of this change, the IREE is induced, leading to a modulation $\Delta \boldsymbol{j}_{\mathrm{D}}$ of the charge current

density in the $5\pi/4$ direction.

6.2.3 Clean interface

In this section, we present the results of the spin density and charge current density induced in the 2DEG by the REMR at the clean interface. Here, we nondimensionalize these physical quantities using the following normalization constants:

$$s_{x,\mathrm{C}} = -\frac{2k_{\mathrm{F}}^2 LD(\epsilon_{\mathrm{F}})S_0|\bar{T}|^2\mathcal{A}eE_x x}{\pi v_{\mathrm{F}}\Gamma^2} \quad (x=\alpha,\beta), \tag{6.53}$$

$$j_{x,\mathrm{C}} = \frac{4k_{\mathrm{F}}Le^2m^*D(\epsilon_{\mathrm{F}})\mathcal{A}S_0|\bar{T}|^2E_x x^2}{\pi\hbar^3\Gamma^2} \quad (x=\alpha,\beta). \tag{6.54}$$

Here, L represents the thickness of the FI. Note that these normalization constants are positive when $E_x > 0$, and, as in the case of the dirty interface, $j_{x,\mathrm{C}}$ is proportional to α^2 or β^2.

Rashba SOC ($\beta/\alpha = 0$)

First, we examine the case in which the 2DEG has only Rashba SOC ($\beta/\alpha = 0$). The left two panels of Fig. 6.4 display the modulation of spin density and charge current density induced in the 2DEG by the REMR as a function of the orientation θ of localized spins in the FI. Here, the reference point is set at $\theta = 0$, with $\Delta\boldsymbol{s}_{\mathrm{C}}(\theta=0)$ and $\Delta\boldsymbol{j}_{\mathrm{C}}(\theta=0)$ taken as zero. These plots show that, similar to the dirty interface case, both spin density and charge current density exhibit a periodic dependence on θ with a period of π, and their orientations rotate with changes in θ. However, a significant difference from the dirty interface case is the reversal of the REMR sign. Specifically, when comparing Fig. 6.4 with Fig. 6.2, it is evident that the clean interface yields maximum (minimum) values for the spin density and charge current density at the θ values where they reach minimum (maximum) values at the dirty interface.

This qualitative difference between the dirty and clean interfaces can be attributed to differences in the interfacial spin-flipping scattering processes. For the dirty interface, the effective Zeeman field from exchange bias predominantly contributed to the spin-flipping of conduction electrons. In contrast, at the clean interface, the spin-flipping of conduction electrons is driven by the dynamic process of magnon absorption and emission. Since magnons carry spins in the $-\boldsymbol{S}$ direction, conduction electrons in the 2DEG with spins *parallel* to the localized spin $\boldsymbol{S}$ in the FI undergo spin-flip relaxation at the clean interface. Due to this difference in the spin-flipping process of conduction electrons, the θ dependence of the modulation in the charge current density and spin density for the clean interface is shifted by $\pi/2$ relative to the dirty interface.

The remaining explanation is largely consistent with the dirty interface case, aside from the difference in the orientation of spin relaxation. The behavior observed in the left two plots of Fig. 6.4 can be explained using the right four panels of Fig. 6.4. For instance, we examine the

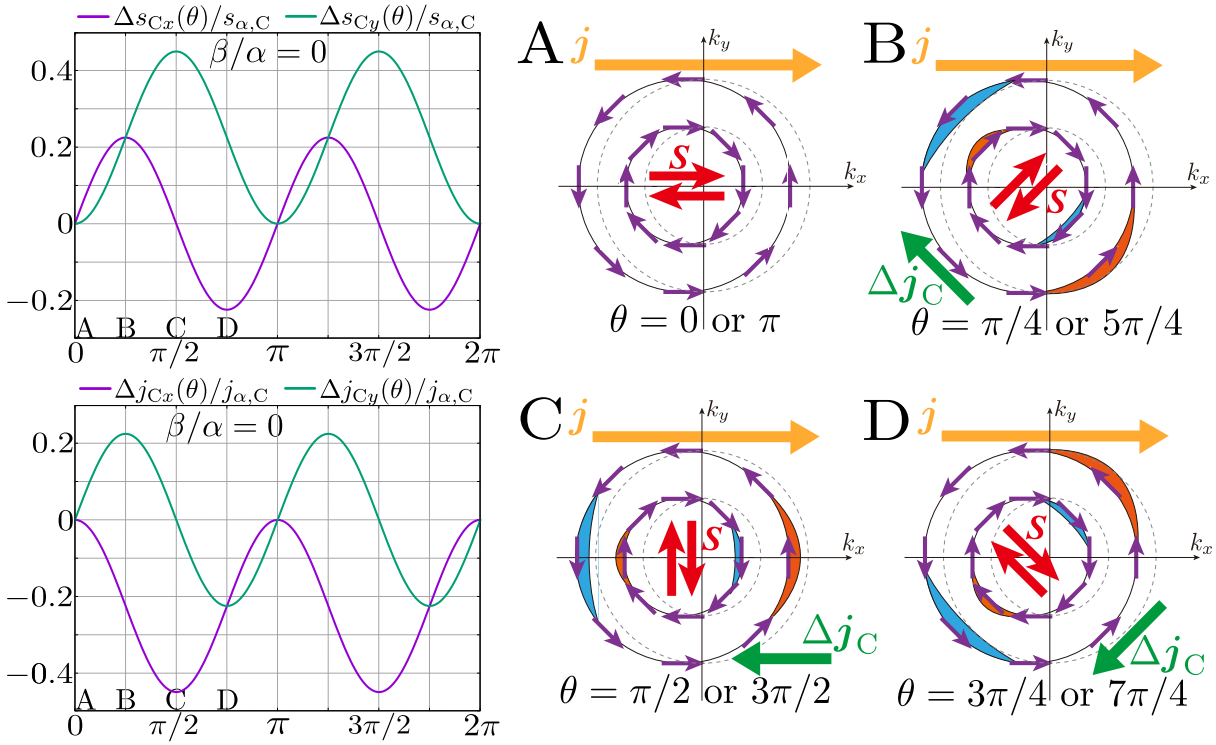

Figure 6.4: Left two panels: For a clean interface with only the Rashba SOC present ($\beta/\alpha = 0$), these plots display the modulation of spin density and charge current density induced by the REMR as functions of the localized spin orientation θ in the FI. The parameters are set to $k_B T/\hbar\omega_0 = 3$, $|\gamma_g|h_{dc}/\omega_0 = 0.1$, and $k_F a = 0.1$, where $\hbar\omega_0 = 4\mathcal{D}k_F^2$ and a is a lattice constant of the FI. To simplify interpretation, note that the modulation is shown relative to reference points at $\theta = 0, \pi$. Right four panels: Schematic representations of the modulation of the 2DEG conduction electron distribution function near the Fermi surface for (A) $\theta = 0, \pi$, (B) $\theta = \pi/4, 5\pi/4$, (C) $\theta = \pi/2, 3\pi/2$, and (D) $\theta = 3\pi/4, 7\pi/4$. Orange (blue) regions indicate areas where the distribution function of 2DEG conduction electrons has increased (decreased) relative to the reference points at $\theta = 0, \pi$. The red and green arrows represent the orientation of the localized spins in the FI and the direction of the charge current density modulation induced in the 2DEG by the REMR, respectively.

case of $\theta = \pi/2, 3\pi/2$. As illustrated in diagram C of Fig. 6.4, 2DEG conduction electrons with spins polarized in the $\pm y$ direction, aligned parallel to $\boldsymbol{S}$, undergo spin-flip relaxation, and the distribution function for the electrons with spins aligned in the $-y$ ($+y$) direction decreases (increases). Note that this change in the distribution function reduces the spin accumulation induced by the REE from the external DC electric field. Consequently, this change induces the IREE, resulting in a modulation $\Delta \boldsymbol{j}_C$ of the charge current density in the $-x$ direction. The behavior of the spin density and charge current density for (B) $\theta = \pi/4, 5\pi/4$ and (D) $\theta = 3\pi/4, 7\pi/4$ can be explained in a similar manner.

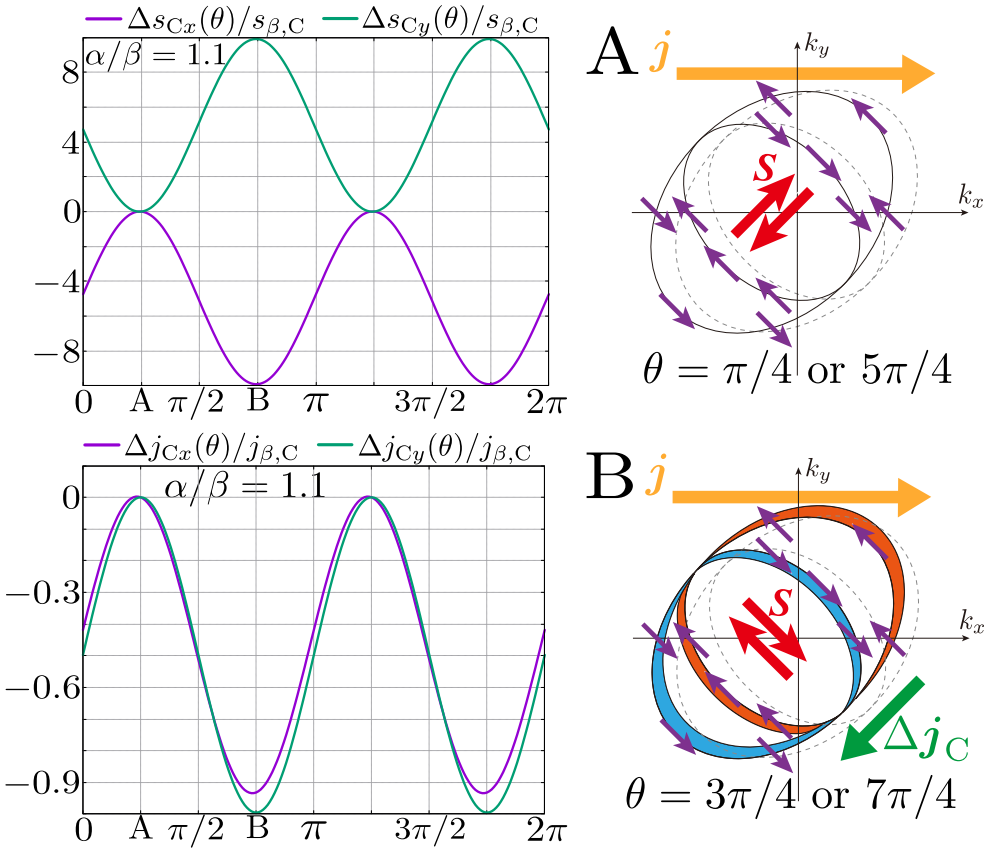

Figure 6.5: Left two panels: For a clean interface with $\alpha/\beta = 1.1$, these plots show the modulation of spin density and charge current density induced by the REMR. The parameters are set to $k_B T/\hbar\omega_0 = 3$, $|\gamma_g| h_{dc}/\omega_0 = 0.1$, and $k_F a = 0.1$, where $\hbar\omega_0 = 4\mathcal{D}k_F^2$ and a is a lattice constant of the FI. Reference points are taken at $\theta = \pi/4$ and $5\pi/4$. Right two panels: Schematic representations of the modulation of the 2DEG conduction electron distribution function for (A) $\theta = \pi/4, 5\pi/4$ and (B) $\theta = 3\pi/4, 7\pi/4$. Orange (blue) regions indicate areas where the distribution function has increased (decreased) relative to the reference points at $\theta = \pi/4$ and $5\pi/4$.

Case of $\alpha/\beta = 1.1$

Next, we consider the case in which the magnitudes of the Rashba and Dresselhaus SOCs are comparable with $\alpha/\beta = 1.1$. The left two plots of Fig. 6.5 show the spin density and charge current density as functions of the localized spin orientation θ in the FI, referenced from $\theta = \pi/4$ and $5\pi/4$. The right two panels of Fig. 6.5 schematically illustrate the changes in the distribution function relative to these reference points. At (B) $\theta = 3\pi/4$ and $7\pi/4$, a modulation $\Delta \boldsymbol{s}_C$ in the spin density appears in the $3\pi/4$ direction. Consequently, due to the IREE, a modulation $\Delta \boldsymbol{j}_C$ in the charge current density arises in the $5\pi/4$ direction for (B) $\theta = 3\pi/4$ and $7\pi/4$.

A comparison of Fig. 6.5 with Fig. 6.3 reveals that the θ dependence of the modulation in spin density and charge current density for the clean interface is shifted by $\pi/2$ relative to the

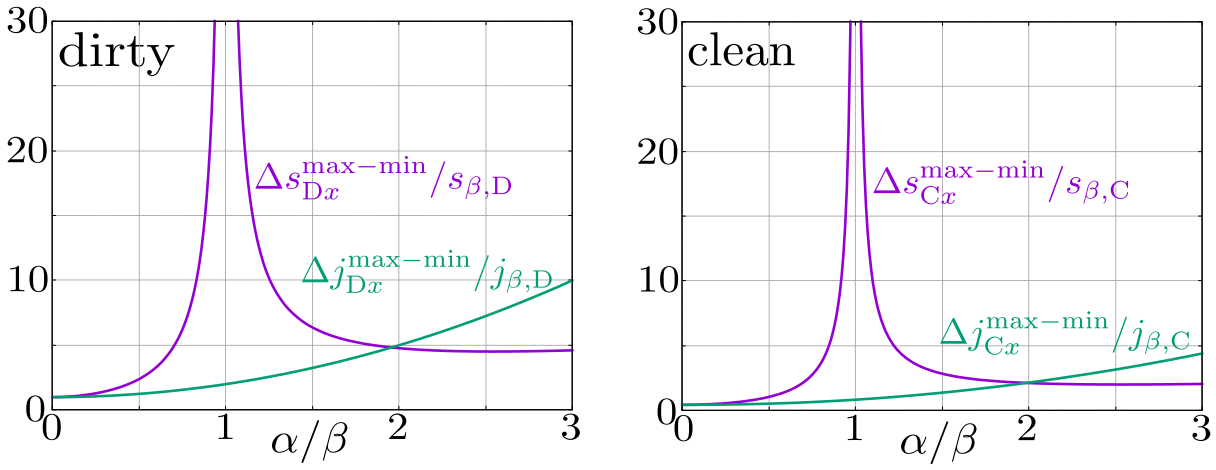

Figure 6.6: Plots of the x-component amplitudes of the modulation in spin density, $\Delta s_x^{\mathrm{max-min}}$, and charge current density, $\Delta j_x^{\mathrm{max-min}}$, as functions of α/β for both dirty and clean interfaces. These amplitudes are defined as the difference between the maximum and minimum values obtained when varying the orientation θ of the localized spin in the FI. For the clean interface, parameters are set to $k_{\mathrm{B}}T/\hbar\omega_{\mathbf{0}} = 3$, $|\gamma_{\mathrm{g}}|h_{\mathrm{dc}}/\omega_{\mathbf{0}} = 0.1$, and $k_{\mathrm{F}}a = 0.1$, where $\hbar\omega_{\mathbf{0}} = 4\mathcal{D}k_{\mathrm{F}}^2$. The left panel is adapted from Ref. [50].

dirty interface case.

6.2.4 Dependence on α/β

Finally, we examine the α/β dependence of the modulation amplitudes for the x components of spin density, $\Delta s_x^{\mathrm{max-min}}$, and charge current density, $\Delta j_x^{\mathrm{max-min}}$. These values represent the difference between the maximum and minimum values of the modulations as θ is varied. Figure 6.6 shows $\Delta s_x^{\mathrm{max-min}}$ and $\Delta j_x^{\mathrm{max-min}}$ as functions of α/β. For both dirty and clean interfaces, $\Delta s_x^{\mathrm{max-min}}$ diverges at $\alpha/\beta = 1$, whereas $\Delta j_x^{\mathrm{max-min}}$ exhibits no such singular behavior and instead increases monotonically as α/β increases.

As illustrated in the right panels of Figs. 6.3 and 6.5, when $\alpha/\beta = 1$, the effective Zeeman field generated by the Rashba and Dresselhaus SOCs aligns in a single direction. In this case, spin relaxation due to nonmagnetic impurities is entirely suppressed, causing $\Delta s_x^{\mathrm{max-min}}$ to diverge. However, the charge current density induced by the IREE does not diverge at $\alpha/\beta = 1$ because the charge currents generated on the inner and outer Fermi surfaces flow in opposite directions, partially canceling each other.

The divergence behavior of $\Delta s_x^{\mathrm{max-min}}$ at $\alpha/\beta = 1$ is illustrated in Fig. 6.7, showing that it diverges with the order of $1/|\delta|$. This behavior is consistent with that shown in Fig. 5.8, indicating that this spin density divergence reflects the divergence of the spin relaxation time.

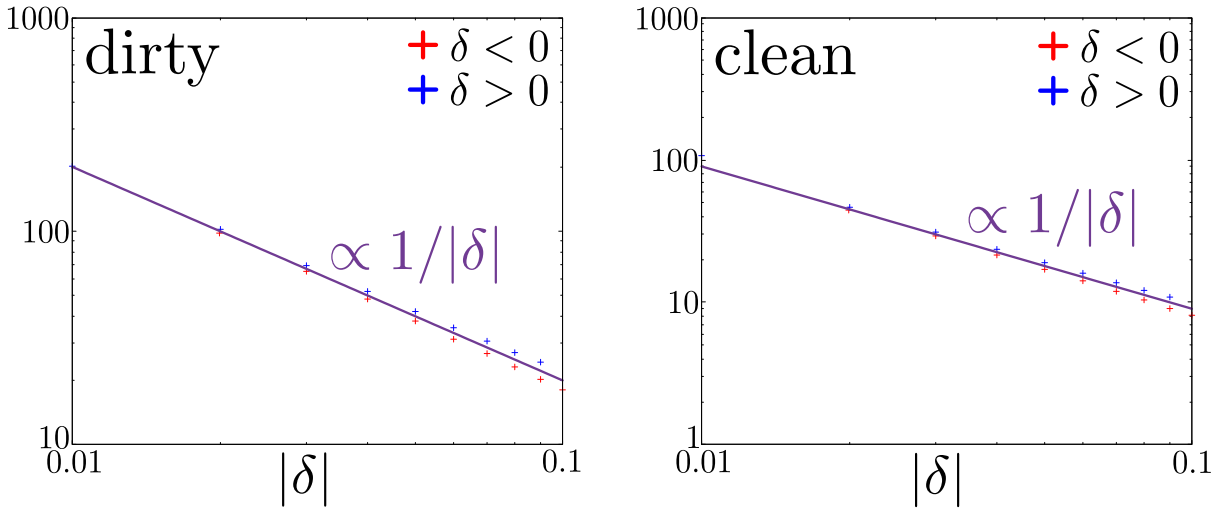

Figure 6.7: Divergence of $\Delta s_x^{\max-\min}/s_\beta$ for dirty and clean interfaces near $\alpha/\beta \simeq 1$, as observed in Fig. 6.6. With $\alpha/\beta = 1 + |\delta|$, the red (blue) points represent the values of $\Delta s_x^{\max-\min}/s_\beta$ as a function of $|\delta|$ for $\delta < 0$ ($\delta > 0$), shown in a log-log plot. The purple lines represent log-log plots of a function proportional to $1/|\delta|$.

6.3 Experimental Relevance

This section provides a brief comparison between the experimental REMR results obtained in the Bi/Ag/CoFeB junction system reported in Ref. [118] and the theoretical findings of this chapter. In the Bi/Ag/CoFeB system, applying an external DC electric field induces the REMR due to the strong Rashba SOC at the Bi/Ag interface. Reference [118] reports that the longitudinal resistance of the REMR varies with the localized spin orientation θ with a period of π, reaching a maximum at $\theta = 0$ and a minimum at $\theta = \pi/2$. In contrast, the transverse resistance exhibits a similar periodic dependence on θ but with a phase shift of $\pi/4$ relative to the longitudinal resistance. These behaviors are qualitatively consistent with the results obtained for the dirty interface in Sec. 6.2.2 [1]. Because the Fermi wavelength of Ag carriers is very short, interfacial randomness is effectively present in the Bi/Ag/CoFeB junction system, making it reasonable for the experimental results to align with the predictions for the dirty interface model presented in this chapter.

In the future, if a junction system with a clean interface—where electron scattering from interfacial randomness is negligible—can be realized, it is expected that the reversed-sign REMR predicted in this chapter will be observed.

[1] Since the localized spin in the FI is aligned opposite to the externally applied DC magnetic field, $\theta + \pi$ in this chapter corresponds to θ in Ref. [118].

Chapter 7

Summary and Future Problems

7.1 Summary

This dissertation intended to establish a theoretical framework for spin transport phenomena in junction systems comprising a ferromagnetic insulator (FI) and a two-dimensional electron gas (2DEG) with the Rashba and Dresselhaus spin-orbit couplings (SOCs). After the introduction given in Chaps. 1 and 2, we described the main results of this dissertation from Chap. 3 to Chap. 6.

In Chap. 3, we introduced a microscopic Hamiltonian describing the FI-2DEG junction system. We modeled the 2DEG using a kinetic Hamiltonian incorporating the Rashba and Dresselhaus SOCs along with a non-magnetic impurity represented by a delta-function-type potential. We described the FI using the Heisenberg model, which is reformulated in terms of magnon creation and annihilation operators under the spin-wave approximation. We described the FI-2DEG interface by a tunneling Hamiltonian that captures the exchange interaction between localized spins in the FI and conduction electron spins in the 2DEG. The interface is categorized into two states: the dirty interface, in which electron momentum is not conserved, and the clean interface, in which momentum conservation is preserved. Based on these microscopic Hamiltonians, the subsequent chapters, Chaps. 4, 5, and 6, established theoretical frameworks for spin pumping (SP), the inverse Rashba-Edelstein effect (IREE) induced by SP, and the Rashba-Edelstein magnetoresistance (REMR), respectively.

Chapter 4 investigated the modulation of the Gilbert damping and the ferromagnetic resonance (FMR) frequency shift induced by SP in FI-2DEG junction systems with the Rashba and Dresselhaus SOCs. Considering the second-order perturbation of interfacial interactions at the FI/2DEG junction, we performed calculations both with and without taking into account the ladder-type vertex correction. Both the modulation of the Gilbert damping and the shift in the FMR frequency exhibit peaks in both the low-frequency and high-frequency ranges. The peak in the low-frequency range is due to an elastic process in which magnons relax by sensing the effective Zeeman field generated by the SOC of the 2DEG as a transverse magnetic field, while the

peak in the high-frequency range is due to an inelastic process in which magnons are absorbed by the conduction electrons of the 2DEG, leading to transitions of the electrons between spin-split subbands. These features are common to both cases with and without the vertex correction. Moreover, for most parameters, the behavior of the modulation of the Gilbert damping with the vertex correction remains largely unchanged from the results without the vertex correction presented in Ref. [78]. However, when the magnitudes of the Rashba and Dresselhaus SOCs are identical, a qualitatively different result emerges: the peak in the modulation of the Gilbert damping in the low-frequency range vanishes only when the vertex corrections are included. This was attributed to the spin conservation law, which holds when the magnitudes of the two SOCs are equal, being incorporated only when the vertex corrections were considered, and suppresses spin relaxation. Additionally, when the magnitudes of the two SOCs are nearly the same but slightly different, we revealed that the modulation of the Gilbert damping sharply increases in the low-frequency range only when the vertex correction was considered. This behavior was interpreted as a consequence of the slight breaking of the spin conservation law, leading to very slow spin relaxation. Furthermore, a sharp increase in the FMR frequency shift in the low-frequency region was also observed, which is consistent with the Kramers-Kronig relation. This study established a theoretical foundation for SP into a 2DEG with spin-split energy bands. The formalism and results presented are not restricted to the specific system examined, but are also anticipated to be valuable for analyzing SP into surface/interface states [37, 100, 102] and atomic-layer materials [109, 111].

Chapter 5 explored the IREE in a 2DEG with the Rashba and Dresselhaus SOCs interfaced with an FI. Using the Boltzmann equation, we calculated the spin density and charge current density induced in the 2DEG by the IREE in the weak-impurity limit, in which energy broadening due to nonmagnetic impurity scattering is significantly smaller than the spin-splitting energy in the conduction band induced by the Rashba and Dresselhaus SOCs. It was shown that these physical quantities depend on the FMR frequency and the orientation of the localized spins in the FI. This dependence was explained by the spin splitting of the energy bands and the spin texture near the Fermi surface of the 2DEG. Additionally, when the Rashba SOC and Dresselhaus SOCs compete with each other, resulting in spin conservation, it was shown that the results derived using the relaxation-time approximation for the impurity scattering collision term qualitatively differed from those obtained through the full solution of the Boltzmann equation. Furthermore, in the case of the full solution, it was found that while the maximum value of the spin density diverged when the Rashba and Dresselhaus SOCs were of equal magnitude, the maximum value of the charge current density did not exhibit such singularity and was instead suppressed. These findings offer a method of determining the spin texture at the Fermi surface of the 2DEG and are expected to aid in the design of spintronic devices utilizing the IREE. In this study, as in Chap. 4, for simplicity, we assumed the energy bands of the 2DEG to have a simple parabolic dispersion and neglected the effects of exchange bias [164] and band modification due to the interface [12, 165]. However, the formulation can be straightforwardly extended to other physical

systems with more complex band structures.

Chapter 6 examined the REMR in FI-2DEG junction systems with the Rashba and Dresselhaus SOCs. By starting from a microscopic Hamiltonian and applying the Boltzmann equation, we calculated the modulation of spin density and charge current density induced in the 2DEG by REMR under an applied DC electric field, focusing on the weak-impurity limit. This analysis elucidated the dependencies of these modulations on both the localized spin orientation in the FI and the ratio of the two SOCs for both dirty and clean FI-2DEG interfaces. In the case of a dirty interface, the effective Zeeman field from interfacial exchange bias primarily contributes to the REMR, whereas in the clean interface, the dynamic process of magnon absorption and emission dominates, resulting in opposite REMR signs between the two interface types. The microscopic approach employed here successfully predicted such sign reversals, which could not be captured by phenomenological models using parameters like spin-mixing conductance. Furthermore, it was shown that for both interfaces, as the Rashba-to-Dresselhaus SOC ratio approaches unity, the modulation of spin density in the 2DEG diverged, while the modulation of charge current did not display such singular behavior. This study advances understanding of the physical mechanisms underlying the REMR and offers insights for experimental comparisons and interpretations. The theoretical framework developed here could, in principle, be extended to analyze the REMR in other systems with more complex band structures.

These findings contribute to the development of energy-efficient spintronic devices and tunable semiconductor spintronics. The microscopic theory developed here addresses dynamic magnon-related processes beyond the scope of phenomenological approaches like the Landau-Lifshitz-Gilbert (LLG) equation or spin mixing conductance, establishing a robust theoretical foundation for spintronics.

7.2 Future Problems

This dissertation investigated the weak-impurity limit, in which the impurity scattering strength is significantly smaller than the spin-splitting width of energy bands induced by the Rashba or Dresselhaus SOCs. However, in systems with low electron mobility, this weak-impurity limit breaks down [49]. In such cases, the off-diagonal components of the 2×2 density matrix, discussed in Chap. C, become non-negligible, giving rise to spin relaxation mechanisms such as the D'yakonov-Perel (DP) and Elliot-Yafet (EY) mechanisms [81,166]. Extending the framework of this study to this crossover presents a significant challenge.

In this dissertation, we focused on the spin orientation dependence of localized spins in the FI. As shown in Eq. (3.27), the interfacial interaction Hamiltonian, which includes magnons, can also capture temperature dependence. In the SP theory, in which the 2DEG density of states is treated as constant, no temperature dependence is observed. Although we can compute temperature-dependent corrections using the Sommerfeld expansion, these corrections remain

small as long as $k_{\mathrm{B}}T$ is much smaller than the Fermi energy. In the case of the REMR, temperature dependence is minimal for dirty interfaces due to the negligible effect of magnons, while for clean interfaces, magnons play a significant role, leading to noticeable temperature dependence. We leave a detailed study of these effects for future work.

The off-diagonal components of the density matrix capture the effects of wavefunction superposition between split subbands, a concept that is gaining attention in the emerging field of orbitronics. Orbitronics focuses on the orbital degrees of freedom of electrons and has been the subject of intense research in recent years [167, 168]. For instance, Ref. [169] demonstrates that these off-diagonal terms are crucial in the orbital Hall effect (OHE), which converts an orbital current into a charge current. While this dissertation primarily addresses spin textures induced by the Rashba effect, orbitronics explores orbital textures arising from the orbital Rashba effect [82, 170]. Phenomena corresponding to spin pumping (SP), the inverse Rashba-Edelstein effect (IREE), and the Rashba-Edelstein magnetoresistance (REMR), such as orbital pumping [171, 172], the orbital inverse Rashba-Edelstein effect [173], and the orbital Rashba-Edelstein magnetoresistance [174], have also been investigated. Developing microscopic theories for these phenomena by extending the methodologies presented in this dissertation is an important direction for future research.

In SP-driven IREE, spins injected from a ferromagnetic material into a Rashba system are converted into a charge current. Conversely, when a charge current is applied to a Rashba system, spin accumulation induced by the Rashba-Edelstein effect (REE) generates spin-orbit torque (SOT) on the magnetization, influencing its dynamics [175]. Experimental studies utilizing this SOT include investigations of spin-orbit ferromagnetic resonance (SO-FMR) [112, 176]. Extending the model Hamiltonian and methods developed in this dissertation to construct a microscopic theory for SO-FMR is an important area of future research.

In the interfacial interaction Hamiltonian introduced in Chap. 3, tunneling scattering strengths were simplified to constants $\bar{T}$ and $\bar{\mathcal{T}}$ [117, 148]. Future developments could involve assessing the effects of interfacial disorder on tunneling scattering strength using model calculations based on the Lippmann-Schwinger equation [177]. Furthermore, to enable precise evaluation of real material junction systems, first-principle calculations could be employed to analyze interfacial states [55]. This approach would enable quantitative comparisons between the findings of this dissertation and experimental results, highlighting a pivotal avenue for future research.

Appendix A

Theoretical Analysis of the REE Using the Boltzmann Equation

Trushin et al. [32] presented the theoretical framework for the REE in a 2DEG with coexisting the Rashba and Dresselhaus SOCs using the Boltzmann equation. In this appendix, an overview of Ref. [32] is provided. The Hamiltonian for the 2DEG can be expressed as follows:

$$\hat{h}_{\boldsymbol{k}} = \frac{\hbar^2(k_x^2 + k_y^2)}{2m^*} + \alpha(k_y\hat{\sigma}_x - k_x\hat{\sigma}_y) + \beta(k_x\hat{\sigma}_x - k_y\hat{\sigma}_y). \tag{A.1}$$

Here, $\boldsymbol{k} = (k_x, k_y)^T = (|\boldsymbol{k}|\cos\varphi, |\boldsymbol{k}|\sin\varphi)^T$ represents the wavevector of the conduction electrons, and m^* denotes the effective mass. The parameters α and β indicate the strengths of the Rashba and Dresselhaus SOCs, respectively, while $\hat{\boldsymbol{\sigma}} = (\hat{\sigma}_x, \hat{\sigma}_y)^T$ represents the Pauli matrices. The eigenvalues and eigenstates of Eq. (A.1) are given as follows:

$$E_{\boldsymbol{k}}^{\gamma} = \frac{\hbar^2(k_x^2 + k_y^2)}{2m^*} + \gamma\sqrt{(\alpha k_x + \beta k_y)^2 + (\beta k_x + \alpha k_y)^2}, \tag{A.2}$$

$$\Psi_{\gamma}(\boldsymbol{r}) = \frac{1}{\sqrt{2}}e^{i\boldsymbol{k}\cdot\boldsymbol{r}}\begin{pmatrix} 1 \\ \gamma e^{-i\zeta_k} \end{pmatrix}, \quad \tan\zeta_k = \frac{\alpha k_x + \beta k_y}{\beta k_x + \alpha k_y}. \tag{A.3}$$

Here, $\gamma = \pm$ is a label that specifies the spin-split bands and $\boldsymbol{r} = (x, y)^T$ represents the position coordinates of an electron. Using Eqs. (A.2) and (A.3), the transition probability between $\boldsymbol{k}, \gamma$ and $\boldsymbol{k}', \gamma'$ due to a delta-function-like impurity potential in the 2DEG is given by the following expression:

$$w(\boldsymbol{k}\gamma; \boldsymbol{k}'\gamma') = \frac{\pi\hbar^2}{m^*\tau}[1 + \gamma\gamma'\cos(\zeta_k)]\delta(E_{\boldsymbol{k}}^{\gamma} - E_{\boldsymbol{k}'}^{\gamma'}). \tag{A.4}$$

Here, τ represents the relaxation time. When an external electric field $\boldsymbol{E}$ is applied to the 2DEG, the distribution function of the conduction electrons can be expressed as follows:

$$f_\gamma(\boldsymbol{k}) = f^0(E^\gamma_{\boldsymbol{k}}) + f^1_\gamma(\boldsymbol{k}) + f^2_\gamma(\boldsymbol{k}), \tag{A.5}$$

where f^0 is the Fermi distribution function and $f^{1,2}_\gamma \ll f^0$. Considering terms up to the first order in the electric field, we can write the Boltzmann equation by the following expression:

$$e\boldsymbol{E}\cdot\boldsymbol{v}\Big[-\frac{\partial f^0(E^\gamma_{\boldsymbol{k}})}{\partial E^\gamma_{\boldsymbol{k}}}\Big] = \mathrm{St}[f_\gamma(\boldsymbol{k})], \tag{A.6}$$

$$\mathrm{St}[f_\gamma(\boldsymbol{k})] = \sum_{\gamma'}\int \frac{d^2k'}{(2\pi)^2}\{w(\boldsymbol{k}\gamma;\boldsymbol{k}'\gamma')[f^1_\gamma(\boldsymbol{k}) + f^2_\gamma(\boldsymbol{k}) - f^1_{\gamma'}(\boldsymbol{k}') - f^2_{\gamma'}(\boldsymbol{k}')]. \tag{A.7}$$

Here, e (< 0) denotes the charge of an electron and $\boldsymbol{v}$ represents the velocity of the conduction electrons. By introducing a_x, b_x, a_y, b_y as unknown constants, the solution to Eq. (A.6) can be expressed in the following form:

$$f^1_\gamma(\boldsymbol{k}) = \tau e\boldsymbol{E}\cdot\boldsymbol{v}\Big[-\frac{\partial f^0(E^\gamma_{\boldsymbol{k}})}{\partial E^\gamma_{\boldsymbol{k}}}\Big], \tag{A.8}$$

$$f^2_\gamma(\boldsymbol{k}) = \frac{\gamma\tau e\boldsymbol{E}}{\hbar\sqrt{\alpha^2+\beta^2+2\alpha\beta\sin 2\varphi}}\Big[-\frac{\partial f^0(E^\gamma_{\boldsymbol{k}})}{\partial E^\gamma_{\boldsymbol{k}}}\Big] \cdot [(a_x\cos\varphi + b_x\sin\varphi)\boldsymbol{e}_x + (a_y\cos\varphi + b_y\sin\varphi)\boldsymbol{e}_y]. \tag{A.9}$$

Substituting $f^{1,2}_\gamma(\boldsymbol{k})$ into Eq. (A.6), we can determine the unknown constants as follows:

$$a_x = b_y = -(\alpha^2+\beta^2), \quad a_y = b_x = -2\alpha\beta. \tag{A.10}$$

By substituting these into Eq. (A.9), the following solution to Eq. (A.6) is obtained:

$$f_\gamma(\boldsymbol{k}) = f^0_\gamma(E^\gamma_{\boldsymbol{k}}) + e\boldsymbol{E}\cdot\boldsymbol{k}\frac{\hbar\tau}{m^*}\Big[-\frac{\partial f^0(E^\gamma_{\boldsymbol{k}})}{\partial E^\gamma_{\boldsymbol{k}}}\Big]. \tag{A.11}$$

The spin accumulation $\boldsymbol{S} = (S_x, S_y)$ induced by the REE can be written as follows:

$$\langle S_x\rangle = \sum_\gamma\int\frac{d^2k}{(2\pi)^2}\frac{\gamma}{2}\cos\zeta_k f_\gamma(\boldsymbol{k}), \quad \langle S_y\rangle = -\sum_\gamma\int\frac{d^2k}{(2\pi)^2}\frac{\gamma}{2}\sin\zeta_k f_\gamma(\boldsymbol{k}), \tag{A.12}$$

and substituting Eq. (A.11) into the above equation yields the following expression:

$$\langle\boldsymbol{S}\rangle = \frac{|e|m^*\tau}{2\pi\hbar^3}\begin{pmatrix}\beta & \alpha\\ -\alpha & -\beta\end{pmatrix}\boldsymbol{E}. \tag{A.13}$$

Here, the approximation $-\frac{\partial f^0(E^\gamma_{\boldsymbol{k}})}{\partial E^\gamma_{\boldsymbol{k}}} \simeq \delta(E^\gamma_{\boldsymbol{k}} - \mu)$ was employed, where $\mu = \hbar^2 k_{\mathrm{F}}^2/2m^*$ is the chemical potential and k_{F} is the Fermi wavevector.

Appendix B

Analytic Expressions for Spin Pumping

B.1 Case of $\beta/\alpha = 0$

First, we derive the analytic expression for the modulation of the Gilbert damping for $\beta/\alpha = 0$, i.e., when only the Rashba SOC is present. In this case, the spin splitting width of the energy band for the conduction electrons in the 2DEG is a constant $2h_{\rm eff} = 2\Delta_0$ and $\tilde{\Lambda}^R_j(\omega)$ $(j = 0, 1, 2, 3)$ from Eq. (4.94) is given as follows:

$$\tilde{\Lambda}^R_0(\omega) = \frac{i\Gamma}{4\Delta_0}\sum_{\gamma\gamma'}\frac{1}{\hbar\omega/\Delta_0 + (\gamma-\gamma') + i\Gamma/\Delta_0}, \tag{B.1}$$

$$\tilde{\Lambda}^R_1(\omega) = \frac{i\Gamma}{4\Delta_0}\sum_{\gamma\gamma'}\frac{\gamma\gamma'}{\hbar\omega/\Delta_0 + (\gamma-\gamma') + i\Gamma/\Delta_0}, \tag{B.2}$$

$$\tilde{\Lambda}^R_2(\omega) = \tilde{\Lambda}^R_3(\omega) = 0. \tag{B.3}$$

Using these expressions, we can write the modulation of the Gilbert damping with and without the vertex corrections, as given in Eqs. (4.96) and (4.100), as follows:

$$\frac{\delta\alpha_{\rm G}}{\alpha_{\rm G,0}} \simeq \frac{\Delta_0}{2\pi\Gamma}{\rm Re}\left[\frac{\tilde{\Lambda}^R_0(\omega_{\mathbf{0}})}{1-\tilde{\Lambda}^R_0(\omega_{\mathbf{0}})} + \frac{\tilde{\Lambda}^R_0(\omega_{\mathbf{0}}) - \tilde{\Lambda}^R_1(\omega_{\mathbf{0}})}{1-\tilde{\Lambda}^R_0(\omega_{\mathbf{0}}) + \tilde{\Lambda}^R_1(\omega_{\mathbf{0}})}\right], \tag{B.4}$$

$$\frac{\delta\alpha^{\rm nv}_{\rm G}}{\alpha_{\rm G,0}} \simeq \frac{\Delta_0}{2\pi\Gamma}{\rm Re}\left[2\tilde{\Lambda}^R_0(\omega_{\mathbf{0}}) - \tilde{\Lambda}^R_1(\omega_{\mathbf{0}})\right]. \tag{B.5}$$

For $\Gamma \ll \Delta_0$, the dominant contribution to the peak at $\omega_{\mathbf{0}} = 0$ comes from the following term with $\gamma = \gamma'$:

$$\frac{\delta\alpha_{\rm G}}{\alpha_{\rm G,0}} \simeq \frac{\Delta_0}{4\pi}\cdot\frac{\Gamma/2}{(\hbar\omega_{\mathbf{0}})^2 + (\Gamma/2)^2}, \tag{B.6}$$

$$\frac{\delta\alpha^{\rm nv}_{\rm G}}{\alpha_{\rm G,0}} \simeq \frac{\Delta_0}{4\pi}\cdot\frac{\Gamma}{(\hbar\omega_{\mathbf{0}})^2 + \Gamma^2}. \tag{B.7}$$

These equations indicate that the linewidth of the peak at $\omega_{\mathbf{0}} = 0$ in $\delta\alpha_{\mathrm{G}}$ is half of that in $\delta\alpha_{\mathrm{G}}^{\mathrm{nv}}$, which is consistent with Figs. 4.8(b) and 4.8(c). Similarly, the peak of the modulation of the Gilbert damping at $\omega_{\mathbf{0}} = 2\Delta_0/\hbar$ for $\beta/\alpha = 0$ can be approximated by the following expression:

$$\frac{\delta\alpha_{\mathrm{G}}}{\alpha_{\mathrm{G},0}} \simeq \frac{\Delta_0}{4\pi} \cdot \left[\frac{1}{2} \frac{3\Gamma/4}{(\hbar\omega_{\mathbf{0}} - 2\Delta_0)^2 + (3\Gamma/4)^2} + \frac{\Gamma/2}{(\hbar\omega_{\mathbf{0}} - 2\Delta_0)^2 + (\Gamma/2)^2} \right], \tag{B.8}$$

$$\frac{\delta\alpha_{\mathrm{G}}^{\mathrm{nv}}}{\alpha_{\mathrm{G},0}} \simeq \frac{\Delta_0}{4\pi} \cdot \frac{3\Gamma/2}{(\hbar\omega_{\mathbf{0}} - 2\Delta_0)^2 + \Gamma^2}. \tag{B.9}$$

These equations show that similar to the peak at $\omega_{\mathbf{0}} = 0$, the linewidth of the peak at $\omega_{\mathbf{0}} = 2\Delta_0/\hbar$ is reduced when the vertex corrections are considered. This result is consistent with Figs. 4.8(b) and 4.8(c). From Eqs. (B.6)-(B.9), it can be seen that the linewidth of the peaks in the modulation of the Gilbert damping is determined by $\Gamma = 2\pi n_{\mathrm{imp}} u^2 D(\epsilon_{\mathrm{F}})$, which represents the strength of impurity scattering.

To highlight the effect of the vertex corrections for $\beta/\alpha = 0$, density plots of $\delta\alpha_{\mathrm{G}} - \delta\alpha_{\mathrm{G}}^{\mathrm{nv}}$ and $\delta\omega_{\mathbf{0}} - \delta\omega_{\mathbf{0}}^{\mathrm{nv}}$, calculated using the original Eqs. (4.95), (4.96), (4.97) and Eqs. (4.99), (4.100), (4.101), are shown in Figs. B.1(a) and B.1(d). These figures show that the effect of the vertex corrections mainly appears near the peaks at $\omega_{\mathbf{0}} = 0$ and $\omega_{\mathbf{0}} = 2\Delta_0/\hbar$. The behavior around these peaks is consistent with the analytic expressions derived in this appendix.

Note that in the case of $\alpha/\beta = 0$, i.e., with only the Dresselhaus SOC, the analytic expressions for $\delta\alpha_{\mathrm{G}}$ and $\delta\alpha_{\mathrm{G}}^{\mathrm{nv}}$ are the same as those derived in this appendix for the case of only the Rashba SOC. For general values of β/α, the Γ dependence of $\delta\alpha_{\mathrm{G}}$ and $\delta\alpha_{\mathrm{G}}^{\mathrm{nv}}$ becomes more complex.

B.2 Case of $\beta/\alpha = 1$

Next, we derive the analytic expression for the modulation of the Gilbert damping for $\beta/\alpha = 1$. When $\beta/\alpha = 1$, as shown in Fig. 4.8(d), the effective Zeeman field generated by the Rashba and Dresselhaus SOCs is aligned in the $(-1, 1)$ direction, with a magnitude given by the following expression, as written in Eq. (4.102):

$$h_{\mathrm{eff}}(\varphi) = 2\Delta_0 |\sin(\varphi + \pi/4)|. \tag{B.10}$$

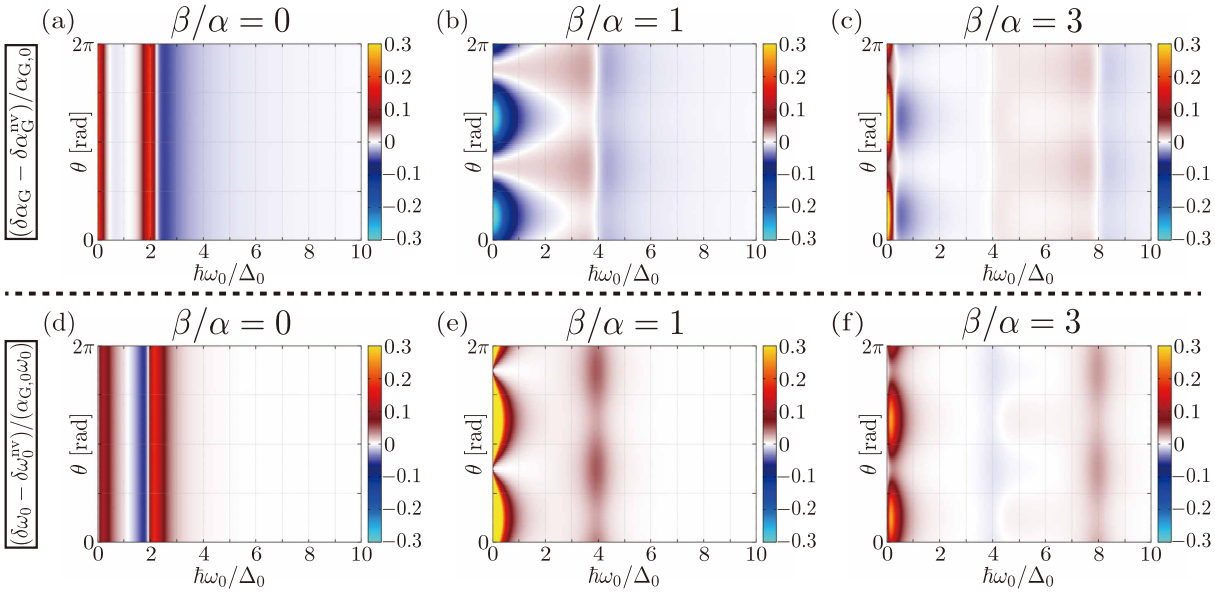

Figure B.1: (Upper panels) Modulation of the Gilbert damping due to the vertex corrections, $\delta\alpha_G - \delta\alpha_G^{nv}$, for (a) $\beta/\alpha = 0$, (b) $\beta/\alpha = 1$, and (c) $\beta/\alpha = 3$. (Lower panels) Change in the FMR frequency due to the vertex corrections, $\delta\omega_{\mathbf{0}} - \delta\omega_{\mathbf{0}}^{nv}$, for (d) $\beta/\alpha = 0$, (e) $\beta/\alpha = 1$, and (f) $\beta/\alpha = 3$. In all panels, the horizontal axis represents the FMR frequency $\omega_{\mathbf{0}}$, the vertical axis indicates the azimuthal angle θ of the localized spin $\boldsymbol{S}$ in the FI, and $\Gamma/\Delta_0 = 0.5$. Adapted from Ref. [48].

By using this, $\tilde{\Lambda}_j^R(\omega)$ $(j = 0, 1, 2, 3)$ from Eq. (4.94) can be expressed as follows:

$$\tilde{\Lambda}_0^R(\omega) = \frac{i\Gamma}{4\Delta_0} \sum_{\gamma\gamma'} \mathcal{J}_{\gamma\gamma'} \tag{B.11}$$

$$\tilde{\Lambda}_1^R(\omega) = \frac{i\Gamma}{4\Delta_0} \sum_{\gamma\gamma'} \gamma\gamma' \mathcal{J}_{\gamma\gamma'}, \tag{B.12}$$

$$\tilde{\Lambda}_2^R(\omega) = -\sin 2\theta\, \tilde{\Lambda}_1^R(\omega), \tag{B.13}$$

$$\tilde{\Lambda}_3^R(\omega) = -\cos 2\theta\, \tilde{\Lambda}_1^R(\omega). \tag{B.14}$$

Here, $\mathcal{J}_{\gamma\gamma'}(\omega)$ is given by the following expression:

$$\mathcal{J}_{\gamma\gamma'}(\omega) \equiv \int_0^{2\pi} \frac{d\varphi}{2\pi} \frac{\Delta_0}{\hbar\omega + (\gamma - \gamma')h_{\text{eff}}(\varphi) + i\Gamma}. \tag{B.15}$$

Using these expressions, we can write the modulation of the Gilbert damping with the vertex corrections for $\beta/\alpha = 1$ at $\theta = \pi/4$ as follows:

$$\frac{\delta\alpha_G}{\alpha_{G,0}} = \frac{\Delta_0}{2\pi\Gamma} \text{Re}\left[-2 + \frac{1}{1 - \tilde{\Lambda}_0^R(\omega_{\mathbf{0}}) + \tilde{\Lambda}_1^R(\omega_{\mathbf{0}})} + \frac{1}{1 - \tilde{\Lambda}_0^R(\omega_{\mathbf{0}}) - \tilde{\Lambda}_1^R(\omega_{\mathbf{0}})}\right]. \tag{B.16}$$

The expansion of this expression up to the first-order term in $\tilde{\Lambda}_j^R$ corresponds to the modulation of the Gilbert damping without the vertex corrections:

$$\frac{\delta\alpha_{\mathrm{G}}^{\mathrm{nv}}}{\alpha_{\mathrm{G},0}} = \frac{\Delta_0}{2\pi\Gamma}\mathrm{Re}\left[2\tilde{\Lambda}_0^R(\omega_{\mathbf{0}})\right]. \tag{B.17}$$

Note that the third term in Eq. (B.16) is calculated as

$$\frac{1}{1-\tilde{\Lambda}_0^R(\omega_{\mathbf{0}})-\tilde{\Lambda}_1^R(\omega_{\mathbf{0}})} = \frac{1}{1-\frac{i\Gamma}{\hbar\omega_{\mathbf{0}}+i\Gamma}} = \frac{\hbar\omega_{\mathbf{0}}+i\Gamma}{\hbar\omega_{\mathbf{0}}}, \tag{B.18}$$

and thus for $\omega_{\mathbf{0}} \ll \Gamma$, Eq. (B.16) cannot be expanded in terms of $\tilde{\Lambda}_j^R$ as in Eq. (B.17). Consequently, the modulation of the Gilbert damping with the vertex corrections, $\delta\alpha_{\mathrm{G}}$, and the modulation without the vertex corrections, $\delta\alpha_{\mathrm{G}}^{\mathrm{nv}}$, the latter being the expansion of $\delta\alpha_{\mathrm{G}}$ in terms of $\tilde{\Lambda}_j^R$, exhibit markedly different behaviors when $\omega_{\mathbf{0}} \ll \Gamma$. To confirm this, we rewrite Eqs. (B.16) and (B.17) using Eqs. (B.11)-(B.14) as follows:

$$\frac{\delta\alpha_{\mathrm{G}}}{\alpha_{\mathrm{G},0}} = \frac{\Delta_0}{2\pi\Gamma}\mathrm{Re}\left[\frac{i\frac{\Gamma}{2\Delta_0}(\mathcal{J}_{+-}+\mathcal{J}_{-+})}{1-i\frac{\Gamma}{2\Delta_0}(\mathcal{J}_{+-}+\mathcal{J}_{-+})}\right], \tag{B.19}$$

$$\frac{\delta\alpha_{\mathrm{G}}^{\mathrm{nv}}}{\alpha_{\mathrm{G},0}} = \frac{1}{4\pi}\mathrm{Re}\left[i\left(\mathcal{J}_{+-}+\mathcal{J}_{-+}+\mathcal{J}_{++}+\mathcal{J}_{--}\right)\right]. \tag{B.20}$$

The terms $\mathcal{J}_{++}$ and $\mathcal{J}_{--}$ produce peaks at $\omega_{\mathbf{0}} = 0$. While $\delta\alpha_{\mathrm{G}}^{\mathrm{nv}}$ contains $\mathcal{J}_{++}$ and $\mathcal{J}_{--}$, these terms do not appear in $\delta\alpha_{\mathrm{G}}$. Consequently, as shown in Figs. 4.8(e) and 4.8(f), $\delta\alpha_{\mathrm{G}}^{\mathrm{nv}}$ exhibits a peak around $\omega_{\mathbf{0}} = 0$ when $\omega_{\mathbf{0}} \ll \Gamma$, whereas $\delta\alpha_{\mathrm{G}}$ does not, indicating qualitatively different behaviors. Next, the modulation of the Gilbert damping with and without the vertex corrections at $\theta = -\pi/4$ can be expressed as follows:

$$\frac{\delta\alpha_{\mathrm{G}}}{\alpha_{\mathrm{G},0}} = \frac{\Delta_0}{\pi\Gamma}\mathrm{Re}\left[\frac{i\frac{\Gamma}{2\Delta_0}(\mathcal{J}_{+-}+\mathcal{J}_{-+})}{1-i\frac{\Gamma}{2\Delta_0}(\mathcal{J}_{+-}+\mathcal{J}_{-+})}\right], \tag{B.21}$$

$$\frac{\delta\alpha_{\mathrm{G}}^{\mathrm{nv}}}{\alpha_{\mathrm{G},0}} = \frac{1}{2\pi}\mathrm{Re}\left[i(\mathcal{J}_{+-}+\mathcal{J}_{-+})\right]. \tag{B.22}$$

Here, Eq. (B.22) is obtained by retaining terms up to the first order in $\tilde{\Lambda}_j^R$ in Eq. (B.21). Since neither of these equations includes $\mathcal{J}_{++}$ and $\mathcal{J}_{--}$, neither $\delta\alpha_{\mathrm{G}}$ nor $\delta\alpha_{\mathrm{G}}^{\mathrm{nv}}$ exhibits a peak at $\omega_{\mathbf{0}} = 0$ for $\theta = -\pi/4$. Furthermore, when $\Gamma \lesssim \Delta_0$, Eqs. (B.22) and (B.21) yield nearly identical results. These characteristics are consistent with Figs. 4.8(e) and 4.8(f). It should be noted that $\delta\alpha_{\mathrm{G}}$ at $\theta = -\pi/4$ in Eq. (B.21) is precisely twice that of $\delta\alpha_{\mathrm{G}}$ at $\theta = \pi/4$ in Eq. (B.19).

To make the effects of the vertex corrections more visible, density plots of $\delta\alpha_{\mathrm{G}} - \delta\alpha_{\mathrm{G}}^{\mathrm{nv}}$ and $\delta\omega_{\mathbf{0}} - \delta\omega_{\mathbf{0}}^{\mathrm{nv}}$ at $\beta/\alpha = 1$ were generated based on Eqs. (4.95), (4.96), (4.97) and Eqs. (4.99),

(4.100), (4.101) in Figs. B.1(b) and B.1(e), respectively. These figures demonstrate that the effects of the vertex corrections mainly appear as changes in peak width around $\omega_{\mathbf{0}} = 0$. Additionally, the broad peaks within $0 < \hbar\omega_{\mathbf{0}} < 2\Delta_0$ are amplified or suppressed depending on the orientation θ of the FI localized spin. These features are consistent with the expressions derived above. Similar characteristics can also be observed in Figs. B.1(c) and B.1(f) for $\beta/\alpha = 3$.

B.3 Approximate Expression for $\beta/\alpha \simeq 1$

Finally, we derive approximate expressions for $\beta/\alpha = 1 + \delta$ ($\delta \ll 1$) and $\omega \simeq 0$, given by Eq. (4.105) and Eq. (4.107). For $\beta/\alpha = 1 + \delta$ ($\delta \ll 1$), we can apply the following approximations:

$$\cos 2(\phi - \theta) \simeq \sin 2\theta\Big(-1 + \frac{(h_x + h_y)^2}{h_{\text{eff}}^2}\Big), \tag{B.23}$$

$$\sin 2(\phi - \theta) \simeq \cos 2\theta\Big(-1 + \frac{(h_x + h_y)^2}{h_{\text{eff}}^2}\Big). \tag{B.24}$$

It follows that $\tilde{\Lambda}_2^R$ and $\tilde{\Lambda}_3^R$ in Eq. (4.94) can be approximated as follows:

$$\tilde{\Lambda}_2^R \simeq X \sin 2\theta, \tag{B.25}$$

$$\tilde{\Lambda}_3^R \simeq X \cos 2\theta, \tag{B.26}$$

$$X \equiv \frac{i\Gamma}{4} \int_0^{2\pi} \frac{d\varphi}{2\pi} \sum_{\gamma\gamma'} \frac{\gamma\gamma'\Big(-1 + \frac{(h_x+h_y)^2}{h_{\text{eff}}^2}\Big)}{\hbar\omega + (\gamma - \gamma')h_{\text{eff}} + i\Gamma} \tag{B.27}$$

As shown in Fig. 4.9(b) and Fig. 4.9(c), $\delta\alpha_{\text{G}}$ exhibits a notable increase around $\omega_{\mathbf{0}} \simeq 0$ when $\beta/\alpha \simeq 1$. However, the second term inside the parentheses of $F(\omega)$, given in Eq. (4.97), does not depend on the effective Zeeman field $\boldsymbol{h}_{\text{eff}}$ and thus contributes minimally to this increase. Therefore, in the region near $\omega_{\mathbf{0}} \simeq 0$ with $\beta/\alpha \simeq 1$, $F(\omega)$ can be approximated as follows:

$$\begin{aligned} F(\omega) &\simeq \frac{\Delta_0}{2\pi i\Gamma} \frac{\tilde{\Lambda}_0^R(1 - \tilde{\Lambda}_0^R) - \tilde{\Lambda}_2^R(1 - \tilde{\Lambda}_2^R) + (\tilde{\Lambda}_3^R)^2}{(1 - \tilde{\Lambda}_0^R)^2 - (\tilde{\Lambda}_2^R)^2 - (\tilde{\Lambda}_3^R)^2} \\ &= \frac{\Delta_0}{2\pi i\Gamma} \left[-1 + \frac{(1 - \sin 2\theta)/2}{1 - \tilde{\Lambda}_0^R - X} + \frac{(1 + \sin 2\theta)/2}{1 - \tilde{\Lambda}_0^R + X}\right]. \end{aligned} \tag{B.28}$$

Since the denominator of the last term in Eq. (B.28) can be computed as

$$1 - \tilde{\Lambda}_0^R + X = \frac{\Gamma_s}{\Gamma} - i\frac{\hbar\omega}{\Gamma} + O(\omega^2), \tag{B.29}$$

and noting that Γ_s is proportional to δ^2 for $\beta/\alpha = 1 + \delta$ ($\delta \ll 1$), the last term in Eq. (B.28) diverges at $\omega = 0$ in the limit of $\delta \to 0$. Substituting Eq. (B.29) into Eq. (B.28), the component that most significantly contributes to the distinctive increase in $\delta\alpha_{\mathrm{G}}$ is given by the following expression:

$$F(\omega) \simeq \frac{\Delta_0}{2\pi i} \frac{\sin^2(\theta + \pi/4)}{\Gamma_s + i\hbar\omega}. \tag{B.30}$$

By substituting Eq. (B.30) into Eqs. (4.95) and (4.96), we obtain Eqs. (4.105) and (4.107).

Appendix C

Matrix-Form Boltzmann Equation

In this appendix, we derive the Boltzmann equation for the distribution function matrix (density matrix) in a 2DEG with the Rashba and Dresselhaus SOCs, following the approach in Ref. [178] in Sec. C.1. Subsequently, as shown in Ref. [81], it is confirmed that in the weak-impurity limit, in which the impurity scattering strength is sufficiently small compared to the energy band splitting induced by these SOCs, the off-diagonal components of the distribution function matrix can be neglected due to their small magnitude in Sec. C.2. In this regime, the collision term in the Boltzmann equation for the diagonal components of the distribution function matrix is shown to match the expression for the collision term calculated using Fermi's golden rule.

C.1 Derivation of Matrix-Form Boltzmann Equation

In this section, following Ref. [178], we derive the Boltzmann equation for the Hamiltonian $H_{\text{kin}} + H_{\text{imp}}$ — the sum of the Hamiltonian for a 2DEG with the Rashba and Dresselhaus SOCs given in Eq. (3.1) and the impurity scattering Hamiltonian given in Eq. (3.12) — using the Keldysh Green's function method. In the calculations that follow, we set $\hbar = 1$. First, the Dyson equation for the Green's function of free electrons, $\hat{g}_0$, given in Eq. (4.5), is expressed as follows:

$$(\hat{g}_0^{-1} - \underline{\hat{\Sigma}})\underline{\hat{g}} = 1, \qquad \underline{\hat{g}} = \begin{pmatrix} \hat{g}_R & \hat{g}_K \\ 0 & \hat{g}_A \end{pmatrix}. \tag{C.1}$$

Here, the underscore denotes matrices in the Keldysh space. Then, by substituting

$$\hat{g}_0^R(\boldsymbol{k}, E) = \frac{1}{2}\sum_{\gamma=\pm} \frac{1}{E - E_{\boldsymbol{k}}^{\gamma}}\left(\hat{1} - \gamma \frac{\boldsymbol{h}_{\text{eff}} \cdot \hat{\boldsymbol{\sigma}}}{h_{\text{eff}}}\right), \tag{C.2}$$

and $\hat{\Sigma}^R = (-i\Gamma/2)\hat{1}$ from Eq. (4.10) into the Dyson equation in Eq. (C.1), we obtain the following expression:

$$\hat{g}^R(\boldsymbol{k}, E) = \frac{1}{E - \xi_{\boldsymbol{k}} + \boldsymbol{h}_{\rm eff}\cdot\hat{\boldsymbol{\sigma}} - \hat{\Sigma}^R} = \frac{1}{2}\sum_{\gamma=\pm}\frac{1}{E - E^{\gamma}_{\boldsymbol{k}} + i\Gamma/2}\Big(\hat{1} - \gamma\frac{\boldsymbol{h}_{\rm eff}\cdot\hat{\boldsymbol{\sigma}}}{h_{\rm eff}}\Big), \tag{C.3}$$

where $\xi_{\boldsymbol{k}} \equiv \epsilon_{\boldsymbol{k}} - \mu$. Equation (C.3) represents the Green's function for electrons with impurity scattering, as given in Eq. (4.9). Furthermore, from the Dyson equation in Eq. (C.1), it can be shown that the following expression holds for $\hat{g}_K$:

$$(\hat{g}^R)^{-1}\hat{g}^K - \hat{g}^K(\hat{g}^A)^{-1} = \hat{\Sigma}^K\hat{g}^A - \hat{g}^R\hat{\Sigma}^K. \tag{C.4}$$

Here, note that $(\hat{g}^R)^{-1}$ and $(\hat{g}^A)^{-1}$ act on the left and right arguments of $\hat{g}_K$, respectively. In the following, we calculate the Wigner representation of Eq. (C.4) [179, 180]. The forward and backward paths on the Keldysh contour are labeled as $i = 1$ and $i = 2$, respectively, and $1^i \equiv \boldsymbol{x}_1 t_1^i$ $(i = 1, 2)$ is defined. The Green's function along these paths is expressed as $g^{ij}(1, 2) \equiv g(1^i, 2^j)$. Then the following matrix is introduced:

$$\check{g}(1, 2) \equiv \begin{pmatrix} g^{11}(1, 2) & g^{12}(1, 2) \\ g^{21}(1, 2) & g^{22}(1, 2) \end{pmatrix}, \tag{C.5}$$

where the check mark $\check{}$ denotes a 2×2 matrix originating from the forward and backward path degrees of freedom. The Wigner representation of this Green's function $\check{g}(1, 2)$, denoted as $\check{\mathfrak{g}}_{\boldsymbol{k}E}(t, \boldsymbol{x})$, is defined by the following expression:

$$\check{g}(1, 2) = \int \frac{d^2\boldsymbol{k}dE}{(2\pi)^3}\check{\mathfrak{g}}_{\boldsymbol{k}E}(t_{12}, \boldsymbol{x}_{12})e^{i\boldsymbol{k}\cdot\bar{\boldsymbol{x}}_{12} - iE\bar{t}_{12}}. \tag{C.6}$$

Here, $\boldsymbol{x}_{12} \equiv (\boldsymbol{x}_1 + \boldsymbol{x}_2)/2$, $t_{12} \equiv (t_1 + t_2)/2$, $\bar{x}_{12} \equiv \boldsymbol{x}_1 - \boldsymbol{x}_2$, and $\bar{t}_{12} \equiv t_1 - t_2$. The Wigner representation of the first term on the left-hand side of Eq. (C.4) can be expressed as follows:

$$\begin{aligned}
&\int \hat{g}^{R-1}(1, 3)\hat{g}^K(3, 2)d3 = \int \frac{d^2\boldsymbol{k}dE}{(2\pi)^3}\hat{g}^{R-1}_{\boldsymbol{k}E}(t_{12}, \boldsymbol{x}_{12}) * \hat{g}^K_{\boldsymbol{k}E}(t_{12}, \boldsymbol{x}_{12})e^{i\boldsymbol{k}\cdot\bar{\boldsymbol{x}}_{12} - iE\bar{t}_{12}} \\
&= \int \frac{d^2\boldsymbol{k}dE}{(2\pi)^3}\Bigg[\hat{g}^{R-1}_{\boldsymbol{k}E}\hat{\mathfrak{g}}_{\boldsymbol{k}E} \\
&\quad + \frac{i}{2}\Big(\frac{\partial\hat{g}^{R-1}_{\boldsymbol{k}E}}{\partial\boldsymbol{x}_{12}}\cdot\frac{\partial\hat{\mathfrak{g}}_{\boldsymbol{k}E}}{\partial\boldsymbol{k}} - \frac{\partial\hat{g}^{R-1}_{\boldsymbol{k}E}}{\partial t_{12}}\frac{\partial\hat{\mathfrak{g}}_{\boldsymbol{k}E}}{\partial E} - \frac{\partial\hat{g}^{R-1}_{\boldsymbol{k}E}}{\partial\boldsymbol{k}}\cdot\frac{\partial\hat{\mathfrak{g}}_{\boldsymbol{k}E}}{\partial\boldsymbol{x}_{12}} + \frac{\partial\hat{g}^{R-1}_{\boldsymbol{k}E}}{\partial E}\frac{\partial\hat{\mathfrak{g}}_{\boldsymbol{k}E}}{\partial t_{12}}\Big)\Bigg]e^{i\boldsymbol{k}\cdot\bar{\boldsymbol{x}}_{12} - iE\bar{t}_{12}}.
\end{aligned} \tag{C.7}$$

Here, the operator $*$ denotes the Moyal product and $\simeq$ indicates that a first-order gradient expansion of the Moyal product is used. By substituting Eq. (C.3) into $\hat{g}^R_{\boldsymbol{k}E}$, Eq. (C.7) becomes

the following:

$$\begin{aligned}
&\int \hat{g}^{R-1}(1,3)\hat{g}^{K}(3,2)d3 \\
&= \int \frac{d^2\boldsymbol{k}dE}{(2\pi)^3}\Bigg[(E-\xi_{\boldsymbol{k}}+\boldsymbol{h}_{\text{eff}}\cdot\hat{\boldsymbol{\sigma}}-\hat{\Sigma}^{R})\hat{\mathfrak{g}}_{\boldsymbol{k}E} \\
&\quad+\frac{i}{2}\Big(-\frac{\partial(-\xi_{\boldsymbol{k}}+\boldsymbol{h}_{\text{eff}}\cdot\hat{\boldsymbol{\sigma}}-\hat{\Sigma}^{R})}{\partial\boldsymbol{k}}\cdot\frac{\partial\hat{\mathfrak{g}}_{\boldsymbol{k}E}}{\partial\boldsymbol{x}_{12}}+\frac{\partial(E-\hat{\Sigma}^{R})}{\partial E}\frac{\partial\hat{\mathfrak{g}}_{\boldsymbol{k}E}}{\partial t_{12}}\Big)\Bigg]e^{i\boldsymbol{k}\cdot\bar{\boldsymbol{x}}_{12}-iE\bar{t}_{12}}.
\end{aligned} \tag{C.8}$$

Similarly, the Wigner representation of the second term on the left-hand side of Eq. (C.4) can also be computed, resulting in the following expression for the Wigner representation of the left-hand side of Eq. (C.4):

$$\begin{aligned}
&\int \hat{g}^{R-1}(1,3)\hat{g}^{K}(3,2)d3-\int \hat{g}^{K}(1,3)\hat{g}^{A-1}(3,2)d3 \\
&=\int \frac{d^2\boldsymbol{k}dE}{(2\pi)^3}\Bigg[i\frac{\partial\hat{\mathfrak{g}}_{\boldsymbol{k}E}}{\partial t_{12}}+\frac{i}{2}\Big\{\frac{\partial(\xi_{\boldsymbol{k}}-\boldsymbol{h}_{\text{eff}}\cdot\hat{\boldsymbol{\sigma}})}{\partial\boldsymbol{k}},\frac{\partial\hat{\mathfrak{g}}_{\boldsymbol{k}E}}{\partial\boldsymbol{x}_{12}}\Big\}+[\boldsymbol{h}_{\text{eff}}\cdot\boldsymbol{\sigma},\hat{\mathfrak{g}}_{\boldsymbol{k}E}]-\hat{\Sigma}^{R}\hat{\mathfrak{g}}_{\boldsymbol{k}E}+\hat{\mathfrak{g}}_{\boldsymbol{k}E}\hat{\Sigma}^{A}\Bigg]e^{i\boldsymbol{k}\cdot\bar{\boldsymbol{x}}_{12}-iE\bar{t}_{12}}.
\end{aligned} \tag{C.9}$$

Next, we compute the Wigner representation of the right-hand side of Eq. (C.4),

$$(\hat{g}^{R})^{-1}\hat{g}^{K}-\hat{g}^{K}(\hat{g}^{A})^{-1}=\hat{\Sigma}^{K}\hat{g}^{A}-\hat{g}^{R}\hat{\Sigma}^{K}. \tag{C.4}$$

For simplicity, using the zeroth-order gradient approximation, the Wigner representation becomes the following:

$$\begin{aligned}
&\int \hat{\Sigma}^{K}(1,3)\hat{g}^{A}(3,2)d3-\int \hat{g}^{R}(1,3)\hat{\Sigma}^{K}(3,2)d3\simeq\int\frac{d^2\boldsymbol{k}dE}{(2\pi)^3}\Big[\hat{\Sigma}^{K}\hat{g}^{A}_{\boldsymbol{k}E}-\hat{g}^{R}_{\boldsymbol{k}E}\hat{\Sigma}^{K}\Big]e^{i\boldsymbol{k}\cdot\bar{\boldsymbol{x}}_{12}-iE\bar{t}_{12}} \\
&\quad=u^2n_{\text{imp}}\int\frac{d^2\boldsymbol{k}dE}{(2\pi)^3}\int\frac{d^2\boldsymbol{k}'}{(2\pi)^2}\Big[\hat{\mathfrak{g}}_{\boldsymbol{k}'E}\hat{g}^{A}(\boldsymbol{k},E)-\hat{g}^{R}(\boldsymbol{k},E)\hat{\mathfrak{g}}_{\boldsymbol{k}'E}\Big]e^{i\boldsymbol{k}\cdot\bar{\boldsymbol{x}}_{12}-iE\bar{t}_{12}}.
\end{aligned} \tag{C.10}$$

Here, u is the coefficient of a delta-function-type impurity potential, $v(\boldsymbol{r})=u\delta(\boldsymbol{r})$, and n_{imp} represents the impurity concentration. From Eqs. (C.9) and (C.10), the Wigner representation of Eq. (C.4) can be expressed as follows:

$$\begin{aligned}
&i\frac{\partial\hat{\mathfrak{g}}_{\boldsymbol{k}E}}{\partial t_{12}}+\frac{i}{2}\Big\{\frac{\partial(\xi_{\boldsymbol{k}}-\boldsymbol{h}_{\text{eff}}\cdot\boldsymbol{\sigma})}{\partial\boldsymbol{k}},\frac{\partial\hat{\mathfrak{g}}_{\boldsymbol{k}E}}{\partial\boldsymbol{x}_{12}}\Big\}+[\boldsymbol{h}_{\text{eff}}\cdot\hat{\boldsymbol{\sigma}},\hat{\mathfrak{g}}_{\boldsymbol{k}E}]-\hat{\Sigma}^{R}\hat{\mathfrak{g}}_{\boldsymbol{k}E}+\hat{\mathfrak{g}}_{\boldsymbol{k}E}\hat{\Sigma}^{A} \\
&=u^2n_{\text{imp}}\int\frac{d^2\boldsymbol{k}'}{(2\pi)^2}\Big[\hat{\mathfrak{g}}_{\boldsymbol{k}'E}\hat{g}^{A}(\boldsymbol{k},E)-\hat{g}^{R}(\boldsymbol{k},E)\hat{\mathfrak{g}}_{\boldsymbol{k}'E}\Big].
\end{aligned} \tag{C.11}$$

Here, by defining a function dependent only on momentum as $\hat{u}_{\boldsymbol{k}}$, $\hat{\mathfrak{g}}_{\boldsymbol{k}E}$ can be written as

$$\hat{\mathfrak{g}}_{\boldsymbol{k}E}=\hat{g}^{R}(\boldsymbol{k},E)\hat{u}_{\boldsymbol{k}}-\hat{u}_{\boldsymbol{k}}\hat{g}^{A}(\boldsymbol{k},E). \tag{C.12}$$

Integrating this expression over E gives

$$\int \frac{dE}{2\pi}\hat{\mathfrak{g}}_{\boldsymbol{k}E} = -i\hat{u}_{\boldsymbol{k}}, \tag{C.13}$$

which is independent of E, allowing transport physical quantities to be calculated using this $\hat{u}_{\boldsymbol{k}}(\boldsymbol{x}, t)$. Substituting Eq. (C.12) into Eq. (C.11) and performing the energy integration yields the following expression:

$$\begin{aligned}&\frac{\partial \hat{u}_{\boldsymbol{k}}}{\partial t} + \frac{1}{2}\left\{\frac{\partial(\xi_{\boldsymbol{k}} - \boldsymbol{h}_{\rm eff}(\boldsymbol{k})\cdot\hat{\boldsymbol{\sigma}})}{\partial \boldsymbol{k}}, \frac{\partial \hat{u}_{\boldsymbol{k}}}{\partial \boldsymbol{x}}\right\} - i[\boldsymbol{h}_{\rm eff}(\boldsymbol{k})\cdot\hat{\boldsymbol{\sigma}}, \hat{u}_{\boldsymbol{k}}] \\ &= \frac{\pi u^2 n_{\rm imp}}{4}\int \frac{d^2\boldsymbol{k}'}{(2\pi)^2}\sum_{\gamma,\gamma'=\pm}\delta(E^{\gamma}_{\boldsymbol{k}} - E^{\gamma'}_{\boldsymbol{k}'})\left[2(\hat{u}_{\boldsymbol{k}'} - \hat{u}_{\boldsymbol{k}}) - \left\{\gamma\frac{\boldsymbol{h}_{\rm eff}(\boldsymbol{k})\cdot\hat{\boldsymbol{\sigma}}}{h_{\rm eff}} + \gamma'\frac{\boldsymbol{h}_{\rm eff}(\boldsymbol{k}')\cdot\hat{\boldsymbol{\sigma}}}{h_{\rm eff}}, \hat{u}_{\boldsymbol{k}'} - \hat{u}_{\boldsymbol{k}}\right\}\right].\end{aligned} \tag{C.14}$$

Here, assuming that Γ is small, we can apply Sokhotsky's formula

$$\frac{1}{E^{\gamma'}_{\boldsymbol{k}'} - E^{\gamma}_{\boldsymbol{k}} + i\Gamma} = P\frac{1}{E^{\gamma'}_{\boldsymbol{k}'} - E^{\gamma}_{\boldsymbol{k}}} - i\pi\delta(E^{\gamma'}_{\boldsymbol{k}'} - E^{\gamma}_{\boldsymbol{k}}), \tag{C.15}$$

and neglect both the second-order terms in $\boldsymbol{h}_{\rm eff}$ and the principal value terms. By expressing the distribution function as $\hat{f}_{\boldsymbol{k}} = 1 - 2\hat{u}_{\boldsymbol{k}}$, the equation for this $\hat{f}_{\boldsymbol{k}}$ is given as follows:

$$\begin{aligned}&\frac{\partial \hat{f}_{\boldsymbol{k}}}{\partial t_{12}} + \frac{1}{2}\left\{\frac{\partial(\xi_{\boldsymbol{k}} - \boldsymbol{h}_{\rm eff}(\boldsymbol{k})\cdot\hat{\boldsymbol{\sigma}})}{\partial \boldsymbol{k}}, \frac{\partial \hat{f}_{\boldsymbol{k}}}{\partial \boldsymbol{x}_{12}}\right\} - i[\boldsymbol{h}_{\rm eff}(\boldsymbol{k})\cdot\hat{\boldsymbol{\sigma}}, \hat{f}_{\boldsymbol{k}}] \\ &\simeq 2\pi u^2 n_{\rm imp}\int \frac{d^2\boldsymbol{k}'}{(2\pi)^2}\left[(\hat{f}_{\boldsymbol{k}'} - \hat{f}_{\boldsymbol{k}})\cdot\delta(\xi_{\boldsymbol{k}} - \xi_{\boldsymbol{k}'}) - \frac{1}{2}\left\{[\boldsymbol{h}_{\rm eff}(\boldsymbol{k}) - \boldsymbol{h}_{\rm eff}(\boldsymbol{k}')]\cdot\hat{\boldsymbol{\sigma}}, \hat{f}_{\boldsymbol{k}'} - \hat{f}_{\boldsymbol{k}}\right\}\delta'(\xi_{\boldsymbol{k}} - \xi_{\boldsymbol{k}'})\right].\end{aligned} \tag{C.16}$$

Here, $\delta(E^{\gamma}_{\boldsymbol{k}} - E^{\gamma'}_{\boldsymbol{k}'})$ is approximated up to the first order in $\boldsymbol{h}_{\rm eff}$ as

$$\delta(E^{\gamma}_{\boldsymbol{k}} - E^{\gamma'}_{\boldsymbol{k}'}) \simeq \delta(\xi_{\boldsymbol{k}} - \xi_{\boldsymbol{k}'}) + [\gamma h_{\rm eff}(\varphi) - \gamma' h_{\rm eff}(\varphi')]\delta'(\xi_{\boldsymbol{k}} - \xi_{\boldsymbol{k}'}). \tag{C.17}$$

Equation (C.16) represents the Boltzmann equation for a 2DEG with the Rashba and Dresselhaus SOCs.

In Eq. (C.16), the 2×2 distribution function $\hat{f}_{\boldsymbol{k}}$ is given by

$$\hat{f}_{\boldsymbol{k}} = \begin{pmatrix} f^{\uparrow\uparrow}_{\boldsymbol{k}} & f^{\uparrow\downarrow}_{\boldsymbol{k}} \\ f^{\downarrow\uparrow}_{\boldsymbol{k}} & f^{\downarrow\downarrow}_{\boldsymbol{k}} \end{pmatrix} \tag{C.18}$$

and is expressed in the basis of the eigenstates $|\uparrow\rangle$, $|\downarrow\rangle$ of σ_z. However, below, Eq. (C.16) will be rewritten in terms of the eigenstates $|\boldsymbol{k}\gamma\rangle$ of Eq. (3.8) as the basis. Here, it is assumed that the 2DEG has translational symmetry and $\hat{f}_{\boldsymbol{k}}$ does not depend on position. Using the unitary

matrix

$$U(\varphi) = \begin{pmatrix} |\boldsymbol{k}+\rangle & |\boldsymbol{k}-\rangle \end{pmatrix} = \frac{1}{\sqrt{2}} \begin{pmatrix} C(\varphi) & C(\varphi) \\ 1 & -1 \end{pmatrix}, \tag{C.19}$$

Eq. (C.16) is unitarily transformed as follows:

$$\begin{aligned} & U^{\dagger}(\varphi)\Big[\frac{\partial \hat{f}_{\boldsymbol{k}}}{\partial t} - i[\boldsymbol{h}_{\mathrm{eff}}(\boldsymbol{k}) \cdot \hat{\boldsymbol{\sigma}}, \hat{f}_{\boldsymbol{k}}]\Big] U(\varphi) \\ & = U^{\dagger}(\varphi)\Big[2\pi u^2 n_{\mathrm{imp}} \int \frac{d^2\boldsymbol{k}'}{(2\pi)^2}\Big((\hat{f}_{\boldsymbol{k}'} - \hat{f}_{\boldsymbol{k}}) \cdot \delta(\xi_{\boldsymbol{k}} - \xi_{\boldsymbol{k}'}) \\ & \quad - \frac{1}{2}\Big\{[\boldsymbol{h}_{\mathrm{eff}}(\boldsymbol{k}) - \boldsymbol{h}_{\mathrm{eff}}(\boldsymbol{k}')] \cdot \hat{\boldsymbol{\sigma}}, \hat{f}_{\boldsymbol{k}'} - \hat{f}_{\boldsymbol{k}}\Big\}\delta'(\xi_{\boldsymbol{k}} - \xi_{\boldsymbol{k}'})\Big)\Big] U(\varphi). \end{aligned} \tag{C.20}$$

The left-hand side of Eq. (C.20) can be computed as follows:

$$U^{\dagger}(\varphi)\Big[\frac{\partial \hat{f}_{\boldsymbol{k}}}{\partial t} - i[\boldsymbol{h}_{\mathrm{eff}}(\boldsymbol{k}) \cdot \hat{\boldsymbol{\sigma}}, \hat{f}_{\boldsymbol{k}}]\Big] U(\varphi) = \begin{pmatrix} \frac{\partial f_{\boldsymbol{k}}^{++}}{\partial t} & \frac{\partial f_{\boldsymbol{k}}^{+-}}{\partial t} \\ \frac{\partial f_{\boldsymbol{k}}^{-+}}{\partial t} & \frac{\partial f_{\boldsymbol{k}}^{--}}{\partial t} \end{pmatrix} - i \begin{pmatrix} 0 & -2h_{\mathrm{eff}}(\varphi) f_{\boldsymbol{k}}^{+-} \\ 2h_{\mathrm{eff}}(\varphi) f_{\boldsymbol{k}}^{-+} & 0 \end{pmatrix}. \tag{C.21}$$

Here, the distribution function in the basis of $|\boldsymbol{k}\gamma\rangle$ is written as follows:

$$U^{\dagger}(\varphi)\hat{f}_{\boldsymbol{k}}U(\varphi) = U^{\dagger}(\varphi) \begin{pmatrix} f_{\boldsymbol{k}}^{\uparrow\uparrow} & f_{\boldsymbol{k}}^{\uparrow\downarrow} \\ f_{\boldsymbol{k}}^{\downarrow\uparrow} & f_{\boldsymbol{k}}^{\downarrow\downarrow} \end{pmatrix} U(\varphi) = \begin{pmatrix} f_{\boldsymbol{k}}^{++} & f_{\boldsymbol{k}}^{+-} \\ f_{\boldsymbol{k}}^{-+} & f_{\boldsymbol{k}}^{--} \end{pmatrix}. \tag{C.22}$$

Then, by further calculating the right-hand side of Eq. (C.20), we obtain the Boltzmann equations for the four components of the distribution function matrix in Eq. (C.22) as follows:

$$\begin{aligned} \frac{\partial f_{\boldsymbol{k}}^{++}}{\partial t} = \pi u^2 n_{\mathrm{imp}} \int \frac{d^2\boldsymbol{k}'}{(2\pi)^2}\Big[& (f_{\boldsymbol{k}'}^{++} - f_{\boldsymbol{k}}^{++})[1 + \hat{\boldsymbol{h}}_{\mathrm{eff}}(\varphi) \cdot \hat{\boldsymbol{h}}_{\mathrm{eff}}(\varphi')]\delta(E_{\boldsymbol{k}}^{+} - E_{\boldsymbol{k}'}^{+}) \\ & + (f_{\boldsymbol{k}'}^{--} - f_{\boldsymbol{k}}^{++})[1 - \hat{\boldsymbol{h}}_{\mathrm{eff}}(\varphi) \cdot \hat{\boldsymbol{h}}_{\mathrm{eff}}(\varphi')]\delta(E_{\boldsymbol{k}}^{+} - E_{\boldsymbol{k}'}^{-}) \\ & + i\hat{\boldsymbol{h}}_{\mathrm{eff}}(\varphi) \cdot \hat{\boldsymbol{h}}_{\mathrm{eff}}^{\perp}(\varphi')\Big\{-f_{\boldsymbol{k}'}^{+-}\delta(\xi_{\boldsymbol{k}} - \xi_{\boldsymbol{k}'}) + f_{\boldsymbol{k}'}^{-+}\delta(\xi_{\boldsymbol{k}} - \xi_{\boldsymbol{k}'}) \\ & + h_{\mathrm{eff}}(\varphi)(-f_{\boldsymbol{k}'}^{+-} + f_{\boldsymbol{k}'}^{-+})\delta'(\xi_{\boldsymbol{k}} - \xi_{\boldsymbol{k}'}) + h_{\mathrm{eff}}(\varphi')(f_{\boldsymbol{k}}^{+-} - f_{\boldsymbol{k}}^{-+})\delta'(\xi_{\boldsymbol{k}} - \xi_{\boldsymbol{k}'})\Big\}\Big], \end{aligned} \tag{C.23}$$

$$\begin{aligned} \frac{\partial f_{\boldsymbol{k}}^{--}}{\partial t} = \pi u^2 n_{\mathrm{imp}} \int \frac{d^2\boldsymbol{k}'}{(2\pi)^2}\Big[& (f_{\boldsymbol{k}'}^{++} - f_{\boldsymbol{k}}^{--})[1 - \hat{\boldsymbol{h}}_{\mathrm{eff}}(\varphi) \cdot \hat{\boldsymbol{h}}_{\mathrm{eff}}(\varphi')]\delta(E_{\boldsymbol{k}}^{-} - E_{\boldsymbol{k}'}^{+}) \\ & + (f_{\boldsymbol{k}'}^{--} - f_{\boldsymbol{k}}^{--})[1 + \hat{\boldsymbol{h}}_{\mathrm{eff}}(\varphi) \cdot \hat{\boldsymbol{h}}_{\mathrm{eff}}(\varphi')]\delta(E_{\boldsymbol{k}}^{-} - E_{\boldsymbol{k}'}^{-}) \\ & + i\hat{\boldsymbol{h}}_{\mathrm{eff}}(\varphi) \cdot \hat{\boldsymbol{h}}_{\mathrm{eff}}^{\perp}(\varphi')\Big\{f_{\boldsymbol{k}'}^{+-}\delta(\xi_{\boldsymbol{k}} - \xi_{\boldsymbol{k}'}) - f_{\boldsymbol{k}'}^{-+}\delta(\xi_{\boldsymbol{k}} - \xi_{\boldsymbol{k}'}) \\ & + h_{\mathrm{eff}}(\varphi)(-f_{\boldsymbol{k}'}^{+-} + f_{\boldsymbol{k}'}^{-+})\delta'(\xi_{\boldsymbol{k}} - \xi_{\boldsymbol{k}'}) + h_{\mathrm{eff}}(\varphi')(f_{\boldsymbol{k}}^{+-} - f_{\boldsymbol{k}}^{-+})\delta'(\xi_{\boldsymbol{k}} - \xi_{\boldsymbol{k}'})\Big\}\Big], \end{aligned} \tag{C.24}$$

$$\frac{\partial f_{\boldsymbol{k}}^{+-}}{\partial t} + 2ih_{\mathrm{eff}}(\varphi) f_{\boldsymbol{k}}^{+-} = \pi u^2 n_{\mathrm{imp}} \int \frac{d^2\boldsymbol{k}'}{(2\pi)^2} \Bigg[\Big\{ (f_{\boldsymbol{k}'}^{+-} - f_{\boldsymbol{k}}^{+-})[1 + \hat{\boldsymbol{h}}_{\mathrm{eff}}(\varphi) \cdot \hat{\boldsymbol{h}}_{\mathrm{eff}}(\varphi')] + (f_{\boldsymbol{k}'}^{-+} - f_{\boldsymbol{k}}^{+-})[1 - \hat{\boldsymbol{h}}_{\mathrm{eff}}(\varphi) \cdot \hat{\boldsymbol{h}}_{\mathrm{eff}}(\varphi')] \Big\} \delta(\xi_{\boldsymbol{k}} - \xi_{\boldsymbol{k}'}) + i\hat{\boldsymbol{h}}_{\mathrm{eff}}(\varphi) \cdot \hat{\boldsymbol{h}}_{\mathrm{eff}}^{\perp}(\varphi') \Big\{ (-f_{\boldsymbol{k}'}^{++} + f_{\boldsymbol{k}'}^{--}) \delta(\xi_{\boldsymbol{k}} - \xi_{\boldsymbol{k}'}) + h_{\mathrm{eff}}(\varphi')(f_{\boldsymbol{k}'}^{++} + f_{\boldsymbol{k}'}^{--} - f_{\boldsymbol{k}}^{++} - f_{\boldsymbol{k}}^{--}) \delta'(\xi_{\boldsymbol{k}} - \xi_{\boldsymbol{k}'}) \Big\} \Bigg], \tag{C.25}$$

$$\frac{\partial f_{\boldsymbol{k}}^{-+}}{\partial t} - 2ih_{\mathrm{eff}}(\varphi) f_{\boldsymbol{k}}^{-+} = \pi u^2 n_{\mathrm{imp}} \int \frac{d^2\boldsymbol{k}'}{(2\pi)^2} \Bigg[\Big\{ (f_{\boldsymbol{k}'}^{+-} - f_{\boldsymbol{k}}^{-+})[1 - \hat{\boldsymbol{h}}_{\mathrm{eff}}(\varphi) \cdot \hat{\boldsymbol{h}}_{\mathrm{eff}}(\varphi')] + (f_{\boldsymbol{k}'}^{-+} - f_{\boldsymbol{k}}^{-+})[1 + \hat{\boldsymbol{h}}_{\mathrm{eff}}(\varphi) \cdot \hat{\boldsymbol{h}}_{\mathrm{eff}}(\varphi')] \Big\} \delta(\xi_{\boldsymbol{k}} - \xi_{\boldsymbol{k}'}) + i\hat{\boldsymbol{h}}_{\mathrm{eff}}(\varphi) \cdot \hat{\boldsymbol{h}}_{\mathrm{eff}}^{\perp}(\varphi') \Big\{ (f_{\boldsymbol{k}'}^{++} - f_{\boldsymbol{k}'}^{--}) \delta(\xi_{\boldsymbol{k}} - \xi_{\boldsymbol{k}'}) - h_{\mathrm{eff}}(\varphi')(f_{\boldsymbol{k}'}^{++} + f_{\boldsymbol{k}'}^{--} - f_{\boldsymbol{k}}^{++} - f_{\boldsymbol{k}}^{--}) \delta'(\xi_{\boldsymbol{k}} - \xi_{\boldsymbol{k}'}) \Big\} \Bigg]. \tag{C.26}$$

Here, the unit vector perpendicular to $\hat{\boldsymbol{h}}_{\mathrm{eff}} = (h_x, h_y)/h_{\mathrm{eff}}$ is denoted as $\hat{\boldsymbol{h}}_{\mathrm{eff}}^{\perp} \equiv (-h_y, h_x)/h_{\mathrm{eff}}$.

C.2 Boltzmann Equation in the Weak-Impurity Limit

In this section, following Ref. [81], we derive the Boltzmann equation in the weak-impurity limit. Here, the steady-state solution of the Boltzmann equation is considered and $\hbar$ is reinstated. First, by applying the relaxation-time approximation to the right-hand side of Eq. (C.25), Eq. (C.25) can be order estimated as follows:

$$\frac{2ih_{\mathrm{eff}}(\varphi) f_{\boldsymbol{k}}^{+-}}{\hbar} \sim \frac{f_{\boldsymbol{k}}^{\gamma\gamma} - f_0(\epsilon_{\boldsymbol{k}})}{\tau}, \frac{f_{\boldsymbol{k}}^{+-}}{\tau}, \frac{f_{\boldsymbol{k}}^{-+}}{\tau}. \tag{C.27}$$

Here, τ is the relaxation time, which can be expressed as $\tau = \hbar/\Gamma$ using Γ. In the weak-impurity limit $\hbar/\tau \ll \max(2k_{\mathrm{F}}\alpha, 2k_{\mathrm{F}}\beta) \ll \epsilon_{\mathrm{F}}$, the following equation holds:

$$\frac{f_{\boldsymbol{k}}^{+-}}{\tau} = \frac{\hbar}{2h_{\mathrm{eff}}(\varphi)\tau} \cdot \frac{2h_{\mathrm{eff}}(\varphi) f_{\boldsymbol{k}}^{+-}}{\hbar} \sim \frac{\hbar}{2k_{\mathrm{F}}\alpha\tau} \cdot \frac{2h_{\mathrm{eff}}(\varphi) f_{\boldsymbol{k}}^{+-}}{\hbar} \ll \frac{2h_{\mathrm{eff}}(\varphi) f_{\boldsymbol{k}}^{+-}}{\hbar}. \tag{C.28}$$

Here, the approximation $h_{\mathrm{eff}}(\varphi) \sim k_{\mathrm{F}}\alpha$ is used. From Eq. (C.28), the leading term on the right-hand side of Eq. (C.27) is $[f_{\boldsymbol{k}}^{\gamma\gamma} - f_0(\epsilon_{\boldsymbol{k}})]/\tau$, and Eq. (C.27) becomes the following:

$$\frac{2ih_{\mathrm{eff}}(\varphi) f_{\boldsymbol{k}}^{+-}}{\hbar} \sim \frac{\hbar}{2k_{\mathrm{F}}\alpha\tau} \cdot \frac{2k_{\mathrm{F}}\alpha[f_{\boldsymbol{k}}^{\gamma\gamma} - f_0(\epsilon_{\boldsymbol{k}})]}{\hbar}, \Rightarrow \frac{f_{\boldsymbol{k}}^{+-}}{f_{\boldsymbol{k}}^{\gamma\gamma} - f_0(\epsilon_{\boldsymbol{k}})} \sim \frac{\hbar}{2k_{\mathrm{F}}\alpha\tau} \ll 1. \tag{C.29}$$

Similarly, from Eq. (C.26), it can be shown that in the weak-impurity limit, $f_{\boldsymbol{k}}^{-+}/[f_{\boldsymbol{k}}^{\gamma\gamma} - f_0(\epsilon_{\boldsymbol{k}})] \ll 1$ holds. Thus, in the weak-impurity limit, the off-diagonal components of the distribution function in Eq. (C.22) are significantly smaller than the diagonal components. By neglecting

these off-diagonal components, Eqs. (C.23) and (C.24) become the following:

$$\frac{\partial f_{\boldsymbol{k}}^{++}}{\partial t} \simeq \frac{\pi u^2 n_{\mathrm{imp}}}{\hbar} \int \frac{d^2\boldsymbol{k}'}{(2\pi)^2} \Big[(f_{\boldsymbol{k}'}^{++} - f_{\boldsymbol{k}}^{++})[1 + \hat{\boldsymbol{h}}_{\mathrm{eff}}(\varphi) \cdot \hat{\boldsymbol{h}}_{\mathrm{eff}}(\varphi')]\delta(E_{\boldsymbol{k}}^{+} - E_{\boldsymbol{k}'}^{+}) + (f_{\boldsymbol{k}'}^{--} - f_{\boldsymbol{k}}^{++})[1 - \hat{\boldsymbol{h}}_{\mathrm{eff}}(\varphi) \cdot \hat{\boldsymbol{h}}_{\mathrm{eff}}(\varphi')]\delta(E_{\boldsymbol{k}}^{+} - E_{\boldsymbol{k}'}^{-}) \Big], \tag{C.30}$$

$$\frac{\partial f_{\boldsymbol{k}}^{--}}{\partial t} \simeq \frac{\pi u^2 n_{\mathrm{imp}}}{\hbar} \int \frac{d^2\boldsymbol{k}'}{(2\pi)^2} \Big[(f_{\boldsymbol{k}'}^{++} - f_{\boldsymbol{k}}^{--})[1 - \hat{\boldsymbol{h}}_{\mathrm{eff}}(\varphi) \cdot \hat{\boldsymbol{h}}_{\mathrm{eff}}(\varphi')]\delta(E_{\boldsymbol{k}}^{-} - E_{\boldsymbol{k}'}^{+}) + (f_{\boldsymbol{k}'}^{--} - f_{\boldsymbol{k}}^{--})[1 + \hat{\boldsymbol{h}}_{\mathrm{eff}}(\varphi) \cdot \hat{\boldsymbol{h}}_{\mathrm{eff}}(\varphi')]\delta(E_{\boldsymbol{k}}^{-} - E_{\boldsymbol{k}'}^{-}) \Big]. \tag{C.31}$$

The collision terms on the right-hand side of Eqs. (C.30) and (C.31) are consistent with the expression for the impurity collision term calculated using Fermi's golden rule in Eq. (5.7). Note that in the main text, $f_{\boldsymbol{k}}^{\gamma\gamma}$ is denoted by $f(\boldsymbol{k}, \gamma)$. This justifies the use of Fermi's golden rule for calculating the collision term in the weak-impurity limit, as conducted in Sec. 5.1.2. Furthermore, as discussed in Ref. [81], the off-diagonal components of the distribution function are negligible compared to the diagonal components when the transition rate of the tunneling Hamiltonian is sufficiently smaller than $2k_{\mathrm{F}}\alpha$. Thus, under this condition, we can calculate the collision term due to interfacial interactions using Fermi's golden rule, as conducted in Sec. 5.1.3.

Appendix D

Comparison with Relaxation-Time Approximation

In Sec. 5.2.5, comparison is made between the results for the charge current density induced by the IREE obtained from the full solution of the Boltzmann equation and those from the relaxation-time approximation in the case of $\alpha/\beta = 1$. This appendix further examines the spin and charge current densities induced by the IREE in the cases of the Rashba SOC ($\alpha/\beta = \infty$), $\alpha/\beta = 1.1$, and $\alpha/\beta = 3$, comparing the results derived from the full solution of the Boltzmann equation with those from the relaxation-time approximation.

Figure D.1 presents the results for the spin and charge current densities in the case of the Rashba SOC ($\alpha/\beta = \infty$). Both the spin and charge current densities exhibit similar qualitative behavior in the results from the full solution of the Boltzmann equation and the relaxation-time approximation. While the magnitude of the spin density differs between these two approaches, as indicated by the color plot range, the difference is not large enough to affect the order of magnitude.

Figure D.2 shows the results for $\alpha/\beta = 1.1$. The spin density displays the same θ dependence in both the full solution and relaxation-time approximation results. However, the charge current density demonstrates qualitatively different behavior, with a sign reversal occurring for $\hbar\omega_{\mathbf{0}} \lesssim 3k_{\mathrm{F}}\beta$ (see Sec. 5.2.5). Additionally, as observed from the color plot range, the spin density in the full solution is significantly larger than that in the relaxation-time approximation (see Fig. 5.7).

Finally, Fig. D.3 illustrates the results for $\alpha/\beta = 3$. In this case, the spin and charge current densities show nearly identical θ dependence in both the full solution and relaxation-time approximation results. Similarly to the case of $\alpha/\beta = \infty$, the magnitude of the spin density differs between the two approaches, but not to the extent of changing the order of magnitude. On the other hand, the θ dependence of the current density clearly differs between the full solution and the relaxation-time approximation, as seen from the angles where the current vanishes (the white regions).

In summary, for values of α/β that deviate from 1, the relaxation-time approximation yields

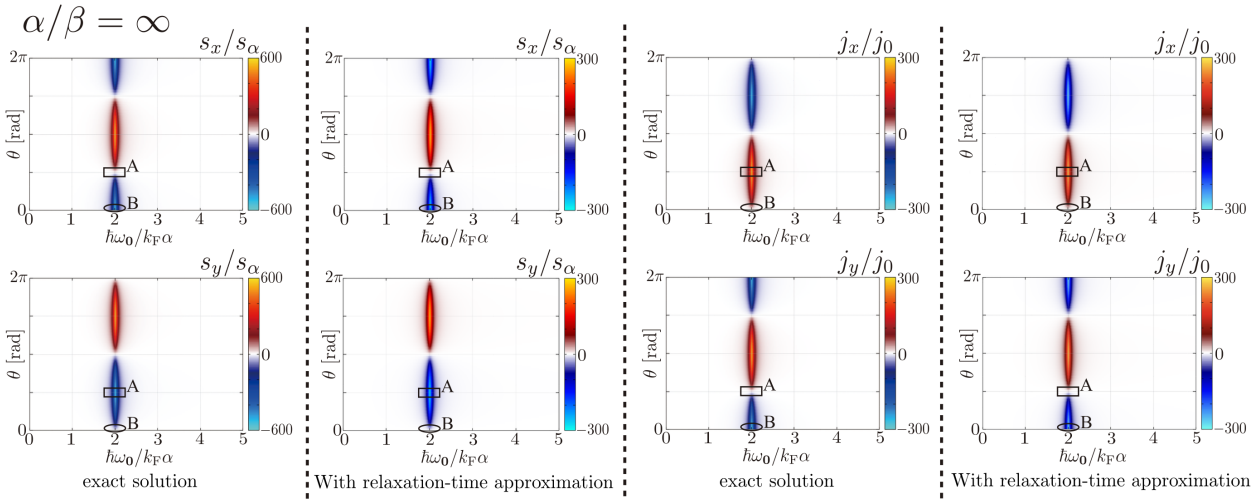

Figure D.1: Spin density $\boldsymbol{s} = (s_x, s_y)$ and charge current density $\boldsymbol{j} = (j_x, j_y)$ induced by the IREE for the Rashba SOC ($\alpha/\beta = \infty$), plotted as functions of the FMR frequency $\omega_\mathbf{0}$ and the local spin orientation θ in the FI. Results from both the full solution of the Boltzmann equation and the relaxation-time approximation are shown. Here, $\Gamma = 0.1 k_F \alpha$.

qualitatively correct results. However, near $\alpha/\beta = 1$, the results from the relaxation-time approximation exhibit qualitatively different behavior compared to those from the full solution. As discussed in Sec. 5.2.6, the spin conservation law holds for electrons on the Fermi surface at $\alpha/\beta = 1$, and the full solution corresponding to considering the vertex corrections in linear response theory captures this spin conservation. In contrast, the relaxation-time approximation does not account for spin conservation, leading to qualitative differences in behavior near $\alpha/\beta = 1$, where spin conservation is preserved. While the vertex corrections do not change the amplitude of the current density by the IREE so much, they change the θ dependence of the current density when α and β are in the same order.

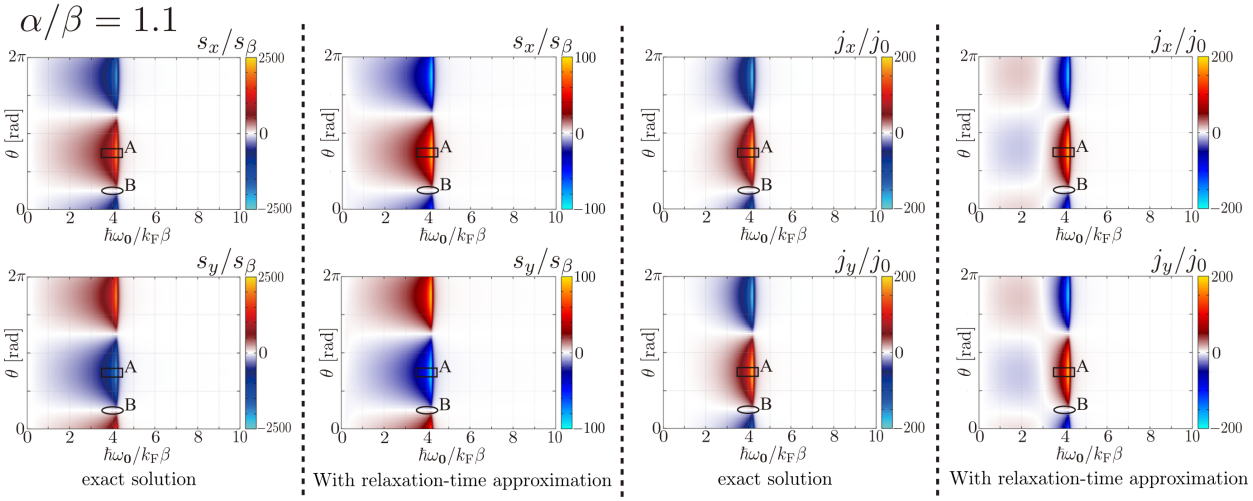

Figure D.2: Spin density $\boldsymbol{s} = (s_x, s_y)$ and charge current density $\boldsymbol{j} = (j_x, j_y)$ for $\alpha/\beta = 1.1$, plotted as functions of $\omega_\mathbf{0}$ and θ. Results from both the full solution and the relaxation-time approximation are shown. Here, $\Gamma = 0.1 k_F \beta$.

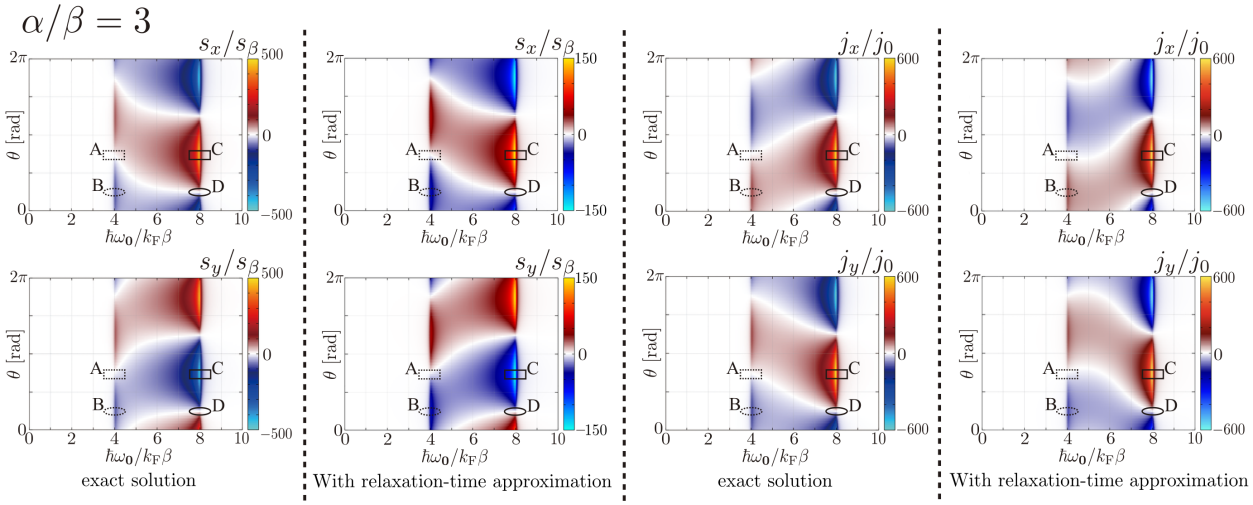

Figure D.3: Spin density $\boldsymbol{s} = (s_x, s_y)$ and charge current density $\boldsymbol{j} = (j_x, j_y)$ for $\alpha/\beta = 3$, plotted as functions of $\omega_\mathbf{0}$ and θ. Results from both the full solution and the relaxation-time approximation are shown. Here, $\Gamma = 0.1 k_F \beta$.

Appendix E

Derivation of $H_{\rm int}$

In this appendix, we derive the interfacial exchange coupling Hamiltonian introduced in Eqs. (6.6)-(6.10) and obtain the expressions for $\bar{T}$ and $\bar{\mathcal{T}}$, which appear in Eqs. (6.9) and (6.10).

First, by utilizing Eqs. (3.16), (3.17), and (3.18), we rewrite $H_{\rm FI}$ in Eq. (3.13) in terms of magnon creation and annihilation operators as follows:

$$H_{\rm FI} = \sum_{\langle i,j \rangle} J_{ij} \boldsymbol{S}_i \cdot \boldsymbol{S}_j - \hbar\gamma_{\rm g} \sum_i \boldsymbol{h}_{\rm dc} \cdot \boldsymbol{S}_i \tag{E.1}$$

$$= \text{const.} + J \sum_{\langle i,j \rangle} S_0(-b_i^\dagger b_i - b_j^\dagger b_j + b_i^\dagger b_j + b_j^\dagger b_i) + \hbar\gamma_{\rm g} h_{\rm dc} \sum_i b_i^\dagger b_i, \tag{E.2}$$

where the exchange coefficient J_{ij} is approximated as a constant J. Accordingly, the Hamiltonian can be rewritten as

$$H_{\rm FI} = \sum_{ij} b_i^\dagger (\hat{h}_{\rm 3D})_{ij} b_j, \tag{E.3}$$

$$(\hat{h}_{\rm 3D})_{ij} = \begin{cases} -6JS_0 + \hbar\gamma_{\rm g} h_{\rm dc}, & (\text{if } i = j), \\ JS_0, & (\text{if } i \text{ and } j \text{ are nearest neighbors}), \\ 0, & (\text{otherwise}). \end{cases} \tag{E.4}$$

In the following, we solve the eigenvalue equation

$$\sum_j (\hat{h}_{\rm 3D})_{ij} \psi_{\boldsymbol{n}}(x, y, z) = E_{\boldsymbol{n}} \psi_{\boldsymbol{n}}(x, y, z), \tag{E.5}$$

under periodic boundary conditions in the x and y directions and a fixed boundary condition in the z direction, where (x, y, z) (x, y, z: integers) is a coordinate of the three-dimensional cubic lattice. Assuming that the FI-2DEG interface is positioned at $z = 0$, with the number of unit cells along the x, y, and z directions denoted by N_x, N_y, and N_z, respectively, and the lattice

constant of the FI given by a, we can express the boundary conditions as

$$\psi(x+N_x a,y,z)=\psi(x,y+N_y a,z)=\psi(x,y,z),\quad \psi(x,y,0)=\psi(x,y,(N_z+1)a)=0. \tag{E.6}$$

By solving Eq. (E.5) subject to the boundary conditions given in Eq. (E.6), we obtain the eigenvalues and eigenfunctions of magnons as

$$E_{\boldsymbol{n}}=2|J|S_0(3-\cos k_x a-\cos k_y a-\cos k_z a)+\hbar\gamma_{\rm g}h_{\rm dc}, \tag{E.7}$$

$$\psi_{\boldsymbol{n}}(\boldsymbol{r}_i)=\frac{1}{\sqrt{N_x}}e^{ik_x x_i}\frac{1}{\sqrt{N_y}}e^{ik_y y_i}\sqrt{\frac{2}{N_z+1}}\sin(k_z z_i). \tag{E.8}$$

Here, by introducing $\boldsymbol{n}=(n_x,n_y,n_z)$, the magnon wavenumbers can be expressed as

$$k_x=\frac{2\pi n_x}{N_x a}\ (n_x \text{ is an integer}), \tag{E.9}$$

$$k_y=\frac{2\pi n_y}{N_y a}\ (n_y \text{ is an integer}), \tag{E.10}$$

$$k_z=\frac{n_z\pi}{(N_z+1)a}\ (n_z \text{ is a natural number}). \tag{E.11}$$

Next, we consider the form of the interfacial exchange coupling Hamiltonian at the FI-2DEG interface, which can be expressed as

$$H_{\rm int}=\sum_{\langle i,j\rangle}2T_{i,j}\boldsymbol{S}_i\cdot\boldsymbol{s}_j=H_{\rm int,d}+H_{\rm int,s}, \tag{E.12}$$

$$H_{\rm int,d}\equiv\sqrt{2S_0}\sum_{\langle i,j\rangle}(T_{i,j}b_i^\dagger s_j^{x'+}+T_{i,j}s_j^{x'-}b_i), \tag{E.13}$$

$$H_{\rm int,s}\equiv\sum_{\langle i,j\rangle}2T_{i,j}S_0 s_j^{x'}. \tag{E.14}$$

Here, i and j label the bonds at the FI-2DEG interface, and $T_{i,j}$ is a real number representing the coupling strength for each bond. Let $\boldsymbol{R}_j=(x_j,y_j)$ denote the in-plane coordinates of the interfacial site and $N_{\rm b}$ the total number of bonds at the FI-2DEG interface. Under these definitions, we obtain the following equations:

$$b_j=\sum_{\boldsymbol{n}}\psi_{\boldsymbol{n}}(\boldsymbol{R}_j,a)b_{\boldsymbol{n}}, \tag{E.15}$$

$$s_j^{x'-}=\frac{1}{N_{\rm b}}\sum_{\bar{\boldsymbol{q}}}e^{-i\bar{\boldsymbol{q}}\cdot\boldsymbol{R}_j}s_{\bar{\boldsymbol{q}}}^{x'-},\quad s_j^{x'+}=(s_j^{x'-})^\dagger=\frac{1}{N_{\rm b}}\sum_{\bar{\boldsymbol{q}}}e^{i\bar{\boldsymbol{q}}\cdot\boldsymbol{R}_j}s_{\bar{\boldsymbol{q}}}^{x'+},\quad s_j^{x'}=\frac{1}{N_{\rm b}}\sum_{\bar{\boldsymbol{q}}}e^{i\bar{\boldsymbol{q}}\cdot\boldsymbol{R}_j}s_{\bar{\boldsymbol{q}}}^{x'}, \tag{E.16}$$

where we assumed that the number of 2DEG unit cells matches the number of interfacial bonds. By applying these transformations, we can rewrite Eqs. (E.13) and (E.14) as

$$H_{\mathrm{int,d}} = \frac{2\sqrt{S_0}}{\sqrt{N_{\mathrm{FI}}}N_{\mathrm{b}}} \sum_{\langle i,j\rangle} \sum_{\boldsymbol{k}} \sum_{\bar{\boldsymbol{q}}} \sin(k_z a) \left[T_{i,j} e^{i(-\boldsymbol{k}_\parallel \cdot \boldsymbol{R}_i + \bar{\boldsymbol{q}} \cdot \boldsymbol{R}_j)} b_{\boldsymbol{k}}^\dagger s_{\bar{\boldsymbol{q}}}^{x'+} + T_{i,j} e^{-i(-\boldsymbol{k}_\parallel \cdot \boldsymbol{R}_i + \bar{\boldsymbol{q}} \cdot \boldsymbol{R}_j)} s_{\bar{\boldsymbol{q}}}^{x'-} b_{\boldsymbol{k}} \right], \tag{E.17}$$

$$H_{\mathrm{int,s}} = \frac{2S_0}{N_{\mathrm{b}}} \sum_j \sum_{\bar{\boldsymbol{q}}} T_j e^{i\bar{\boldsymbol{q}} \cdot \boldsymbol{R}_j} s_{\bar{\boldsymbol{q}}}^{x'}. \tag{E.18}$$

Here, we used the approximation $1/\sqrt{N_z+1} \simeq 1/\sqrt{N_z}$ under the condition $N_z \gg 1$. The constant $N_{\mathrm{FI}} = N_x N_y N_z$ represents the total number of unit cells in the FI, $\boldsymbol{k}_\parallel = (k_x, k_y)$ denotes the in-plane components of the magnon wavevector $\boldsymbol{k} = (k_x, k_y, k_z)$, and $\bar{\boldsymbol{q}} = (\bar{q}_x, \bar{q}_y)$ corresponds to the wavevector of the 2DEG electrons. Using Eqs. (E.17) and (E.18), we can express the transition rate induced by interfacial interactions as Eq. (6.11):

$$\begin{aligned} Q_{\boldsymbol{k},\gamma \to \boldsymbol{k}',\gamma'} = \sum_{\boldsymbol{q},\boldsymbol{q}'} \sum_{N_{\boldsymbol{q}}, N'_{\boldsymbol{q}'}} & \frac{2\pi}{\hbar} |\langle \boldsymbol{k}'\gamma' | \langle N'_{\boldsymbol{q}'} | H_{\mathrm{int,d}} | \boldsymbol{k}\gamma \rangle | N_{\boldsymbol{q}} \rangle|^2 \delta(E_{\boldsymbol{k}'}^{\gamma'} + N'_{\boldsymbol{q}'} \hbar\omega_{\boldsymbol{q}'} - E_{\boldsymbol{k}}^{\gamma} - N_{\boldsymbol{q}} \hbar\omega_{\boldsymbol{q}}) \rho(N_{\boldsymbol{q}}) \\ & + \frac{2\pi}{\hbar} |\langle \boldsymbol{k}'\gamma' | H_{\mathrm{int,s}} | \boldsymbol{k}\gamma \rangle|^2 \delta(E_{\boldsymbol{k}'}^{\gamma'} - E_{\boldsymbol{k}}^{\gamma}). \end{aligned} \tag{E.19}$$

We evaluate the squared matrix elements appearing in this expression. In the following analysis, we assume that the lattice constants of the FI and 2DEG are identical and that only the bonds directly facing each other at the FI-2DEG interface contribute to the coupling. Defining $T_j \equiv \sum_i T_{i,j}$, we adopt the following interfacial model for the FI-2DEG interface:

$$\langle T_j \rangle_{\mathrm{ave}} = T_1, \quad \langle \delta T_j \delta T_{j'} \rangle_{\mathrm{ave}} = T_2^2 \delta_{j,j'}, \tag{E.20}$$

$$\delta T_j \equiv T_j - \langle T_j \rangle_{\mathrm{ave}}. \tag{E.21}$$

Here, $\langle \cdots \rangle_{\mathrm{ave}}$ represents the configurational average over interfacial bonds, and T_1 and T_2 are constants. Based on this interfacial model, we compute the configurationally averaged squared matrix elements as follows:

$$\begin{aligned} & \langle |\langle \boldsymbol{k}'\gamma' | \langle N'_{\boldsymbol{q}'} | H_{\mathrm{int,d}} | \boldsymbol{k}\gamma \rangle | N_{\boldsymbol{q}} \rangle|^2 \rangle_{\mathrm{ave}} \\ & = \frac{4S_0}{N_{\mathrm{FI}} N_{\mathrm{b}}^2} \sum_{\boldsymbol{k}_1} \sum_{\bar{\boldsymbol{q}}_1} \sum_{\boldsymbol{k}_2} \sum_{\bar{\boldsymbol{q}}_2} \sin(k_{1z} a) \sin(k_{2z} a) \left[T_1^2 N_{\mathrm{b}}^2 \delta_{\boldsymbol{k}_{2\parallel}, \bar{\boldsymbol{q}}_2} \delta_{\boldsymbol{k}_{1\parallel}, \bar{\boldsymbol{q}}_1} + \sum_{j_1} T_2^2 e^{i(-\boldsymbol{k}_{1\parallel} + \bar{\boldsymbol{q}}_1 + \boldsymbol{k}_{2\parallel} - \bar{\boldsymbol{q}}_2) \cdot \boldsymbol{R}_{j_1}} \right] \\ & \quad \times \langle \boldsymbol{k}'\gamma' | \langle N'_{\boldsymbol{q}'} | b_{\boldsymbol{k}_1}^\dagger s_{\bar{\boldsymbol{q}}_1}^{x'+} | \boldsymbol{k}\gamma \rangle | N_{\boldsymbol{q}} \rangle \langle \boldsymbol{k}\gamma | \langle N_{\boldsymbol{q}} | b_{\boldsymbol{k}_2} s_{\bar{\boldsymbol{q}}_2}^{x'-} | \boldsymbol{k}'\gamma' \rangle | N'_{\boldsymbol{q}'} \rangle + \mathrm{h.c.}, \end{aligned} \tag{E.22}$$

$$\begin{aligned} & \langle |\langle \boldsymbol{k}'\gamma' | H_{\mathrm{int,s}} | \boldsymbol{k}\gamma \rangle|^2 \rangle_{\mathrm{ave}} \\ & = \left(\frac{2S_0}{N_{\mathrm{b}}} \right)^2 \sum_{\bar{\boldsymbol{q}}_1} \sum_{\bar{\boldsymbol{q}}_2} N_{\mathrm{b}} \left[T_1^2 N_{\mathrm{b}} \delta_{\bar{\boldsymbol{q}}_2, \boldsymbol{0}} \delta_{\bar{\boldsymbol{q}}_1, \boldsymbol{0}} + T_2^2 \delta_{\bar{\boldsymbol{q}}_1, \bar{\boldsymbol{q}}_2} \right] \langle \boldsymbol{k}'\gamma' | s_{\bar{\boldsymbol{q}}_1}^{x'} | \boldsymbol{k}\gamma \rangle \langle \boldsymbol{k}\gamma | (s_{\bar{\boldsymbol{q}}_2}^{x'})^\dagger | \boldsymbol{k}'\gamma' \rangle. \end{aligned} \tag{E.23}$$

Here, h.c. denotes the Hermitian conjugate.

Next, we evaluate the squared matrix elements using the momentum representation of H_{int} provided in Eqs. (6.6)-(6.10):

$$H_{\mathrm{int}} = H_{\mathrm{int,d}} + H_{\mathrm{int,s}}, \tag{E.24}$$

$$H_{\mathrm{int,d}} = \sum_{\boldsymbol{q}} \sum_{\bar{\boldsymbol{q}}} (T_{\boldsymbol{q},\bar{\boldsymbol{q}}} S_{\boldsymbol{q}}^{x'+} s_{\bar{\boldsymbol{q}}}^{x'-} + T_{\boldsymbol{q},\bar{\boldsymbol{q}}}^{*} S_{\boldsymbol{q}}^{x'-} s_{\bar{\boldsymbol{q}}}^{x'+}), \tag{E.25}$$

$$H_{\mathrm{int,s}} = \sum_{\bar{\boldsymbol{q}}} \mathcal{T}_{\boldsymbol{0},\bar{\boldsymbol{q}}} S_0 s_{\bar{\boldsymbol{q}}}^{x'}, \tag{E.26}$$

$$\text{dirty interface} : T_{\boldsymbol{q},\bar{\boldsymbol{q}}} = \bar{T} \sin(q_z a),\ \mathcal{T}_{\boldsymbol{0},\bar{\boldsymbol{q}}} = \bar{\mathcal{T}}, \tag{E.27}$$

$$\text{clean interface} : T_{\boldsymbol{q},\bar{\boldsymbol{q}}} = \bar{T} \sin(q_z a) \delta_{\boldsymbol{q}_\parallel,\bar{\boldsymbol{q}}},\ \mathcal{T}_{\boldsymbol{0},\bar{\boldsymbol{q}}} = \bar{\mathcal{T}} \delta_{\bar{\boldsymbol{q}},\boldsymbol{0}}. \tag{E.28}$$

First, using Eq. (E.27), the squared matrix elements for a dirty interface can be calculated as:

$$\begin{aligned}
&|\langle \boldsymbol{k}'\gamma'|\langle N'_{\boldsymbol{q}'}|H_{\mathrm{int,d}}|\boldsymbol{k}\gamma\rangle|N_{\boldsymbol{q}}\rangle|^2 \\
&= \sum_{\boldsymbol{k}_1} \sum_{\bar{\boldsymbol{q}}_1} \sum_{\boldsymbol{k}_2} \sum_{\bar{\boldsymbol{q}}_2} \Big[\bar{T}^2 \sin(k_{1z}a) \sin(k_{2z}a) \langle \boldsymbol{k}'\gamma'|\langle N'_{\boldsymbol{q}'}|S_{\boldsymbol{k}_1}^{x'-} s_{\bar{\boldsymbol{q}}_1}^{x'+}|\boldsymbol{k}\gamma\rangle|N_{\boldsymbol{q}}\rangle\langle \boldsymbol{k}\gamma|\langle N_{\boldsymbol{q}}|S_{\boldsymbol{k}_2}^{x'+} s_{\bar{\boldsymbol{q}}_2}^{x'-}|\boldsymbol{k}'\gamma'\rangle|N'_{\boldsymbol{q}'}\rangle \Big] \\
&\quad + \text{h.c.},
\end{aligned} \tag{E.29}$$

$$|\langle \boldsymbol{k}'\gamma'|H_{\mathrm{int,s}}|\boldsymbol{k}\gamma\rangle|^2 = \sum_{\bar{\boldsymbol{q}}_1} \sum_{\bar{\boldsymbol{q}}_2} \bar{\mathcal{T}}^2 S_0^2 \langle \boldsymbol{k}'\gamma'|s_{\bar{\boldsymbol{q}}_1}^{x'}|\boldsymbol{k}\gamma\rangle\langle \boldsymbol{k}\gamma|(s_{\bar{\boldsymbol{q}}_2}^{x'})^\dagger|\boldsymbol{k}'\gamma'\rangle. \tag{E.30}$$

Next, using Eq. (E.28), we obtain the squared matrix elements for a clean interface as

$$\begin{aligned}
&|\langle \boldsymbol{k}'\gamma'|\langle N'_{\boldsymbol{q}'}|H_{\mathrm{int,d}}|\boldsymbol{k}\gamma\rangle|N_{\boldsymbol{q}}\rangle|^2 \\
&= \sum_{\boldsymbol{k}_1} \sum_{\bar{\boldsymbol{q}}_1} \sum_{\boldsymbol{k}_2} \sum_{\bar{\boldsymbol{q}}_2} \bar{T}^2 \sin(k_{1z}a) \sin(k_{2z}a) \delta_{\boldsymbol{k}_{1\parallel},\bar{\boldsymbol{q}}_1} \delta_{\boldsymbol{k}_{2\parallel},\bar{\boldsymbol{q}}_2} \\
&\quad \times \Big[\langle \boldsymbol{k}'\gamma'|\langle N'_{\boldsymbol{q}'}|S_{\boldsymbol{k}_1}^{x'-} s_{\bar{\boldsymbol{q}}_1}^{x'+}|\boldsymbol{k}\gamma\rangle|N_{\boldsymbol{q}}\rangle\langle \boldsymbol{k}\gamma|\langle N_{\boldsymbol{q}}|S_{\boldsymbol{k}_2}^{x'+} s_{\bar{\boldsymbol{q}}_2}^{x'-}|\boldsymbol{k}'\gamma'\rangle|N'_{\boldsymbol{q}'}\rangle \Big] + \text{h.c.},
\end{aligned} \tag{E.31}$$

$$|\langle \boldsymbol{k}'\gamma'|H_{\mathrm{int,s}}|\boldsymbol{k}\gamma\rangle|^2 = \sum_{\bar{\boldsymbol{q}}_1} \sum_{\bar{\boldsymbol{q}}_2} \bar{\mathcal{T}}^2 \delta_{\bar{\boldsymbol{q}}_1,\boldsymbol{0}} \delta_{\bar{\boldsymbol{q}}_2,\boldsymbol{0}} S_0^2 \langle \boldsymbol{k}'\gamma'|s_{\bar{\boldsymbol{q}}_1}^{x'}|\boldsymbol{k}\gamma\rangle\langle \boldsymbol{k}\gamma|(s_{\bar{\boldsymbol{q}}_2}^{x'})^\dagger|\boldsymbol{k}'\gamma'\rangle. \tag{E.32}$$

For a dirty interface with $T_1 \ll T_2$, by comparing Eqs. (E.22) and (E.23) with Eqs. (E.29) and (E.30), the coefficients $\bar{T}$ and $\bar{\mathcal{T}}$ can be expressed as

$$\bar{T}^2 = \frac{2T_2^2}{N_{\mathrm{FI}} N_{\mathrm{b}}}, \quad \bar{\mathcal{T}}^2 = \frac{4T_2^2}{N_{\mathrm{b}}}. \tag{E.33}$$

For a clean interface with $T_1 \gg T_2$, comparing Eqs. (E.22) and (E.23) with Eqs. (E.31) and

(E.32), we obtain the following relationships:

$$\bar{T}^2 = \frac{2T_1^2}{N_{\mathrm{FI}}}, \quad \bar{\mathcal{T}}^2 = 4T_1^2. \tag{E.34}$$

From the above equations, we find that $\bar{\mathcal{T}}^2$ is larger than $\bar{T}^2$ by an order of N_{FI}.

Appendix F

Detailed Calculations of REMR

This appendix presents the detailed calculations related to Chap. 6. Sections F.1 and F.2 provide detailed calculations for the dirty and clean interfaces, respectively, along with plots illustrating the shift in chemical potential.

F.1 Detailed Calculations for the Dirty Interface

This section presents the detailed calculations in the case of a dirty interface as discussed in Sec. 6.1.3. The interfacial interaction Hamiltonian H_{int} for the dirty interface given by Eqs. (3.27) and (3.28) is expressed as $H_{\text{int}} = H_{\text{int,d}} + H_{\text{int,s}}$. Here, $H_{\text{int,d}}$ represents the dynamic contribution associated with magnon absorption and emission, while $H_{\text{int,s}}$ describes the static contribution that characterizes the exchange bias at the FI-2DEG interface. We can write the matrix elements for these contributions as follows:

$$\begin{aligned}\langle \boldsymbol{k}'\sigma'|H_{\text{int,d}}|\boldsymbol{k}\sigma\rangle = &\frac{\sqrt{2S_0}\bar{T}}{2}(\hat{\sigma}^{x'-})_{\sigma'\sigma}\sum_{\boldsymbol{q}}\sin(q_z a)b_{\boldsymbol{q}} \\ &+\frac{\sqrt{2S_0}\bar{T}^*}{2}(\hat{\sigma}^{x'+})_{\sigma'\sigma}\sum_{\boldsymbol{q}}\sin(q_z a)b^\dagger_{\boldsymbol{q}},\end{aligned} \tag{F.1}$$

$$\langle \boldsymbol{k}'\sigma'|H_{\text{int,s}}|\boldsymbol{k}\sigma\rangle = \frac{S_0\bar{\mathcal{T}}}{2}(\hat{\sigma}^{x'})_{\sigma'\sigma}. \tag{F.2}$$

Here, $\sigma, \sigma' = \uparrow, \downarrow$, and $b^\dagger_{\boldsymbol{q}}$ and $b_{\boldsymbol{q}}$ denote the magnon creation and annihilation operators, respectively. Through a basis transformation, it is found that the matrix elements for the energy

eigenstate $|\boldsymbol{k}\gamma\rangle$ in Eq. (3.8) are given by the following:

$$\langle \boldsymbol{k}'\gamma'|H_{\mathrm{int,d}}|\boldsymbol{k}\gamma\rangle = \frac{\sqrt{2S_0}\bar{T}}{2}\sum_{\sigma,\sigma'} C^*_{\sigma'\gamma'}(\boldsymbol{k}')(\hat{\sigma}^{x'-})_{\sigma'\sigma}C_{\sigma\gamma}(\boldsymbol{k})\sum_{\boldsymbol{q}}\sin(q_z a)b_{\boldsymbol{q}} + \frac{\sqrt{2S_0}\bar{T}^*}{2}\sum_{\sigma,\sigma'} C^*_{\sigma'\gamma'}(\boldsymbol{k}')(\hat{\sigma}^{x'+})_{\sigma'\sigma}C_{\sigma\gamma}(\boldsymbol{k})\sum_{\boldsymbol{q}}\sin(q_z a)b^\dagger_{\boldsymbol{q}}, \tag{F.3}$$

$$\langle \boldsymbol{k}'\gamma'|H_{\mathrm{int,s}}|\boldsymbol{k}\gamma\rangle = \frac{S_0\bar{\mathcal{T}}}{2}\sum_{\sigma,\sigma'} C^*_{\sigma'\gamma'}(\boldsymbol{k}')(\hat{\sigma}^{x'})_{\sigma'\sigma}C_{\sigma\gamma}(\boldsymbol{k}). \tag{F.4}$$

Substituting these matrix elements into the collision term due to interfacial scattering given by Eqs. (6.5) and (6.11) yields the following expression:

$$\begin{aligned}\left.\frac{\partial f(\boldsymbol{k},\gamma)}{\partial t}\right|_{\mathrm{int}} &= -\frac{\pi S_0|\bar{T}|^2}{\hbar}\sum_{\boldsymbol{k}',\gamma'}\sum_{\boldsymbol{q}}\langle N_{\boldsymbol{q}}\rangle\sin^2(q_z a)\\ &\times\Big(\big[1-\gamma\hat{\boldsymbol{h}}_{\mathrm{eff}}(\varphi)\cdot\hat{\boldsymbol{m}}\big]\big[1+\gamma'\hat{\boldsymbol{h}}_{\mathrm{eff}}(\varphi')\cdot\hat{\boldsymbol{m}}\big]A(\boldsymbol{k},\gamma,\boldsymbol{k}',\gamma')\delta(E^{\gamma'}_{\boldsymbol{k}'}-E^{\gamma}_{\boldsymbol{k}}-\hbar\omega_{\boldsymbol{q}})\\ &\quad-\big[1+\gamma\hat{\boldsymbol{h}}_{\mathrm{eff}}(\varphi)\cdot\hat{\boldsymbol{m}}\big]\big[1-\gamma'\hat{\boldsymbol{h}}_{\mathrm{eff}}(\varphi')\cdot\hat{\boldsymbol{m}}\big]A(\boldsymbol{k}',\gamma',\boldsymbol{k},\gamma)\delta(E^{\gamma'}_{\boldsymbol{k}'}-E^{\gamma}_{\boldsymbol{k}}+\hbar\omega_{\boldsymbol{q}})\Big)\\ &-\frac{\pi S_0^2|\bar{\mathcal{T}}|^2}{4\hbar}\sum_{\boldsymbol{k}',\gamma'}\Big(1+2\gamma\gamma'\big[\hat{\boldsymbol{h}}_{\mathrm{eff}}(\varphi)\cdot\hat{\boldsymbol{m}}\big]\big[\hat{\boldsymbol{h}}_{\mathrm{eff}}(\varphi')\cdot\hat{\boldsymbol{m}}\big]-\gamma\gamma'\hat{\boldsymbol{h}}_{\mathrm{eff}}(\varphi)\cdot\hat{\boldsymbol{h}}_{\mathrm{eff}}(\varphi')\Big)\\ &\quad\times A(\boldsymbol{k},\gamma,\boldsymbol{k}',\gamma')\delta(E^{\gamma'}_{\boldsymbol{k}'}-E^{\gamma}_{\boldsymbol{k}}).\end{aligned} \tag{F.5}$$

Here, $\hat{\boldsymbol{m}} = (\cos\theta, \sin\theta)^T$ is a unit vector representing the direction of the localized spins in the FI and N_{FI} denotes the number of unit cells in the FI. Additionally,

$$A(\boldsymbol{k},\gamma,\boldsymbol{k}',\gamma') = \beta f_0(\boldsymbol{k},\gamma)[1-f_0(\boldsymbol{k}',\gamma')][\delta\mu(\boldsymbol{k},\gamma)-\delta\mu(\boldsymbol{k}',\gamma')], \tag{F.6}$$

where $\delta\mu(\boldsymbol{k},\gamma)$ represents the shift in chemical potential. In the following, assuming that $\hbar\omega_{\boldsymbol{q}}$ is small, we approximate $\delta(E^{\gamma'}_{\boldsymbol{k}'}-E^{\gamma}_{\boldsymbol{k}}\pm\hbar\omega_{\boldsymbol{q}})$ by $\delta(E^{\gamma'}_{\boldsymbol{k}'}-E^{\gamma}_{\boldsymbol{k}})$. Assuming that the interfacial scattering is sufficiently weak and applying the perturbative relation in Eq. (6.29), we obtain the following integral equation for $f_{\mathrm{D}}(\boldsymbol{k},\gamma)$

$$\begin{aligned}f_{\mathrm{D}}(\boldsymbol{k},\gamma) &= \mathcal{G}_{\mathrm{D}}(\boldsymbol{k},\gamma,\theta)\\ &\quad+\frac{\hbar^2}{2m^*}\int_0^{2\pi}\frac{d\varphi'}{2\pi}\sum_{\gamma'=\pm}\int_0^{\infty}dk'\,|\boldsymbol{k}'|\big[1+\gamma\gamma'\hat{\boldsymbol{h}}_{\mathrm{eff}}(\varphi)\cdot\hat{\boldsymbol{h}}_{\mathrm{eff}}(\varphi')\big]\delta(E^{\gamma'}_{\boldsymbol{k}'}-E^{\gamma}_{\boldsymbol{k}})f_{\mathrm{D}}(\boldsymbol{k}',\gamma'),\end{aligned} \tag{F.7}$$

where $\mathcal{G}_{\mathrm{D}}(\boldsymbol{k},\gamma,\theta)$ is defined as

$$
\begin{aligned}
&\mathcal{G}_{\mathrm{D}}(\boldsymbol{k},\gamma,\theta)\\
&=\frac{\pi D(\epsilon_{\mathrm{F}})S_0\hbar^2 eE_x\mathcal{A}}{2\Gamma^2 m^*}\frac{\partial f_0(E_{\boldsymbol{k}}^{\gamma})}{\partial E_{\boldsymbol{k}}^{\gamma}}\int_0^{2\pi}\frac{d\varphi'}{2\pi}\\
&\times\Bigg[8|\bar{T}|^2\sum_{\boldsymbol{q}}\langle N_{\boldsymbol{q}}\rangle\sin^2(q_z a)\Big\{|\boldsymbol{k}|\cos\varphi-\gamma[\hat{\boldsymbol{h}}_{\mathrm{eff}}(\varphi)\cdot\hat{\boldsymbol{m}}(\theta)][\hat{\boldsymbol{h}}_{\mathrm{eff}}(\varphi')\cdot\hat{\boldsymbol{m}}(\theta)]\frac{2m^*\kappa(\varphi')}{\hbar^2}\cos\varphi'\Big\}\\
&\quad+S_0|\bar{\mathcal{T}}|^2\Big\{|\boldsymbol{k}|\cos\varphi\\
&\quad+\gamma\Big(2[\hat{\boldsymbol{h}}_{\mathrm{eff}}(\varphi)\cdot\hat{\boldsymbol{m}}(\theta)][\hat{\boldsymbol{h}}_{\mathrm{eff}}(\varphi')\cdot\hat{\boldsymbol{m}}(\theta)]-\hat{\boldsymbol{h}}_{\mathrm{eff}}(\varphi)\cdot\hat{\boldsymbol{h}}_{\mathrm{eff}}(\varphi')\Big)\frac{2m^*\kappa(\varphi')}{\hbar^2}\cos\varphi'\Big\}\Bigg],
\end{aligned}
\tag{F.8}
$$

where $\kappa(\varphi)=\sqrt{\alpha^2+\beta^2+2\alpha\beta\sin 2\varphi}$. By successively substituting $f_{\mathrm{D}}(\boldsymbol{k},\gamma)$ into the right-hand side of Eq. (F.7), we obtain the following solution to Eq. (F.7):

$$
\begin{aligned}
f_{\mathrm{D}}(\boldsymbol{k},\gamma)=\mathcal{G}_{\mathrm{D}}(\boldsymbol{k},\gamma,\theta)+\frac{\hbar^2}{2m^*}\int_0^{2\pi}\frac{d\varphi''}{2\pi}\sum_{\gamma''}\gamma\gamma''\int_0^{\infty}dk''\,|\boldsymbol{k}''|\,\delta(E_{k''}^{\gamma''}-E_{\boldsymbol{k}}^{\gamma})\\
\times\hat{\boldsymbol{h}}_{\mathrm{eff}}^{T}(\varphi)\left(\hat{1}-\int_0^{2\pi}\frac{d\varphi'}{2\pi}\hat{\boldsymbol{h}}_{\mathrm{eff}}(\varphi')\cdot\hat{\boldsymbol{h}}_{\mathrm{eff}}^{T}(\varphi')\right)^{-1}\hat{\boldsymbol{h}}_{\mathrm{eff}}(\varphi'')\mathcal{G}_{\mathrm{D}}(\boldsymbol{k}'',\gamma'',\theta).
\end{aligned}
\tag{F.9}
$$

By performing the radial integration over the wavenumber in Eq. (F.9) and retaining only the terms dependent on θ, we obtain the following expression:

$$
f_{\mathrm{D}}(\boldsymbol{k},\gamma)=\gamma\frac{\partial f_0(E_{\boldsymbol{k}}^{\gamma})}{\partial E_{\boldsymbol{k}}^{\gamma}}\hat{\boldsymbol{h}}_{\mathrm{eff}}(\varphi)\cdot\boldsymbol{V}(\theta),
\tag{F.10}
$$

$$
\begin{aligned}
\boldsymbol{V}(\theta)=\frac{\pi D(\epsilon_{\mathrm{F}})S_0 eE_x\mathcal{A}}{\Gamma^2}\Big[-8|\bar{T}|^2\sum_{\boldsymbol{q}}\langle N_{\boldsymbol{q}}\rangle\sin^2(q_z a)+2S_0|\bar{\mathcal{T}}|^2\Big]\\
\times\int_0^{2\pi}\frac{d\varphi''}{2\pi}[\hat{\boldsymbol{h}}_{\mathrm{eff}}(\varphi'')\cdot\hat{\boldsymbol{m}}]\kappa(\varphi'')\cos\varphi''\left(\hat{1}-\int_0^{2\pi}\frac{d\varphi'}{2\pi}\hat{\boldsymbol{h}}_{\mathrm{eff}}(\varphi')\cdot\hat{\boldsymbol{h}}_{\mathrm{eff}}^{T}(\varphi')\right)^{-1}\hat{\boldsymbol{m}}.
\end{aligned}
\tag{F.11}
$$

Then, using η defined in Eq. (5.25), we can write the matrix appearing in the above expression as

$$
\hat{M}\equiv\left(\hat{1}-\int_0^{2\pi}\frac{d\varphi'}{2\pi}\hat{\boldsymbol{h}}_{\mathrm{eff}}(\varphi')\cdot\hat{\boldsymbol{h}}_{\mathrm{eff}}^{T}(\varphi')\right)^{-1}=\frac{2}{1-\eta^2}\begin{pmatrix}1&-\eta\\-\eta&1\end{pmatrix},
\tag{F.12}
$$

and obtain the analytical solution expressed in Eqs. (6.30)-(6.32).

To elucidate the modulation of the distribution function, Fig. F.1 presents the chemical potential shift $\delta\mu_{\mathrm{D}}(\varphi,\gamma=+)$ plotted as a function of the wavevector orientation φ. In these plots, terms proportional to $|\bar{T}|^2$ have been omitted as in Eq. (6.50) and the following normalization

constant has been applied:

$$\mu_{x,\mathrm{D}} = -\frac{2\pi D(\epsilon_\mathrm{F}) S_0^2 e E_x \mathcal{A} |\bar{\mathcal{T}}|^2 x}{\Gamma^2}, \quad (x = \alpha, \beta). \tag{F.13}$$

These plots are consistent with the schematic diagrams of the distribution function modulation shown in Figs. 6.2 and 6.3.

From Eq. (6.12), the spin density induced in the 2DEG by the REMR at the dirty interface can be expressed using $f_\mathrm{D}(\boldsymbol{k}, \gamma)$ as follows:

$$\Delta \boldsymbol{s}_\mathrm{D} = \frac{\hbar}{2\mathcal{A}} \sum_{\boldsymbol{k},\gamma} \langle \boldsymbol{k}\gamma | \hat{\boldsymbol{\sigma}} | \boldsymbol{k}\gamma \rangle \, f_\mathrm{D}(\boldsymbol{k}, \gamma). \tag{F.14}$$

Substituting the analytical solution of $f_\mathrm{D}(\boldsymbol{k}, \gamma)$ into this expression and using Eq. (5.8) to replace the sum over wavevectors with an integral yields the following expression for the spin density:

$$\begin{aligned}
\Delta \boldsymbol{s}_\mathrm{D} &= \frac{k_\mathrm{F}}{2\pi v_\mathrm{F}} \int_0^{2\pi} \frac{d\varphi}{2\pi} \hat{\boldsymbol{h}}_\mathrm{eff}(\varphi) [\hat{\boldsymbol{h}}_\mathrm{eff}(\varphi) \cdot \boldsymbol{V}(\theta)] \\
&= \frac{k_\mathrm{F} D(\epsilon_\mathrm{F}) S_0 e E_x \mathcal{A}}{2 v_\mathrm{F} \Gamma^2} \Big[-4|\bar{T}|^2 \sum_{\boldsymbol{q}} \langle N_{\boldsymbol{q}} \rangle \sin^2(q_z a) + S_0 |\bar{\mathcal{T}}|^2 \Big] \\
&\quad \times \frac{\alpha \sin\theta - \beta \cos\theta}{1 - \eta^2} \begin{pmatrix} \cos\theta & \sin\theta \\ \sin\theta & \cos\theta \end{pmatrix} \begin{pmatrix} 1 + \eta^2 \\ -2\eta \end{pmatrix},
\end{aligned} \tag{F.15}$$

In this calculation, we used the following approximation:

$$\frac{\partial f_0(E_{\boldsymbol{k}}^\gamma)}{\partial E_{\boldsymbol{k}}^\gamma} \simeq -\delta(E_{\boldsymbol{k}}^\gamma - \mu). \tag{F.16}$$

Thus, we obtain Eq. (6.35).

Next, by performing a similar calculation using Eq. (6.13), we obtain the following expression for the charge current density induced in the 2DEG by the REMR:

$$\begin{aligned}
\Delta \boldsymbol{j}_\mathrm{D} &= \frac{e}{\mathcal{A}} \sum_{\gamma=\pm} \sum_{\boldsymbol{k}} \boldsymbol{v}(\boldsymbol{k}, \gamma) f_\mathrm{D}(\boldsymbol{k}, \gamma) \\
&= \frac{e k_\mathrm{F}}{\pi \hbar^2 v_\mathrm{F}} \int_0^{2\pi} \frac{d\varphi}{2\pi} \frac{\hat{\boldsymbol{h}}_\mathrm{eff}(\varphi) \cdot \boldsymbol{V}(\theta)}{\kappa(\varphi)} \begin{pmatrix} (\alpha^2 + \beta^2)\cos\varphi + 2\alpha\beta \sin 3\varphi \\ (\alpha^2 + \beta^2)\sin\varphi - 2\alpha\beta \cos 3\varphi \end{pmatrix}.
\end{aligned} \tag{F.17}$$

Substituting Eq. (F.11) into Eq. (F.17) yields the following expression:

$$\Delta \boldsymbol{j}_\mathrm{D} = \frac{e^2 k_\mathrm{F} D(\epsilon_\mathrm{F}) S_0 E_x \mathcal{A}}{\hbar^2 v_\mathrm{F} \Gamma^2} \Big[-4|\bar{T}|^2 \sum_{\boldsymbol{q}} \langle N_{\boldsymbol{q}} \rangle \sin^2(q_z a) + S_0 |\bar{\mathcal{T}}|^2 \Big] \begin{pmatrix} (\alpha \sin\theta - \beta\cos\theta)^2 \\ -(\alpha^2 + \beta^2)\cos\theta\sin\theta + \alpha\beta \end{pmatrix}. \tag{F.18}$$

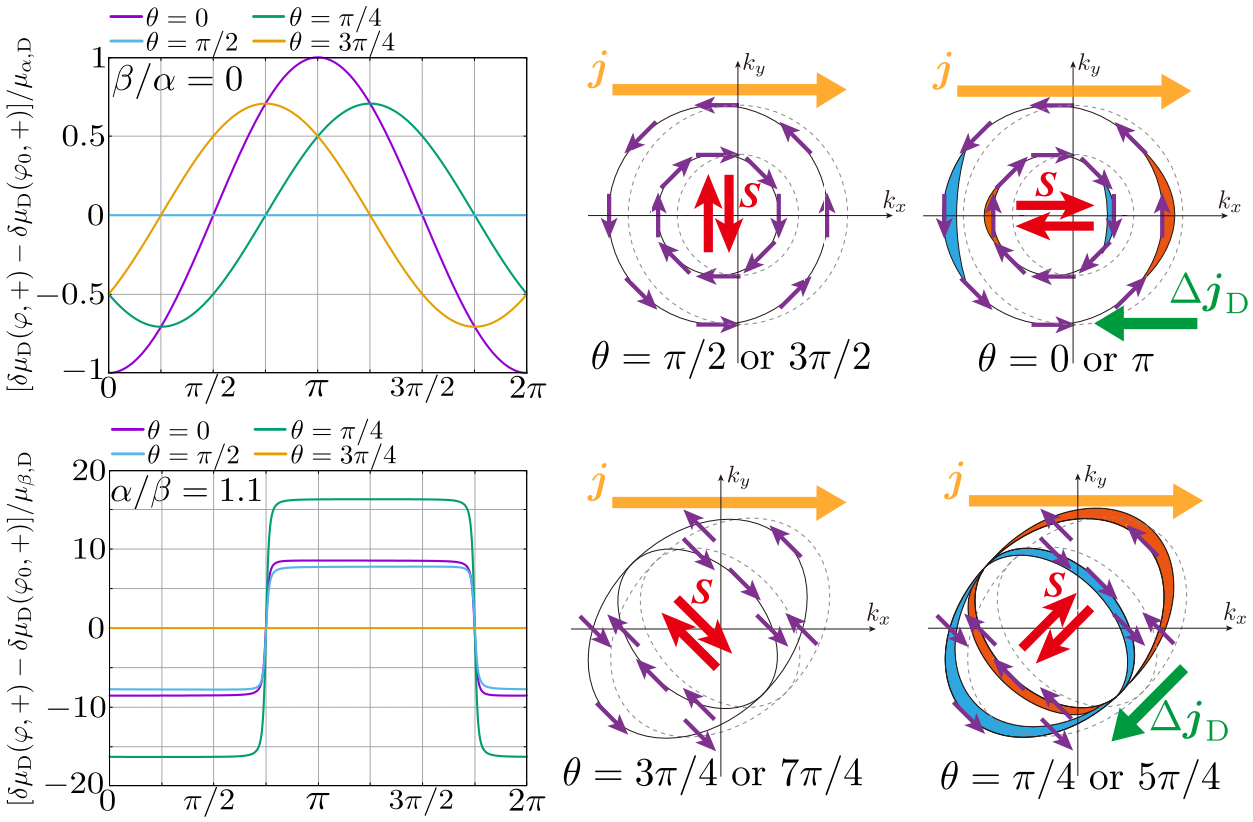

Figure F.1: Left Panels: The chemical potential shift $\delta\mu_{\rm D}(\varphi,+)-\delta\mu_{\rm D}(\varphi_0,+)$ for a dirty interface, plotted as a function of the electron wavevector orientation φ, is shown for $\beta/\alpha = 0$ (top plot) and $\alpha/\beta = 1.1$ (bottom plot). For $\beta/\alpha = 0$ ($\alpha/\beta = 1.1$), the reference point for the chemical potential shift is taken at $\varphi_0 = \pi/2, 3\pi/2$ ($\varphi_0 = 3\pi/4, 7\pi/4$). Note that $\gamma = +$ indicates the inner Fermi surface. Right Panels: Schematic diagrams of the distribution function deviation for $\beta = 0$ (upper diagrams) and $\alpha/\beta = 1.1$ (lower diagrams). The orange (blue) regions indicate areas where the distribution function increases (decreases) relative to the reference point. Adapted from Ref. [50].

By excluding the term that does not depend on θ, we obtain Eq. (6.36).

F.2 Detailed Calculations for the Clean Interface

This section provides the detailed calculations for the clean interface discussed in Sec. 6.1.4. The interfacial interaction Hamiltonian $H_{\rm int}$ for the clean interface, described by Eqs. (3.27) and (3.29), is divided into dynamic and static contributions expressed as $H_{\rm int} = H_{\rm int,d} + H_{\rm int,s}$. We

can write the matrix elements for these contributions as follows:

$$\langle \boldsymbol{k}'\sigma'|H_{\mathrm{int,d}}|\boldsymbol{k}\sigma\rangle = \frac{\sqrt{2S_0}\bar{T}}{2}(\hat{\sigma}^{x'-})_{\sigma'\sigma}\sum_{\boldsymbol{q}} b_{\boldsymbol{q}}\sin(q_z a)\delta_{\boldsymbol{q}_\parallel,\boldsymbol{k}'-\boldsymbol{k}} + \frac{\sqrt{2S_0}\bar{T}^*}{2}(\hat{\sigma}^{x'+})_{\sigma'\sigma}\sum_{\boldsymbol{q}} b^\dagger_{\boldsymbol{q}}\sin(q_z a)\delta_{\boldsymbol{q}_\parallel,\boldsymbol{k}-\boldsymbol{k}'}, \tag{F.19}$$

$$\langle \boldsymbol{k}'\sigma'|H_{\mathrm{int,s}}|\boldsymbol{k}\sigma\rangle = \frac{S_0\bar{\mathcal{T}}}{2}(\hat{\sigma}^{x'})_{\sigma'\sigma}\delta_{\boldsymbol{k},\boldsymbol{k}'}. \tag{F.20}$$

Through a basis transformation, we can write the matrix elements in the basis of the energy eigenstates $|\boldsymbol{k}\gamma\rangle$ as follows:

$$\langle \boldsymbol{k}'\gamma'|H_{\mathrm{int,d}}|\boldsymbol{k}\gamma\rangle = \frac{\sqrt{2S_0}\bar{T}}{2}\sum_{\sigma,\sigma'} C^*_{\sigma'\gamma'}(\boldsymbol{k}')(\hat{\sigma}^{x'-})_{\sigma'\sigma}C_{\sigma\gamma}(\boldsymbol{k})\sum_{\boldsymbol{q}} b_{\boldsymbol{q}}\sin(q_z a)\delta_{\boldsymbol{q}_\parallel,\boldsymbol{k}'-\boldsymbol{k}} + \frac{\sqrt{2S_0}\bar{T}^*}{2}\sum_{\sigma,\sigma'} C^*_{\sigma'\gamma'}(\boldsymbol{k}')(\hat{\sigma}^{x'+})_{\sigma'\sigma}C_{\sigma\gamma}(\boldsymbol{k})\sum_{\boldsymbol{q}} b^\dagger_{\boldsymbol{q}}\sin(q_z a)\delta_{\boldsymbol{q}_\parallel,\boldsymbol{k}-\boldsymbol{k}'}, \tag{F.21}$$

$$\langle \boldsymbol{k}'\gamma'|H_{\mathrm{int,s}}|\boldsymbol{k}\gamma\rangle = \frac{S_0\bar{\mathcal{T}}}{2}\sum_{\sigma,\sigma'} C^*_{\sigma'\gamma'}(\boldsymbol{k}')(\hat{\sigma}^{x'})_{\sigma'\sigma}C_{\sigma\gamma}(\boldsymbol{k})\delta_{\boldsymbol{k},\boldsymbol{k}'}. \tag{F.22}$$

Here, compared to the case of the dirty interface, it can be seen that in the case of the clean interface, the in-plane momentum conservation introduces a Kronecker delta.

The subsequent calculation is nearly identical to that of the dirty interface, except for the fact that the in-plane momentum conservation law holds. From the Boltzmann equation, we obtain the following integral equation for the distribution function $f_{\mathrm{C}}(\boldsymbol{k},\gamma)$:

$$f_{\mathrm{C}}(\boldsymbol{k},\gamma) = \mathcal{G}_{\mathrm{C}}(\boldsymbol{k},\gamma,\theta) + \frac{\hbar^2}{2m^*}\int_0^{2\pi}\frac{d\varphi'}{2\pi}\sum_{\gamma'}\int_0^\infty dk'\,|\boldsymbol{k}'|[1+\gamma\gamma'\hat{\boldsymbol{h}}_{\mathrm{eff}}(\varphi)\cdot\hat{\boldsymbol{h}}_{\mathrm{eff}}(\varphi')]\delta(E^{\gamma'}_{\boldsymbol{k}'}-E^{\gamma}_{\boldsymbol{k}})f_{\mathrm{C}}(\boldsymbol{k}',\gamma'), \tag{F.23}$$

$$\mathcal{G}_{\mathrm{C}}(\boldsymbol{k},\gamma,\theta) \simeq \frac{4\hbar^2\pi D(\epsilon_{\mathrm{F}})S_0|\bar{T}|^2\mathcal{A}eE_x}{\Gamma^2 m^*}\frac{\partial f_0(E^\gamma_{\boldsymbol{k}})}{\partial E^\gamma_{\boldsymbol{k}}} \times\sum_{q_z>0}\int_0^{2\pi}\frac{d\varphi'}{2\pi}N(\varphi-\varphi',q_z)\sin^2(q_z a)\mathcal{F}(\boldsymbol{k},\gamma,\varphi',\theta), \tag{F.24}$$

$$\mathcal{F}(\boldsymbol{k},\gamma,\varphi',\theta) = |\boldsymbol{k}|\cos\varphi - \sqrt{2m^*E^\gamma_{\boldsymbol{k}}/\hbar^2}\cos\varphi' + \frac{m^*h_{\mathrm{eff}}(\varphi')}{\hbar^2 k_{\mathrm{F}}}\gamma[\hat{\boldsymbol{h}}_{\mathrm{eff}}(\varphi)\cdot\hat{\boldsymbol{m}}(\theta)][\hat{\boldsymbol{h}}_{\mathrm{eff}}(\varphi')\cdot\hat{\boldsymbol{m}}(\theta)]\left(\frac{|\boldsymbol{k}|\cos\varphi}{\sqrt{2m^*E^\gamma_{\boldsymbol{k}}/\hbar^2}}-2\cos\varphi'\right). \tag{F.25}$$

Here, $N(\varphi, q_z)$ denotes the magnon Bose distribution given by Eq. (6.48). Assuming that the magnon energy $\hbar\omega_{\boldsymbol{q}} = \hbar\omega_{\boldsymbol{q}_\parallel, q_z}$ is sufficiently small compared to the spin-splitting width of the energy band for 2DEG conduction electrons, we employed the approximation $\delta(E^{\gamma'}_{\boldsymbol{k}'} - E^{\gamma}_{\boldsymbol{k}} \pm \hbar\omega_{\pm(\boldsymbol{k}-\boldsymbol{k}'),q_z}) \simeq \delta(E^{\gamma'}_{\boldsymbol{k}'} - E^{\gamma}_{\boldsymbol{k}})$. Solving Eq. (F.23) through successive substitution yields the following solution for Eq. (F.23):

$$f_{\rm C}(\boldsymbol{k},\gamma) = \mathcal{G}_{\rm C}(\boldsymbol{k},\gamma,\theta) + \frac{\hbar^2}{2m^*}\int_0^{2\pi}\frac{d\varphi''}{2\pi}\sum_{\gamma''}\gamma\gamma''\int_0^{\infty}dk''\,|\boldsymbol{k}''| \\ \times \hat{\boldsymbol{h}}^T_{\rm eff}(\varphi)\left(\hat{1} - \int_0^{2\pi}\frac{d\varphi'}{2\pi}\hat{\boldsymbol{h}}_{\rm eff}(\varphi')\cdot\hat{\boldsymbol{h}}^T_{\rm eff}(\varphi')\right)^{-1}\hat{\boldsymbol{h}}_{\rm eff}(\varphi'')\delta(E^{\gamma''}_{\boldsymbol{k}''} - E^{\gamma}_{\boldsymbol{k}})\mathcal{G}_{\rm C}(\boldsymbol{k}'',\gamma'',\theta). \tag{F.26}$$

For the clean interface, the modulation of the spin density and charge current density induced in the 2DEG by the REMR can be expressed using the distribution function $f_{\rm C}(\boldsymbol{k},\gamma)$ as follows:

$$\Delta\boldsymbol{s}_{\rm C}(\theta) = \frac{\hbar}{4\pi}\sum_{\gamma}\int_0^{\infty}dk\,|\boldsymbol{k}|\int_0^{2\pi}\frac{d\varphi}{2\pi}\langle\boldsymbol{k}\gamma|\hat{\boldsymbol{\sigma}}|\boldsymbol{k}\gamma\rangle f_{\rm C}(\boldsymbol{k},\gamma), \tag{F.27}$$

$$\Delta\boldsymbol{j}_{\rm C}(\theta) = \frac{e}{2\pi}\sum_{\gamma}\int_0^{\infty}dk\,|\boldsymbol{k}|\int_0^{2\pi}\frac{d\varphi}{2\pi}\boldsymbol{v}(\boldsymbol{k},\gamma)f_{\rm C}(\boldsymbol{k},\gamma). \tag{F.28}$$

Substituting the solution given by Eq. (F.26) into Eqs. (F.27) and (F.28) and applying Eq. (F.16) yields the results Eqs. (6.40)-(6.45) in the main text.

Using Eqs. (F.26) and (6.38), we obtain an analytical solution for the chemical potential shift at the Fermi surface, $\delta\mu_{\rm C}(\varphi,\gamma) \equiv \delta\mu_{\rm C}(\boldsymbol{k},\gamma)|_{E^{\gamma}_{\boldsymbol{k}}=\mu}$:

$$\delta\mu_{\rm C}(\varphi,\gamma) = -\frac{4\pi D(\epsilon_{\rm F})S_0|\bar{T}|^2\mathcal{A}eE_x\gamma}{\Gamma^2}\mathcal{J}(\varphi). \tag{F.29}$$

Here, $\mathcal{J}(\varphi)$ is as introduced in Eq. (6.42). Note that in Eq. (F.29), terms independent of γ and θ have been omitted. In Fig. F.2, we plot $\delta\mu_{\rm C}(\varphi,\gamma=+)$ from Eq. (F.29) as a function of φ. The normalization constant used for these plots is as follows:

$$\mu_{x,{\rm C}} = -\frac{4k_{\rm F}LD(\epsilon_{\rm F})S_0eE_x\mathcal{A}|\bar{T}|^2x}{\Gamma^2}, \quad (x=\alpha,\beta). \tag{F.30}$$

These plots are consistent with the schematic diagrams illustrating the modulation of the distribution function shown in Figs. 6.4 and 6.5.

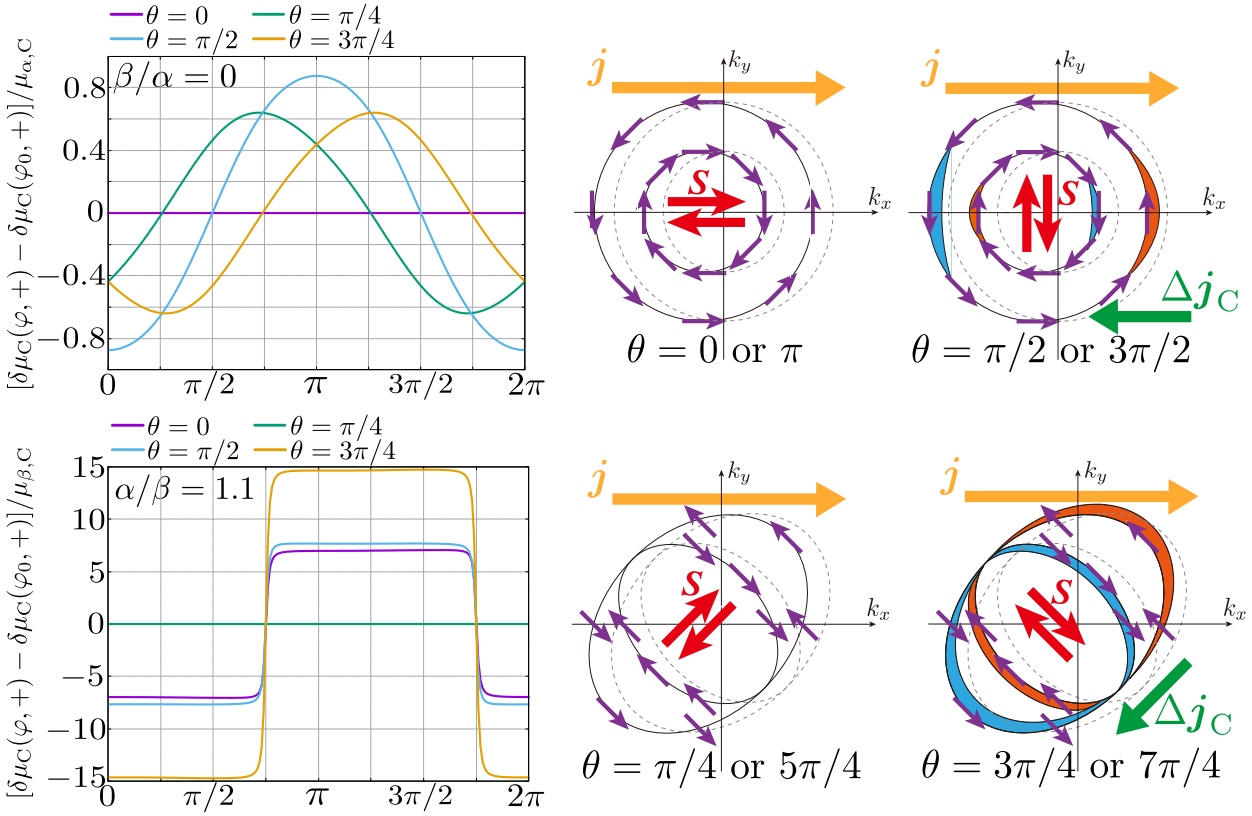

Figure F.2: Left Panels: The chemical potential shift $\delta\mu_C(\varphi,+)-\delta\mu_C(\varphi_0,+)$ for a clean interface, plotted as a function of the electron wavevector orientation φ, is shown for $\beta/\alpha = 0$ (top plot) and $\alpha/\beta = 1.1$ (bottom plot). For $\beta/\alpha = 0$ ($\alpha/\beta = 1.1$), the reference point for the chemical potential shift is taken at $\varphi_0 = 0, \pi$ ($\varphi_0 = \pi/4, 5\pi/4$). Note that $\gamma = +$ indicates the inner Fermi surface. The parameters are set to $k_BT/\hbar\omega_0 = 3$, $|\gamma_g|h_{dc}/\omega_0 = 0.1$, and $k_Fa = 0.1$. Right Panels: Schematic diagrams of the distribution function deviation for $\beta = 0$ (upper diagrams) and $\alpha/\beta = 1.1$ (lower diagrams). The orange (blue) regions indicate areas where the distribution function increases (decreases) relative to the reference point.

Bibliography

[1] S. Bhatti, R. Sbiaa, A. Hirohata, H. Ohno, S. Fukami, and S. Piramanayagam, "Spintronics based random access memory: a review," Mater. Today **20**, 530 (2017).

[2] A. Fert, "Nobel Lecture: Origin, development, and future of spintronics," Rev. Mod. Phys. **80**, 1517 (2008).

[3] M. N. Baibich, J. M. Broto, A. Fert, F. N. Van Dau, F. Petroff, P. Etienne, G. Creuzet, A. Friederich, and J. Chazelas, "Giant Magnetoresistance of (001)Fe/(001)Cr Magnetic Superlattices," Phys. Rev. Lett. **61**, 2472 (1988).

[4] G. Binasch, P. Grünberg, F. Saurenbach, and W. Zinn, "Enhanced magnetoresistance in layered magnetic structures with antiferromagnetic interlayer exchange," Phys. Rev. B **39**, 4828(R) (1989).

[5] B. Dieny, V. S. Speriosu, S. S. P. Parkin, B. A. Gurney, D. R. Wilhoit, and D. Mauri, "Giant magnetoresistive in soft ferromagnetic multilayers," Phys. Rev. B **43**, 1297(R) (1991).

[6] J. S. Moodera, L. R. Kinder, T. M. Wong, and R. Meservey, "Large Magnetoresistance at Room Temperature in Ferromagnetic Thin Film Tunnel Junctions," Phys. Rev. Lett. **74**, 3273 (1995).

[7] T. Miyazaki and N. Tezuka, "Giant magnetic tunneling effect in Fe/Al_2O_3/Fe junction," J. Magn. Magn. Mater. **139**, L231 (1995).

[8] S. Yuasa, T. Nagahama, A. Fukushima, Y. Suzuki, and K. Ando, "Giant room-temperature magnetoresistance in single-crystal Fe/MgO/Fe magnetic tunnel junctions," Nat. Mater. **3**, 868 (2004).

[9] S. S. Parkin, C. Kaiser, A. Panchula, P. M. Rice, B. Hughes, M. Samant, and S.-H. Yang, "Giant tunnelling magnetoresistance at room temperature with MgO (100) tunnel barriers," Nat. Mater. **3**, 862 (2004).

[10] L. Liu, C.-F. Pai, Y. Li, H. Tseng, D. Ralph, and R. Buhrman, "Spin-Torque Switching with the Giant Spin Hall Effect of Tantalum," Science **336**, 555 (2012).

[11] I. M. Miron, K. Garello, G. Gaudin, P.-J. Zermatten, M. V. Costache, S. Auffret, S. Bandiera, B. Rodmacq, A. Schuhl, and P. Gambardella, "Perpendicular switching of a single ferromagnetic layer induced by in-plane current injection," Nature (London) **476**, 189 (2011).

[12] P. Gambardella and I. M. Miron, "Current-induced spin–orbit torques," Philos. Trans. R. Soc. London A **369**, 3175 (2011).

[13] I. Žutić, J. Fabian, and S. D. Sarma, "Spintronics: Fundamentals and applications," Rev. Mod. Phys. **76**, 323 (2004).

[14] M. Kohda and G. Salis, "Physics and application of persistent spin helix state in semiconductor heterostructures," Semicond. Sci. Technol. **32**, 073002 (2017).

[15] E. Saitoh, M. Ueda, H. Miyajima, and G. Tatara, "Conversion of spin current into charge current at room temperature: Inverse spin-Hall effect," Appl. Phys. Lett. **88**, 182509 (2006).

[16] T. Kimura, Y. Otani, T. Sato, S. Takahashi, and S. Maekawa, "Room-Temperature Reversible Spin Hall Effect," Phys. Rev. Lett. **98**, 156601 (2007).

[17] L. Berger, "Emission of spin waves by a magnetic multilayer traversed by a current," Phys. Rev. B **54**, 9353 (1996).

[18] Y. Tserkovnyak, A. Brataas, and G. E. W. Bauer, "Enhanced Gilbert Damping in Thin Ferromagnetic Films," Phys. Rev. Lett. **88**, 117601 (2002).

[19] S. Mizukami, Y. Ando, and T. Miyazaki, "The Study on Ferromagnetic Resonance Linewidth for NM/80NiFe/NM (NM= Cu, Ta, Pd and Pt) Films," Jpn. J. Appl. Phys. **40**, 580 (2001).

[20] S. Mizukami, Y. Ando, and T. Miyazaki, "Effect of spin diffusion on Gilbert damping for a very thin permalloy layer in Cu/permalloy/Cu/Pt films," Phys. Rev. B **66**, 104413 (2002).

[21] J. Fabian, A. Matos-Abiague, C. Ertler, P. Stano, and I. Žutić, "Semiconductor spintronics," Acta Phys. Slov. **57**, 565 (2007).

[22] S. Datta and B. Das, "Electronic analog of the electro- optic modulator," Appl. Phys. Lett. **56**, 665 (1990).

[23] Y. A. Bychkov and E. I. Rashba, "Oscillatory effects and the magnetic susceptibility of carriers in inversion layers," J. Phys. C: Solid State Phys. **17**, 6039 (1984).

[24] E. I. Rashba, "Semiconductors with a loop of extrema," J. Electron Spectrosc. Relat. Phenom. **201**, 4 (2015).

[25] Z. Chen, P. Chen, Y. Wang, W. Wang, Z. Zhang, X. Lu, R. Liu, X. Fan, G. Yu, and F. Ma, "Experimental observation of interfacial Rashba-Edelstein magnetoresistance in Cr/YIG heterostructures," Phys. Rev. B **107**, 014408 (2023).

[26] J. Nitta, T. Akazaki, H. Takayanagi, and T. Enoki, "Gate Control of Spin-Orbit Interaction in an Inverted $In_{0.53}Ga_{0.47}As/In_{0.52}Al_{0.48}As$ Heterostructure," Phys. Rev. Lett. **78**, 1335 (1997).

[27] V. Edelstein, "Spin polarization of conduction electrons induced by electric current in two-dimensional asymmetric electron systems," Solid State Commun. **73**, 233 (1990).

[28] J.-i. Inoue, G. E. W. Bauer, and L. W. Molenkamp, "Diffuse transport and spin accumulation in a Rashba two-dimensional electron gas," Phys. Rev. B **67**, 033104 (2003).

[29] Y. K. Kato, R. C. Myers, A. C. Gossard, and D. D. Awschalom, "Current-Induced Spin Polarization in Strained Semiconductors," Phys. Rev. Lett. **93**, 176601 (2004).

[30] A. Y. Silov, P. A. Blajnov, J. H. Wolter, R. Hey, K. H. Ploog, and N. S. Averkiev, "Current-induced spin polarization at a single heterojunction," Appl. Phys. Lett. **85**, 5929 (2004).

[31] S. Ganichev, S. Danilov, P. Schneider, V. Bel ' kov, L. Golub, W. Wegscheider, D. Weiss, and W. Prettl, "Electric current-induced spin orientation in quantum well structures," J. Magn. Magn. Mater. **300**, 127 (2006). The third Moscow International Symposium on Magnetism 2005.

[32] M. Trushin and J. Schliemann, "Anisotropic current-induced spin accumulation in the two-dimensional electron gas with spin-orbit coupling," Phys. Rev. B **75**, 155323 (2007).

[33] E. L. Ivchenko, Y. B. Lyanda-Geller, and G. E. Pikus, "Photocurrent in structures with quantum wells with an optical orientation of free carriers," JETP Lett. **50**, 175 (1989).

[34] E. L. Ivchenko, Y. B. Lyanda-Geller, and G. E. Pikus, "Current of thermalized spin-oriented photocarriers," Sov. Phys. JETP **71**, 550 (1990).

[35] S. D. Ganichev, E. L. Ivchenko, S. N. Danilov, J. Eroms, W. Wegscheider, D. Weiss, and W. Prettl, "Conversion of Spin into Directed Electric Current in Quantum Wells," Phys. Rev. Lett. **86**, 4358 (2001).

[36] S. D. Ganichev, E. L. Ivchenko, V. V. Bel'kov, S. A. Tarasenko, M. Sollinger, D. Weiss, W. Wegscheider, and W. Prettl, "Spin-galvanic effect," Nature (London) **417**, 153 (2002).

[37] J.-C. R. Rojas-Sánchez, L. Vila, G. Desfonds, S. Gambarelli, J. P. Attané, J. M. De Teresa, C. Magén, and A. Fert, "Spin-to-charge conversion using Rashba coupling at the interface between non-magnetic materials," Nat. Commun. **4**, 2944 (2013).

[38] K. Shen, G. Vignale, and R. Raimondi, "Microscopic Theory of the Inverse Edelstein Effect," Phys. Rev. Lett. **112**, 096601 (2014).

[39] A. Manchon, H. C. Koo, J. Nitta, S. M. Frolov, and R. A. Duine, "New perspectives for Rashba spin-orbit coupling," Nat. Mater. **14**, 871 (2015).

[40] J. Nitta, "Spin–orbit interaction and spintronics," JSAP Review **2023**, 230102 (2023).

[41] G. Dresselhaus, "Spin-Orbit Coupling Effects in Zinc Blende Structures," Phys. Rev. **100**, 580 (1955).

[42] R. Winkler, "*Spin-Orbit Coupling Effects in Two-Dimensional Electron and Hole Systems*," Springer Tracts Mod. Phys. Vol. 191 (Springer, Berlin, 2003) (2003).

[43] B. A. Bernevig, J. Orenstein, and S.-C. Zhang, "Exact SU(2) Symmetry and Persistent Spin Helix in a Spin-Orbit Coupled System," Phys. Rev. Lett. **97**, 236601 (2006).

[44] C. P. Weber, J. Orenstein, B. A. Bernevig, S.-C. Zhang, J. Stephens, and D. D. Awschalom, "Nondiffusive Spin Dynamics in a Two-Dimensional Electron Gas," Phys. Rev. Lett. **98**, 076604 (2007).

[45] J. D. Koralek, C. P. Weber, J. Orenstein, B. A. Bernevig, S.-C. Zhang, S. Mack, and D. D. Awschalom, "Emergence of the persistent spin helix in semiconductor quantum wells," Nature (London) **458**, 610 (2009).

[46] M. Kohda, V. Lechner, Y. Kunihashi, T. Dollinger, P. Olbrich, C. Schönhuber, I. Caspers, V. V. Bel'kov, L. E. Golub, D. Weiss, K. Richter, J. Nitta, and S. D. Ganichev, "Gate-controlled persistent spin helix state in (In,Ga)As quantum wells," Phys. Rev. B **86**, 081306(R) (2012).

[47] A. Sasaki, S. Nonaka, Y. Kunihashi, M. Kohda, T. Bauernfeind, T. Dollinger, K. Richter, and J. Nitta, "Direct determination of spin–orbit interaction coefficients and realization of the persistent spin helix symmetry," Nat. Nanotechnol. **9**, 703 (2014).

[48] M. Yama, M. Matsuo, and T. Kato, "Effect of vertex corrections on the enhancement of Gilbert damping in spin pumping into a two-dimensional electron gas," Phys. Rev. B **107**, 174414 (2023).

[49] M. Yama, M. Matsuo, and T. Kato, "Theory of inverse Rashba-Edelstein effect induced by spin pumping into a two-dimensional electron gas," Phys. Rev. B **108**, 144430 (2023).

[50] M. Yama, M. Matsuo, and T. Kato, "Microscopic Theory of Rashba-Edelstein Magnetoresistance," arXiv preprint arXiv:2409.00874 (2024).

[51] M. Yama, M. Matsuo, and T. Kato, "Theory of spin pumping and inverse Rashba-Edelstein effect in a two-dimensional electron gas," in [*Spintronics XVII*], J.-E. Wegrowe, J. S. Friedman, M. Razeghi, and H. Jaffrès, eds., **13119**, 131190J, International Society for Optics and Photonics, SPIE (2024).

[52] M. Yama, M. Matsuo, and T. Kato, "Theory of spin pumping and inverse Rashba-Edelstein effect in a two-dimensional electron gas (Erratum)," in [*Spintronics XVII*], J.-E. Wegrowe, J. S. Friedman, M. Razeghi, and H. Jaffrès, eds., **13119**, 131190O, International Society for Optics and Photonics, SPIE (2024).

[53] T. Aruga and S. Hatta, "Rashba Effect at Surfaces," J. Vac. Soc. Japan **52**, 577 (2009).

[54] M. Nagano, A. Kodama, T. Shishidou, and T. Oguchi, "A first-principles study on the Rashba effect in surface systems," J. Phys.: Condens. Matter **21**, 064239 (2009).

[55] R. Noguchi, K. Kuroda, M. Kawamura, K. Yaji, A. Harasawa, T. Iimori, S. Shin, F. Komori, T. Ozaki, and T. Kondo, "Scaling law for Rashba-type spin splitting in quantum-well films," Phys. Rev. B **104**, L180409 (2021).

[56] Y. M. Koroteev, G. Bihlmayer, J. E. Gayone, E. V. Chulkov, S. Blügel, P. M. Echenique, and P. Hofmann, "Strong Spin-Orbit Splitting on Bi Surfaces," Phys. Rev. Lett. **93**, 046403 (2004).

[57] C. R. Ast, J. Henk, A. Ernst, L. Moreschini, M. C. Falub, D. Pacilé, P. Bruno, K. Kern, and M. Grioni, "Giant Spin Splitting through Surface Alloying," Phys. Rev. Lett. **98**, 186807 (2007).

[58] F. Nagasawa, A. A. Reynoso, J. P. Baltanás, D. Frustaglia, H. Saarikoski, and J. Nitta, "Gate-controlled anisotropy in Aharonov-Casher spin interference: Signatures of Dresselhaus spin-orbit inversion and spin phases," Phys. Rev. B **98**, 245301 (2018).

[59] Y. Kunihashi, H. Sanada, H. Gotoh, K. Onomitsu, M. Kohda, J. Nitta, and T. Sogawa, "Drift transport of helical spin coherence with tailored spin–orbit interactions," Nature communications **7**, 10722 (2016).

[60] S. V. Vonsovskii, "*Ferromagnetic Resonance: The Phenomenon of Resonant Absorption of a High-Frequency Magnetic Field in Ferromagnetic Substances*," Pergamon, Oxford (1966).

[61] T. Gilbert, "A phenomenological theory of damping in ferromagnetic materials," IEEE Trans. Magn. **40**, 3443 (2004).

[62] G. Tatara, "*Physics of Spintronics: From the Perspective of Field Theory*," Uchida Rokakuho, Tokyo, Japan (2019). In Japanese.

[63] T. Funato, T. Kato, and M. Matsuo, "Spin pumping into anisotropic Dirac electrons," Phys. Rev. B **106**, 144418 (2022).

[64] H. L. Wang, C. H. Du, Y. Pu, R. Adur, P. C. Hammel, and F. Y. Yang, "Scaling of Spin Hall Angle in 3d, 4d, and 5d Metals from $Y_3Fe_5O_{12}$/Metal Spin Pumping," Phys. Rev. Lett. **112**, 197201 (2014).

[65] F. Yang and P. C. Hammel, "FMR-driven spin pumping in $Y_3Fe_5O_{12}$-based structures," J. Phys. D: Appl. Phys. **51**, 253001 (2018).

[66] Y. K. Kato, R. C. Myers, A. C. Gossard, and D. D. Awschalom, "Observation of the Spin Hall Effect in Semiconductors," Science **306**, 1910 (2004).

[67] J. Wunderlich, B. Kaestner, J. Sinova, and T. Jungwirth, "Experimental Observation of the Spin-Hall Effect in a Two-Dimensional Spin-Orbit Coupled Semiconductor System," Phys. Rev. Lett. **94**, 047204 (2005).

[68] Y. Tserkovnyak, A. Brataas, G. E. W. Bauer, and B. I. Halperin, "Nonlocal magnetization dynamics in ferromagnetic heterostructures," Rev. Mod. Phys. **77**, 1375 (2005).

[69] M. Yama, "Theoretical study of spin pumping into a two-dimensional electron system with Rashba and Dresselhaus spin-orbit interactions," Master thesis, The Univ. of Tokyo (2022).

[70] Y. Ohnuma, H. Adachi, E. Saitoh, and S. Maekawa, "Enhanced dc spin pumping into a fluctuating ferromagnet near T_C," Phys. Rev. B **89**, 174417 (2014).

[71] M. Matsuo, Y. Ohnuma, T. Kato, and S. Maekawa, "Spin Current Noise of the Spin Seebeck Effect and Spin Pumping," Phys. Rev. Lett. **120**, 037201 (2018).

[72] T. Kato, Y. Ohnuma, M. Matsuo, J. Rech, T. Jonckheere, and T. Martin, "Microscopic theory of spin transport at the interface between a superconductor and a ferromagnetic insulator," Phys. Rev. B **99**, 144411 (2019).

[73] T. Kato, Y. Ohnuma, and M. Matsuo, "Microscopic theory of spin Hall magnetoresistance," Phys. Rev. B **102**, 094437 (2020).

[74] Y. Ominato and M. Matsuo, "Quantum Oscillations of Gilbert Damping in Ferromagnetic/Graphene Bilayer Systems," J. Phys. Soc. Jpn. **89**, 053704 (2020).

[75] Y. Ominato, J. Fujimoto, and M. Matsuo, "Valley-Dependent Spin Transport in Monolayer Transition-Metal Dichalcogenides," Phys. Rev. Lett. **124**, 166803 (2020).

[76] Y. Ominato, A. Yamakage, T. Kato, and M. Matsuo, "Ferromagnetic resonance modulation in d-wave superconductor/ferromagnetic insulator bilayer systems," Phys. Rev. B **105**, 205406 (2022).

[77] H. Tajima, D. Oue, and M. Matsuo, "Multiparticle tunneling transport at strongly correlated interfaces," Phys. Rev. A **106**, 033310 (2022).

[78] M. Yama, M. Tatsuno, T. Kato, and M. Matsuo, "Spin pumping of two-dimensional electron gas with Rashba and Dresselhaus spin-orbit interactions," Phys. Rev. B **104**, 054410 (2021).

[79] K. Hosokawa, M. Yama, M. Matsuo, and T. Kato, "Theory of the inverse Rashba-Edelstein effect induced by thermal spin injection," Phys. Rev. B **110**, 035309 (2024).

[80] R. H. Silsbee, "Spin–orbit induced coupling of charge current and spin polarization," J. Phys.: Condens. Matter **16**, R179 (2004).

[81] Y. Suzuki and Y. Kato, "Spin relaxation, diffusion, and Edelstein effect in chiral metal surface," Phys. Rev. B **107**, 115305 (2023).

[82] A. Johansson, "Theory of spin and orbital Edelstein effects," J. Phys.: Condens. Matter **36**, 423002 (2024).

[83] Y. Kato, Y. Suzuki, T. Sato, H. M. Yamamoto, Y. Togawa, H. Kusunose, and J.-i. Kishine, "Chirality-dependent spin polarization in diffusive metals: linear and quadratic responses," arXiv preprint arXiv:2408.04450 (2024).

[84] S. D. Ganichev, V. V. Bel'kov, L. E. Golub, E. L. Ivchenko, P. Schneider, S. Giglberger, J. Eroms, J. De Boeck, G. Borghs, W. Wegscheider, D. Weiss, and W. Prettl, "Experimental Separation of Rashba and Dresselhaus Spin Splittings in Semiconductor Quantum Wells," Phys. Rev. Lett. **92**, 256601 (2004).

[85] H. Isshiki, P. Muduli, J. Kim, K. Kondou, and Y. Otani, "Phenomenological model for the direct and inverse Edelstein effects," Phys. Rev. B **102**, 184411 (2020).

[86] A. Nomura, T. Tashiro, H. Nakayama, and K. Ando, "Temperature dependence of inverse Rashba-Edelstein effect at metallic interface," Appl. Phys. Lett. **106**, 212403 (2015).

[87] S. Sangiao, J. M. De Teresa, L. Morellon, I. Lucas, M. C. Martínez-Velarte, and M. Viret, "Control of the spin to charge conversion using the inverse Rashba-Edelstein effect," Appl. Phys. Lett. **106**, 172403 (2015).

[88] W. Zhang, M. B. Jungfleisch, W. Jiang, J. E. Pearson, and A. Hoffmann, "Spin pumping and inverse Rashba-Edelstein effect in NiFe/Ag/Bi and NiFe/Ag/Sb," J. Appl. Phys. **117**, 17C727 (2015).

[89] M. Matsushima, Y. Ando, S. Dushenko, R. Ohshima, R. Kumamoto, T. Shinjo, and M. Shiraishi, "Quantitative investigation of the inverse Rashba-Edelstein effect in Bi/Ag and Ag/Bi on YIG," Appl. Phys. Lett. **110**, 072404 (2017).

[90] Y. Shiomi, K. Nomura, Y. Kajiwara, K. Eto, M. Novak, K. Segawa, Y. Ando, and E. Saitoh, "Spin-Electricity Conversion Induced by Spin Injection into Topological Insulators," Phys. Rev. Lett. **113**, 196601 (2014).

[91] J.-C. Rojas-Sánchez, S. Oyarzún, Y. Fu, A. Marty, C. Vergnaud, S. Gambarelli, L. Vila, M. Jamet, Y. Ohtsubo, A. Taleb-Ibrahimi, P. Le Fèvre, F. Bertran, N. Reyren, J.-M. George, and A. Fert, "Spin to Charge Conversion at Room Temperature by Spin Pumping into a New Type of Topological Insulator: α-Sn Films," Phys. Rev. Lett. **116**, 096602 (2016).

[92] H. Wang, J. Kally, J. S. Lee, T. Liu, H. Chang, D. R. Hickey, K. A. Mkhoyan, M. Wu, A. Richardella, and N. Samarth, "Surface-State-Dominated Spin-Charge Current Conversion in Topological-Insulator–Ferromagnetic-Insulator Heterostructures," Phys. Rev. Lett. **117**, 076601 (2016).

[93] Q. Song, J. Mi, D. Zhao, T. Su, W. Yuan, W. Xing, Y. Chen, T. Wang, T. Wu, X. H. Chen, X. C. Xie, C. Zhang, J. Shi, and W. Han, "Spin injection and inverse Edelstein effect in the surface states of topological Kondo insulator SmB_6," Nat. Commun. **7**, 13485 (2016).

[94] J. B. S. Mendes, O. Alves Santos, J. Holanda, R. P. Loreto, C. I. L. de Araujo, C.-Z. Chang, J. S. Moodera, A. Azevedo, and S. M. Rezende, "Dirac-surface-state-dominated spin to charge current conversion in the topological insulator $(Bi_{0.22}Sb_{0.78})_2Te_3$ films at room temperature," Phys. Rev. B **96**, 180415(R) (2017).

[95] R. Sun, S. Yang, X. Yang, E. Vetter, D. Sun, N. Li, L. Su, Y. Li, Y. Li, Z.-z. Gong, Z.-k. Xie, K.-y. Hou, Q. Gul, W. He, X.-q. Zhang, and Z.-h. Cheng, "Large Tunable Spin-to-Charge Conversion Induced by Hybrid Rashba and Dirac Surface States in Topological Insulator Heterostructures," Nano Lett. **19**, 4420 (2019).

[96] B. B. Singh, S. K. Jena, M. Samanta, K. Biswas, and S. Bedanta, "High Spin to Charge Conversion Efficiency in Electron Beam-Evaporated Topological Insulator Bi_2Se_3," ACS Appl. Mater. Interfaces **12**, 53409 (2020).

[97] R. Dey, A. Roy, L. F. Register, and S. K. Banerjee, "Recent progress on measurement of spin–charge interconversion in topological insulators using ferromagnetic resonance," APL Mater. **9**, 060702 (2021).

[98] H. He, L. Tai, H. Wu, D. Wu, A. Razavi, T. A. Gosavi, E. S. Walker, K. Oguz, C.-C. Lin, K. Wong, Y. Liu, B. Dai, and K. L. Wang, "Conversion between spin and charge currents in topological-insulator/nonmagnetic-metal systems," Phys. Rev. B **104**, L220407 (2021).

[99] S. Zhang and A. Fert, "Conversion between spin and charge currents with topological insulators," Phys. Rev. B **94**, 184423 (2016).

[100] E. Lesne, Y. Fu, S. Oyarzun, J. C. Rojas-Sánchez, D. C. Vaz, H. Naganuma, G. Sicoli, J.-P. Attané, M. Jamet, E. Jacquet, J.-M. George, A. Barthélémy, H. Jaffrès, A. Fert, M. Bibes, and L. Vila, "Highly efficient and tunable spin-to-charge conversion through Rashba coupling at oxide interfaces," Nat. Mater. **15**, 1261 (2016).

[101] Q. Song, H. Zhang, T. Su, W. Yuan, Y. Chen, W. Xing, J. Shi, J. Sun, and W. Han, "Observation of inverse Edelstein effect in Rashba-split 2DEG between $SrTiO_3$ and $LaAlO_3$ at room temperature," Sci. Adv. **3**, e1602312 (2017).

[102] D. C. Vaz, P. Noël, A. Johansson, B. Göbel, F. Y. Bruno, G. Singh, S. Mckeown-Walker, F. Trier, L. M. Vicente-Arche, A. Sander, S. Valencia, P. Bruneel, M. Vivek, M. Gabay, N. Bergeal, F. Baumberger, H. Okuno, A. Barthélémy, A. Fert, L. Vila, I. Mertig, J.-P. Attané, and M. Bibes, "Mapping spin-charge conversion to the band structure in a topological oxide two-dimensional electron gas," Nat. Mater. **18**, 1187 (2019).

[103] P. Noël, F. Trier, L. M. Vicente Arche, J. Bréhin, D. C. Vaz, V. Garcia, S. Fusil, A. Barthélémy, L. Vila, M. Bibes, and J.-P. Attané, "Non-volatile electric control of spin-charge conversion in a $SrTiO_3$ Rashba system," Nature (London) **580**, 483 (2020).

[104] S. Ohya, D. Araki, L. D. Anh, S. Kaneta, M. Seki, H. Tabata, and M. Tanaka, "Efficient intrinsic spin-to-charge current conversion in an all-epitaxial single-crystal perovskite-oxide heterostructure of $La_{0.67}Sr_{0.33}MnO_3/LaAlO_3/SrTiO_3$," Phys. Rev. Res. **2**, 012014(R) (2020).

[105] P. Bruneel and M. Gabay, "Spin texture driven spintronic enhancement at the $LaAlO_3/SrTiO_3$ interface," Phys. Rev. B **102**, 144407 (2020).

[106] D. Q. To, T. H. Dang, L. Vila, J. P. Attané, M. Bibes, and H. Jaffrès, "Spin to charge conversion at Rashba-split $SrTiO_3$ interfaces from resonant tunneling," Phys. Rev. Res. **3**, 043170 (2021).

[107] F. Trier, P. Noël, J.-V. Kim, J.-P. Attané, L. Vila, and M. Bibes, "Oxide spin-orbitronics: spin-charge interconversion and topological spin textures," Nat. Rev. Mater. **7**, 258 (2022).

[108] J. B. S. Mendes, O. Alves Santos, L. M. Meireles, R. G. Lacerda, L. H. Vilela-Leão, F. L. A. Machado, R. L. Rodríguez-Suárez, A. Azevedo, and S. M. Rezende, "Spin-Current to Charge-Current Conversion and Magnetoresistance in a Hybrid Structure of Graphene and Yttrium Iron Garnet," Phys. Rev. Lett. **115**, 226601 (2015).

[109] S. Dushenko, H. Ago, K. Kawahara, T. Tsuda, S. Kuwabata, T. Takenobu, T. Shinjo, Y. Ando, and M. Shiraishi, "Gate-Tunable Spin-Charge Conversion and the Role of Spin-Orbit Interaction in Graphene," Phys. Rev. Lett. **116**, 166102 (2016).

[110] J. B. S. Mendes, O. Alves Santos, T. Chagas, R. Magalhães Paniago, T. J. A. Mori, J. Holanda, L. M. Meireles, R. G. Lacerda, A. Azevedo, and S. M. Rezende, "Direct detection of induced magnetic moment and efficient spin-to-charge conversion in graphene/ferromagnetic structures," Phys. Rev. B **99**, 214446 (2019).

[111] H. Bangar, A. Kumar, N. Chowdhury, R. Mudgal, P. Gupta, R. S. Yadav, S. Das, and P. K. Muduli, "Large Spin-To-Charge Conversion at the Two-Dimensional Interface of Transition-Metal Dichalcogenides and Permalloy," ACS Appl. Mater. Interfaces **14**, 41598 (2022).

[112] L. Chen, M. Decker, M. Kronseder, R. Islinger, M. Gmitra, D. Schuh, D. Bougeard, J. Fabian, D. Weiss, and C. H. Back, "Robust spin-orbit torque and spin-galvanic effect at the Fe/GaAs (001) interface at room temperature," Nat. Commun. **7**, 13802 (2016).

[113] S. Oyarzún, A. Nandy, F. Rortais, J.-C. Rojas-Sánchez, M.-T. Dau, P. Noël, P. Laczkowski, S. Pouget, H. Okuno, L. Vila, C. Vergnaud, C. Beigné, A. Marty, J.-P. Attané, S. Gambarelli, J.-M. George, H. Jaffrès, S. Blügel, and M. Jamet, "Evidence for spin-to-charge conversion by Rashba coupling in metallic states at the Fe/Ge (111) interface," Nat. Commun. **7**, 13857 (2016).

[114] R. H. Silsbee, "Theory of the detection of current-induced spin polarization in a two-dimensional electron gas," Phys. Rev. B **63**, 155305 (2001).

[115] S. Tölle, U. Eckern, and C. Gorini, "Spin-charge coupled dynamics driven by a time-dependent magnetization," Phys. Rev. B **95**, 115404 (2017).

[116] R. Dey, N. Prasad, L. F. Register, and S. K. Banerjee, "Conversion of spin current into charge current in a topological insulator: Role of the interface," Phys. Rev. B **97**, 174406 (2018).

[117] J. Bardeen, "Tunnelling from a Many-Particle Point of View," Phys. Rev. Lett. **6**, 57 (1961).

[118] H. Nakayama, Y. Kanno, H. An, T. Tashiro, S. Haku, A. Nomura, and K. Ando, "Rashba-Edelstein Magnetoresistance in Metallic Heterostructures," Phys. Rev. Lett. **117**, 116602 (2016).

[119] H. Nakayama, M. Althammer, Y.-T. Chen, K. Uchida, Y. Kajiwara, D. Kikuchi, T. Ohtani, S. Geprägs, M. Opel, S. Takahashi, R. Gross, G. E. W. Bauer, S. T. B. Goennenwein, and E. Saitoh, "Spin Hall Magnetoresistance Induced by a Nonequilibrium Proximity Effect," Phys. Rev. Lett. **110**, 206601 (2013).

[120] Y.-T. Chen, S. Takahashi, H. Nakayama, M. Althammer, S. T. B. Goennenwein, E. Saitoh, and G. E. W. Bauer, "Theory of spin Hall magnetoresistance," Phys. Rev. B **87**, 144411 (2013).

[121] T. Ishikawa, M. Matsuo, and T. Kato, "Spin Hall magnetoresistance in quasi-two-dimensional antiferromagnetic-insulator/metal bilayer systems," Phys. Rev. B **107**, 054426 (2023).

[122] X.-P. Zhang, F. S. Bergeret, and V. N. Golovach, "Theory of Spin Hall Magnetoresistance from a Microscopic Perspective," Nano Lett. **19**, 6330 (2019).

[123] S. Vélez, V. N. Golovach, J. M. Gomez-Perez, A. Chuvilin, C. T. Bui, F. Rivadulla, L. E. Hueso, F. S. Bergeret, and F. Casanova, "Spin Hall magnetoresistance in a low-dimensional Heisenberg ferromagnet," Phys. Rev. B **100**, 180401(R) (2019).

[124] K. Sugi, T. Ishikawa, M. Kimata, Y. Shiota, T. Ono, T. Kato, and T. Moriyama, "Spin Hall magnetoresistive detection of easy-plane magnetic order in the van der Waals antiferromagnet $NiPS_3$," Phys. Rev. B **108**, 064434 (2023).

[125] H. Nakayama, H. An, A. Nomura, Y. Kanno, S. Haku, Y. Kuwahara, H. Sakimura, and K. Ando, "Temperature dependence of Rashba-Edelstein magnetoresistance in Bi/Ag/CoFeB trilayer structures," Appl. Phys. Lett. **110**, 222406 (2017).

[126] H. Nakayama, T. Yamamoto, H. An, K. Tsuda, Y. Einaga, and K. Ando, "Molecular engineering of Rashba spin-charge converter," Sci. Adv. **4**, eaar3899 (2018).

[127] J. Kim, Y.-T. Chen, S. Karube, S. Takahashi, K. Kondou, G. Tatara, and Y. Otani, "Evaluation of bulk-interface contributions to Edelstein magnetoresistance at metal/oxide interfaces," Phys. Rev. B **96**, 140409(R) (2017).

[128] R. Thompson, J. Ryu, Y. Du, S. Karube, M. Kohda, and J. Nitta, "Current direction dependent spin Hall magnetoresistance in epitaxial Pt/Co bilayers on MgO(110)," Phys. Rev. B **101**, 214415 (2020).

[129] Y. Du, S. Takahashi, and J. Nitta, "Spin current related magnetoresistance in epitaxial Pt/Co bilayers in the presence of spin Hall effect and Rashba-Edelstein effect," Phys. Rev. B **103**, 094419 (2021).

[130] L. Zhou, H. Song, K. Liu, Z. Luan, P. Wang, L. Sun, S. Jiang, H. Xiang, Y. Chen, J. Du, H. Ding, K. Xia, J. Xiao, and D. Wu, "Observation of spin-orbit magnetoresistance in metallic thin films on magnetic insulators," Sci. Adv. **4**, eaao3318 (2018).

[131] K. Narayanapillai, G. Go, R. Ramaswamy, K. Gopinadhan, D. Go, H.-W. Lee, T. Venkatesan, K.-J. Lee, and H. Yang, "Interfacial Rashba magnetoresistance of the two-dimensional electron gas at the $LaAlO_3/SrTiO_3$ interface," Phys. Rev. B **96**, 064401 (2017).

[132] J. B. S. Mendes, S. M. Rezende, and J. Holanda, "Rashba-Edelstein magnetoresistance in two-dimensional materials at room temperature," Phys. Rev. B **104**, 014408 (2021).

[133] V. L. Grigoryan, W. Guo, G. E. W. Bauer, and J. Xiao, "Intrinsic magnetoresistance in metal films on ferromagnetic insulators," Phys. Rev. B **90**, 161412(R) (2014).

[134] S. S.-L. Zhang and S. Zhang, "Angular dependence of anisotropic magnetoresistance in magnetic systems," J. Appl. Phys. **115**, 17C703 (2014).

[135] S. S.-L. Zhang, G. Vignale, and S. Zhang, "Anisotropic magnetoresistance driven by surface spin-orbit scattering," Phys. Rev. B **92**, 024412 (2015).

[136] R. Iguchi, K. Sato, K. ichi Uchida, and E. Saitoh, "Spin-current-induced magnetoresistance in trilayer structure with nonmagnetic metallic interlayer," Jpn. J. Appl. Phys. **56**, 040306 (2017).

[137] S. Tölle, M. Dzierzawa, U. Eckern, and C. Gorini, "Spin Hall Magnetoresistance and Spin Nernst Magnetothermopower in a Rashba System: Role of the Inverse Spin Galvanic Effect," Ann. Phys. (Berlin) **530**, 1700303 (2018).

[138] S. Tölle, M. Dzierzawa, U. Eckern, and C. Gorini, "Quasiclassical theory of the spin–orbit magnetoresistance of three-dimensional Rashba metals," New J. Phys. **20**, 103024 (2018).

[139] C. Sanz-Fernández, V. T. Pham, E. Sagasta, L. E. Hueso, I. V. Tokatly, F. Casanova, and F. S. Bergeret, "Quantification of interfacial spin-charge conversion in hybrid devices with a metal/insulator interface," Appl. Phys. Lett. **117**, 142405 (2020).

[140] W. W. Silva and J. Holanda, "One analytical approach of Rashba–Edelstein magnetoresistance in 2D materials," Eur. Phys. J. B **96**, 47 (2023).

[141] A. Khaetskii, "Nonexistence of Intrinsic Spin Currents," Phys. Rev. Lett. **96**, 056602 (2006).

[142] A. Shitade and G. Tatara, "Spin accumulation without spin current," Phys. Rev. B **105**, L201202 (2022).

[143] V. Umansky, R. de Picciotto, and M. Heiblum, "Extremely high-mobility two dimensional electron gas: Evaluation of scattering mechanisms," Appl. Phys. Lett. **71**, 683 (1997).

[144] K. Výborný, A. A. Kovalev, J. Sinova, and T. Jungwirth, "Semiclassical framework for the calculation of transport anisotropies," Phys. Rev. B **79**, 045427 (2009).

[145] M. Trushin, K. Výborný, P. Moraczewski, A. A. Kovalev, J. Schliemann, and T. Jungwirth, "Anisotropic magnetoresistance of spin-orbit coupled carriers scattered from polarized magnetic impurities," Phys. Rev. B **80**, 134405 (2009).

[146] J. B. Miller, D. M. Zumbühl, C. M. Marcus, Y. B. Lyanda-Geller, D. Goldhaber-Gordon, K. Campman, and A. C. Gossard, "Gate-Controlled Spin-Orbit Quantum Interference Effects in Lateral Transport," Phys. Rev. Lett. **90**, 076807 (2003).

[147] W. T. Masselink, P. J. Pearah, J. Klem, C. K. Peng, H. Morkoç, G. D. Sanders, and Y.-C. Chang, "Absorption coefficients and exciton oscillator strengths in AlGaAs-GaAs superlattices," Phys. Rev. B **32**, 8027 (1985).

[148] H. Bruus and K. Flensberg, "*Many-Body Quantum Theory in Condensed Matter Physics*," Oxford University Press, Oxford (2004).

[149] G. Baym, "Self-Consistent Approximations in Many-Body Systems," Phys. Rev. **127**, 1391 (1962).

[150] L. P. Kadanoff and G. Baym, "*Quantum Statistical Mechanics*," Benjamin, New York (1962).

[151] P. Fulde and A. Luther, "Spin Relaxation and Transport in Magnetic Alloys," Phys. Rev. **175**, 337 (1968).

[152] E. Akkermans and G. Montambaux, "*Mesoscopic Physics of Electrons and Photons*," Cambridge University Press, Cambridge, UK (2007).

[153] E. E. Mendez, P. J. Price, and M. Heiblum, "Temperature dependence of the electron mobility in GaAs- GaAlAs heterostructures," Appl. Phys. Lett. **45**, 294 (1984).

[154] S. Datta, "*Electronic Transport in Mesoscopic Systems*," Cambridge University Press, Cambridge, England (1997).

[155] J.-i. Inoue, G. E. W. Bauer, and L. W. Molenkamp, "Suppression of the persistent spin Hall current by defect scattering," Phys. Rev. B **70**, 041303(R) (2004).

[156] J.-i. Inoue, T. Kato, Y. Ishikawa, H. Itoh, G. E. W. Bauer, and L. W. Molenkamp, "Vertex Corrections to the Anomalous Hall Effect in Spin-Polarized Two-Dimensional Electron Gases with a Rashba Spin-Orbit Interaction," Phys. Rev. Lett. **97**, 046604 (2006).

[157] A. V. Sadovnikov, E. N. Beginin, S. E. Sheshukova, Y. P. Sharaevskii, A. I. Stognij, N. N. Novitski, V. K. Sakharov, Y. V. Khivintsev, and S. A. Nikitov, "Route toward semiconductor magnonics: Light-induced spin-wave nonreciprocity in a YIG/GaAs structure," Phys. Rev. B **99**, 054424 (2019).

[158] S. A. Nikitov, A. R. Safin, D. V. Kalyabin, A. V. Sadovnikov, E. N. Beginin, M. V. Logunov, M. A. Morozova, S. A. Odintsov, S. A. Osokin, A. Y. Sharaevskaya, Y. P. Sharaevsky, and A. I. Kirilyuk, "Dielectric magnonics: from gigahertz to terahertz," Phys. Usp. **63**, 945 (2020).

[159] A. Barman, G. Gubbiotti, S. Ladak, A. O. Adeyeye, M. Krawczyk, J. Gräfe, C. Adelmann, S. Cotofana, A. Naeemi, V. I. Vasyuchka, B. Hillebrands, S. A. Nikitov, H. Yu, D. Grundler, A. V. Sadovnikov, A. A. Grachev, S. E. Sheshukova, J.-Y. Duquesne, M. Marangolo, G. Csaba, W. Porod, V. E. Demidov, S. Urazhdin, S. O. Demokritov, E. Albisetti, D. Petti, R. Bertacco, H. Schultheiss, V. V. Kruglyak, V. D. Poimanov, S. Sahoo, J. Sinha, H. Yang, M. Münzenberg, T. Moriyama, S. Mizukami, P. Landeros, R. A. Gallardo, G. Carlotti, J.-V. Kim, R. L. Stamps, R. E. Camley, B. Rana, Y. Otani, W. Yu, T. Yu, G. E. W. Bauer, C. Back, G. S. Uhrig, O. V. Dobrovolskiy, B. Budinska, H. Qin, S. van Dijken, A. V. Chumak, A. Khitun, D. E. Nikonov, I. A. Young, B. W. Zingsem, and M. Winklhofer, "The 2021 Magnonics Roadmap," J. Phys.: Condens. Matter **33**, 413001 (2021).

[160] D. L. Rode and S. Knight, "Electron Transport in GaAs," Phys. Rev. B **3**, 2534 (1971).

[161] D. L. Rode, "*Low-Field Electron Transport*," edited by R. K. Willardson and A. C. Beer, Academic Press, New York (1975).

[162] M. Levinshtein, S. Rumyantsev, and M. Shur, "*Handbook Series on Semiconductor Parameters*," Vol. 1, World Scientific, London (1996).

[163] A. Kindyak, A. Boardman, and V. Kindyak, "Surface magnetostatic spin wave envelope solitons in ferrite semiconductor structure," J. Magn. Magn. Mater. **253**, 8 (2002).

[164] J. Nogués and I. K. Schuller, "Exchange bias," J. Magn. Magn. Mater. **192**, 203 (1999).

[165] O. Rousseau, C. Gorini, F. Ibrahim, J.-Y. Chauleau, A. Solignac, A. Hallal, S. Tölle, M. Chshiev, and M. Viret, "Spin-charge conversion in ferromagnetic Rashba states," Phys. Rev. B **104**, 134438 (2021).

[166] L. Szolnoki, B. Dóra, A. Kiss, J. Fabian, and F. Simon, "Intuitive approach to the unified theory of spin relaxation," Phys. Rev. B **96**, 245123 (2017).

[167] D. Go, D. Jo, H.-W. Lee, M. Kläui, and Y. Mokrousov, "Orbitronics: Orbital currents in solids," Europhys. Lett. **135**, 37001 (2021).

[168] D. Jo, D. Go, G.-M. Choi, and H.-W. Lee, "Spintronics meets orbitronics: Emergence of orbital angular momentum in solids," npj Spintronics **2**, 19 (2024).

[169] P. Tang and G. E. W. Bauer, "Role of Disorder in the Intrinsic Orbital Hall Effect," Phys. Rev. Lett. **133**, 186302 (2024).

[170] T. Adamantopoulos, M. Merte, D. Go, F. Freimuth, S. Blügel, and Y. Mokrousov, "Orbital Rashba Effect as a Platform for Robust Orbital Photocurrents," Phys. Rev. Lett. **132**, 076901 (2024).

[171] H. Hayashi, D. Go, S. Haku, Y. Mokrousov, and K. Ando, "Observation of orbital pumping," Nat. Electron. **7**, 646 (2024).

[172] D. Go, K. Ando, A. Pezo, S. Blügel, A. Manchon, and Y. Mokrousov, "Orbital Pumping by Magnetization Dynamics in Ferromagnets," arXiv preprint arXiv:2309.14817 (2023).

[173] A. El Hamdi, J.-Y. Chauleau, M. Boselli, C. Thibault, C. Gorini, A. Smogunov, C. Barreteau, S. Gariglio, J.-M. Triscone, and M. Viret, "Observation of the orbital inverse Rashba–Edelstein effect," Nat. Phys. **19**, 1855 (2023).

[174] S. Ding, Z. Liang, D. Go, C. Yun, M. Xue, Z. Liu, S. Becker, W. Yang, H. Du, C. Wang, Y. Yang, G. Jakob, M. Kläui, Y. Mokrousov, and J. Yang, "Observation of the Orbital Rashba-Edelstein Magnetoresistance," Phys. Rev. Lett. **128**, 067201 (2022).

[175] I. A. Ado, O. A. Tretiakov, and M. Titov, "Microscopic theory of spin-orbit torques in two dimensions," Phys. Rev. B **95**, 094401 (2017).

[176] D. Fang, H. Kurebayashi, J. Wunderlich, K. Vỳbornỳ, L. P. Zârbo, R. Campion, A. Casiraghi, B. Gallagher, T. Jungwirth, and A. Ferguson, "Spin-orbit-driven ferromagnetic resonance," Nat. Nanotechnol. **6**, 413 (2011).

[177] J. Leo and A. H. MacDonald, "Disorder-assisted tunneling through a double-barrier structure," Phys. Rev. Lett. **64**, 817 (1990).

[178] A. V. Shytov, E. G. Mishchenko, H.-A. Engel, and B. I. Halperin, "Small-angle impurity scattering and the spin Hall conductivity in two-dimensional semiconductor systems," Phys. Rev. B **73**, 075316 (2006).

[179] T. Kita, "Quantum Transport Equation and Nonequilibrium Entropy: Nonequilibrium Statistical Mechanics Using Quantum Field Theory," Bussei Kenkyu **90**, 1 (2008). In Japanese.

[180] T. Kita, "Introduction to Nonequilibrium Statistical Mechanics with Quantum Field Theory," Prog. Theor. Phys. **123**, 581 (2010).